



Provided by the author(s) and University of Galway in accordance with publisher policies. Please cite the published version when available.

Title	Physical and numerical modelling of impeded tidal flows: Effects of aquaculture structures on hydrodynamics and material transport
Author(s)	O Donohue, Fearghal
Publication Date	2012-04-13
Item record	<a href="http://hdl.handle.net/10379/3066">http://hdl.handle.net/10379/3066</a>

Downloaded 2024-04-18T04:37:42Z

Some rights reserved. For more information, please see the item record link above.



# **Physical and numerical modelling of impeded tidal flows: Effects of aquaculture structures on hydrodynamics and material transport**

by Fearghal O Donohue

Supervisor: Dr. Michael Hartnett



A thesis submitted in partial fulfillment of the requirements for the degree of  
Doctor of Philosophy,  
in the College of Engineering and Informatics

April 2012



## **Abstract**

---

The effects of aquaculture structures on flows are investigated in this thesis through a two-pronged approach. Small-scale flow interactions between the structures and the surrounding waterbody are studied through physical model studies conducted in a tidal basin facility. The second approach is the use of numerical models to investigate the far-field effects of the structures on hydrodynamic and transport patterns. Two separate models are used: a two-dimensional, model (DIVAST); and a three-dimensional, model (EFDC).

Laboratory studies show that the local near-field effects of the aquaculture structures are significant; results demonstrate that flow speeds within the scaled long-line structure are reduced by 25-40% from ambient, while material transport distances are reduced by up to 50%. Scale model investigations of flows through bottom-feeding aquaculture installations were also conducted.

An existing two-dimensional depth integrated model has been refined to better predict hydrodynamics and solute transport within suspended aquaculture farms. The numerical model has been refined to include both the form drag imparted by the individual mussel droppers and the blockage effect that the suspended canopy presents. It has been demonstrated that predicted velocities and solute transport correlate well with experimental results. The numerical model was applied to a designated aquaculture site. The effects of long-lines on hydrodynamics and solute transport were analysed. Flushing studies were used to study particle renewal terms in the embayment.

During this research the EFDC model was amended to include the effects of a suspended canopy, with free-stream flows developing beneath. The canopy was shown to have significant effects on the vertical structure of the flow regime; retarded flows are developed within the canopy and accelerated flows developed beneath the canopy. The model accurately predicts observed shear turbulence production at the bottom of the canopy; the associated implications for flow processes and mixing are discussed. A case study conducts numerical simulation of baroclinic flows within a partially stratified estuary with large-scale aquaculture developments. This development has broader applications than just suspended canopy flows. Natural and manufactured structural arrangements like kelp and sea grass beds, float breakwaters, and wave and offshore wind energy extraction arrays will all influence local currents.

## Table of contents

---

<b>Abstract .....</b>	<b>iii</b>
<b>Table of contents.....</b>	<b>v</b>
<b>List of figures .....</b>	<b>xii</b>
<b>List of tables .....</b>	<b>xxii</b>
<b>Declarations.....</b>	<b>xxiv</b>
<b>Acknowledgments.....</b>	<b>xxv</b>
<b>Mathematical notations.....</b>	<b>xxvii</b>
<b>Chapter 1 : Introduction.....</b>	<b>1</b>
1.1    General introduction.....	2
1.2    Physical modelling .....	2
1.3    Numerical modelling.....	4
1.4    Aims and scope of research.....	5
1.5    Thesis outline.....	7
<b>Chapter 2 : Literature review .....</b>	<b>9</b>
2.1    Introduction .....	10
2.2    Hydrodynamic effects of aquaculture structures.....	11
2.2.1 Effects on flows .....	11

2.2.2	Effects on mixing.....	19
2.3	Physical modelling literature review .....	23
2.3.1	Flow around single smooth cylinder.....	24
2.3.2	Surface roughness .....	26
2.3.3	Free-end effects.....	27
2.3.4	Cylinder arrays.....	28
2.3.5	Conclusions.....	31
2.4	Review of flushing analysis methods .....	32
2.4.1	Average residence time.....	34
2.4.2	Exchange per tidal cycle coefficient .....	35
2.4.3	Estuarine Residence Time and Pulse Residence Time .....	35
2.4.4	Conclusions.....	36
<b>Chapter 3</b>	<b>Description of numerical models .....</b>	<b>37</b>
3.1	Introduction .....	38
3.2	DIVAST model .....	38
3.2.1	Model history and description .....	38
3.2.2	Hydrodynamic and solute transport basic equations .....	40
3.2.3	Numerical representation of impeded flows .....	42
3.2.3.1	Dropper drag force .....	45
3.2.3.2	Mixing length turbulence model .....	46
3.2.4	Finite difference formulation .....	47
3.2.5	Hydrodynamic solution.....	50
3.2.6	Turbulence closure models .....	55

3.2.6.1	Two-equation k- $\epsilon$ model.....	58
3.2.6.2	Amended k- $\epsilon$ model.....	60
3.3	Environmental Fluid Dynamics Code (EFDC) model .....	64
3.3.1	Model history and description .....	64
3.3.2	Governing equations .....	65
3.3.2.1	Boundary conditions in sigma coordinate system .....	68
(a)	Vertical boundary conditions .....	68
(b)	Horizontal boundary conditions .....	69
3.3.2.2	Vertical mixing and turbulence models.....	70
3.3.2.3	Mode-splitting .....	71
3.3.2.4	External mode solution.....	72
3.3.2.5	Internal mode solution.....	75
3.3.3	Numerical representation of impeded flows .....	76
3.3.3.1	Hydrodynamic solution procedure .....	79
3.3.3.2	Amended turbulence closure model .....	82
	<b>Chapter 4 : Physical Modelling.....</b>	<b>88</b>
4.1	Introduction .....	89
4.2	Similitude .....	90
4.3	Dynamic similarity .....	92
4.4	Force relationships.....	94
4.4.1	Froude criterion.....	94
4.4.2	Reynolds criterion.....	95
4.5	Laboratory set-up.....	96

4.5.1	Tidal basin specifications.....	98
4.5.2	Data acquisition .....	99
4.6	Validation of tidal basin unit .....	101
4.7	Dampening of reflected flow.....	104
4.8	Laboratory tests and analysis.....	106
4.8.1	Scale model of mussel droppers .....	108
4.8.2	Smooth droppers .....	112
4.8.3	Roughened droppers .....	113
4.8.4	Scaled mussel dropper dye tracer experiment .....	116
4.9	Discussion.....	121
4.10	Scale modelling and difficulties encountered.....	121
<b>Chapter 5 : Two-dimensional numerical modelling.....</b>		<b>124</b>
5.1	Introduction .....	125
5.2	Numerical modelling.....	126
5.2.1	General circulation model.....	126
5.2.2	APM circulation patterns .....	128
5.2.3	Kinetic energy losses analysis .....	129
5.2.4	Numerical simulation of impeded flow .....	133
5.2.5	Effect of drag coefficient .....	135
5.2.6	Solute transport .....	138
5.3	Assessment of standard k- $\epsilon$ model.....	142
5.4	Assessment of modified k- $\epsilon$ model.....	145
5.5	Case study: Casheen Bay.....	148

5.5.1	General circulation model.....	148
5.5.2	Modelling of aquaculture installations.....	150
5.5.3	Flushing studies .....	158
5.6	Discussion and conclusions.....	162
<b>Chapter 6</b>	<b>: Three-dimensional numerical modelling.....</b>	<b>166</b>
6.1	Introduction .....	167
6.2	Experimental flow profile.....	168
6.3	General circulation model .....	172
6.4	Amended numerical model.....	173
6.4.1	Constant drag term model (CDM) .....	174
6.4.2	Drag and shear term model (DSM).....	179
6.4.3	Drag and turbulence model (DTM) .....	183
6.5	Variable drag coefficient .....	192
6.5.1	Dunn Lopez Garcia model (DLGM).....	193
6.5.2	Ghisalberti and Nepf model (GNM).....	200
6.5.3	EFDC Aquaculture Model (EAM).....	206
6.6	Discussion and conclusions.....	213
<b>Chapter 7</b>	<b>: Case study: Killary Harbour .....</b>	<b>217</b>
7.1	Introduction .....	218
7.1	Physical features and hydrography of Killary Harbour.....	219
7.1.1	Geographical distribution and topography.....	219
7.1.2	Tidal currents and general circulation.....	219
7.2	Implementation of EFDC model .....	221

7.2.1 Model set-up .....	221
7.2.2 Hydrodynamic calibration .....	223
7.2.3 Flushing studies .....	229
7.3 Aquaculture effects.....	232
7.4 Flushing time scales .....	237
7.5 Discussion.....	241
<b>Chapter 8 : Summary and conclusions.....</b>	<b>244</b>
8.1 Summary.....	245
8.2 Discussion and Conclusion.....	249
8.3 Recommendations for Future Work .....	258
<b>Bibliography.....</b>	<b>260</b>
<b>Appendix A Scale modelling and 2D numerical modelling: bottom trestles .....</b>	<b>273</b>
A.1 Flow through scaled oyster trestles .....	274
A.1.1 Tidal basin circulation patterns .....	275
A.1.1 Scaling of trestles .....	279
A.1.2 Numerical model .....	281
A.1.3 Flows parallel to trestles.....	282
A.1.4 Flow at 15 degree to trestles.....	285
A.1.5 Trestles at 45 degree to direction of flow .....	287
A.2 Dye tracer experiments.....	289
A.2.1 Scale model solute transport studies.....	290
A.2.2 Numerical model solute transport studies .....	294
A.3 Discussion and conclusions.....	298

<b>Appendix B Meteorological data.....</b>	<b>302</b>
B.2 Met Eireann .....	303

## List of figures

Figure 1.1: Typical suspended long-line .....	4
Figure 2.1: Regions of flow around a cylinder. Illustration adopted from Plew (2005). .....	24
Figure 2.2: Visualization of Karman vortex streets downstream from a cylinder. Illustration adopted from (Williamson, 1996) .....	25
Figure 2.3: Drag coefficient of circular cylinders versus Reynolds number. Graph reproduced from Achenbach (1971) .....	27
Figure 2.4: Flow around a finite height circular cylinder reproduced from Kawamura et al., (1984).....	28
Figure 2.5: Flow visualization of two side-by-side circular cylinders in steady cross flow with a biased flow pattern for Re=1000-3000 (a) T/D=1.5 (b) T/D=2.0. Reproduced from Sumner et al., (1999) .....	30
Figure 2.6: Drag coefficients of four cylinders. Reproduced from Igarashi, (1986) .....	31
Figure 3.1: The space-staggered grid scheme and $(i,j)$ coordinate system. Adapted from Nash, (2010).....	39
Figure 3.2: A shallow well-mixed waterbody (M.W.L =Mean water level with $\eta$ height above or below water level .....	40
Figure 3.3: Control volume incorporating dropper resistance.....	43
Figure 3.4: DIVAST two-dimensional grid. ....	48
Figure 3.5: (a) Sample model grid showing x-direction integration sections and (b) individual section (land cells are grey, wet cells are white and boundary cells are blue) (Nash, 2010) .....	53
Figure 3.6: Primary modules of the EFDC model .....	64
Figure 3.7: Structure of the EFDC hydrodynamic module .....	65

Figure 3.8: The sigma coordinate system. $z^*$ = Cartesian coordinate in the vertical and $z$ = the sigma coordinate. Illustration adapted from Ji, (2008) .....	66
Figure 3.9: Boundary conditions. Illustration adapted from Ji, (2008) .....	68
Figure 3.10: The location of variables on the (a) sigma coordinate system and (b) the finite difference solution scheme .....	72
Figure 3.11: Examples of emergent, submerged and suspended canopies with representative velocity profiles. Illustration adapted from Plew (2010).....	77
Figure 4.1: Schematic illustration of tidal basin.....	97
Figure 4.2: Tidal basin arrangement .....	97
Figure 4.3: Schematic layout of tidal basin (a) plan view and (b) cross-section (Olbert, 2006).....	98
Figure 4.4: Wallingford water level gauge .....	99
Figure 4.5: Schematic of ADV probe .....	100
Figure 4.6: Water levels recorded in the tidal basin plotted against those predicted by DIVAST .....	102
Figure 4.7: Location of measured velocities (red circles) in working area .....	103
Figure 4.8: Comparison between experimental and numerical velocities. Location of sampling points within tidal basin are illustrated in Figure 4.7 Tidal amplitude is 6.9cm and tidal period is 586 seconds .....	104
Figure 4.9: Comparison between experimental and numerical velocities. Figure 4.7 displays location of sampling points. Tidal amplitude is 6.9cm and tidal period is 586 seconds. Foam material wave absorber installed within tidal basin .....	106
Figure 4.10: Suspended longline showing (a) typical farm deployment, (b) flotation units and (c) vertically hanging droppers .....	109
Figure 4.11: Schematic of tidal basin scaled long-line detailing: (a) exploded view of long-line design detailing velocity measurement points A1-A4, (b) schematic detailing location of long-line in tidal basin and (c) scaled long-line installed in tidal basin. ....	111
Figure 4.12: Comparison between velocities collected in tidal basin with no structures in place (benchmark) and Froude scaled long-line installed (scale model). Figure 4.11 displays the location of sampling points.....	112
Figure 4.13: Exploded view of mussel dropper illustrating surface irregularities. Illustration adopted from (Plew, 2005) .....	113

Figure 4.14: Comparison between velocities collected in tidal basin with no structures in place (benchmark) and Froude scaled, artificially roughened, long-line installed (scale model). Figure 4.11 displays location of sampling points. ....115

Figure 4.15: Dye transport recorded in the tidal basin at four different stages of the flood tide tidal cycle (displayed on sinusoidal curve): (a) early-flood, (b) mid-flood, (c) late-flood and (d) high water mark. Dye transport with no impediment to flow (LHS) and through a Froude-scaled roughened long-line (RHS) are presented .....118

Figure 4.16: Dye transport recorded in the tidal basin at four different stages of the flood tide tidal cycle (displayed on sinusoidal curve): (a) early-ebb, (b) mid-ebb, (c) late-ebb and (d) low water mark. Dye transport with no impediment to flow (LHS) and through a Froude-scaled roughened long-line (RHS) are presented .....120

Figure 5.1: Comparison between velocities collected in tidal basin with no structures in place (experimental) and SNM predicted velocities. Figure 4.12 displays location of sampling points. ....127

Figure 5.2: Comparison between APM experimental velocities, and SNM predicted velocities. Figure 4.12 displays location of sampling points. ....128

Figure 5.3: Comparison of APM and KNM velocities. Shading factor = 1.0. Figure 4.12 displays the location of sampling points.....131

Figure 5.4: Comparison between APM experimental velocities and KNM predicted velocities, with a shading factor of 0.7. Figure 4.12 displays the location of sampling points .....132

Figure 5.5: Comparison of aquaculture physical model (APM) observed velocities with those predicted by the aquaculture numerical model (ANM). Drag coefficient =1.0. Figure 4.12 the location of sampling points .....135

Figure 5.6: Comparison of APM observed velocities with those predicted by the ANM. Drag coefficient =1.8. Figure 4.12 displays the location of sampling points .....136

Figure 5.7: Comparison of SNM velocities and those predicted by the ANM. ANM drag coefficient=1.8. Figure 4.12 displays the location of sampling points .....137

Figure 5.8: Comparison of SNM water elevations and those predicted by the ANM. ANM drag coefficient=1.8. Figure 4.12 displays the location of sampling points .....138

Figure 5.9: Numerically predicted dye transport at four stages of the tidal cycle; (a) mid-flood, (b) high water mark, (c) mid-ebb and (d) low water mark. The LHS presents dye transport predicted by the SNM

while the right hand side presents transport predicted by ANM. The location of the aquaculture installation is denoted by the red rectangle while the purple rectangle denotes the area of dye release. 141

Figure 5.10: ANM predicted dye transport incorporating the k- $\epsilon$  turbulence closure model at four stages of the tidal cycle: (a) mid-flood, (b) high water mark, (c) mid-ebb and (d) low water mark. ....144

Figure 5.11: Comparison of velocities predicted by ANM with the mixing length model and the k-epsilon model. Figure 4.12 presents the location of sampling points.....145

Figure 5.12: ANM predicted dye transport incorporating the user-modified k- $\epsilon$  turbulence closure model at four stages of the tidal cycle: (a) mid-flood, (b) high water mark, (c) mid-ebb and (d) low water mark. ...146

Figure 5.13: Approximate location of Casheen Bay on the West Coast of Ireland .....148

Figure 5.14: Bathymetry map of Casheen Bay. Tidal boundary conditions were specified on the western open boundary with zero flow assumed at the northern and southern boundary .....149

Figure 5.15: Hydrodynamic snapshots of (a) mid ebb and (b) mid flood.....150

Figure 5.16: Location of modelled aquaculture structures within bay (displayed in yellow), and time series locations A and B. Highlighted area denotes scale up view presented in Figure 5.20.....151

Figure 5.17: Numerically predicted velocity time series predicted by the SNM and the ANM at, (a) location A within long-lines and, (b) location B between farms .....152

Figure 5.18: Hydrodynamic snapshots at mid flood (a) SNM (b) ANM .....153

Figure 5.19: Hydrodynamic snapshots at mid ebb (a) SNM (b) ANM .....153

Figure 5.20: Exploded view of model predicted flow fields on flood tide (a) SNM and (b) ANM .....154

Figure 5.21: Hydrodynamic snapshots of velocities at mid-flood displaying effect of aquaculture structures. ....154

Figure 5.22: Absolute value differentials of velocity at mid-flood.....157

Figure 5.23: Relative differential of velocity at mid-flood .....157

Figure 5.24: Casheen Bay flushing study sub-regions .....158

Figure 5.25: Decay curves of the average dye concentration in Region A of Casheen Bay obtained from simulations based on DIVAST.....162

Figure 5.26: Spatial distributions of the residence time in Casheen Bay sub-regions obtained from dye studies base on DIVAST. Simulations were performed at spring tide conditions.....161

Figure 6.1: Schematic of experimental flume set-up. Cylinders were arranged in rows with  $l$  the spacing between rows and  $b$  the spacing between cylinders. Cylinders extended the full width and entire working length of the flume .....169

Figure 6.2: Definition diagram for the suspended canopy laboratory experiments.  $H$  is the water depth;  $h_g$  the gap beneath the canopy;  $h_c$  the height of the canopy; and  $U_0$  the depth-averaged velocity. Illustration adopted from Plew (2011b) .....169

Figure 6.3: Effect of canopy density  $\alpha$  on profiles of (a) mean velocity and (b) turbulence. The height of the canopy  $z/H = 0.5$  and  $H = 0.20\text{m}$ , and flow rate were constant. Reproduced Plew (2011b). .....171

Figure 6.4: Numerical simulation of (a) vertical velocity profile and (b) vertical turbulent structure within an experimental flume .....173

Figure 6.5: CDM model results plotted against experimental data for mean velocity (LHS) and turbulent shear stress variance of turbulence fluctuations (RHS). Drag coefficient = 1.0. Details on model runs A-D are provided in Table 6-1 .....176

Figure 6.6: CDM model results plotted against experimental data for mean velocity (LHS) and turbulent shear stress variance of turbulence fluctuations (RHS). Drag coefficient = 2.0. Table 6-1 presents details on model runs A-D .....178

Figure 6.7: DSM model results plotted against experimental data for mean velocity (LHS) and turbulent shear stress variance of turbulence fluctuations (RHS). Table 6-1 presents details on model runs A-D. Drag coefficient = 2.0 .....182

Figure 6.8: DTM model results plotted against experimental data for mean velocity (LHS) and turbulent shear stress variance of turbulence fluctuations (RHS).  $C_{fk} = 0.07$ ;  $C_{fl} = 0.16$ . Table 6-1 provides details on model runs A-D. Drag coefficient = 2.0. ....186

Figure 6.9: DTM model results plotted against experimental data for mean velocity (LHS) and turbulent shear stress variance of turbulence fluctuations (RHS).  $C_{fk} = 1.0$ ;  $C_{fl} = 1.33$ . Table 6-1 provides details on model runs A-D. Drag coefficient = 2.0. ....188

Figure 6.10: DTM model results plotted against experimental data for mean velocity (LHS) and turbulent shear stress variance of turbulence fluctuations (RHS).  $C_{fk} = 0.07$ ;  $C_{fl} = 0.16$ . Table 6-1 provides details on model runs A-D. Drag coefficient = 2.5. ....190

Figure 6.11: DSTM model (incorporating mechanical friction layer) results plotted against experimental data for mean velocity (LHS) and turbulent shear stress variance of turbulence fluctuations (RHS).  $C_{fk} = 0.07$ ;  $C_{fl} = 0.16$ . Table 6-1 presents details on model runs A-D. Drag coefficient = 2.0. ....192

Figure 6.12 Vertical variation of the drag coefficient inside the canopy (Dunn et al., 1996) .....	194
Figure 6.13: DLGM model results plotted against experimental data for mean velocity (LHS) and turbulent shear stress variance of turbulence fluctuations (RHS). Table 6-1 provides details on model runs A-D. Drag coefficient, $C_{DA} = 2.0$ . Details on drag coefficient provided in Figure 6.12 .....	196
Figure 6.14: DLGM model results with MECHANICAL FRICTION LAYER plotted against experimental data for mean velocity (LHS), and turbulent shear stress variance of turbulence fluctuations (RHS). Table 6-1 provides details on model runs A-D. Drag coefficient, $C_{DA} = 2.0$ . .....	198
Figure 6.15: DLGM model results with additional TURBULENCE PRODUCTION term plotted against experimental data for mean velocity (LHS) and turbulent shear stress variance of turbulence fluctuations (RHS). Table 6-1 presents details on model runs A-D. $C_{fk} = 0.07$ ; $C_{fl} = 0.16$ . Drag coefficient, $C_{DA} = 2.0$ . ....	199
Figure 6.16: Vertical variation of the drag coefficient inside the canopy computed by Ghisalberti and Nepf, (2004). DLGM computed profile (dashed line) presented for comparison.....	200
Figure 6.17: GNM model results plotted against experimental data for mean velocity (LHS) and turbulent shear stress variance of turbulence fluctuations (RHS). Table 6-1 presents details on model runs A-D. Drag coefficient, $C_{DA} = 2.4$ . .....	203
Figure 6.18: GNM model results with MECHANICAL FRICTION LAYER plotted against experimental data for mean velocity (LHS) and turbulent shear stress variance of turbulence fluctuations (RHS). Table 6-1 provides details on model runs A-D. Drag coefficient, $C_{DA} = 2.4$ .....	204
Figure 6.19: GNM model results with additional TURBULENCE PRODUCTION term plotted against experimental data for mean velocity (LHS) and turbulent shear stress variance of turbulence fluctuations (RHS). Table 6-1 presents details on model runs A-D. $C_{fk} = 0.07$ ; $C_{fl} = 0.16$ . Drag coefficient, $C_{DA} = 3.4$ . ....	206
Figure 6.20: Computed profile of vertical drag coefficient based on experimental data (EAM) plotted against that computed by Ghisalberti and Nepf, (2004) (GNM) .....	207
Figure 6.21: EAM model results plotted against experimental data for mean velocity (LHS), and turbulent shear stress variance of turbulence fluctuations (RHS). Table 6-1 presents details on model runs. Drag coefficient, $C_{DA} = 1.8$ . Details on drag coefficient provided in Figure 6.20 .....	209
Figure 6.22: EAM model results incorporating MECHANICAL FRICTION LAYER plotted against experimental data for mean velocity (LHS), and turbulent shear stress variance of turbulence fluctuations (RHS). Table 6-1 presents details on model runs. Drag coefficient, $C_{DA} = 1.8$ . Details on drag coefficient provided in Figure 6.12 .....	210

Figure 6.23: EAM model results incorporating additional TURBULENCE PRODUCTION term plotted against experimental data for mean velocity (LHS), and turbulent shear stress variance of turbulence fluctuations (RHS). Table 6-1 presents details on model runs. Drag coefficient, $C_{DA} = 2.4$ . $C_{fk} = 0.07$ ; $C_{fl} = 0.16$ . Details on drag coefficient provided in Figure 6.20 .....	211
Figure 7.1: Location of Killary Harbour (left); and detailed map of harbour detailing location of licensed sites outlined in yellow and tide gauges (T1 and T2) and current meters (C1 and C2). .....	220
Figure 7.2: Bathymetry map of Killary Harbour .....	221
Figure 7.3: Water elevations and temperature recorded in outer Killary Harbour, at location T1 in Figure 7.1. Tide gauge was deployed over the course of a one month period in March 2007. ....	222
Figure 7.4: Comparison of computed and measure water elevations at location T1 in Figure 7.1 .....	224
Figure 7.5: EFDC predicted profiles of (a) current velocity and (b) current direction, plotted against RDCP current meter data recorded at location C2 detailed in Figure 7.1. ....	225
Figure 7.6: EFDC predicted profiles of (a) current velocity and (b) current direction, plotted against RDCP current meter data recorded at location C1 detailed in Figure 7.1. ....	226
Figure 7.7: Hydrodynamic snapshots of depth-integrated velocities (a) mid-flood and (b) mid-ebb within Killary Harbour .....	228
Figure 7.8: (a)Regions of Killary Harbour selected for flushing studies and (b)spatial distribution of residence times obtained from EFDC.....	230
Figure 7.9: Decay curves of the average dye concentration in region A-C in Killary Harbour .....	232
Figure 7.10: Killary Harbour aquaculture farm locations.....	233
Figure 7.11: Hydrodynamic snapshots at mid flood for (a) no aquaculture structures and (b) aquaculture structures included. The yellow cells represent the location of the farms.....	234
Figure 7.12: Hydrodynamic snapshots at mid ebb for (a) no aquaculture structures and (b) aquaculture structures included. The yellow cells represent the location of the farms.....	235
Figure 7.13: Absolute differentials of velocity (a) within the mussel dropper farms and (b)beneath the mussel dropper farms. ....	236
Figure 7.14: Relative percentage differentials of velocity (a) within mussel dropper farms and (b) beneath mussel dropper farms. ....	236

Figure 7.15: Absolute differential of velocity at different dropper densities (a) medium density of droppers and (b) low density of droppers. ....	237
Figure 7.16: Regions of Killary Harbour selected for flushing studies. Region A corresponds to farmed area in outer Killary and Region B corresponds to farmed area in inner Killary. ....	238
Figure 7.17: PRT 63% (the time to flush 63% of conservative tracer) for (a) no aquaculture structures included and (b) aquaculture installations included. ....	238
Figure 7.18: PRT 75% (the time to flush 75% of conservative tracer) for (a) no aquaculture structures included and (b) aquaculture installations included. ....	238
Figure 7.19: Pulse residence times differentials. Increase in residence times induced by the presence of the droppers. (a) 63% of material removed and (b) 75% of material removed. ....	239
Figure 7.20: Decay curves of the average dye concentration in Region A of Killary obtained from simulations based on EFDC. ....	240
Figure A-1: Typical oyster trestle farm; (a) oyster trestle farm, (b) double trestle configuration and (c) oyster bag	275
Figure A-2: Tidal basin schematic detailing location of raised platform (2500mm from back wall) and velocity testing points (red circles)	277
Figure A-3: Comparison between experimental and numerical velocities Location of sampling points within tidal basin are illustrated in Figure A-2	278
Figure A-4: Trestles in Dungarvan Harbour	279
Figure A-5: Predicted flow distribution within a typical oyster trestle system. Average values of approach flow speed and water depth were used as boundary conditions. Adopted from Richardson, (2009)	281
Figure A-6: Tidal basin schematic detailing location of scaled trestle system (hatched) and velocity testing points (red circles)	283
Figure A-7: Comparison between experimental and numerical velocities. Figure A-6 details location of sampling points	284
Figure A-8: Tidal basin schematic detailing location of scaled trestle system (hatched) and velocity testing points (red circles). Trestles system aligned at 15° to direction of flow	285
Figure A-9: Comparison between experimental and numerical velocities. Figure A-8 presents location of sampling points within tidal basin.	286

Figure A-10: Tidal basin schematic detailing location of scaled trestle system (hatched) and velocity testing points (red circles). Trestles system aligned at 45° to direction of flow	287
Figure A-11: Comparison between experimental and numerical velocities. Figure A-10 displays location of sampling points.	288
Figure A-12: Schematic detailing sampling locations of physical and numerical models	289
Figure A-13: Dye transport recorded in the tidal basin with trestles orientated parallel to the direction of flow at four different stages of the tidal cycle; (a) flood tide, (b) high water mark, (c) ebb tide and (d) low water mark	290
Figure A-14: Dye transport recorded in the tidal basin with trestles orientated at 15° to the direction of flow at four different stages of the tidal cycle; (a) flood tide, (b) high water mark, (c) ebb tide and (d) low water mark	291
Figure A-15: Dye transport recorded in the tidal basin with trestles orientated at 45° to the direction of flow at four different stages of the tidal cycle; (a) flood tide, (b) high water mark, (c) ebb tide and (d) low water mark	292
Figure A-16: Vertical profile of tracer transport through a scale model of bottom-feeding bivalves (a) transport of tracer over trestles and (b) transport of tracer between trestles	294
Figure A-17: Tracer transport predicted by DIVAST at mid-flood with four different mariculture scenarios: (a) no oyster trestle installations, (b) trestles parallel to the direction of flow (c) trestles at a 15° to the direction of flow and (d) trestles at a 45° angle to the direction of flow. Dye released upstream of the system at the low water mark.	295
Figure A-18: Tracer transport predicted by DIVAST at high water with four different mariculture scenarios: (a) no oyster trestle installations, (b) trestles parallel to the direction of flow (c) trestles at a 15° to the direction of flow and (d) trestles at a 45° angle to the direction of flow. Dye released upstream of the system at the low water mark.	296
Figure A-19: Tracer transport predicted by DIVAST at mid-ebb with four different mariculture scenarios: (a) no oyster trestle installations, (b) trestles parallel to the direction of flow (c) trestles at a 15° to the direction of flow and (d) trestles at a 45° angle to the direction of flow. Dye released upstream of the system at the low water mark.	297
Figure A-20: Tracer transport predicted by DIVAST at low water with four different mariculture scenarios: (a) no oyster trestle installations, (b) trestles parallel to the direction of flow (c) trestles at a 15° to the	

direction of flow and (d) trestles at a  $45^\circ$  angle to the direction of flow. Dye released upstream of the system at the low water mark.

298

## List of tables

---

Table 2-1: Flow states for single smooth cylinder in undisturbed flow, from Zdravkovich, (1997) .....	25
Table 3-1: Generic length scale parameters (Warner et al., 2005), where $\kappa=0.41$ and $E_2=1.33$ . The parameters $d_s$ and $d_b$ are the distances to the bottom and surface respectively. ....	84
Table 4-1: Individual long-line and scale model configuration. Scale factor = 30.....	110
Table 5-1: Dimensional values prescribed for the scale and numerical models. A scaling factor of 30 was adopted with appropriate Froude scaling laws applied.....	127
Table 5-2: Physical and numerical model design configurations. Scale factor = 30.....	133
Table 5-3: Variables used for Casheen Bay modelling study .....	150
Table 5-4: Summary of hydrodynamic model detailing turbulence scheme and level of user modification .....	159
Table 5-5: Flushing characteristics of Casheen Bay sub-regions.....	160
Table 6-1: Summary of experiments conducted to investigate suspended canopy effect on flows. $H$ is the water depth, $h_g$ the gap between the canopy and the bed, $h_c$ the height of the canopy, $l$ and $b$ streamwise and cross-stream spacing between cylinders, $a$ projected area per unit volume inside the canopy and $Q$ is flow rate. Reproduced from Plew (2011b) .....	170
Table 6-2: Description of methodologies used to represent canopy flow processes .....	174
Table 7-1: Variables used for Killary Harbour modelling study.....	227
Table 7-2: Flushing characteristics of Killary Harbour sub-regions .....	231
Table 7-3: Pulse residence times within the aquaculture farms.....	240

Table A-1: Individual Trestle Configuration .....	275
Table A-2: Dimensional values prescribed for the scale and numerical models. A scaling factor of 40 in the horizontal and 15 in the vertical was adopted with appropriate Froude scaling laws applied .....	277
Table A-3: Prototype and model design configuration .....	280
Table B-1: Belmullet weather station data, April-May 2007.....	303

## **Declarations**

---

This thesis or any part thereof, has not been, or is not currently being submitted for any degree at any other university.

---

Fearghal O Donohue

The work reported herein is as a result of my own investigations, except where acknowledged and referenced.

---

Fearghal O Donohue

## **Acknowledgments**

---

During the course of this research I enjoyed a lot of advice, help, encouragement and assistance from my colleagues, my friends and my family. Without them, I would not have enjoyed my time in Galway as much as I did.

In the first place, I would like to thank Professor Pádraig O'Donoghue for providing me the opportunity to conduct this research at NUI, Galway.

The support of RPS and BIM who funded this research is gratefully acknowledged.

A special thanks to my supervisor, Dr. Michael Hartnett, for his technical advice and encouragement during the course of this research. I look forward to many fruitful collaborations in the near future.

I would like to express my gratitude to my colleagues in NUI, Galway: Dr. Agnieszka Olbert for her help with DIVAST; Dr. Steven Nash for many useful contributions to this research; and to all my fellow occupants of the, now retired, E304 office who together created an atmosphere that I will miss a lot.

Finally, I would like to express my gratitude to my family, and in particular, my parents, Pádraig and Brid, for their endless support. To Pat, for laying the earliest foundation to my education and Josie for his many words of advice

Go raibh maith agaibh go leir



## Mathematical notations

---

$A, B$	empirical constants of the decay curve remnant function
$a$	projected area of mussel dropper per unit volume
$AD$	absolute differential between standard and amended model variable
$AD_T$	tidally-averaged absolute error
$A_d$	farm drag representation
$A_H, A_\phi$	horizontal diffusion coefficients
$b$	fluid buoyancy
$B$	width of weir
$B_1, E_1, E_2,$ $E_3$	empirical constants in the Mellor-Yamada turbulence closure model
$C$	Chezy bed roughness coefficient
$C_b$	bed friction coefficient
$C_{cn}$	Courant number
$C_d$	mussel dropper drag coefficient
$C_{DT}$	mussel dropper turbulence production coefficient
$C_{DA}$	bulk drag coefficient
$C_{d,weir}$	coefficient of discharge over the weir
$C_e$	coefficient of eddy viscosity
$C_{fk}, C_{fe}, C_{fl}$	weighting coefficients for dropper turbulence production term
$C_n$	spatial average tracer concentration after n tidal cycles
$C_0$	initial spatial average tracer concentration for the volume considered
$C_t$	total friction coefficient incorporating bed and canopy frictional resistance
$C_w$	air fluid resistance coefficient

$c_k, c_\varepsilon$	constants in depth-averaged k- $\varepsilon$ model
$c_{1z}, c_{2z}, \sigma_k$ and $\sigma_\varepsilon$	empirical constants in the k- $\varepsilon$ turbulence closure model
$D$	diameter of dropper
$D_{xx}, D_{xy}, D_{yx}$ $D_{yy}$	depth-averaged dispersion diffusion coefficients in the x and y directions respectively
$E$	exchange per tidal cycle coefficient
$f$	Coriolis parameter
$F_d$	drag force induced by mussel droppers
$F_e$	elastic compression
$F_g$	gravitational force
$F_i$	inertial force
$F_{pr}$	pressure force
$F_{st}$	surface tension
$F_T$	dropper turbulence production term
$F_\mu$	viscous force
$g$	gravity
$h$	water depth below datum
$h'$	distance from water surface into canopy ( $h'=H-z$ )
$H$	total water depth ( $h+\eta$ )
$h_c$	height of the canopy
$h_g$	height beneath canopy
$I, J$	x and y coordinate direction of computational grid used by model
$k$	turbulent kinetic energy
$k_s$	equivalent sand grain diameter surface roughness
$l$	length scale characteristic of large turbulence eddies
$L_d$	dropper length
$m$	mass
$M(0)$	mass of material within reservoir at time 0
$M(t)$	mass of material within reservoir at time t
$n$	timestep level
$p_k, q_k$	layer integrated volumetric flux in the x, y direction ( $p_k = u_k H$ ,

	$q_k = v_k H$ )
$P_{kv}$	bed shear stress production term for kinetic energy
$P_{\varepsilon v}$	bed shear stress production term for dissipation rate of kinetic energy
$Q$	flow rate
$q_x, q_y$	depth integrated volumetric flux in the x,y directions ( $q_x=UH, q_y=VH$ )
$Q_u, Q_v, Q_\phi$	momentum source sink terms incorporating subgrid scale processes
$RE$	absolute differential between standard and amended model variable
$RD_T$	tidally-averaged relative error
$R_e$	average per cycle retention coefficient
$R_q$	Richardson number
$r(t)$	remnant function describing the decay of conservative material in a water body
$S$	solute concentration
$S_f$	shading factor
$S_M, S_H$	coefficients that describe the effects of shear and stratification on turbulence
$T_d$	number of tidal cycles
$U, V$	depth integrated velocity components in the x,y directions
$u, v, w$	velocities in the x, y, and z direction respectively
$u_k, v_k, w_k$	layer integrated velocities
$u', v', w'$	components of fluctuations of velocity about the mean velocity
$\overline{u'w'}, \overline{v'w'}$	Reynolds stress components
$\tilde{u}, \tilde{v}, \tilde{w}$	components of instantaneous velocity
$U_b$	velocity beneath suspended canopy
$u_b$	non-dimensionalised velocity beneath suspended canopy
$U_c$	velocity within suspended canopy
$u_c$	non-dimensionalised velocity within suspended canopy
$U_0$	ambient free-stream flow velocity
$U_w, V_w$	wind speed components
$\tilde{V}$	velocity characteristic turbulence scale
$z_0^*$	bed roughness height
$\alpha$	parameter relating the shear in the mixing layer to the difference in velocity within and beneath the farm canopy
$\beta$	momentum correction factor for non-uniform vertical velocity profile

$\Delta$	layer thickness
$\Delta t$	model timestep
$\sigma_k, \sigma_l$	turbulence Schmidt number for k and l
$\theta$	porosity of mussel droppers
$\eta$	water elevation above or below datum
$\eta_{weir}$	head over the weir
$\phi$	concentration variable
$\phi_v, \phi_b$	stability functions
$\kappa$	von Karman constant
$\rho$	fluid density
$\rho_a$	density of air
$\rho_t$	density of droppers per m <sup>2</sup>
$\tau$	shear stress
$\tau_r$	average residence time
$\tau_e$	time required to reduce an initial material concentration within a waterbody by a factor e
$\tau_{xz}, \tau_{yz}$	shear stresses
$(\tau_{xz})_{ML}$	mechanical friction layer
$\nu_q$	vertical kinetic energy diffusion coefficient
$\nu_t$	depth integrated mean eddy viscosity
$\nu_v$	vertical eddy viscosity
$\nu_b$	vertical eddy diffusivity

## **Chapter 1: Introduction**

---

*“If nature were not beautiful it would not be worth studying it.  
And life would not be worth living”  
- Henry Poincaré*

## **1.1 General introduction**

The rapid growth of global aquaculture cultivation has brought to light the need to consider the sustainability and potential environmental impacts of the industry. Recognition and investigation of the effects of these structures on flow dynamics and mixing are of primary importance in the development of a sustainable aquaculture sector. Previous studies in the area have centred on the optimal growth and feeding conditions of marine organisms; with environmental impact assessments focusing on the effects of excess fish food and faecal matter on the surrounding waters. The impacts of the aquaculture structures themselves on flows and circulation patterns are often ignored. The purpose of this thesis is to gain an understanding of the impacts of aquaculture installations, through numerical modelling and laboratory based studies.

In the following sections of this introductory chapter the methodologies adopted, physical and numerical modelling are discussed. A comprehensive discussion of the aims and objectives of this study follows. Finally, the general structure of this thesis is outlined.

## **1.2 Physical modelling**

A physical model is a scaled down version of a prototype and is usually applied to investigate complex flow regimes for which little empirical or theoretical information exists. Research on physical (scale) models is based on the theory of similarity between model and prototype. This theory provides guidance on the preparation of the physical model to accurately simulate prototype flow features; while acknowledging inherent limitations and effects of scaling. Both the boundary conditions and the flow field must be scaled in an appropriate manner.

Historically, physical models were used extensively in many engineering studies to gain insight into the hydrodynamic features associated with potential projects. The advantage of a physical model over field tests is the small size of a model, which permits easier data collection at a reduced cost, while the output may be more easily visualized. A third advantage of physical models is the degree of experimental control that allows simulation of particular environmental conditions, while neglecting others.

While physical models have been supplanted in many areas by numerical models, they still have certain advantages. For complex hydrodynamic regimes, the nonlinear character of the governing equations of fluid motion, and our still limited analytical knowledge, limits the viability of theory alone. In these situations, the use of physical models may be of benefit. As numerical modelling continues to advance, the marriage of these two methods offers great scope for the investigation of different aspects of a project. Accuracy of numerical models is currently limited by the accuracy of solution of the underlying mathematical equations; physical models can bridge this gap between actual flow processes and the approximate solution that the numerical model proposes. Hence, physical models serve as a tool to fine-tune and validate a numerical model, which can then be extended to more complex investigations of various aspects of hydraulic and environmental engineering. The above serves as an outline of the approach adopted for this research.

In the study herein flows through a suspended canopy were the focus of the research. A mathematically correct, Froude-scaled model of a suspended long-line was constructed and installed in a tidal basin facility. The model was scaled from an analysis of a typical mussel dropper double long-line, as presented in Figure 1.1. The scaled long-line consists of an array of cylinders, with each cylinder representing an individual mussel dropper. Flow patterns within and around the scale model were investigated by means of velocity measurements and dye dispersion studies. The data was used to gain an insight into impeded flow processes, and to fine-tune and validate the numerical models.

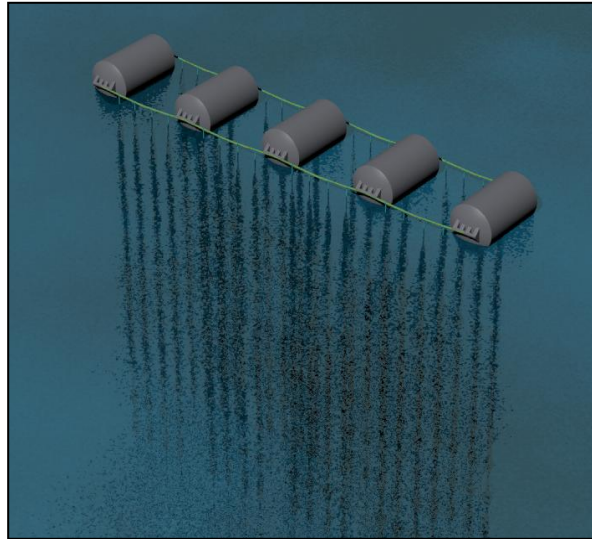


**Figure 1.1: Typical suspended long-line**

### **1.3 Numerical modelling**

In hydrodynamics, models can be divided into two general categories, physical models and mathematical models. A physical model, as described above, is developed to produce a scaled flow that can be measured and related back to the real water system. A mathematical model, on the other hand, represents flow dynamics with a system of mathematical equations, which often needs to be solved numerically by a computer. Numerical models possess several advantages over scale models or field data. Chief amongst these is the reduced cost, and ease of development of a numerical model. In addition, a numerical model can be more easily modified to investigate different flow conditions and scenarios.

A mathematical model is not an exact mathematical description encompassing all aspects of the natural environment; rather the aim is to incorporate only those features of the problem that are most relevant. As no two water systems are alike, parameters of mathematical models need to be adjusted to suit the local circumstances, or new parameterizations or mechanisms developed to describe the flow dynamics appropriately (Ji, 2008). Hence, the accuracy of the numerical model is dependent on the values of empirical constants used, and on the formulation of terms in the fundamental equations of motion. The discretization of the governing equations can also introduce

errors to the solution. These include truncation errors due to discrepancies between the model governing equations and the numerically discretized representation, and round-off error inherent in an iterative solution scheme.

Factors distinguishing modelling approaches can be split into four basic groups: forces and boundary conditions, dimensionality, grid structure and numerical solution scheme. The study herein considers both, a two-dimensional depth-integrated model and a three-dimensional baroclinic model. The governing equations were extended to describe the fluid-structure interaction that develops between flows past a bluff body. The effects on both small-scale turbulent structure, and flow dynamics and mixing patterns were investigated.

While, equations describing the above flow structure are readily derived; the verification of the mathematical equations requires experimental data to assess the model performance and provide empirical model coefficients. Hence, by combining numerical and physical model studies, the research aims to develop a mathematically-valid, laboratory-verified model of flows within a suspended aquaculture canopy.

#### **1.4 Aims and scope of research**

The primary objective of this research was to refine two existing models to include the effects of suspended aquaculture installations. The depth-integrated, DIVAST model, and the three-dimensional EFDC model were adopted for this study. The study can be separated into three primary research objectives:

- Investigate the effects of an idealized aquaculture installation by physical modelling studies. A scale model long-line was developed and installed in a tidal basin facility and the effects on flows and material transport flux analysed.
- A mathematically valid representation of the aquaculture installation was developed and incorporated into the existing numerical models.
- The amended model was assessed and verified by comparison with laboratory data. The applicability of the model to coastal waters was assessed by case studies

conducted in actual aquaculture sites on the West Coast of Ireland, namely, Casheen Bay and Killary Harbour.

The DIVAST model was amended to simulate aquaculture-impeded flows on the assumption that the canopy extended the full depth of the water column. A wide range of studies has demonstrated the suitability of a two-dimensional approach to modelling processes in well-mixed waterbodies (Hartnett et al., (2003), Struve et al., (2003), Dabrowski and Hartnett, (2008)). The hydrodynamic equations were extended to simulate the form drag and blockage effects that the canopy presents. Existing turbulence models were reviewed with regards to their ability to simulate canopy flows, and a two-equation  $k-\varepsilon$  turbulence scheme was further developed to simulate the direct effects of the canopy on turbulence production. The performance of the model in simulating actual bay dynamics was investigated by flow-fields and flushing study analysis.

The EFDC model was adopted for this study to provide a more comprehensive analysis of suspended canopy flows. The more extensive description of flows comes at the cost of increased computational requirements. The model was amended to simulate canopy flows extending over a user-specified region of the water column, with free-stream flow developing beneath. The effects of a suspended canopy on flows and turbulent structure were investigated by comparison with experimental data. The amended three-dimensional model provides a unique insight into a range of canopy flow processes, including: reduced current speed within the canopy; accelerated flows beneath the canopy; pronounced velocity shear layers within the water column; and complex canopy momentum exchange mechanisms.

The amended DIVAST model presents a computationally efficient option to investigate the effects of an aquaculture installation on flows and material transport. EFDC, on the other hand, presents a comprehensive, technically defensible, modelling package to simulate canopy flows processes to a high degree of realism.

## **1.5 Thesis outline**

The layout and content of this thesis are as follows:

Chapter 2 presents a literature review of aquaculture development and the current research standing on their implications. To put the research into context, the scale of current aquaculture production is discussed. The reported effects on currents and mixing are discussed, in addition to the associated implications for production capacity of the farms, and adverse environmental effects. Numerical modelling studies investigating the effects of aquaculture are discussed in detail. Literature related to the physical modelling studies is also reviewed; this predominantly relates to the effects of different cylindrical configurations on flows. Finally, some preliminary details on a time scale analysis of material transport is discussed, and relevant formulae presented.

Chapter 3 deals with the numerical models used in this study. The relevant theory for both DIVAST and EFDC is presented. A description of the amended equations describing canopy flows follows, in addition to a mathematical justification of the extended equations. The numerical discretization and hydrodynamic solution scheme is also presented. Details are presented on the relevant turbulence closure schemes used, namely: a simple mixing length turbulence model; a two-equation  $k$ - $\epsilon$  model; an amended  $k$ - $\epsilon$  model; a Mellor-Yamada turbulence model; and an amended Mellor-Yamada scheme.

Chapter 4 presents the physical modelling studies conducted as part of this study. The conditions for similitude between model and prototype are provided and the Reynolds and Froude scaling laws are derived from force relationships. The tidal basin set-up, equipment specification, laboratory tests and tank calibration are presented in detail. The dimensioning and design of a Froude scaled double long-line is discussed and details on flow measurements and dye dispersion studies within the model presented.

Chapter 5 presents the validation of the amended DIVAST model against physical model data. Both hydrodynamic and solute transport studies are conducted, and results compared with physical modelling data. The performance of a number of turbulence schemes are assessed, namely, a mixing length model, a two-equation  $k$ - $\epsilon$  model, and an

amended k- $\epsilon$  model. The model is applied to a designated aquaculture development site, and the effects of an aquaculture installation on hydrodynamics and solute transport assessed. Flushing studies are used to investigate particle renewal terms in the embayment. The implications of the research are discussed from the point of view of aquaculture carrying capacity and environmental implications.

Chapter 6 presents the validation of the amended EFDC model against experimental data. The study adopted a number of techniques of simulating canopy flow processes in a comprehensive manner, including:

- A bluff body drag term representing canopy effects
- A depth-varying drag term derived based on laboratory data and literature
- A mechanical friction layer describing flow processes induced as the free-stream flow beneath the canopy interacts with the physical impediment.
- A mathematically valid, amended turbulence closure model describing enhanced production and mechanical stirring induced by the canopy

By comparison with experimental data, an optimum representation of canopy flow processes is derived.

Chapter 7 presents a case study application of the EFDC model. The model is applied to Killary Harbour, an aquaculture site on the West Coast of Ireland. A comprehensive field monitoring program provides data to force and validate the numerical model. The flushing characteristics of the bay is investigated and quantified in terms of average residence times. The amended model simulates the effects of aquaculture activities in the bay. The effects of the farms on flow-field and tidal exchange mechanisms is investigated in detail.

Finally, in Chapter 8 a summary of the study, discussion of results and final conclusions are presented to highlight useful findings of the study. Recommendation for possible future progression of the research is then presented.

## Chapter 2: Literature review

---

*“By three methods we may learn wisdom: First, by reflection, which is noblest; second, by imitation, which is easiest; and third by experience, which is the bitterest”*

*- Confucius*

## **2.1 Introduction**

Global aquaculture currently stands at a reported production of about 142 million tonnes, accounting for 46% of total fish food supply (FAO, 2010); aquaculture has become the fastest-growing food-production sector on the planet with an annual growth rate of 10% (FAO, 2006). The relative increase in farmed production, compared to wild fisheries has generated enthusiasm for the potential of a sustainable supply of seafood to the global population, having the promise of food security. This rapid development of aquaculture in recent years has been likened to a ‘Blue Revolution’ that matches the ‘Grain Revolution’ of higher grain yields from the 1950s onwards (Sachs, 2007).

The aquaculture industry’s rapid growth and expansion globally, however, has caused a wide increase in negative environmental impacts, such as, pollution of nearby waters through excess nutrient loads, habitat destruction and biodiversity loss. The expansion of aquaculture, particularly salmon and shrimp farms, has been proven to be destructive to the natural environment and populations of aquatic animals (Gowen and Bradbury, (1987), Folke et al., (1994), Kautsky et al., (1997), Naylor et al., (2000), and Milewski, (2001)).

In Europe, annual growth of aquaculture has declined to 1%, partly because of market factors, but also because the industry is subject to stringent regulation regarding sustainable development (Nunes et al., 2011). There is a strong focus on the ecological carrying capacity of aquaculture in marine systems (e.g. Goldberg and Naylor, (2005), McKindsey et al., (2006) and Mirto et al., (2010), leading to the promotion of terms such as ecoaquaculture (Sequeira et al., 2008) and ecological aquaculture (Costa-Pierce, 2002). Recent legislation such as the European Union’s Water Framework Directive has implicitly promoted the three objectives of Ecosystems Approach to Aquaculture (EAA), namely (i) human well-being; (ii) ecological well-being; and (iii) multisectorial integration (Soto et al., (2008), Nunes et al., (2011)).

With increasing demands on arable land (diminishing with desertification of agricultural land) and continuing strain on freshwater resources, mariculture (the production of aquatic organisms in marine and brackish waters) is the leading candidate

to meet humanity's growing food demands (Neori et al., 2007). The development of the aquaculture industry to match these demands requires a holistic consideration of the ecological and social implications of aquaculture, in addition to economic considerations (White et al., 2004).

Central to a holistic approach to aquaculture is considering the effects of the aquaculture installations themselves on the local ecosystem. These effects include the depletion of particulate food from waters due to feeding; while the presence of the aquaculture structure can impact particle renewal by retarding flow via enhanced drag. This chapter presents a review of the literature on the impacts of aquaculture structures, or other comparable obstacles (e.g. kelp beds, submerged vegetation), on hydrodynamic flows, circulation patterns and flushing characteristics.

## **2.2 Hydrodynamic effects of aquaculture structures**

Marine organisms are cultured globally by several methods that fit into two broad categories: bottom cultures and suspended cultures. Suspended and bottom feeding mariculture involves dense aggregations of animals in nets, droppers, or other containment systems introduced into the marine environment. While there has been large amounts of research carried out on the growth and feeding patterns of marine bivalves (e.g. Gibbs et al., (1992); Grant, (1996)), most carrying capacity studies focus on budgeting of particulate food depletion and renewal (Pilditch et al., 2001; Raillard and Menesguen, 1994; Simpson et al., 2007). The effects that frictional resistance of mariculture structures have on flow has often been ignored. This is particularly true of numerical modelling studies on the subject (McKindsey et al., 2006). This section summarises the current research standing on the effects of the mariculture installations on flows and mixing patterns.

### **2.2.1 Effects on flows**

Early studies of aquaculture farms identified that current speed has an influence on growth rates, but did not show that the physical structures restricted flows (Rosenberg and Loo, 1983). The physical effects of aquaculture installations were often evaluated from the point of view of reduced access to other users in addition to loss of functional

use facilities such as safe anchorage for leisure and fishing crafts (Stewart, 1995). The earliest studies that showed that mariculture installation caused a reduction in flow speeds were carried out in Pelorus Sound, New Zealand in 1984 (Waite, (1989), Gibbs et al., (1991) and Plew (2005)).

Gibbs et al., (1991) took measurements around mussel farms in Pelorus Sound, New Zealand. Measurements were taken at various depths in the water column (1, 4, 7, 10, 20 and 30m). Hydrodynamic and water quality data was recorded beside the mussel curtain, and at a distance of 25m from the mussel farms. Results indicated that water movement through the farm was attenuated to approximately 30% of the ambient upstream flows. Beside the mussel ropes, the mean velocity was 1.3cm/s, whereas well below the mussel farm the mean velocity was 2.5cm/s. Just below the mussel curtain, however, the mean velocity was 4cm/s, indicating a significant diversion of flow under the mussel farm. The authors noted the effects of the decreased flow speeds on material residence times and supply of nutrients to the organisms.

Current meters deployed in and around a suspended long-line farm for two months showed that velocities within the farm was lower than beneath the farm (Waite, 1989). The velocity decreases were 44% adjacent to a long-line with 55mm mussels, and 66% next to 100mm mussels. Flow through the mussel farm was strongly aligned with the direction of the long-lines, in contrast to flow under the long-lines; suggesting that the long-line structures were relatively impermeable to currents, preventing transverse flow across the long-lines (Plew, 2005).

An alternative method of suspended cultivation to long-lines is raft cultivation. Suspended raft cultivation involves the hanging of mussel droppers from rectangular rafts. These rafts form a type of three-dimensional, porous blockage, as opposed to the two-dimensional fence-like structure a long-line presents.

Blanco et al., (1994) measured current speeds and direction within five mussel dropper rafts in the Ria de Arousa, Spain. Flow speeds at the downstream extents of the rafts were consistently higher than at the centre of the rafts; the authors suggest this to be a result of lateral inflows into the raft. This, more complex, three-dimensional flow

patterns has implications for traditional means of estimating flow attenuation within farms; which consists of taking measurements of flow speeds upstream and downstream of the farm, and thereby calculating energy losses through the farm. An implied assumption in the analysis is that flows are unidirectional through the farm.

Boyd and Heasman (1998) conducted a study of flow patterns through culture leases in South Africa, using current meters and tracker drogues. Droppers of length 6m hung from rectangular rafts, with droppers spaced at 0.6m intervals in the long axis and either 0.6 or 0.9m spacing across the raft, depending upon the particular raft configurations. The across raft spacing, together with the maturity of the raft, determined the amount of 'free water' between ropes. In-raft velocities were found to be influenced by mussel maturity (the fastest through flows was observed in immature rafts) and rope spacing. For mature rafts, mean velocities within rafts as a percentage of ambient was 13% for 3.0 droppers  $m^{-2}$  and 25% for 2.0 droppers  $m^{-2}$ . This attenuation of flow can limit nutrient supply to the bivalves, with better growth rate observed in mussel droppers spaced at 0.9m as opposed to 0.6m. The study noted in particular the implications for farms located sequentially; which would receive less food than upstream farms (due to assimilation), and would also receive it more slowly through reduced ambient flow. A number of studies have linked a reduction in flow speeds directly with poorer growth rates of cultured organisms (Lenihan et al., 1996). Drogue studies conducted as part of the study demonstrated a significant diversion of flows around the farms. No retardation of flows was observed beneath the farms; however, the acceleration of flows beneath farms reported in other studies (e.g. Gibbs et al., (1991)) was not detected. A note of caution was added to these results however, due to the dominant forcing factor over much of the bay being wind, which would not be significant at depth.

Pilditch et al., (2001) investigated both current speed and chlorophyll\_a concentration within a suspended scallop farm in Nova Scotia. Chlorophyll\_a concentration is an appropriate tracer due to its preferential ingestion by the bivalves. A current meter and a SeaTech fluorometer and transmissometer were deployed at two points: a control point 100m outside the farm; and an aquaculture sampling point at the centre of the lease.

Mean flow speed outside the farm was 40% higher than that at the centre of the lease. The field data was used to parameterize a quasi two-dimensional model that quantified the relationship between the tidally driven seston supply and consumption by the scallops. Despite the 40% reduction in seston flux due to the flow attenuation, there was no evidence to suggest that feeding by the scallops reduced seston concentration to a point where the growth of animals downstream was affected. The authors suggested this to be a result of the variations of seston supply being driven by processes operating at a larger scale than the culture lease. Expanding the culture lease (80 x 50m) to the total area available for cultivation (1000 x 250m) reduced the seston concentration in the centre of the lease by 20-50%, potentially limiting growth.

Plew et al., (2005) carried out a study of the hydrodynamic effect of a suspended long-line mussel farm in Golden Bay, New Zealand. The farm is one of the largest in New Zealand and has plan area dimensions of 2450m by 650m. Dropper density was estimated at 0.06-0.07 droppers  $m^{-2}$ . Current profilers were deployed both within and beneath the farm. Results indicated an average reduction of 36-63% within the farm; with a strong undercurrent detected beneath the farm, generating flows nearly twice that within the farm. Depth averaged velocities outside the farm were 32% higher than inside the farm supporting the theory of an acceleration of flow around the farm. Given the large horizontal dimension of the farm width (~ 650m) relative to the depth (~ 10m), one would expect that flow would be more readily diverted under the farm than around. However, the small increase in velocity beneath the farm (relative to ambient upstream flows), indicates that most of the fluid is instead diverted horizontally around the farm. This may be partly explained by the fact that the mussel droppers extended a greater length of the water column (average dropper length ~8m, average water depth ~11m) than in the previous study by Gibbs, James et al. (1991). The strength of the density stratification may also promote a horizontal diversion; stratification can result in distinct flow layers developing, and restrict vertical movement or mixing between layers. The study suggested that two-dimensional numerical models should be sufficient to obtain reasonable prediction of the velocity drop within, and the flow diversion around, mussel farms, in appropriate waterbodies.

Stroheimer et al., (2005) measured flow speed, meat content and food availability in a commercial long-line mussel farm in Southern Norway. Friction from the mussels and farm structure reduced current speed inside the farm to less than 30% of ambient. Chlorophyll\_a depletion was significant, with more than 50% of depletion occurring within the first 30m of the farm. After this, concentrations remained constant for the remaining 200m of the farm length, suggesting that concentrations fell below a minimum threshold level for mussel feeding. The reduction in current speed led to both food depletion and consequently, lower meat content of the mussels within the farm.

Drapeau et al., (2006) conducted a field study on the association between long-line design and mussel growth rates in Prince Edward Island, Canada. Data was collected on a number of farm parameters, including: typical long-line spacing, dropper length, dropper density and individual mussel shell length and condition index. A correlative analysis of the data demonstrated a positive link between dropper spacing and farm productivity. It was reported that increasing the dropper spacing by 30% could lead to an 18% increase in mussel weight. Hence, a reduction in initial larvae deployment and any preliminary husbandry effort of 22% would curtail production by only 8%.

The hydrodynamic effects of an aquaculture installation are similar in many ways to the impediment to flow posed by submerged aquatic vegetation and seaweed. A significant amount of research exists in this area. Jackson and Winant, (1983) analysed the effect that kelp forests had on coastal flows. Field data demonstrated that currents through the kelp farm were between 43% and 54% that of velocities at the control point outside the farm. Drag exerted by the farms was found to be up to ten times greater than that of a non-kelp area. Andersen et al., (1996) measured velocities in and above a kelp forest of *Laminaria hyperborea*, using ultrasonic currents. The depth of the water column was about 6m with circa 1.3m of the water column containing the kelp structures. A current meter was deployed at various heights within the kelp forest, and a second, benchmark, current meter was deployed at a fixed height above the canopy. Results indicated that flows measured within the canopy were 5-8% less than that measured above the canopy. The velocity profile was uniform within the canopy with

the effects of the kelp farm extending some distance up into the water-column. Leonard and Luther, (1995) investigated current attenuation within salt marsh canopies in Cedar Creek, Florida. Mean flow speed was found to be inversely related to the vegetation density and distance from edge of marsh. The vertical flow profile was also affected with lower flow speed observed within the canopy than above.

Naot et al., (1996) investigated the hydrodynamic behaviour of partly vegetated open channel flow via a three dimensional empirically-based model that included detailed turbulence modelling. The vegetation was modelled as an internal resistance that exerts drag force, produces energy of turbulence and interferes with its anisotropy and length scale. Struve et al., (2003) developed a numerical model of flow through mangrove vegetation. Experiments conducted in a hydraulic flume quantified the additional resistance created by mangrove trees. The numerical model reproduced the influence of the model trees by including a refined expression for drag on cylinders and the porosity effect of distributed vegetation.

Numerical modelling of the hydrodynamic effects of aquaculture structures include: studies on the distribution of wastes from fish cages in the Gulf of Maine (Panchang et al., 1997); a model of the effect of kelp and scallop culture on tidal current speed and flow patterns in Sungo Bay, China (Grant and Bacher, 2001); and a depth-averaged model of the effects of suspension farms on flows (Plew, 2011a).

Panchang et al., (1997) applied a depth-averaged finite-difference model to simulate tidal currents and wind effects in coastal Maine; the hydrodynamic model was then used to simulate the transport of excess fish food and faecal pellets. The effects of farm drag were not considered in the model simulations.

Grant and Bacher, (2001) developed a two-dimensional finite element model of Sungo Bay, China. The effect of suspended mariculture of marine bivalves was parameterized by means of local increases in bottom friction, and the results compared with the default case of no aquaculture. The numerical model predicted a 20% decrease in velocities in the navigation channel through the farm and a 54% reduction in current speed through the main culture area.

Aure et al., (2007) developed a rate conditional box model to simulate carrying capacity and flow reduction within a long-line farm as a function of the physical properties of the farm and ambient upstream velocity. The long-line farms were simulated as several longitudinal channels, with the suspended mussel ropes acting as vertical boundaries, allowing no-flow across the boundaries. Flows between the long-lines were influenced by a frictional resistance coefficient determined empirically from field data. Results demonstrated a reduction in current speed within the farm as long-line length increased and long-line spacing decreased. The width-to-length ratio was also found to be of importance, with a ratio approaching unity being optimum.

Plew (2011a), used a numerical model to consider the effects of long-line mussel farms on tidal currents within two embayment in Pelorus Sound, New Zealand. The study adopted the hydrodynamic model RiCOM (Walters, 2005), to conduct depth-averaged simulations of tidal currents. RiCOM is a finite element model that uses an unstructured grid with triangular elements, semi-implicit time stepping and a semi-Lagrangian advection scheme. The long-line farms were parameterised in the model by modifying the bed friction coefficient to account for drag from the farm structures as well as the increased bed shear resulting from accelerated flow beneath the farms. Shear stress from bottom friction was applied in the model through:

$$\tau_{xz} = \rho C_b U |U| \quad (2.1)$$

where  $C_b$  is a bed friction coefficient and  $U$  the depth averaged velocity. Within farmed areas, the bed friction coefficient  $C_b$  in equation (2.1) was replaced with a total friction coefficient  $C_t$ :

$$C_t = A_d h_c u_c^2 + C_b u_b^2 \quad (2.2)$$

The farm drag is represented by  $A_d = C_D a H/2$  where  $C_D$  is the drag coefficient of a single mussel dropper,  $a$  the projected area of mussel droppers per unit volume and  $H$  the water depth.  $u_c = U_c/U$  is the velocity within the farm canopy non-dimensionalised by the depth-averaged velocity,  $u_b = U_b/U$  is the non-dimensional velocity beneath the farm canopy, and  $h_c$  is the proportion of the water depth covered by the canopy. The

friction coefficient  $C_t$  was obtained by first calculating the non-dimensional velocities within and beneath the canopy:

$$u_c = \frac{-\alpha^2 - C_b h^2 + (1 - h)\sqrt{Ah(1 - h)(\alpha^2 + C_b h) - \alpha^2 C_b h}}{Ah(1 - h)^3 - \alpha^2 - C_b h^3} \quad (2.3)$$

$$u_b = \frac{1 - u_c h}{1 - h} \quad (2.4)$$

$\alpha = 0.2$  is a parameter relating the shear in the mixing layer to the difference in velocity within and beneath the farm canopy (Plew, 2011b). Droppers were assumed to extend to 80% of the water depth, and to have an average diameter of 0.16m. Based on these assumptions the non-dimensionalised velocities within, and beneath the canopy were  $u_c=0.89$  and  $u_b=1.43$ , respectively.

Plew applied the model to investigate the effects of several small farms located around the perimeter of the bay, and compared the effects to a single large farm of equal area. Results suggested that the cumulative effects of several small farms can be similar, or in some cases greater, than a single larger farm of equivalent area.

Simulations demonstrated that, in all cases, the farms had a significant effect on flow dynamics within the bay. Depth-averaged flows within farms areas were reduced by 25-45% compared to ambient; diversion of flows around farms was also observed, with increased mean water speed of up to 160% predicted in places. In addition, simulations predicted that the influence of drag from the mussel farms extended beyond the immediate area of the farms. Mussel farms occupied about 10% of the bay, yet simulations predicted that flow speeds were reduced over most of the bay.

The effects of the farms on seston depletion were simulated, using a tracer to represent the amount of seston consumed. Tracer was continuously released from the farms at a rate of  $1\text{gm}^3\text{h}^{-1}$  of farm volume, to simulate consumption by the mussels. No allowance was made for any dependence of feeding rates on concentration. Results demonstrated that seston depletion was least likely to occur in farms placed in the outer parts of the bay where currents are faster. Seston depletion within individual, existing,

farms was not significant, however the cumulative effects of farms, or the effects of a single large farm, was noted.

The simulations conducted by Plew demonstrate the potential of using numerical models to aid in choosing suitable locations for shellfish farms, and in determining optimal stocking densities and farm layouts; provided the models incorporate farm drag. However, the model neglects a number of features. Tidal forcing alone drives the model. However, studies have shown that the effects of wind (Boyd and Heasman, 1998), and river inflows (Plew et al., 2006), also affect flow dynamics within aquaculture regions. Flows within and beneath the suspended canopy were estimated by means of an analytical expression given by equations (2.3) and (2.4), respectively. These expressions do not account for the effects of stratification or vertical circulation patterns within the bays. In addition, the relative proportions do not change depending on local bathymetry. The model also neglects baroclinic features of flow. For a comprehensive analysis of the effects of a suspended farm structure on the vertical flow regime, these features require consideration.

The studies summarised here show that the effects of aquaculture structures on hydrodynamics are significant. Some important issues still need to be addressed. Central to these, is the need for a comprehensive numerical model that could simulate the likely effects of an aquaculture installation on hydrodynamics. The development of such a model requires a significant body of information on the actual local effects of an aquaculture installation. A review of the literature yielded little data on the effects of a single aquaculture installation on flow dynamics; with studies focusing on a bay-scale analysis of the effects on flows. Further research is required to identify a relationship between the physical properties of an aquaculture structure and the associated hydrodynamic implications. These areas are investigated as part of this research.

### **2.2.2 Effects on mixing**

There is significant evidence in the literature to suggest that the drag from a mussel farm may result in some modification to water currents. Turbulence will be generated as the water flows past the physical impediment. This turbulence has the potential to

enhance mixing, both laterally and vertically (Plew, 2005). Waite, (1989) observed that large fluctuations in velocities were observed at a depth 2m beneath a suspended aquaculture installation, and suggested the development of a mixing layer between the retarded flow within the canopy and the faster flow beneath the long-line

Frechette et al., (1989) conducted a study of phytoplankton concentrations over an intertidal, bottom-feeding, mussel bed in Quebec, Canada. Concentrations were monitored at three heights above the mussel bed, 1.0m, 0.5m and as close as possible to the bed. Phytoplankton was found to decrease towards the bed to about half its value at 1.0m due to mussel assimilation. Analysis of the field data indicated that near-bed phytoplankton concentrations increased almost linearly with increasing current speed. The field observations displayed a link between increased vertical diffusivity and near bottom phytoplankton concentrations. An increase in vertical mixing at greater current speeds increased near-bottom phytoplankton replenishment from the relatively food-rich surface layers. The authors noted that increased bottom roughness would enhance turbulent mixing and increase the flux of food to the organisms. In the absence of comparable bed roughness scales, such as stones and pebbles, the mussels themselves constitute the dominant bed roughness for the flow.

Grant and Bacher, (2001) investigated the effects of a suspended scallop culture on mixing and tracer exchange rates via numerical models studies. The suspended culture was parameterised into a two-dimensional, finite element model by means of a localised non-directional increases in bed roughness. Exchange rates were estimated by introducing a constant source of conservative tracer at the mouth of the bay and examining the time at which a given node achieved 95% of this external concentration. The inclusion of the suspended mariculture installations resulted in a 41% decrease in exchange rates within the cultured regions.

Helsey and Kim, (2005) investigated mixing downstream of a submerged fish cage by means of high-resolution CFD modelling using the FLOW3D model, and adopting the Fractal Area/Volume Obstacle Representation (FLAVOR) methodology to simulate the fish cages. The cages were incorporated into the CFD model by means of a prescribed

porosity, based on the mesh size. Model simulations demonstrated that the inclusion of the fish cages significantly increased turbulence production and large scale vortical flow in the downstream regions. The corresponding effects on mixing were discussed, but not quantified. The authors noted the significant effect that asymmetries in the cage design and orientation has for mixing processes, and recommended the creation of “*small, but perhaps environmentally significant, asymmetries during the design of future cages to enhance the generation of lateral vortices*”.

Plew et al., (2006) investigated the effects of a suspended mussel dropper farm on stratified flows by Acoustic Doppler Profilers and vertical measurements of temperature and conductivity. Salinity and density were calculated from the conductivity and temperature data; from which the effects of the canopy on density stratifications were assessed. The current profilers were used to estimate turbulent energy dissipation rates from velocity spectra data. The study considered the effects of the suspended canopy on vertical mixing. Results demonstrated a shear layer developing beneath the canopy and additional turbulence production within the canopy. However, the instabilities and associated mixing from the shear layer was suppressed by the stratified nature of the flows; thereby increasing the relative importance of vertical mixing associated with the canopy generated turbulence. The implications of highly stratified flows for a suspended canopy was noted; these implications include, reduced vertical diversion of flows, favouring instead a horizontal diversion, and a reduction in vertical mixing due to reduced shear-induced mixing layer instabilities.

Plew (2011b), conducted laboratory experiments examining the effects of a suspended canopy on flows. The experiments, using both acoustic Doppler and two-dimensional particle tracking velocimetry, gave details of the flow structure, allowing the identification of three distinct regions: a bottom boundary layer (BBL), a canopy shear layer and an internal canopy layer. The BBL is a typical fluid mechanics feature characterized by the transition from the no-flow bottom boundary to the free-stream condition. It is typically defined by the law-of-the-wall (Bradshaw and Huang, 1995). Measurements of turbulence revealed a shear layer extending from the top of the BBL

into the canopy; the shear layer was characterised by an inflection point in vertical velocity gradients, and a sharp increase in turbulence production. Plew approximated a mixing layer thickness equal to the depth of this shear layer. Equating the laboratory results to other studies on vegetated flows allows one to infer the impacts of the canopy shear layer on vertical mixing and momentum transfer. Ghisalberti and Nepf, (2002), investigated flows within and above a submerged vegetated canopy. Similar to the suspended canopy, a velocity inflection point was observed at the canopy interface, which made the flow susceptible to Kelvin-Helmholtz instabilities. This instability led to the generation of large coherent vortices within the mixing layer, which dominated the vertical transport of momentum through the layer. Within a suspended canopy, this would have significant implications for the supply of nutrients to the nutrient depleted canopy layer, from the nutrient rich layers beneath.

In the area of impeded canopy flows, the largest body of research relates to submerged and emergent canopies (e.g. mangrove forests, kelp beds, etc.). While differences exist between a suspended canopy and the submerged or emergent type, some of the effects are comparable. Studies of submerged vegetated canopies have revealed a number of features relevant to suspended canopies, namely: the development of shear flows above the canopy; additional turbulence dynamics at the scale of the canopy; and a mixing layer developing at the interface of the canopy which dominates vertical mixing and transport into and out of the canopy (Raupach and Thom, 1981).

Nepf and Vivoni, (2000) divided a submerged canopy into two regions in the vertical. In the upper canopy, called the “*vertical exchange zone*”, vertical turbulent exchange with the overlying water is dynamically significant to the momentum balance and turbulence; and turbulence produced by mean shear at the top of the canopy is important. The lower canopy was termed the “*longitudinal exchange zone*”, because mixing and transfer with surrounding water is predominantly through longitudinal advection. The generation of vortical flows above the canopy was observed to be influenced by the effects of the free surface. When flow depth above the submerged canopy is reduced below  $H/h_c < 2$ , (where  $h_c$  is height of canopy and  $H$  is water

depth), the depth-induced restriction on eddy length-scales results in a decrease in the penetration depth of turbulent stresses into the canopy. This has important implications for vertical transfer of momentum and mixing between the canopy and the overlying waters. This effect would be even more pronounced for a suspended canopy where the effects of the free surface are replaced by the solid bottom boundary condition at the bed (Plew, 2011b).

The studies summarised here demonstrates that both bottom-feeding and suspended aquaculture installations affect mixing patterns in a number of ways. These include: increased vertical transfer of momentum, additional turbulent energy production, the generation of vortical flows, and amended tidal exchange patterns. However, there are a number of important issues that remain to be addressed. The velocity shear that develops beneath a suspended canopy can have very significant implications for vertical mixing patterns. Plew (2011b), investigated this by means of laboratory measurements in an experimental flume. However, the limited depth of the flume (0.2m) may affect the generation of coherent vortices at the bottom of the canopy, due to flow interactions with the no-slip boundary at the bottom. These features are investigated in this thesis by means of three-dimensional numerical studies at both the laboratory and bay-scale level.

### **2.3 Physical modelling literature review**

As part of this research, laboratory experiments were carried out investigating the effects of both bottom-feeding and suspended aquaculture installations on flows. The experiments were conducted to scale, in a tidal basin facility. The main focus of the laboratory studies was to quantify the effects of a suspended mussel dropper canopy on tidal flows and mixing patterns. Details on the physical modelling studies are prescribed in Chapter 4.

Prior to undertaking the laboratory experiments, the literature was reviewed. The purpose of the literature review was twofold: (i) to establish a knowledge base that may be applied to flows around mussel droppers and (ii) to identify areas in which there are gaps in the literature.

### 2.3.1 Flow around single smooth cylinder

A large volume of work exists on the structure of flow around a cylinder; it is considered one of the classical problems of fluid mechanics. Nevertheless, our understanding of the flow is still limited. Roshko (1993) remarked that, ‘*the problem of bluff body flow remains almost entirely in the empirical, descriptive realm of knowledge*’.

Flow around a cylinder is complex and consists fundamentally of the interactions of three different flow regimes, namely, a boundary layer, a separating free shear layer, and a wake (Figure 2.1). The classical view of flow behind a cylinder is displayed in Figure 2.2, and is termed a “Karman vortex street”, after Von Karman (1911). This consists of regions of vorticity shedding in the downstream direction from alternating sides of the body.

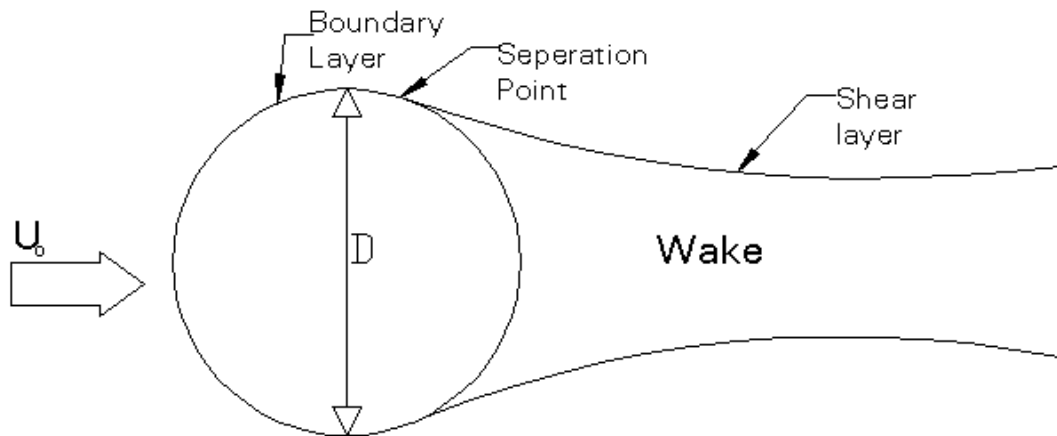
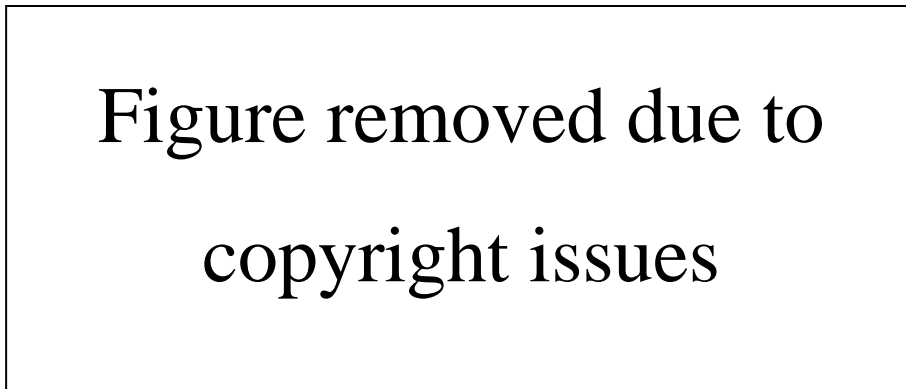


Figure 2.1: Regions of flow around a cylinder. Illustration adopted from Plew (2005).



**Figure 2.2: Visualization of Karman vortex streets downstream from a cylinder. Illustration adopted from (Williamson, 1996)**

The flow around a circular cylinder passes through a range of successive regimes as the flow transitions from fully laminar to fully turbulent. Under very low Reynolds number, the wake structure downstream of the cylinder is nonexistent and the flow fits exactly around the cylinder. As the Reynolds number increases, turbulence spreads progressively downstream of the cylinder. Referencing Figure 2.1, turbulence around the cylinder occurs first in the wake, followed by development of turbulence in the free shear layers; the third and final region to become turbulent is the boundary layer.

Zdravkovich (1997) classified the flow regimes around a single cylinder based on the development of turbulence around the cylinder; Table 2-1 presents the flow states. This classification is based on the assumption of undisturbed flow around a smooth cylinder. Small disturbances such as surface roughness or distortion can have a significant effect on the flow regimes and induce turbulence at lower Reynolds numbers.

**Table 2-1: Flow states for single smooth cylinder in undisturbed flow, from Zdravkovich, (1997)**

State	Flow description	Reynolds number
La	Laminar	0 to 180-200
TrW	Transition in wake, laminar elsewhere	180-200 to 350-4006
TrSL	Transition in shear layers, turbulent wake	350-400 to $10^5 - 2 \times 10^5$
TrBL	Transition in boundary layers	$10^5 - 2 \times 10^5$ to $10^6 - 8 \times 10^6$
Tu	Fully turbulent flow	$> 8 \times 10^6$

### 2.3.2 Surface roughness

While the governing parameter for the state of flow for smooth cylinders is the Reynolds number, surface roughness can lower the Reynolds number at which the transition to different flow states occur, and in some cases govern the flow state. Surface roughness is defined as the mean size of surface irregularities; and is commonly expressed as an equivalent sand grain diameter,  $k_s$  (Nikuradse, 1933).

The influence of surface roughness on flow past a cylinder has received much attention in fluid mechanics. The primary effect of surface roughness on flow is the acceleration of the transition to turbulent boundary layer at lower Reynolds numbers; along with an associated drop in drag coefficient. From literature, only very small surface roughness is required to trigger the onset of boundary layer turbulence at lower Reynolds number. As the Reynolds number increases past the critical value, the drag coefficient approaches a near constant value that is determined by the cylinder surface roughness.

Achenbach (1971) carried out wind tunnel test on flows around rough cylinders. The total drag coefficient on the cylinder was calculated by integrating the local stresses around the cylinder. Figure 2.3 displays a plot of drag coefficient versus Reynolds number for a range of roughness ratios. As the surface roughness ratio increases, the drop in drag coefficient occurs at lower Reynolds number; however, the minimum drag coefficient is also higher. At Reynolds numbers greater than the point of the minimum drag coefficient,  $C_D$ , recovers to higher values as surface roughness increases. This relationship appears asymptotic in that  $C_D$  approaches a value of circa 1.0 for surface roughness,  $k_s/D > 0.0045$  (Güven et al., 1980).

Figure removed due to  
copyright issues

**Figure 2.3: Drag coefficient of circular cylinders versus Reynolds number. Graph reproduced from Achenbach (1971)**

### **2.3.3 Free-end effects**

In the preceding sections, the analysis of flow around a cylinder was based on the underlying assumption of an infinite cylinder. The situation where the cylinder does not extend the length of the water column complicates the flow significantly. While the flow around an infinite cylinder contains some three-dimensional features, it can be simplified to two-dimensional flow. This is not the case for a finite cylinder. The main feature of interest of a finite cylinder is the flows around the free end.

Kawamura et al., (1984) investigated flows around a finite cylinder by means of flow visualization and surface pressure measurements. The study noted a number of distinct features: (i) the separation velocity at the side of the cylinder was lower than that of a two-dimensional cylinder; which decreased the drag coefficients, (ii) a pair of trailing vortices existed at the free end. (iii) down-wash flow and the trailing vortex near the free-end dominated the behaviour of Karman vortex shedding (Figure 2.4).

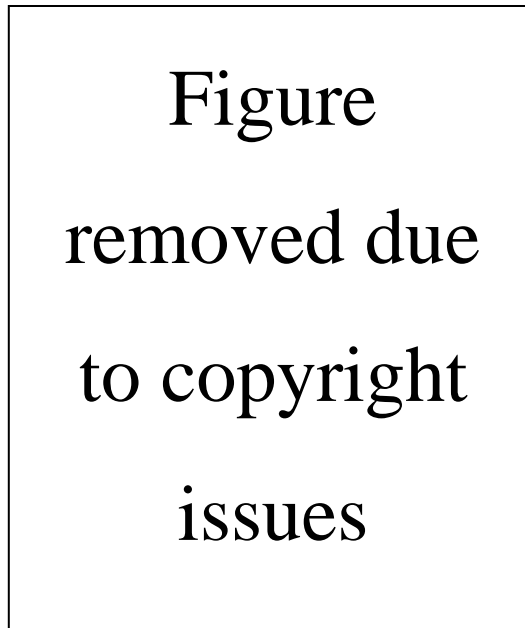


**Figure 2.4: Flow around a finite height circular cylinder reproduced from Kawamura et al., (1984)**

The counter-rotating pair of vortices that form at the free end interact with the Karman vortex shedding from the cylinder sides such that the dimensionless vortex shedding frequency may vary along the height of the cylinder (Sumer and Fredsoe, 1997). The region where shedding is suppressed may extend a distance of about  $2D$  from the tip (Sumner et al., 2004). For small aspect ratios (ratio of length to diameter of cylinder), the flow around the free end may completely suppress Karman vortex shedding from the base to the tip. Moving away from the free end, the shedding frequency increases and, if, the cylinder is of high enough aspect ratio, will eventually behave like an infinite cylinder. In addition to their influence on vortex shedding, the tip vortex structures are thought to be responsible for a downward-directed local velocity field near the free end (directed along the cylinder), known as “downwash”.

#### **2.3.4 Cylinder arrays**

For widely spaced cylinders, there is little interaction between the flows and they essentially behave as independent single cylinders. On the other hand, if cylinders are closely spaced, various interactions can develop between the cylinders depending on the orientation and spacing. Zdravkovich (2003) classified flows around double cylinder

arrays based on the level of interference between cylinders. For the side-by-side double cylinder configuration, the arrays were classified into three distinct interference flow regimes based on the spacing ratio,  $S/D$ , between cylinders:

- $1 < S/D < 1.2$ ; a single eddy street is formed behind both cylinders, which appears as a single bluff body with a weak flow through the gap.
- $1.1-1.2 < S/D < 2-2.2$ ; narrow and wide wakes are formed between two identical cylinders. The gap flow forms a jet biased towards the narrow wake. The biased gap flow is bistable (stable in two states) and may intermittently switch to either side.
- $2-2.2 < S/D < 4-5$ ; the coupled wakes regime. Both wakes are equal in size, and eddy shedding is synchronized in frequency and phase. The predominant out-of-phase coupling produces two eddy streets, which mirror each other relative to the gap axis. At a transverse spacing greater than this the cylinders behave independently.

A wealth of published data exists on the flow that occurs behind closely spaced cylinders. The primary feature of interest is the apparent non-uniformity of flow behind identical cylinders spaced at regular intervals. A clear demonstration of this behaviour is visible in the photo by Sumner et al., (1999) reproduced in Figure 2.5. Sumner et al. used flow visualization techniques to investigate the flow-fields around two cylinders of equal diameter arranged in a side-by-side configuration. When this behaviour is extrapolated to a row of cylinders arranged side-by-side, a non-uniform pattern of wakes is visible downstream of the cylinders.

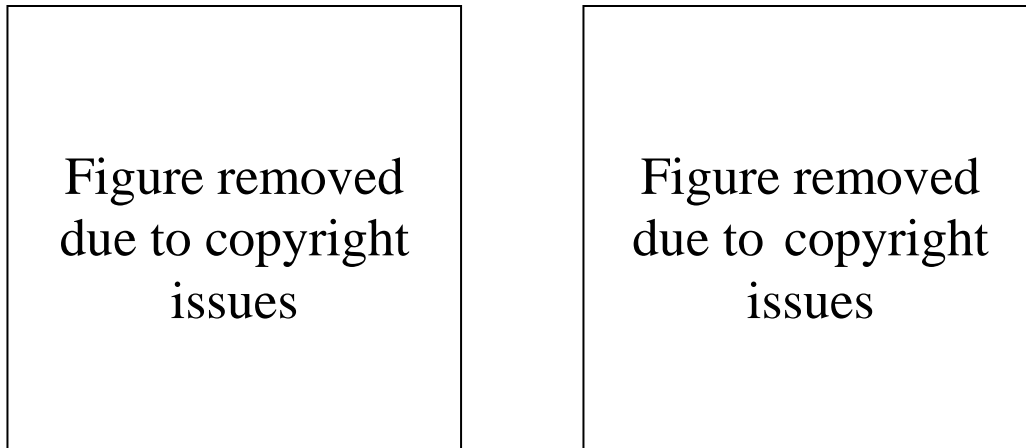


**Figure 2.5: Flow visualization of two side-by-side circular cylinders in steady cross flow with a biased flow pattern for  $Re=1000-3000$  (a)  $T/D=1.5$  (b)  $T/D=2.0$ . Reproduced from Sumner et al., (1999)**

Zdravkovich and Stonebanks, (1990) investigated this phenomenon of non-uniform flows being produced downstream of a row of uniformly spaced identical cylinders. The study examined flows behind a row of cylinders. Significant variation in drag on the bodies was detected due to the asymmetry of flow beyond the cylinders and it was noted that, “*the flow was grossly non-uniform and there was little evidence left downstream to show that the flow originated from a regular row of jets*”. The term metastable flow was used to describe these flow patterns that remain stable for a period, but change seemingly at random.

Significant interactions also occur when the cylinder array is aligned in-line with the flow. Investigation of flow past an in-line array of three cylinders was carried out by Igarashi and Suzuki, (1984), and four cylinders by Igarashi, (1986). The pressure distribution and drag coefficients of each cylinder were measured. Figure 2.6 displays the drag coefficient on each cylinder at different spacing configurations. The dashed line represents drag coefficient for the case where only three cylinders are arranged in line (Igarashi, 1986). As expected, the upstream cylinder is subjected to the highest drag due to its position in the path of the uninterrupted free stream velocity. The value of the drag coefficient for the second cylinder  $C_{D2}$  is negative and it acts as a thrust. An interesting feature is the similarity between the drag coefficient on the third ( $C_{D3}$ ) and fourth ( $C_{D4}$ )

cylinders. This implies that while a three in-line cylinder configuration has distinct features, this is not the case for the addition of subsequent cylinders. This feature is supported by the close correlation between the drag coefficient for each cylinder and that for the three cylinder configuration (dashed line). These results are similar to experiments conducted by Aiba et al., (1982), who investigated flows through multi-cylinder arrays. Results demonstrated that the drag coefficient on the first cylinder was significantly greater than for subsequent cylinders; while the drag coefficients on the second and further downstream cylinders were found to be nearly equal.

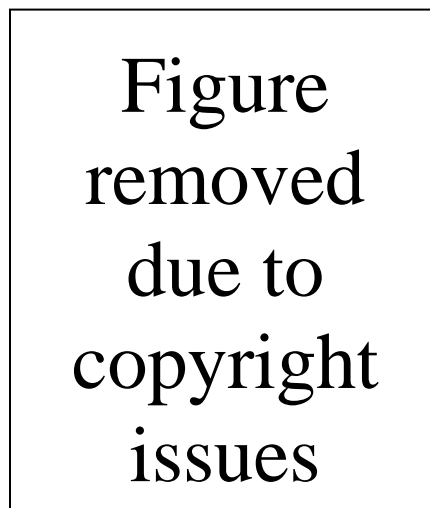


**Figure 2.6: Drag coefficients of four cylinders. Reproduced from Igarashi, (1986)**

Plew (2005), conducted drag tests on seven-cylinder arrays of both smooth and rough cylinders. The spacing was varied between  $S/D=1.15$  to  $6.93$ . Results showed an increase in drag as spacing decreased. Interestingly, the drag coefficient of an array of cylinders with high surface roughness increased at a faster rate (up to 10 to 15% faster) than an array of smooth cylinders. This differs with the studies carried out by *Plew*, on single cylinders, which showed that surface roughness had little effect on drag.

### **2.3.5 Conclusions**

It is clear from the review of literature that there is a wealth of published research on flow past circular cylinders. However, a number of issues related to suspended aquaculture remain to be addressed. Extreme surface roughness and irregularities are an

inherent property of a mussel dropper. However, little data exists in literature for surface roughness ratios greater than  $k_s/D \sim 0.02$ . The effects of these features on flows requires further study to determine if the droppers can be approximated to a smooth cylinder for numerical modelling studies, or if the roughness affects flows and mixing patterns. Arrays of cylinders, in particular single rows normal to the flow and in-line to the flow have been studied quite extensively. Existing data demonstrates that the first cylinder in an in-line array experiences drag force significantly higher than subsequent cylinders; this suggest that a significant proportion of the energy dissipation occurs at this first cylinder. Extrapolating to a long-line, the data implies that the greatest portion of flow attenuation occurs at the entrance to the long-line, rather than as a gradual dissipation due to friction effects along the length of the structure. In addition, little research has been conducted on the effects of surface roughness and irregularities (similar to mussels) on flows within an in-line array. Intuitively, surface roughness effects would result in greater frictional forces, in addition to the form drag of the bluff body cylinder. The effects of multiple rows of cylinders also require attention. These areas are investigated as part of this research. Namely, studies are conducted on the effects of a double-array of in-line cylinders on flows; the effects of different roughness ratios of the cylinders are investigated.

#### **2.4 Review of flushing analysis methods**

Once a numerical model of hydrodynamics and solute transport is properly validated and calibrated, one may analyse features of flow and transport of material within the water. In such studies, flushing theory may be very useful, as it allows understanding and accounting for a variation in velocity and concentration fields. In general, it is well known that the flow behaviour within a domain, as well as properties of the basin itself, are responsible for certain flushing characteristics. These characteristics are unique for a given domain, and flushing calculations are efficient tools particularly in water quality predictions.

Flushing theory provides valuable information for a wide spectrum of physical, biological and chemical processes. A number of studies have linked the exchange rates

and flushing characteristics of a waterbody directly to the carrying capacity of a bay for aquaculture developments. The carrying capacity concept lacks a clear and concise definition and may have different meanings depending on the context. Inglis et al., (2000) suggested four different definitions of carrying capacity with reference to the physical, production, ecological and social level and scales of aquaculture. Dame and Prins, (1998) investigated the carrying capacity of 11 coastal and estuarine ecosystems; the carrying capacity was defined in terms of water mass residence time, primary production time and bivalve clearance time (the theoretical time for the total bivalve filter feeder biomass within an ecosystem to filter particles from a volume of water equivalent to the total system volume). Results suggested that the most successful aquaculture developments were found in systems with relatively short residence times (<40 days) and short primary production times (<4 days).

Lee et al., (2003) investigated the carrying capacity of six designated fish culture zones in Hong Kong by means of flushing studies. A systematic methodology was developed that investigated the exchange rate of the culture zones in terms of “local” and “system-wide” flushing times to represent the effectiveness of the mass exchange with the surrounding waterbody and the open sea respectively. With the flushing rate reliably computed, the carrying capacity of the bay was determined in terms of key water quality parameters: chlorophyll\_a, dissolved oxygen and organic nitrogen. The predictions were well supported by field data. These studies demonstrate the potential of using relatively simple flushing studies formulae to assess the development potential and environmental impact of small-scale aquaculture projects, as opposed to other relatively more expensive modelling technique

This section presents a number of methodologies describing flushing characteristics and properties of a particular domain.

### 2.4.1 Average residence time

The ‘*average residence time*’ can be defined through its relation to ‘*average age*’, which is the average amount of time that a particle has spent in a reservoir (Eriksson, (1961), (1971)). A number of approaches have been adopted to define the average residence time; Bolin and Rodhe, (1973) related it to the average transit time of particles leaving the reservoir, while Zimmerman, (1976) revised this definition in terms of an ensemble average, relating the average residence time to the average age of each element in the reservoir. Takeoka, (1984) summarized these concepts to develop age and residence time distribution functions. A remnant function  $r(t)$  was defined, relating the ratio of the mass of material within a reservoir at a given time  $M(t)$ , to the initial mass of this material  $M_0$

$$r(t) = \frac{M(t)}{M_0} \quad (2.5)$$

Takeoka, (1984) demonstrated that average residence time of a reservoir is an integral of the remnant function.

$$\tau_r = \int_0^{\infty} r(t)dt \quad (2.6)$$

Murakami, (1991) utilised the above definition of  $\tau_r$  and demonstrated that in most cases  $r(t)$  can be approximated by the following exponential function

$$r(t) = \exp(-AT_d^B) \quad (2.7)$$

where  $T_d$  is the number of tidal cycles, and A and B are empirical constants to be determined. Both A and B are dependent on the shape of the dye decay curve and have to be determined in each case by approximating to the actual numerically predicted decay curve. Equation (2.7) has the advantage of being easily integrable giving an accurate value of  $\tau_r$ .

As was proved by van de Kreeke, (1983), the residence time determined by the above calculations should equal the time scale  $\tau_e$ , which is the time required to reduce the initial mass of an instantaneous injection by a factor e, if a basin with a continuous exchange is considered.

#### **2.4.2 Exchange per tidal cycle coefficient**

While the average residence time provides a time scale assessment of the characteristics of a waterbody, the exchange per tidal cycle coefficient quantifies the exchange of water between a considered domain and ambient water. It indicates the fraction of water in a basin or segment of a basin that is removed and replaced with ambient water during each tidal cycle, (Nece and Falconer, 1989):

$$E = 1 - R_e \quad (2.8)$$

$$R_e = \left( \frac{C_n}{C_0} \right)^{1/n} \quad (2.9)$$

Where E is average per cycle exchange coefficient,  $R_e$  is average per cycle retention coefficient,  $C_0$  is initial spatial average tracer concentration for the volume considered, and  $C_n$  is spatial average tracer concentration for the same volume after n tidal cycles

#### **2.4.3 Estuarine Residence Time and Pulse Residence Time**

Miller and McPherson, (1991) distinguished two specialised groups of the residence time. Estuarine Residence Time (ERT) is identical to the average residence time by Takeoka, (1984) and is the time required to flush a given fraction of the water, or a conservative constituent from the estuary, if it is initially uniformly distributed through the estuary. Pulse Residence Time (PRT) is the time required to flush a conservative constituent from the estuary if it is introduced at a certain location as an instantaneous injection. PRT will always be greater than the ERT if the pulse is introduced in the upper estuary.

#### **2.4.4 Conclusions**

The flushing characteristics of a waterbody provide significant information on the water quality of a waterbody, coupling the major abiotic and biotic components in a straightforward manner. A number of studies have linked short turnover times to greater production capacity due to increased particle renewal. Flushing studies therefore provide a useful means of assessing and comparing the carrying capacity of a bay, and identifying zones of limited production capacity.

This section presents a review of important flushing study characteristics used in this thesis. The different characteristics provided details on the average time material spends in a waterbody; exchange between the basin and surrounding waters; and the flushing characteristics of individual sub-sections of a waterbody.

## Chapter 3: Description of numerical models

---

*"One cannot come up with a list of rules on how to achieve the best possible solution for conventional modelling of hydraulic phenomenon. Indeed, each particular case has its own peculiarities and difficulties and consequently its own best solution "*

*- M. S. Yalin*

### **3.1 Introduction**

The general purpose, open-source, codes used in this study are DIVAST and EFDC. DIVAST is a two-dimensional depth-integrated finite difference model, which consists of two coupled modules: (1) a hydrodynamic module, and (2) a solute transport module. It is suitable for water bodies dominated by horizontal, unsteady flows, and that do not display significant vertical stratification. The hydrodynamic module is based on the solution of the depth-integrated Navier-Stokes equations and includes the effects of local and advective accelerations, the rotation of the earth, barotropic and free surface pressure gradients, wind action, bed resistance and a simple mixing length turbulence model.

EFDC is a general-purpose modelling package for simulating three-dimensional flows, transport and biogeochemical processes in surface water systems. It solves the vertically hydrostatic momentum and continuity equations in a coordinate system which is curvilinear and orthogonal in the horizontal and sigma-stretched or terrain-following in the vertical. Three-dimensional transport equations for temperature, salinity, dye tracer and suspended sediment can also be computed simultaneously in EFDC. A second-order turbulence closure model developed by Mellor and Yamada, (1982), and modified by Galperin et al., (1988), is solved to provide vertical turbulent viscosity in the model.

### **3.2 DIVAST model**

#### **3.2.1 Model history and description**

DIVAST was first developed by Professor R.A. Falconer in 1976, and has been extensively developed and refined by Professor Falconer and his research team. The model simulates two-dimensional distribution of currents, water surface elevations and various water quality parameters within the modelling domain, taking into account the hydraulic characteristics governed by the bed topography and boundary conditions (Falconer and Lin, 2001). The model has been extensively calibrated and verified against laboratory and field measured data, with details of the model refinement and verification being reported in over 100 papers by the original model author. The model has been used to date on over 200 projects in Ireland and the UK and is considered an industry standard for many aspects of water quality management.

The governing differential equations are solved using the finite difference technique and a scheme based on the ADI formulation which involves the subdivision of each timestep into two half timesteps. This allows a two-dimensional implicit scheme to be applied but considering only one dimension implicitly for each half timestep, eliminating the need for the solution of a full two-dimensional matrix (Falconer and Lin, 2001). The model grid is discretized on an I-J plane where the I and J axes correspond to the x and y directions respectively (Figure 3.1). The solution scheme proceeds in the x-direction during the first half timestep and computes the water surface elevation  $\eta$ , and the x-direction velocity component,  $U$ , using the method of Gauss elimination and back substitution. Solute concentrations,  $\phi$ , are then computed before proceeding to the second half timestep and repeating the process in the y-direction, computing,  $\eta$ , the y-direction velocity component,  $V$ , and,  $S$  (Nash, 2010). Figure 3.1 presents the discretization of the model grid on a finite difference grid. A space-staggered orthogonal grid is adopted with water elevation and solute concentration discretized at the centre of the grid cell and velocity components and water depths discretized at the centre of the cell sides. The staggered grid representation has the advantage that for the computation of each model variable in time, centrally located spatial derivatives for each of the other variables are available.

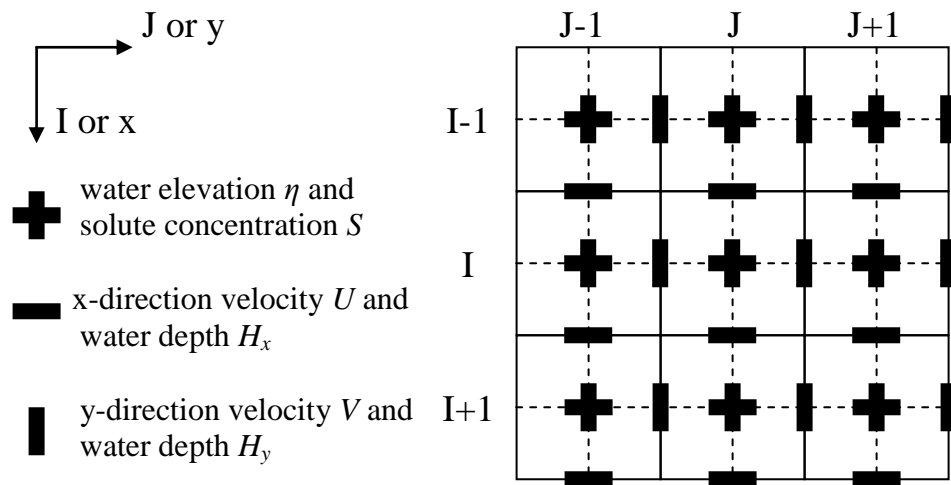


**Figure 3.1: The space-staggered grid scheme and  $(I, J)$  coordinate system. Adapted from Nash, (2010)**

### 3.2.2 Hydrodynamic and solute transport basic equations

In a shallow well mixed waterbody (see Figure 3.2) the vertical velocity component  $w$  is usually small relative to the horizontal velocity components,  $u$  and  $v$ .

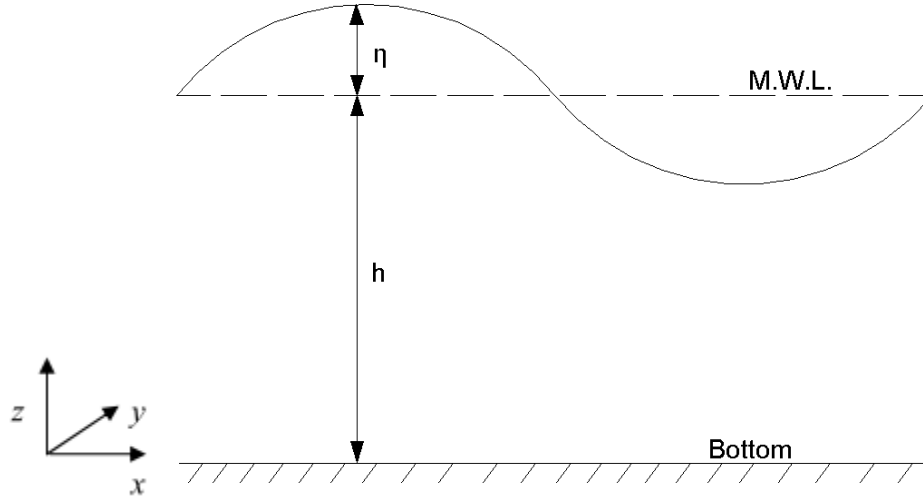


**Figure 3.2: A shallow well-mixed waterbody (M.W.L =Mean water level with  $\eta$  height above or below water level**

In such cases, the horizontal velocity components can be integrated over the depth to give the depth integrated velocity components such that:

$$U = \frac{1}{h} \int_{-h}^{\eta} u dz; \quad V = \frac{1}{h} \int_{-h}^{\eta} v dz \quad (3.1)$$

where  $H=h+\eta$ , is total water depth;  $h$  is water depth below MWL; and  $\eta$  is water depth above or below MWL. As a result, the model environment is reduced from a complex three-dimensional problem (in  $x$ ,  $y$ , and  $z$ ) to a two-dimensional problem (in  $x$  and  $y$ ). Assuming that the vertical accelerations are negligible compared to gravity and that the Reynolds stresses in the vertical plane can be represented by a Boussinesq approximation then the model hydrodynamic governing equations can be expressed as (Falconer, 1994):

*Continuity equation:*

$$\frac{\partial \eta}{\partial t} + \frac{\partial q_x}{\partial x} + \frac{\partial q_y}{\partial y} \quad (3.2)$$

*x-direction momentum equation:*

$$\begin{aligned} \frac{\partial q_x}{\partial t} + \beta \left[ \frac{\partial U q_x}{\partial x} + \frac{\partial U q_y}{\partial y} \right] \\ = f q_y - gH \frac{\partial \eta}{\partial x} - \frac{gU\sqrt{U^2 + V^2}}{C^2} + \frac{\rho_a}{\rho} C_w W_x \sqrt{W_x^2 + W_y^2} \\ + 2 \frac{\partial}{\partial x} \left[ \nu_t H \frac{\partial U}{\partial x} \right] + \frac{\partial}{\partial y} \left[ \nu_t H \left[ \frac{\partial U}{\partial y} + \frac{\partial V}{\partial x} \right] \right] \end{aligned} \quad (3.3)$$

*y-direction momentum equation:*

$$\begin{aligned} \frac{\partial q_y}{\partial t} + \beta \left[ \frac{\partial V q_x}{\partial x} + \frac{\partial V q_y}{\partial y} \right] \\ = f q_x - gH \frac{\partial \eta}{\partial y} - \frac{gV\sqrt{U^2 + V^2}}{C^2} + \frac{\rho_a}{\rho} C_w W_y \sqrt{W_x^2 + W_y^2} \\ + 2 \frac{\partial}{\partial y} \left[ \nu_t H \frac{\partial V}{\partial y} \right] + \frac{\partial}{\partial x} \left[ \nu_t H \left[ \frac{\partial V}{\partial x} + \frac{\partial U}{\partial y} \right] \right] \end{aligned} \quad (3.4)$$

where:

- $\eta$  = water elevation above or below datum
- $q_x, q_y$  = depth integrated volumetric flux in the x,y directions ( $q_x=UH$ ,  $q_y=VH$ )
- $\beta$  = momentum correction factor for non-uniform vertical velocity profile
- $f$  = Coriolis parameter
- $C$  = Chezy bed roughness coefficient
- $\nu_t$  = depth-averaged mean eddy viscosity
- $\rho_a$  = density of air (1.292kg/m<sup>3</sup>)
- $C_w$  = air fluid resistance coefficient (assumed to be 2.6 x 10<sup>-3</sup>)
- $\rho$  = fluid density

The equation governing the solute transport, describing also the tracer distribution used to study the flushing process, is an advective-diffusion equation in the two-dimensional depth integrated form according to Falconer and Lin, (2001):

$$\begin{aligned}
 & \frac{\partial H\phi}{\partial t} + \frac{\partial HU\phi}{\partial x} + \frac{\partial HV\phi}{\partial y} \\
 &= \frac{\partial}{\partial x} \left[ D_{xx}H \frac{\partial \phi}{\partial x} + D_{xy}H \frac{\partial \phi}{\partial y} \right] + \frac{\partial}{\partial y} \left[ D_{yx}H \frac{\partial \phi}{\partial x} + D_{yy}H \frac{\partial \phi}{\partial y} \right] \\
 &+ \Phi_{\phi}
 \end{aligned} \tag{3.5}$$

where,  $\phi$  is the depth averaged solute concentration (unit/volume) or temperature, and  $D_{xx}$ ,  $D_{xy}$ ,  $D_{yx}$ ,  $D_{yy}$  are the depth-averaged dispersion diffusion coefficients in the x and y directions respectively ( $m^2/s$ ). The first three terms represent the local change with time of a solute and its advective flux; whereas the next two terms are the dispersion-diffusion fluxes, summarizing all non-advective transport processes, such as molecular diffusion, turbulent diffusion and dispersion due to shear flow. The last term,  $\Phi_{\phi}$ , represents all other sources and sinks such as discharge from outfalls and rivers, as well as chemical and biological transformations.

### 3.2.3 Numerical representation of impeded flows

Falconer, (1994) derived the depth-averaged continuity and momentum equations for nearly horizontal flows by considering flows through an infinitesimal control volume. The derivation of the equations was based on the conservation laws of mass (continuity equation) and momentum (Newton's second law of motion). The equations can be expressed in words as, respectively:

1. The mass inflow per unit time equals the mass outflow per unit time plus the change in mass within the control volume per unit time.
2. The rate of change of momentum is proportional to the resultant applied force and is along the line of action of the force.

This section applies an equivalent procedure to deriving the equations of motion describing flows through a cultivated aquaculture farm. The control volume considered by Falconer, (1994), was modified to simulate flows through a typical idealised aquaculture installation. The full derivation is not presented here for brevity; for further details, the reader is referred to Falconer, (1994) and Westwater, (2001).

A suspended mussel dropper farm is considered. The most significant source of drag from a mussel-long line is the dropper ropes. A typical 120m long long-line may have 3-5km of dropper rope hanging vertically; with a typical diameter of 0.3m at maturity, the combined projected area (not accounting for any sheltering effect) is circa 1500m<sup>2</sup>. In comparison, the same long-line may have up to 20 buoys, which are cylindrical, with diameter ~1m and length ~1.2m. If completely submerged (a rare and undesirable occurrence), the combine projected area of the buoys will be 15m<sup>2</sup>, less than 1% of the total submerged area (Plew, 2005). Drag on the buoys will therefore be considered negligible and is not considered further.

Figure 3.3 presents an infinitesimal control volume incorporating a hypothetical cylindrical resistance element representing an idealised mussel dropper, of diameter  $D$ . The continuity equation can be derived by considering mass flux components in the  $x$ ,  $y$  and  $z$  direction of the control volume.

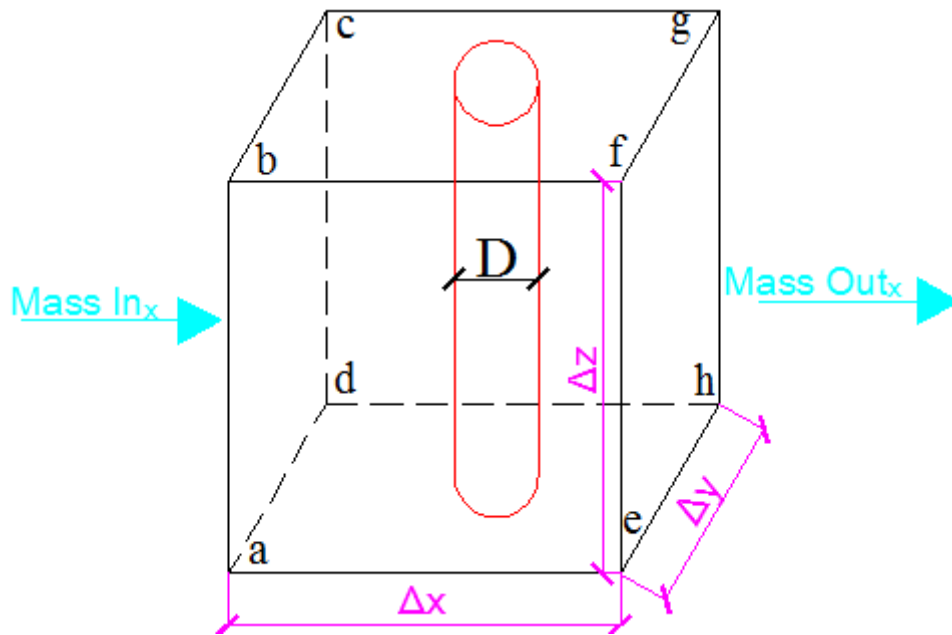


**Figure 3.3: Control volume incorporating dropper resistance**

For steady incompressible flow, the continuity equation can be expressed as

$$\frac{\partial u}{\partial x} + \frac{\partial v}{\partial y} + \theta \frac{\partial w}{\partial z} \tag{3.6}$$

$$\text{where } \theta = 1 - \rho_d \frac{\pi D^2}{4}$$

The term  $\theta$  is defined as the porosity of the cell and describes the reduction in cross-sectional flow area due to the presence of the droppers with  $\rho_d$  representing the density of droppers.

The continuity equation can then be integrated over the depth to form the two-dimensional partial difference continuity equation. By depth integrating and applying Leibnitz rule (Sokolnikoff and Redheffer, 1966) –assuming a no-slip boundary condition at the bed, and the kinematic free surface condition at the surface which assumes that fluid particle remains at the surface (Vallentine, 1959) –the depth-integrated continuity equation incorporating the resistance of the droppers can be expressed as:

$$\theta \frac{\partial \eta}{\partial t} + \frac{\partial UH}{\partial x} + \frac{\partial VH}{\partial y} = 0 \quad (3.7)$$

The momentum equations, incorporating dropper resistance, can be derived (see Falconer, (1994) and Westwater, (2001)) by considering Newton's second law of motion, which states that the sum of the external forces acting on a body must equal the rate of change of linear momentum.

$$\sum \vec{F} = m \frac{d\vec{V}}{dt} \quad (3.8)$$

where  $\vec{F}$ , is the resultant force,  $m$  is the mass and  $\vec{V}$  is the velocity.

The equations can be derived by considering the force components acting on the infinitesimal control volume of sides  $\Delta x$ ,  $\Delta y$ ,  $\Delta z$  shown in Figure 3.3. The force components acting on an element of fluid include the shear stress component acting tangential to the plane, the normal stress component acting perpendicular to the plane and the body force per unit mass due to the earth's rotation. Assuming that the Reynolds stresses in the vertical plane can be represented by a Boussinesq approximation; the momentum equations in the  $x$  and  $y$  direction, incorporating the dropper resistance, can be expressed respectively, as:

$$\begin{aligned}
 \theta \frac{\partial q_x}{\partial t} + \beta \theta \left[ \frac{\partial U q_x}{\partial x} + \frac{\partial U q_y}{\partial y} \right] \\
 = \theta f q_y - gH \frac{\partial \eta}{\partial x} - \theta \frac{gU(U^2 + V^2)^{1/2}}{C^2} + 2\theta \frac{\partial}{\partial x} \left[ \nu_t H \frac{\partial U}{\partial x} \right] \\
 + \frac{\partial}{\partial y} \theta \left[ \nu_t H \left[ \frac{\partial U}{\partial y} + \frac{\partial V}{\partial x} \right] \right]
 \end{aligned} \tag{3.9}$$

$$\begin{aligned}
 \theta \frac{\partial q_y}{\partial t} + \beta \theta \left[ \frac{\partial V q_x}{\partial x} + \frac{\partial V q_y}{\partial y} \right] \\
 = \theta f q_x - gH \frac{\partial \eta}{\partial y} - \theta \frac{gV(U^2 + V^2)^{1/2}}{C^2} + 2\theta \frac{\partial}{\partial y} \left[ \nu_t H \frac{\partial V}{\partial y} \right] \\
 + \frac{\partial}{\partial x} \theta \left[ \nu_t H \left[ \frac{\partial V}{\partial x} + \frac{\partial U}{\partial y} \right] \right]
 \end{aligned} \tag{3.10}$$

### 3.2.3.1 Dropper drag force

When flow passes through a cultivated aquaculture domain, both velocity field and pressure field will be changed by the dropper resistance. This is a typical fluid-structure interaction problem with the scale of structure being relatively small. In this section, the drag imparted by the droppers is expressed by assuming the droppers can be described as a collection of a straight rigid and emergent cylinder.

The form drag exerted by a single infinite cylinder in a uniform flow of velocity,  $u$ , is typically parameterised through a drag coefficient as follows (Streeter, 1962):

$$F_D = \frac{\rho a C_D u^2}{2} \tag{3.11}$$

Where  $F_D$  is drag force,  $a$  is projected area of the cylinder, and  $C_D$  is a drag coefficient.

Refining the above equation for depth-averaged flows and expressing in terms of an array of distributed droppers:

$$F_D = \frac{\rho a \rho_d \beta C_D \sqrt{U^2 + V^2}}{2} \tag{3.12}$$

where,  $\rho_d$  is density of droppers per unit area,  $\beta$  is a momentum correction factor based on the assumption of a logarithmic velocity profile. The value of  $\beta$  is typically taken to be 1.016 for an assumed seventh power law velocity distribution (Falconer and Lin, 2001).

Therefore the continuity and momentum equations incorporating the effects of mussel dropper structure can be expressed as

*Continuity equation:*

$$\theta \frac{\partial \eta}{\partial t} + \frac{\partial UH}{\partial x} + \frac{\partial VH}{\partial y} = 0 \quad (3.13)$$

*x-direction momentum equations:*

$$\begin{aligned} \theta \frac{\partial q_x}{\partial t} + \beta \theta \left[ \frac{\partial Uq_x}{\partial x} + \frac{\partial Uq_y}{\partial y} \right] \\ = \theta f q_y - gH \frac{\partial \eta}{\partial x} - \theta \frac{gU(U^2 + V^2)^{1/2}}{C^2} + 2\theta \frac{\partial}{\partial x} \left[ v_t H \frac{\partial U}{\partial x} \right] \\ + \frac{\partial}{\partial y} \theta \left[ v_t H \left[ \frac{\partial U}{\partial y} + \frac{\partial V}{\partial x} \right] \right] - \frac{F_D U}{\rho} \end{aligned} \quad (3.14)$$

*y-direction momentum equations:*

$$\begin{aligned} \theta \frac{\partial q_y}{\partial t} + \beta \theta \left[ \frac{\partial Vq_x}{\partial x} + \frac{\partial Vq_y}{\partial y} \right] \\ = \theta f q_x - gH \frac{\partial \eta}{\partial y} - \theta \frac{gV(U^2 + V^2)^{1/2}}{C^2} + 2\theta \frac{\partial}{\partial y} \left[ v_t H \frac{\partial V}{\partial y} \right] \\ + \frac{\partial}{\partial x} \theta \left[ v_t H \left[ \frac{\partial V}{\partial x} + \frac{\partial U}{\partial y} \right] \right] - \frac{F_D V}{\rho} \end{aligned} \quad (3.15)$$

### 3.2.3.2 Mixing length turbulence model

Turbulence in DIVAST is considered to be dominated by bottom friction. Thus, the eddy viscosity is calculated from the simple mixing length concept. The mixing length model is based on the assumption that the eddy viscosity is proportional to a mean

fluctuating velocity  $\tilde{V}$ , (velocity scale) and a length scale characteristic of large turbulence eddies,  $l$ , according to the equation

$$v_t \propto \tilde{V}l \quad (3.16)$$

where the scales  $l$  and  $\tilde{V}$  need to be determined. DIVAST adopts a depth-averaged form of the mixing length model which can be expressed in the form of (Falconer and Lin, 2001):

$$v_t = C_e \frac{H}{C} \sqrt{g(U^2 + V^2)} \quad (3.17)$$

where  $C_e$  is the coefficient of eddy viscosity. Fischer, (1979) suggested a value of 0.15 for  $C_e$  based on laboratory data. However, for actual tidal flows in estuaries and coastal waters a much larger value is required and  $C_e \approx 1.0$  is generally recommended (Falconer and Lin, 2001)

The mixing length model has the advantage of being simple and economical, and in many cases reasonable results can be obtained provided appropriate empirical constants are chosen. However, it does have certain limitations, in particular the lack of universality of the empirical input. In addition, the mixing length model assumes that turbulence everywhere is in a state of local equilibrium, which means the turbulence produced at a certain point is dissipated at this point at the same rate. Thus, the mixing length model does not account for the transport of turbulence, or for history effects.

#### 3.2.4 Finite difference formulation

The amended differential equations (3.13)-(3.15), are resolved using the finite difference scheme with a Cartesian grid that has to be developed for the modelled area. The domain of solution in DIVAST is discretized using a uniform space staggered mesh. In this system, water elevations and solute concentrations are calculated at the centres of the grids, whereas velocity and flow components are located at the centres of the sides. This calculation technique is known as the Marker and Cell method (Harlow, 1972). The mesh configuration is given in Figure 3.4.

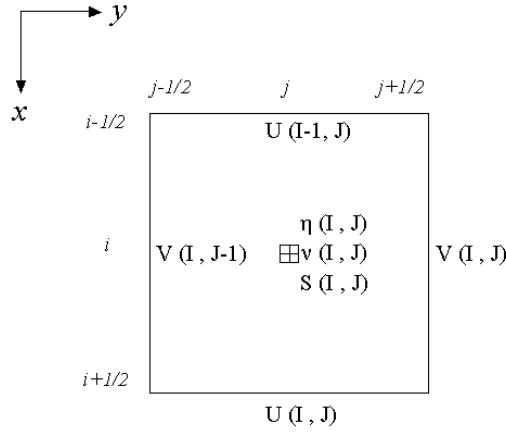


**Figure 3.4: DIVAST two-dimensional grid.**

The resulting space discretized equations of continuity and momentum are discretized with regard to time using a multi-time interval Alternating Difference Implicit (ADI). The ADI technique requires that each timestep  $\Delta t$  is split into two successive time level operations of equal length  $\Delta t/2$ . For the first half-timestep, from time  $\Delta t$  to time  $\Delta t+1/2$ , the derivatives and terms referring to conditions in the x-direction are expressed in an implicit form, whereas those in the y-direction are expressed explicitly. Likewise, for the second half-timestep, the derivatives and terms referring to conditions in the y-direction are expressed in an implicit form while those in the x-direction are expressed explicitly (Falconer, 1976). The alternating formulation decreases computational requirements since the implicit scheme is only applied in one direction in each timestep without the need to solve a full two dimensional matrix. The discretized form of continuity (3.13), and momentum equations, (3.14) and (3.15), are given below.

Continuity equation, first half time step ( $n$  to  $n + 1/2$ )

$$\theta \eta_{i,j}^{n+1/2} - \theta \eta_{i,j}^n + \frac{\Delta t}{2\Delta x} \left[ q_x|_{i+1/2,j}^{n+1/2} - q_x|_{i-1/2,j}^{n+1/2} + q_y|_{i,j+1/2}^n - q_y|_{i,j-1/2}^n \right] = 0 \quad (3.18)$$

Momentum equation in the x-direction, first half time step ( $n$  to  $n + 1/2$ )

$$\underbrace{\theta q_x|_{i+1/2}^{n+1/2}}_{(1)} = \theta q_x|_{i+1/2}^{n-1/2} \quad (3.19)$$

$$-\frac{\beta\theta\Delta t}{\Delta x} \left[ U'q'_x|_{i+1,j}^n - U'q'_x|_{i,j}^n + U'q'_y|_{i+1/2,j+1/2}^n - U'q'_y|_{i+1/2,j-1/2}^n \right] \quad (2)$$

$$+\theta\Delta t f q_y|_{i+1/2,j}^n - \frac{g\Delta t}{2\Delta x} H_{i+1/2,j}^n \left[ \eta_{i+1,j}^{n+1/2} + \eta_{i+1,j}^{n-1/2} - \eta_{i,j}^{n+1/2} - \eta_{i,j}^{n-1/2} \right] \quad (3) \quad (4)$$

$$-\frac{C_D D H_{i+1/2,j}^n \beta (U^{n+1/2} + U^{n-1/2}) (U'^2 + V^2)^{1/2}}{2} \Big|_{i+1/2,j}^n \quad (5)$$

$$\frac{\rho_a \Delta t C^* W_x (W_x^2 + W_y^2)^{1/2}}{\rho} \quad (6)$$

$$\theta \frac{g\Delta t (U^{n+1/2} + U^{n-1/2}) (U'^2 + V^2)^{1/2}}{2C^2} \Big|_{i+1/2,j}^n \quad (7)$$

$$\frac{\Delta t}{\Delta x^2} \theta v_t H_{i+1/2,j}^n \left[ U'_{i+1/2,j} + U'_{i-1/2,j} + U'_{i+1/2,j+1} + U'_{i+1/2,j-1} - 4U'_{i+1/2,j} \right] \quad (8)$$

where n is the timestep level, and i,j are grid point locations as detailed in Figure 3.4. The individual terms as numbered in equation (3.19) correspond to the depth-integrated:

- Local acceleration ... (1)
- Advective accelerations ... (2)
- Coriolis force ... (3)
- Pressure gradient ... (4)

- Dropper drag component ... (5)
- Wind shear component ... (6)
- Bed shear component ... (7)
- Turbulence induced shear force ... (8)

For the first half-timestep, from  $n$  to  $n+1/2$ , equations (3.18) and (3.19) are solved implicitly to compute values of  $q_x$  and  $\eta$ . Due to the non-linearity of the momentum equations, the solution of the advective accelerations are centred in time to avoid problems associated with non-linear instability.  $U'$ ,  $q'_x$  denote values corrected by iteration as:

$$U'|_{i+1/2,j}^n = U|_{i+1/2,j}^{n-1/2} \quad \text{for the first iteration}$$

$$U'|_{i+1/2,j}^n = \frac{1}{2} \left( U|_{i+1/2,j}^{n+1/2} + U|_{i+1/2,j}^{n-1/2} \right) \quad \text{for the second iteration}$$

For the second half-timestep, from time level  $n+1/2$  to  $n+1$ , similar formulations of the continuity and y-direction momentum equations are solved to compute values for  $q_y$  and  $\eta$ .

The formulation of the dropper drag component,  $F_D$ , and areal reduction coefficient,  $\theta$ , into the numerical model modifies the solution procedure; an amended set of recursion coefficients results. The process is explained in the following section.

### 3.2.5 Hydrodynamic solution

For an implicit solution scheme, the computed solution at any particular grid point depends on the solution at the adjacent grid points and for the same time level; unlike explicit schemes where the unknown variable is expressed directly in terms of known values. Therefore, the equation of motion for an implicit scheme cannot be solved directly for the required solution of  $U$ ,  $V$  and  $\eta$ , but must be solved simultaneously. The known values are typically those values calculated at the previous timestep and the unknowns are those variable values required at the current timestep. A system of equations, which requires the solution of a number of simultaneous equations, is most readily solved by setting up the simultaneous equations in a tri-diagonal matrix form and

applying the method of Gauss elimination and back substitution (Falconer, 1976). The solution of the hydrodynamic equations in DIVAST proceeds in this manner.

Analysing equations (3.18) and (3.19), the unknown variables are  $U$  and  $\eta$  at time level  $n+1$ . Bringing the unknown terms to the left hand side and rearranging the momentum equation (3.19), can be expressed as

x-direction momentum equation

$$\left[ \frac{g\Delta t}{2\Delta x} H_{i+1/2,j}^n \right] \eta_{i,j}^{n+1/2} + \theta \left[ 1 + \frac{g\Delta t (q_x'^2 + q_y'^2)^{1/2}}{2(HC)^2} \right]_{i+1/2,j}^n q_x|_{i+1/2,j}^{n+1/2} + \left[ \frac{g\Delta t}{2\Delta x} H_{i+1/2,j}^n \right] \eta_{i+1,j}^{n+1/2} = B_i^n \quad (3.20)$$

Replacing known terms gives:

$$-a_i \eta_{i,j}^{n+1/2} + b_i q_x|_{i+1/2,j}^{n+1/2} + c_i \eta_{i+1,j}^{n+1/2} = B_i^n \quad (3.21)$$

where:

$$a_i = b_i = \frac{g\Delta t}{2\Delta x} H_{i+1/2,j}^n; \quad b_i = \theta \left[ 1 + \frac{g\Delta t (q_x'^2 + q_y'^2)^{1/2}}{2(HC)^2} \right]_{i+1/2,j}^n$$

$$B_i^n = \theta q_x|_{i+1/2}^{n-1/2} - \frac{\beta\theta\Delta t}{\Delta x} \left[ U' q_x'|_{i+1,j}^n - U' q_x'|_{i,j}^n + U' q_y'|_{i+1/2,j+1/2}^n - U' q_y'|_{i+1/2,j-1/2}^n \right] +$$

$$\theta\Delta t f q_y|_{i+1/2,j}^n - \frac{g\Delta t}{2\Delta x} H_{i+1/2,j}^n \left[ \eta_{i+1,j}^{n-1/2} - \eta_{i,j}^{n-1/2} \right] - \frac{C_D A \beta (q_x'^2 + q_y'^2)^{1/2}}{2H} \Big|_{i+1/2,j}^n \frac{q_x|_{i+1/2,j}^n}{H} +$$

$$\frac{\rho_a \Delta t C^* W_x (W_x^2 + W_y^2)^{1/2}}{\rho} - \theta \frac{g\Delta t (q_x'^2 + q_y'^2)^{1/2}}{2(HC)^2} \Big|_{i+1/2,j}^n q_x^{n-1/2} +$$

$$\left[ U'_{i+1/2,j} + U'_{i-1/2,j} + U'_{i+1/2,j+1} + U'_{i+1/2,j-1} - 4U'_{i+1/2,j} \right]$$

A similar rearrangement of terms is applied to the continuity equation (3.18).

Rearranging terms, and bringing all unknowns to the LHS:

$$-\frac{\Delta t}{2\Delta x} q_x|_{i-1/2,j}^{n+1/2} + \theta \eta_{i,j}^{n+1/2} + \frac{\Delta t}{2\Delta x} q_x|_{i+1/2,j}^{n+1/2} = A_i^n \quad (3.22)$$

Replacing known terms:

$$-d_i q_x|_{i-1/2,j}^{n+1/2} + e_i \eta_{i,j}^{n+1/2} + f_i q_x|_{i+1/2,j}^{n+1/2} = A_i^n \quad (3.23)$$

where

$$d_i = f_i = \frac{\Delta t}{2\Delta x}; \quad e_i = \theta$$

$$A_i^n = \theta \eta_{i,j}^n - \frac{\Delta t}{2\Delta x} \left[ q_y|_{i,j+1/2}^n - q_y|_{i,j-1/2}^n \right]$$

$a_i, b_i, c_i, d_i, e_i,$  and  $f_i$  are recursion coefficients, while  $A_i$  and  $B_i$  are a combination of terms containing known values of  $\eta$  and  $q_x$ . Values may then be computed for  $\eta$  and  $q_x$  provided appropriate conditions are specified at the open boundary.

Open boundary conditions for hydrodynamics are specified as either time varying water elevations or some velocity functions normal to the prescribed boundary. When a flow boundary is applied, then the velocity outside the domain is set equal to the boundary value. If a water elevation boundary is applied, then the known water elevations are prescribed at the boundaries and both  $x$  and  $y$  components of the velocities at the boundaries can be calculated.

The computation of unknown variables commences with equations (3.21) and (3.23). Taking a sample section of contiguous grid as presented in Figure 3.5(b); which is located in the computational domain presented in Figure 3.5(a). Grid cells (2,2) to (12,2) are bounded by a lower open boundary condition at (1,2) and an upper, closed boundary at (13,2). The unknown values of  $q_x|_{i,j}^{n+1/2}$  and  $\eta|_{i,j}^{n+1/2}$  in (3.21) and (3.23) can now be evaluated for the grid cells in the computational domain by a process of elimination.

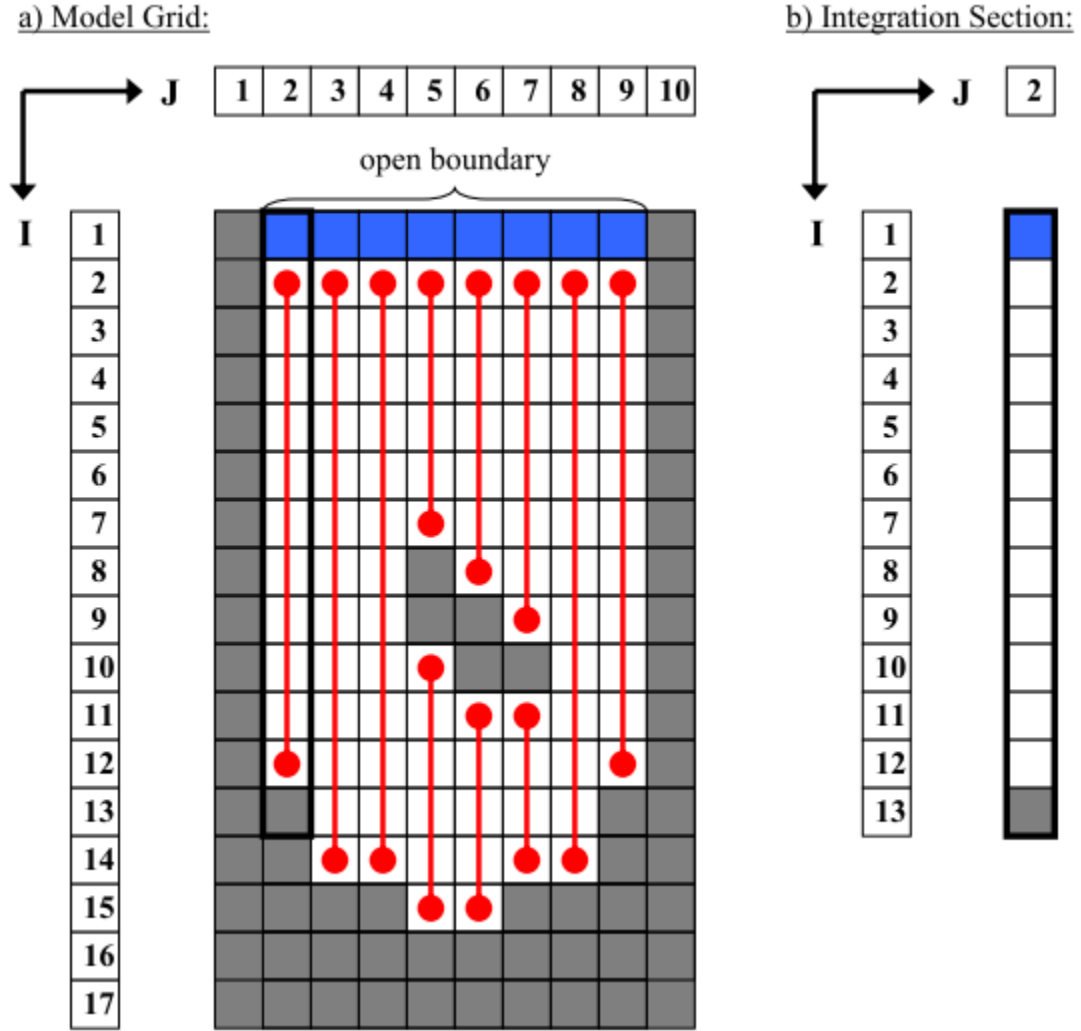


Figure 3.5: (a) Sample model grid showing x-direction integration sections and (b) individual section (land cells are grey, wet cells are white and boundary cells are blue) (Nash, 2010)

Starting at  $i=1$ , and given that  $\eta_{1,j}^{n+1/2}$  is a known boundary condition, the unknown  $q_x|_{1^{1/2},j}^{n+1/2}$  in (3.21) can be written in the form:

$$q_x|_{1^{1/2},j}^{n+1/2} = -R_1\eta_{2,j}^{n+1/2} + S_1 \quad (3.24)$$

At  $i=2$ , expression (3.24) can then be substituted into equation (3.23) to eliminate the flux  $q_x|_{1^{1/2},j}^{n+1/2}$  to obtain an equation for  $\eta_{2,j}^{n+1/2}$  which takes the form:

$$\eta_{2,j}^{n+1/2} = -P_2 q_x|_{2^{1/2},j}^{n+1/2} + Q_2 \quad (3.25)$$

At  $i=3$ , expression (3.25) can be substituted back into equation (3.23) to eliminate  $\eta_{2,j}^{n+1/2}$ . Applying this procedure for all cells  $i=1, \dots, i_{\max}$ , allows all unknowns be expressed in terms of known variables. In their general recursive forms, the continuity and momentum equations may be written as, respectively:

$$\eta_{i,j}^{n+1/2} = -P_i q_x|_{i+1/2,j}^{n+1/2} + Q_i \quad (3.26)$$

$$q_x|_{i+1/2,j}^{n+1/2} = -R_i \eta_{i+1,j}^{n+1/2} + S_i \quad (3.27)$$

Where  $P_i$ ,  $Q_i$ ,  $R_i$  and  $S_i$  are recursion terms computed as follows for  $i=1, \dots, i_{\max}$ :

$$P_i = \frac{f_i}{e_i + d_i R_{i-1}}; \quad Q_i = \frac{A_i^n + d_i S_{i-1}}{e_i + d_i R_{i-1}}$$

$$R_i = \frac{c_i}{b_i + a_i P_i}; \quad S_i = \frac{B_i^n + a_i Q_i}{b_i + a_i P_i}$$

For the special case  $i=1$ , the recursion terms computed at the open boundary are,

$$R_1 = \frac{c_1}{b_1}; \quad S_1 = B_1^n + \frac{a_1}{b_1} \eta_{1,j}^{n+1/2}$$

The recursion terms  $P_i$  and  $Q_i$  are not required at  $i=1$ .

Upon reaching  $i_{\max}$  one arrives at an equation for  $\eta_{i_{\max},j}^{n+1/2}$  with a single unknown,  $q_x|_{i_{\max},j}^{n+1/2}$ ; this unknown flux is specified by means of an upper boundary condition; in this case a closed boundary, giving  $q_x|_{i_{\max},j}^{n+1/2} = 0$  allowing  $\eta_{i_{\max},j}^{n+1/2}$  to be calculated. Backward substitution is then used to determine  $q_x|_{i+1/2,j}^{n+1/2}$  and  $\eta_{i,j}^{n+1/2}$  at each value of  $i$ .

This procedure is then repeated for the  $j+1$  rows etc., until all the  $N$  rows parallel to the  $x$ -direction have been solved. When completed the values of the water levels  $\eta^{n+1/2}$  and velocities  $q_x^{n+1/2}$  are known throughout the domain.

As previously mentioned, the stability of the solution requires that all non-linear terms are centred in time and space. The solution algorithm presented, computes all unknown values of  $\eta_{i,j}^{n+1/2}$  and  $q_x|_{i+1/2,j}^{n+1/2}$  during the first half timestep. A similar algorithm is then applied to the  $y$ -direction integration sections during the second half-timestep to compute all unknown values of  $\eta_{i,j}^{n+1}$  and  $q_y|_{i+1/2,j}^{n+1}$ .

This solution scheme is second order accurate, both in time and space, with no stability constraints due to the time centred implicit character of the ADI technique. However, in order to achieve a reasonable computational accuracy, the time step cannot exceed a maximum Courant number,  $C_{cn}$ , as suggested by Stelling et al., (1986):

$$C_{cn} = 2\Delta t \sqrt{gH \left( \frac{1}{\Delta x^2} + \frac{1}{\Delta y^2} \right)} \leq 4\sqrt{2} \quad (3.28)$$

Practically, extensive tests showed that the stability and accuracy of the scheme is preserved when the Courant number does not exceed eight.

### 3.2.6 Turbulence closure models

A turbulence model is a computational procedure to close the system of mean flow equations. For most engineering applications, it is unnecessary to resolve the details of the turbulent fluctuations. Turbulence models allow the calculation of the mean flow without first calculating the full time-dependent flow-field; only how turbulence affects the mean flow.

As mentioned, the mixing length turbulence closure model has certain limitations in the simulation of flow processes (Rodi. W., 1993). The mixing length theory is most appropriate when a unique length scale of turbulence exists (Tennekes and Lumley, 1972). This is not the case for flow through an aquaculture installation, in which there

will usually be two characteristic length scales, one associated with the mean velocity gradients and one with the wake generated eddies. In addition, the mixing length model assumes that the production of kinetic energy is in approximate balance with the viscous dissipation of kinetic energy. This is not the case within a suspended aquaculture canopy, where production significantly exceeds dissipation (Nepf, 1999). The model therefore performs poorly, unless appropriate empirical coefficients are computed *for the particular flow regime* (Burke and Stolzenbach, 1983).

Therefore, a more sophisticated turbulence closure model was deemed a necessity to simulate these processes. This section expands on the work of Olbert, (2006), who incorporated a two-equation k- $\epsilon$  model into DIVAST.

The two-equation models discussed here rely on a local turbulent eddy viscosity  $\nu_t$  that parameterizes turbulence in terms of mean flow quantities (vertical shear) as:

$$-\overline{u'v'} = \nu_t \frac{\partial u}{\partial y}; \quad -\overline{v'u'} = \nu_t \frac{\partial v}{\partial x} \quad (3.29)$$

The standard Reynolds decomposition has been used with  $\tilde{u} = u + u'$ ;  $\tilde{v} = v + v'$ ; and  $\tilde{w} = w + w'$ ; where  $\tilde{u}$ ,  $\tilde{v}$ , and  $\tilde{w}$  are instantaneous velocity components in the x, y, and vertical z direction respectively;  $u$ ,  $v$ , and  $w$  are resolvable mean velocity components; and  $u'$ ,  $v'$  and  $w'$  are components of fluctuations of velocity about the mean velocity.

The product terms on the left hand side,  $\overline{u'w'}$ , and  $\overline{v'w'}$  represent correlation between the fluctuating components of velocity; which describes the transport of momentum by turbulent motion. The term  $-\overline{u'w'}$  describes the transport of x-momentum in the z-direction, and it effectively acts as a stress on the fluid. The over bar denotes time-averaging, as described by Hinze, (1975):

$$\bar{f} = \frac{1}{t_2 - t_1} \int_{t_1}^{t_2} f dt \quad (3.30)$$

The time interval of averaging  $t_2 - t_1$  is long compared with the scale of turbulent motion, but small compared with the scale of mean flow variation. Time averaging describes the effects of the instantaneous quantities on the mean flow.

Prandtl, (1945) and Kolmogorov, (1942), independently suggested that the eddy viscosity is proportional to the product of a characteristic velocity and length scale, known as the Kolmogorov-Prandtl expression:

$$\nu_t = c'_\mu \sqrt{k} l \quad (3.31)$$

Where  $c'_\mu$  is an empirical constant,  $l$  is the characteristic length scale and  $k$  is the turbulent kinetic energy, defined as  $k = \frac{1}{2}(u'^2 + v'^2 + w'^2)$

The distribution of  $k$  is relatively easily calculated via a transport equation that describes advection, diffusion, production and dissipation of kinetic energy. Defining and providing an equation for the length scale,  $l$ , is more difficult and uncertain. A number of two-equation models are commonly used that prescribe an equation for  $l$  using different transport equations.

The length scale characterizing the size of the large energy containing eddies, is subject to transport processes in a similar manner to the energy  $k$ . Processes influencing the length scale include dissipation, which destroys the small eddies and thus effectively increases the eddy size; and vortex stretching connected with the energy cascade, which reduces the energy size (Rodi, 1993). A length scale equation doesn't need to have the length scale equation itself as dependent variable; any combination of the form  $Z = k^m L^n$  will suffice since  $k$  is known from solving the  $k$  transport equation (Rodi, 1993). For example, the  $k$ - $\epsilon$  closure model makes use of the relationship  $l = \alpha k^{3/2} \epsilon^{-1}$  to compute the length scale.

Despite the different formulations used in calculating the characteristic length scale the results are very similar; in fact all the equations possess a common form and can be expressed in the standard Einstein summation convention as (Rodi. W., 1993):

$$\underbrace{\frac{\partial Z}{\partial t}}_{\text{rate of change}} + \underbrace{u_i \frac{\partial Z}{\partial x_i}}_{\text{convection}} = \underbrace{\frac{\partial}{\partial x_i} \left( \frac{\sqrt{k} L}{\sigma_z} \frac{\partial Z}{\partial x_i} \right)}_{\text{diffusion}} + \underbrace{c_{z1} \frac{z}{k} P}_{\text{production}} - \underbrace{c_{z2} Z \frac{\sqrt{k}}{L}}_{\text{destruction}} + S \quad (3.32)$$

Where  $\sigma_z$ ,  $c_{z1}$  and  $c_{z2}$  are empirical constants, P is the production of kinetic energy and S represents a secondary source term which differs according to the choice of L.

### 3.2.6.1 Two-equation k-ε model

The k-ε model is the most popular two-equation model (Wilcox, 1998). It can be expressed as:

$$\begin{aligned} \frac{\partial k}{\partial t} + u \frac{\partial k}{\partial x} + v \frac{\partial k}{\partial y} + w \frac{\partial k}{\partial z} \\ = \frac{\partial}{\partial z} \left( \frac{\nu_v}{\sigma_k} \frac{\partial k}{\partial z} \right) + \nu_v \left( \left( \frac{\partial u}{\partial z} \right)^2 + \left( \frac{\partial v}{\partial z} \right)^2 \right) + \nu_h \frac{g}{\rho_0} \frac{\partial \rho}{\partial z} - \varepsilon \end{aligned} \quad (3.33)$$

$$\begin{aligned} \frac{\partial \varepsilon}{\partial t} + u \frac{\partial \varepsilon}{\partial x} + v \frac{\partial \varepsilon}{\partial y} + w \frac{\partial \varepsilon}{\partial z} \\ = \frac{\partial}{\partial z} \left( \frac{\nu_v}{\sigma_\varepsilon} \frac{\partial \varepsilon}{\partial z} \right) + \frac{\varepsilon}{k} \left( c_1 \nu_v \left( \left( \frac{\partial u}{\partial z} \right)^2 + \left( \frac{\partial v}{\partial z} \right)^2 \right) + c_3 \nu_h \frac{g}{\rho_0} \frac{\partial \rho}{\partial z} - c_2 \varepsilon \right) \end{aligned} \quad (3.34)$$

where:

$\varepsilon$  - dissipation of turbulent kinetic energy

$\nu_v$  - vertical eddy viscosity for momentum defined as  $\nu_v = c\sqrt{2kl}S_M + \nu$

$\nu_h$  - eddy diffusivity for temperature defined as  $\nu_h = c\sqrt{2kl}S_H + \nu_\theta$

where,  $S_M$  and  $S_H$  are stability functions that describe the effects of shear and stratification and c is a coefficient with a value of c=1.0 for the stability functions of (Galperin et al., 1988).

Eddy viscosity is determined from the Kolmogorov-Prandtl expression and the relationship between eddy viscosity and length scale, L, in the form:

$$\nu_v = c'_\mu \frac{k^2}{\varepsilon} \quad (3.35)$$

The k-ε model may be used in the depth-average calculations when the local depth-averaged state of turbulence is characterized by  $\bar{k}$  and,  $\bar{\varepsilon}$ , and depth-averaged turbulent stresses are related to depth-averaged velocity gradients. A widely-used k-ε model for shallow water flows was proposed by Rastogi and Rodi, (1978).

The depth-integrated form of the k-ε model can be derived by first integrating the three-dimensional turbulence transport equations (3.33) and (3.34) over a water depth and then applying the appropriate boundary conditions. This technique gives (Olbert, 2006):

$$\frac{\delta H \bar{k}}{\delta t} + UH \frac{\delta \bar{k}}{\delta x} + VH \frac{\delta \bar{k}}{\delta y} = \frac{\delta}{\delta x} \left( \frac{Hv_t}{\sigma_k} \frac{\delta k}{\delta x} \right) + \frac{\delta}{\delta y} \left( \frac{Hv_t}{\sigma_k} \frac{\delta k}{\delta y} \right) + HP_h + HP_{kv} - H\bar{\varepsilon} \quad (3.36)$$

$$\begin{aligned} \frac{\delta H \bar{\varepsilon}}{\delta t} + UH \frac{\delta \bar{\varepsilon}}{\delta x} + VH \frac{\delta \bar{\varepsilon}}{\delta y} \\ = \frac{\delta}{\delta x} \left( \frac{Hv_t}{\sigma_\varepsilon} \frac{\delta \bar{\varepsilon}}{\delta x} \right) + \frac{\delta}{\delta y} \left( \frac{Hv_t}{\sigma_\varepsilon} \frac{\delta \bar{\varepsilon}}{\delta y} \right) + c_{1z} \frac{\bar{\varepsilon}}{\bar{k}} HP_h + HP_{\varepsilon v} - c_{2z} H \frac{\bar{\varepsilon}^2}{\bar{k}} \end{aligned} \quad (3.37)$$

The depth-averaged horizontal production,  $P_h$ , is due to the action of 2D Reynolds stresses and mean-velocity gradients as:

$$P_h = v_t \left( \left( \frac{\delta U}{\delta x} + \frac{\delta U}{\delta x} \right) \frac{\delta U}{\delta x} + \left( \frac{\delta V}{\delta x} + \frac{\delta U}{\delta y} \right) \frac{\delta V}{\delta x} \right) \quad (3.38)$$

$\bar{k}$ ,  $\bar{v}_t$  and  $\bar{\varepsilon}$ , can be considered a depth-averaged representation of the three dimensional forms (Rodi, 1993).  $c_{1z}$ ,  $c_{2z}$ ,  $\sigma_k$  and  $\sigma_\varepsilon$  are empirical constants. Standard values were adopted as follows  $C_{1z}=1.44$ ,  $C_{2z}=1.92$ ,  $\sigma_k=1.0$ ,  $\sigma_\varepsilon=1.3$  (Launder and Spalding, 1974).

The vertical production is in addition to the horizontal production, due to horizontal velocity gradients, and depends strongly on the bottom roughness. Thus, this extra source term refers to the resultant bottom shear stress through frictional velocity  $U_*$  and it can be expressed as:

$$P_{kv} = c_k \frac{U_*^3}{H} \quad (3.39)$$

$$P_{\varepsilon v} = c_{\varepsilon} \frac{U_*^4}{H} \quad (3.40)$$

where  $c_k$  and  $c_{\varepsilon}$  are empirical constants.

The depth-averaged k- $\varepsilon$  model considers turbulence production due to vertical velocity gradients near the bed. Significantly, with regards to simulating impeded flow profiles, it also simulates turbulence production due to horizontal velocity gradients. The standard k- $\varepsilon$  model has been applied to many kinds of flows, including, two-dimensional wall boundary layers (Jones and Launder, 1972), flows past hydraulic structures (Cea et al., 2007) and flows through a horizontal axis wind turbine (El Kasmi and Masson, 2008). The next section considers a mathematical representation of the turbulence production associated with a mussel dropper farm.

#### ***3.2.6.2 Amended k- $\varepsilon$ model***

In addition to affecting the hydrodynamics as detailed above, the presence of droppers also affects the turbulent intensity and diffusion via the conversion of mean kinetic energy to turbulent kinetic energy (Nepf, 1999). This contribution augments the turbulence intensity, while the characteristic turbulence length scale is redefined in terms of the dropper scale. This means, that turbulence within a cultivated mussel dropper region is dominated by the dropper structures as opposed to the bottom-boundary shear, as in open channel flow (Nepf et al., 1997).

As part of this research, the k- $\varepsilon$  turbulence closure model was amended to incorporate this conversion of kinetic energy into the numerical model by introducing an additional term representing canopy drag. The system of partial different equations expressing the budget of turbulent kinetic energy, k, and dissipation  $\varepsilon$  can be expressed as (Shimizu and Tsujimoto, 1994):

$$\begin{aligned}
 \frac{\partial H\bar{k}}{\partial t} + UH \frac{\partial \bar{k}}{\partial x} + VH \frac{\partial \bar{k}}{\partial y} \\
 = \frac{\partial}{\partial x} \left[ \frac{Hv_t}{\sigma_k} \frac{\partial \bar{k}}{\partial x} \right] + \frac{\partial}{\partial y} \left[ \frac{Hv_t}{\sigma_k} \frac{\partial \bar{k}}{\partial y} \right] + HP_h + HP_{kv} - H\bar{\varepsilon} \\
 + C_{fk}H(F_T U^2 + F_T V^2)
 \end{aligned} \tag{3.41}$$

$$\begin{aligned}
 \frac{\partial H\bar{\varepsilon}}{\partial t} + UH \frac{\partial \bar{\varepsilon}}{\partial x} + VH \frac{\partial \bar{\varepsilon}}{\partial y} \\
 = \frac{\partial}{\partial x} \left[ \frac{Hv_t}{\sigma_\varepsilon} \frac{\partial \bar{\varepsilon}}{\partial x} \right] + \frac{\partial}{\partial y} \left[ \frac{Hv_t}{\sigma_\varepsilon} \frac{\partial \bar{\varepsilon}}{\partial y} \right] + HP_{\varepsilon v} \\
 + \frac{H\bar{\varepsilon}}{k} \{ C_{1z} [P_h + C_{f\varepsilon}(F_T U^2 + F_T V^2)] - C_{2z} H\bar{\varepsilon} \}
 \end{aligned} \tag{3.42}$$

The weighting coefficients attached to the additional turbulence production of the aquaculture installations,  $C_{fk}$  and  $C_{f\varepsilon}$ , can be considered results of the model calibration (Shimizu and Tsujimoto, 1994). For this study, the values were prescribed a priori based on a consideration of literature and mathematical analysis (Lopez and Garcia, 2001); it can be shown that for the  $\varepsilon$ -equation to be in balance, the value of  $C_{f\varepsilon}$  has to be dependent upon the value of  $C_{fk}$  (Burke, 1983). This can be derived by considering steady, horizontal flow through vertical infinitely long cylinders, where all the derivatives in the vertical direction vanish. Then from the  $k$ -equation  $\bar{\varepsilon} = C_{fk}(F_T U + F_t V)$  and from the  $\varepsilon$ -equation,  $C_{1z} C_{f\varepsilon}(F_T U + F_t V) = C_{2z} \bar{\varepsilon}$ , so that  $C_{f\varepsilon} = (C_{2z}/C_{1z})C_{fk}$ . For this study, a value of 1.0 was prescribed for  $C_{fk}$ , and a corresponding value of  $C_{f\varepsilon}=1.33$  (Neary, 2003).

The effect of the mussel dropper longlines are included via an additional turbulence production term included in the  $k - \varepsilon$  transport equation (Naot et al., 1996):

$$F_T = \frac{1}{2} \rho_d D C_{DT} \sqrt{U^2 + V^2} \tag{3.43}$$

The two transport equations are discretized in a similar manner to the hydrodynamic equations discussed in the previous section. For discrete representation of  $k$  and  $\varepsilon$  a space staggered system of Mark and Cell grid type is used with positions of key variables

described and illustrated in Figure 3.4 The discrete form of the kinetic energy equation for the first half time step ( $n$  to  $n + 1/2$ ) can be written as:

$$\begin{aligned}
 & (\bar{k}H)_{i,j}^{n+1/2} - (\bar{k}H)_{i,j}^n + \frac{\Delta t}{2\Delta x} \left( \bar{k}_{i+1/2,j}^{n+1/2} (UH)_{i+1/2,j}^{n+1/2} - \bar{k}_{i-1/2,j}^{n+1/2} (UH)_{i-1/2,j}^{n+1/2} \right) + \\
 & \quad \frac{\Delta t}{2\Delta y} \left( \bar{k}_{i,j+1/2}^n (VH)_{i,j+1/2}^n - \bar{k}_{i,j-1/2}^n (VH)_{i,j-1/2}^n \right) \\
 & = \frac{\Delta t}{2\Delta x^2} \left[ \left( \frac{v_t H}{\sigma_k} \right)_{i+1/2,j}^{n+1/2} \left( \bar{k}_{i+1,j}^{n+1/2} - \bar{k}_{i,j}^{n+1/2} \right) - \left( \frac{v_t H}{\sigma_k} \right)_{i-1/2,j}^{n+1/2} \left( \bar{k}_{i,j}^{n+1/2} - \bar{k}_{i-1,j}^{n+1/2} \right) \right] \\
 & \quad + \frac{\Delta t}{2\Delta y^2} \left[ \left( \frac{v_t H}{\sigma_k} \right)_{i,j+1/2}^n \left( \bar{k}_{i,j+1}^n - \bar{k}_{i,j}^n \right) - \left( \frac{v_t H}{\sigma_k} \right)_{i,j-1/2}^n \left( \bar{k}_{i,j}^n - \bar{k}_{i,j-1}^n \right) \right] \\
 & \quad + (v_t H)_{i,j}^n \cdot \frac{\Delta t}{2} \left[ 2 \left( \frac{U_{i+1/2,j}^{n+1/2} - U_{i-1/2,j}^{n+1/2}}{\Delta x} \right)^2 + 2 \left( \frac{V_{i,j+1/2}^n - V_{i,j-1/2}^n}{\Delta y} \right)^2 \right. \\
 & \quad \quad \left. + \left( \frac{U_{i,j+1/2}^{n+1/2} - U_{i,j-1/2}^{n+1/2}}{\Delta y} + \frac{V_{i+1/2,j}^n - V_{i-1/2,j}^n}{\Delta x} \right)^2 \right] \\
 & \quad + \frac{\Delta t}{2} \cdot [(C_f)_{i,j}^n] \left[ (U_{i,j}^{n+1/2})^2 + (V_{i,j}^n)^2 \right]^{1/2} - \frac{\Delta t}{2} (\varepsilon H)_{i,j}^{n+1/2} \\
 & \quad \frac{\Delta t}{4} C_T C_{fk} D H_{i+1/2,j}^n \left( U_{i+1/2,j}^{n+1/2} U_{i+1/2,j}^{n+1/2} + U_{i+1/2,j}^{n-1/2} U_{i+1/2,j}^{n-1/2} \right) (U^2 + V^2)^{1/2} \Big|_{i+1/2,j}^n \\
 & \quad + \frac{\Delta t}{2} C_T C_{fk} D H_{i,j+1/2}^n \left( V_{i,j+1/2}^n V_{i,j+1/2}^n \right) (U^2 + V^2)^{1/2} \Big|_{i,j+1/2}^n
 \end{aligned} \tag{3.44}$$

The depth integrated representation of the  $k$  and  $\varepsilon$  equations are calculated for the first half time step at the centre of point  $i,j$ . According to ADI technique, all derivatives in the  $x$ -direction are expressed implicitly and those in the  $y$ -coordinate direction are represented explicitly. Because the backward implicit scheme is not fully centred in time, the advective components are subject to time centred iteration. Terms indicated by prime in the above equation were updated by the iteration in two steps:

$$\text{First iteration } -\bar{k}_{i,j}^{n+1/2} = \bar{k}_{i,j}^n$$

$$\text{Second iteration } -\bar{k}_{i,j}^{n+1/2} = \frac{1}{2} \left( \bar{k}_{i,j}^n + \bar{k}_{i,j}^{n+1/2} \right)$$

Likewise, a similar discretization procedure and solution method is applied to the dissipation equation. The discrete form of the  $\varepsilon$ -equation for the first half time step ( $n$  to  $n + 1/2$ ) has the form:

$$\begin{aligned}
 & (\bar{\varepsilon}H)_{i,j}^{n+1/2} - (\bar{\varepsilon}H)_{i,j}^n + \frac{\Delta t}{2\Delta x} \left( \bar{\varepsilon}_{i+1/2,j}^{n+1/2} (UH)_{i+1/2,j}^{n+1/2} - \bar{\varepsilon}_{i-1/2,j}^{n+1/2} (UH)_{i-1/2,j}^{n+1/2} \right) + \\
 & \quad \frac{\Delta t}{2\Delta y} \left( \bar{\varepsilon}_{i,j+1/2}^n (VH)_{i,j+1/2}^n - \bar{\varepsilon}_{i,j-1/2}^n (VH)_{i,j-1/2}^n \right) \\
 = & \frac{\Delta t}{2\Delta x^2} \left[ \left( \frac{v_t H}{\sigma_\varepsilon} \right)_{i+1/2,j}^{n+1/2} \left( \bar{\varepsilon}_{i+1,j}^{n+1/2} - \bar{\varepsilon}_{i,j}^{n+1/2} \right) - \left( \frac{v_t H}{\sigma_\varepsilon} \right)_{i-1/2,j}^{n+1/2} \left( \bar{\varepsilon}_{i,j}^{n+1/2} - \bar{\varepsilon}_{i-1,j}^{n+1/2} \right) \right] \\
 & + \frac{\Delta t}{2\Delta y^2} \left[ \left( \frac{v_t H}{\sigma_\varepsilon} \right)_{i,j+1/2}^n \left( \bar{\varepsilon}_{i,j+1}^n - \bar{\varepsilon}_{i,j}^n \right) - \left( \frac{v_t H}{\sigma_\varepsilon} \right)_{i,j-1/2}^n \left( \bar{\varepsilon}_{i,j}^n - \bar{\varepsilon}_{i,j-1}^n \right) \right] \\
 & \quad C_{1z} C_\mu (\bar{k}H)_{i,j}^n \frac{\Delta t}{2} \left[ 2 \left( \frac{U_{i+1/2,j}^{n+1/2} - U_{i-1/2,j}^{n+1/2}}{\Delta x} \right)^2 + 2 \left( \frac{V_{i,j+1/2}^n - V_{i,j-1/2}^n}{\Delta y} \right)^2 \right. \\
 & \quad \left. + \left( \frac{U_{i,j+1/2}^{n+1/2} - U_{i,j-1/2}^{n+1/2}}{\Delta y} + \frac{V_{i+1/2,j}^n - V_{i-1/2,j}^n}{\Delta x} \right)^2 \right] \\
 & \quad + \frac{\Delta t}{2H_{i,j}^n} \cdot (C_\varepsilon)_{i,j}^2 \left[ (C_f)_{i,j}^n \right]^2 \left[ \left( U_{i,j}^{n+1/2} \right)^2 + \left( V_{i,j}^n \right)^2 \right] - C_{2z} H_{i,j}^{n+1/2} \frac{\Delta t}{2} \left( \frac{\bar{\varepsilon}^2}{\bar{k}} \right)_{i,j}^{n+1/2} \\
 & \quad + \frac{\Delta t \bar{\varepsilon}}{4\bar{k}} C_{1z} C_T C_{f\varepsilon} D H_{i+1/2,j}^n \left( U_{i+1/2,j}^{n+1/2} U_{i+1/2,j}^{n+1/2} + U_{i+1/2,j}^{n-1/2} U_{i+1/2,j}^{n-1/2} \right) (U^2 + V^2)^{1/2} \Big|_{i+1/2,j}^n \\
 & \quad + \frac{\Delta t \bar{\varepsilon}}{2\bar{k}} C_{1z} C_T C_{f\varepsilon} D H_{i,j+1/2}^n \left( V_{i,j+1/2}^n V_{i,j+1/2}^n \right) (U^2 + V^2)^{1/2} \Big|_{i,j+1/2}^n
 \end{aligned} \tag{3.45}$$

The solution of the k- $\varepsilon$  turbulence model proceeds in a similar fashion to that discussed for the hydrodynamic solution. Thus, for the equation of turbulent kinetic energy the backward implicit scheme at time level  $n+1/2$  gives in  $x$ -direction three unknowns of form  $k_{i-1}^{n+1/2}, k_{i,j}^{n+1/2}, k_{i+1}^{n+1/2}$ ; with similar unknown terms for the dissipation equation  $\varepsilon$ . These terms are later evaluated using the method of Gauss elimination and back substitution, where the first and last variable in an integration range are defined from boundary conditions.

### 3.3 Environmental Fluid Dynamics Code (EFDC) model

#### 3.3.1 Model history and description

The EFDC model was originally developed at the Virginia Institute of Marine Science and is currently supported by the U. S. Environmental Protection Agency (EPA) (Hamrick, 1996). The EFDC model has been extensively tested and documented in over 100 modelling studies. The model has been applied to a wide range of modelling studies, including: environmental impact assessment studies (Hamrick, 1992a), salinity transport (Moustafa and Hamrick, 1994), suspended sediment transport (Bai and Lung, 2005), larval transport (Shen et al., 1999) and hydrothermal responses (Khangaonkar et al., 2005). The model is presently being used by universities, research organisations, governmental agencies, and consulting firms (Ji, 2008).

The EFDC model is an advanced three-dimensional time-variable model that provides the capability of internally linking four major modules: hydrodynamic, water quality and eutrophication, sediment transport, and toxic chemical transport and fate submodels (Figure 3.6). The EFDC hydrodynamic model itself, is composed of six transport module, namely, dynamics, dye, temperature, salinity, near field plume and drifter (see Figure 3.7)

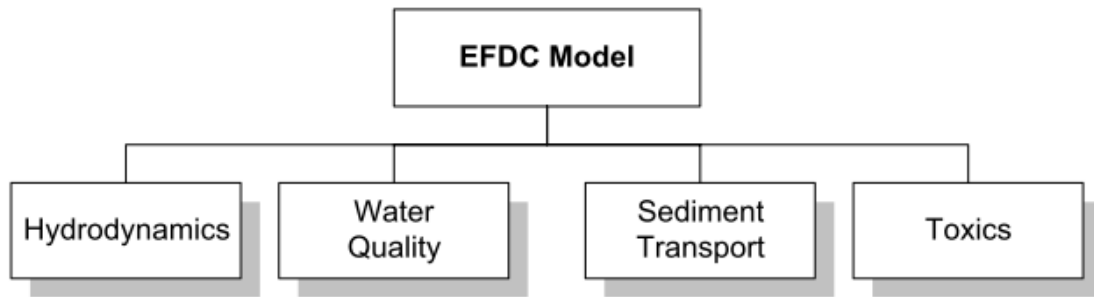


Figure 3.6: Primary modules of the EFDC model

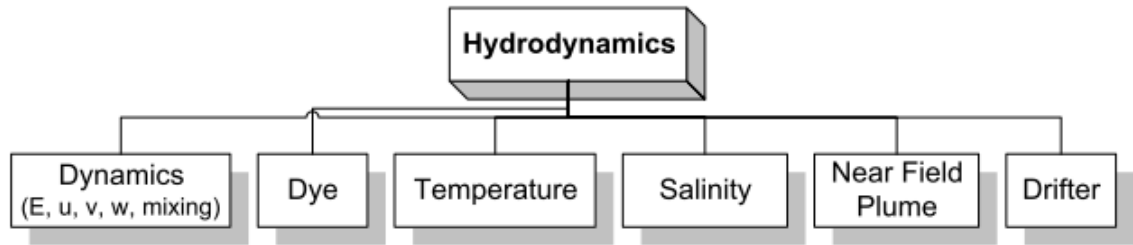


Figure 3.7: Structure of the EFDC hydrodynamic module

### 3.3.2 Governing equations

The hydrodynamics of the EFDC model and many aspects of the computational scheme are equivalent to the widely used Princeton Ocean Model (Blumberg and Mellor, 1987) (Hamrick and Wu, 1997). The EFDC model solves the three-dimensional, vertically hydrostatic, free surface, turbulent averaged equations of motion for a variable density fluid. Dynamically coupled transport equations for turbulent kinetic energy, turbulent length scale, salinity and temperature are also solved. The two turbulence parameter transport equations implement the Mellor-Yamada level 2.5 turbulence closure scheme (Mellor and Yamada, (1974), Galperin et al., (1988)).

The equations that form the basis for the EFDC hydrodynamic model are based on the continuity, Reynolds-averaged Navier-Stokes and concentration equations. It has often been noted that the ordinary  $x,y,z$  coordinate system has certain disadvantages in the vicinity of large bathymetric irregularities (Blumberg and Mellor, 1987). To provide uniform resolution in the vertical direction and a free surface permitting long wave motion, a time variable mapping or stretching transformation is desirable. The mapping or stretching is given by (Phillips, 1957):

$$z = \frac{z^* + h}{h + \eta} \quad (3.46)$$

where  $z$  = the stretched, dimensionless vertical coordinate, or so-called sigma coordinate, and  $z^*$  = the physical vertical or Cartesian coordinate. The so-called sigma coordinate system gives:

z = 0	at bottom topography	z*=-h
z=1	at free surface	z*=η

As shown in Figure 3.8, the sigma coordinate system allows smooth representation of the bathymetry and same order of accuracy in shallow and deep waters. Details of the transformation may be found in Vinokur, (1974) or Blumberg and Mellor, (1987).



**Figure 3.8: The sigma coordinate system.  $z^*$  = Cartesian coordinate in the vertical and  $z$  = the sigma coordinate. Illustration adapted from Ji, (2008)**

Adopting the Boussinesq approximation for variable density fluid; which states that, density differences are sufficiently small to be neglected except where they appear in terms multiplied by  $g$ ; the model governing equations can be expressed as:

*Continuity equation*

$$\frac{\partial \eta}{\partial t} + \frac{\partial Hu}{\partial x} + \frac{\partial Hv}{\partial y} + \frac{\partial w}{\partial z} = Q_H \quad (3.47)$$

*Depth-integrated continuity equation*

$$\frac{\partial \eta}{\partial t} + \frac{\partial \left( H \int_0^1 u dz \right)}{\partial x} + \frac{\partial \left( H \int_0^1 v dz \right)}{\partial y} \quad (3.48)$$

*x-direction momentum equation*

$$\begin{aligned} & \frac{\partial Hu}{\partial t} + \frac{\partial (Huu)}{\partial x} + \frac{\partial (Hvu)}{\partial y} + \frac{\partial wu}{\partial z} - fHv \\ & = -H \frac{\partial (p + g\eta)}{\partial x} + Hgb \frac{\partial h}{\partial x} - Hgbz \frac{\partial H}{\partial x} + \frac{\partial \left( \frac{\nu_v}{H} \frac{\partial u}{\partial z} \right)}{\partial z} + Q_u \end{aligned} \quad (3.49)$$

*y*-direction momentum equation

$$\begin{aligned} \frac{\partial H v}{\partial t} + \frac{\partial(H u v)}{\partial x} + \frac{\partial(H v v)}{\partial y} + \frac{\partial w v}{\partial z} + f H u \\ = -H \frac{\partial(p + g \eta)}{\partial y} + H g b \frac{\partial h}{\partial y} - H g b z \frac{\partial H}{\partial y} + \frac{\partial\left(\frac{\nu_v}{H} \frac{\partial v}{\partial z}\right)}{\partial z} + Q_v \end{aligned} \quad (3.50)$$

$$\frac{\partial p}{\partial z} = -g H \frac{\rho - \rho_0}{\rho_0} = -g H b \quad (3.51)$$

$$\rho = \rho(p, S, T) \quad (3.52)$$

where  $p$  is excess water column hydrostatic pressure;  $b$  is the buoyancy;  $\nu_v$  is the vertical turbulent viscosity; and  $Q_u$ ,  $Q_v$  are momentum source sink terms incorporating subgrid scale processes.

The hydrodynamic module also contains a pair of transport equations describing the evolution of temperature (T) and salinity (S). The three-dimensional, advection-diffusion transport equation can be expressed as:

$$\frac{\partial H \phi}{\partial t} + \frac{\partial H u \phi}{\partial x} + \frac{\partial H v \phi}{\partial y} + \frac{\partial w \phi}{\partial z} = \frac{\partial\left(\frac{\nu_b}{H} \frac{\partial \phi}{\partial z}\right)}{\partial z} + Q_\phi \quad (3.53)$$

where  $\phi$  represents concentration variable of salinity or temperature,  $\nu_b$  is the vertical turbulent diffusivity, and  $Q_\phi$  describe relevant source and sink terms.

The terms  $Q_u$ ,  $Q_v$  and  $Q_\phi$ , found in (3.49), (3.50) and (3.53) include subgrid scale horizontal diffusion and momentum or thermal sources and sinks. These terms represent motions induced by small-scale processes and not directly resolved by the model grid. They are parameterised in terms of horizontal diffusion and can be expressed as:

$$Q_u = \frac{\partial}{\partial x} \left( 2A_H \frac{\partial u}{\partial x} \right) + \frac{\partial}{\partial y} \left( A_H \left[ \frac{\partial u}{\partial y} + \frac{\partial v}{\partial x} \right] \right) \quad (3.54)$$

$$Q_v = \frac{\partial}{\partial x} \left( A_H \left[ \frac{\partial u}{\partial y} + \frac{\partial v}{\partial x} \right] \right) + \frac{\partial}{\partial y} \left( 2A_H \frac{\partial u}{\partial x} \right) \quad (3.55)$$

$$Q_\phi = \frac{\partial}{\partial x} \left( A_\phi \frac{\partial \phi}{\partial x} \right) + \frac{\partial}{\partial y} \left( A_\phi \frac{\partial \phi}{\partial x} \right) \quad (3.56)$$

The function of the horizontal diffusion terms is to parameterise subgrid scale processes; in practise the horizontal viscosity and diffusivity terms,  $A_H$  and  $A_\phi$ , are often specified as a minimum value necessary to smooth cell to cell spatial oscillations. The diffusivities are chosen so that they do not produce excessive smoothing of real features. Values as low as  $10\text{m}^2/\text{s}$  have been successfully used in various modelling studies (Blumberg and Mellor, 1987). In this study, the relatively fine vertical resolution adopted resulted in a reduced need for horizontal diffusion because horizontal advection followed by vertical mixing effectively acts like horizontal diffusion in a physical sense (Aiguo, 2003). When the horizontal turbulent diffusion is used to represent subgrid scale mixing  $A_H$  and  $A_\phi$ , may be represented as suggested by Smagorinsky, (1963) (Hamrick, 1992b).

### 3.3.2.1 Boundary conditions in sigma coordinate system

Initial conditions and boundary conditions are needed to solve hydrodynamic equations. Prescribed boundary conditions serve as driving forces for the model simulation. The types of boundary conditions present in a three-dimensional hydrodynamic model are presented in Figure 3.9, and include both horizontal and vertical boundary conditions.



**Figure 3.9: Boundary conditions. Illustration adapted from Ji, (2008)**

(a) Vertical boundary conditions

The vertical boundary conditions for vertical velocity are

$$w(0) = w(1) = 0 \quad (3.57)$$

which means that the vertical velocities at the surface and at the bottom are zero.

Vertical boundary conditions for the momentum equations are kinematic shear stresses at the water bottom ( $z=0$ ) and water surface ( $z=1$ ). Expressions for shear stresses are (Ji, 2008):

$$\frac{\nu_v}{H} \frac{\partial}{\partial z} (u, v)_{z=0} = (\tau_{xz}, \tau_{yz})_{z=0} = c_b \sqrt{u_1^2 + v_1^2} (u_1, v_1) \quad (3.58)$$

$$\frac{\nu_v}{H} \frac{\partial}{\partial z} (u, v)_{z=1} = (\tau_{xz}, \tau_{yz})_{z=1} = c_w \sqrt{U_w^2 + V_w^2} (U_w, V_w) \quad (3.59)$$

where  $\tau_{xz}$  and  $\tau_{xy}$  are shear stresses at the bottom ( $z=0$ ) and shear stresses at the surface ( $z=1$ );  $U_w$  and  $V_w$  are wind speed components at 10m above the water surface;  $c_b$  is bottom drag coefficient;  $c_w$  is wind stress coefficient; and  $u_1, v_1$  refers to velocities computed at mid-height of the bottom layer. The bottom drag coefficient  $c_b$  is computed using:

$$c_b = \frac{\kappa^2}{\left( \ln \left( \Delta_1 / 2z_0 \right) \right)^2} \quad (3.60)$$

where  $\kappa=0.4$  is the von Karman constant,  $\Delta_1$  is the dimensionless thickness of the bottom layer,  $z_0 = z_0^*/H$  is the dimensionless bottom roughness height, and  $z_0^*$  is the bottom roughness height

The wind stress coefficient  $C_w$  can be expressed as:

$$C_w = 1.2 \times 10^{-6} \left( 0.8 + 0.065 \sqrt{U_w^2 + V_w^2} \right) \quad (3.61)$$

#### (b) Horizontal boundary conditions

Horizontal boundary conditions can be classed as open or closed boundaries. The purpose of the open boundary conditions is to describe interactions between the modelled domain and the open oceans. Generally, water surface elevations provide the open boundary conditions; while salinity, temperature and water quality variables may also be required (Ji, 2008). For the coastal open boundaries, the input of the surface elevation can

be either the measured tidal elevation or the tide described by the summation of the tidal constituents (Shen, 2002):

$$\eta = \sum_{n=1}^N H_n \cos\left(\frac{2\pi t}{T_n} + \xi_n\right) \quad (3.62)$$

Where  $H_n$ ,  $T_n$  and  $\xi_n$  are the mean amplitude, period and phase angle of tidal constituent,  $n$ , respectively.

The closed boundary condition describes the influences of shorelines on the interior domain of the model. The solid boundary conditions include no-slip and free-slip conditions. The no-slip condition prohibits flow both through and along the boundary; while the free-slip condition permits flow along the boundary but not through it. EFDC adopts the partial-slip boundary condition. This means that only the velocities that are normal to the boundary go to zero and non-normal velocities are reflected back into the domain without loss of energy (Tuckey et al., 2006).

### **3.3.2.2 Vertical mixing and turbulence models**

The system of equations, (3.47) - (3.53) provides a closed system for the variables  $u$ ,  $v$ ,  $w$ ,  $\eta$ ,  $p$ ,  $\rho$ ,  $S$  and  $T$ , provided that the vertical turbulent viscosity and diffusivity, and the momentum source-sink terms are specified. To provide the vertical turbulent viscosity and diffusivity, the second moment closure model developed by Mellor and Yamada, (1982), and modified by Galperin et al., (1988), is adopted. The model relates the vertical turbulent viscosity and diffusivity to the turbulent kinetic energy  $k$ , a turbulent length scale,  $l$ , and a Richardson number  $R_q$ , by:

$$\nu_v = \phi_v \sqrt{kl} = 0.4 \frac{(1 + 8R_q)\sqrt{kl}}{(1 + 36R_q)(1 + 6R_q)} \quad (3.63)$$

$$\nu_b = \phi_b \sqrt{kl} = 0.4 \frac{0.5\sqrt{kl}}{(1 + 36R_q)} \quad (3.64)$$

$$R_q = -\frac{g}{\rho} \frac{\partial \rho / \partial z}{(\partial v / \partial z)^2} \quad (3.65)$$

where the stability functions  $\phi_v$  and  $\phi_b$  (Galperin et al., 1988) account for reduced and enhanced vertical mixing in stable and unstable, vertically stratified environments, respectively. The Richardson number quantifies the vertical stratification, which represents the ratio of the buoyancy force to the vertical velocity shear. The gradient Richardson number provides quantitative information on the stabilizing effect of buoyancy and the destabilizing effect of velocity shear. It indicates the tendency of the water column to either mix (weak stratification), or resist mixing (strong stratification), (Ji, 2008).

A pair of transport equations determines the turbulence kinetic energy and the turbulence length scale:

$$\begin{aligned} \frac{\partial Hk}{\partial t} + \frac{\partial Huk}{\partial x} + \frac{\partial Hvk}{\partial y} + \frac{\partial wk}{\partial z} \\ = \frac{\partial}{\partial z} \left( \frac{v_q}{H} \frac{\partial k}{\partial z} \right) + 2 \frac{v_v}{H} \left( \left( \frac{\partial u}{\partial z} \right)^2 + \left( \frac{\partial v}{\partial z} \right)^2 \right) + 2g v_b \frac{\partial b}{\partial z} - 2 \frac{Hq^3}{B_1 l} \\ + Q_q \end{aligned} \quad (3.66)$$

$$\begin{aligned} \frac{\partial Hkl}{\partial t} + \frac{\partial Hukl}{\partial x} + \frac{\partial Hvkl}{\partial y} + \frac{\partial wkl}{\partial z} \\ = \frac{\partial}{\partial z} \left( \frac{v_q}{H} \frac{\partial kl}{\partial z} \right) + E_1 l \frac{v_v}{H} \left[ \left( \frac{\partial u}{\partial z} \right)^2 + \left( \frac{\partial v}{\partial z} \right)^2 \right] + g E_1 l A_b \frac{\partial b}{\partial z} \\ - \frac{Hq^3}{B_1} \left[ 1 + E_2 \left( \frac{l}{\kappa H z} \right)^2 + E_3 \left( \frac{l}{\kappa H (1-z)} \right)^2 \right] + Q_l \end{aligned} \quad (3.67)$$

where  $B_1$ ,  $E_1$ ,  $E_2$  and  $E_3$  are empirical constants equal to 16.6, 1.8, 1.33, and 0.25 respectively.  $Q_q$  and  $Q_l$  are additional source-sink terms such as subgrid scale horizontal diffusion. The vertical kinetic energy diffusion coefficient,  $v_q$  has the form  $v_q = 0.2ql$  and is often taken equal to the vertical eddy viscosity  $v_v$  (Hamrick, 1992b).

### 3.3.2.3 Mode-splitting

The numerical scheme employed in EFDC to solve the equations of motion uses second order accurate spatial finite differencing on a staggered or C grid (Arakawa and

Lamb, 1977). The velocity components are located on the face of the model grid with the depth, free surface potential, buoyancy and concentration of transported constituents located at the centroid. The computation of a pair of transport equations for turbulence parameters is carried out at the centre of the cell in a vertically staggered manner (Hamrick and Wu, 1997) (see Figure 3.10(a)). This type of grid has been shown by Batteen and Han, (1981) to be the most effective grid for high-resolution ocean circulation models. Figure 3.10(b) presents the location of the discrete variables of momentum equations on the finite difference grid. As illustrated, the grid has  $u$  located at  $\pm\Delta x/2$  away from where the water depth,  $H$  and the free surface elevation  $\eta$  are defined, and  $v$  located at  $\pm\Delta y/2$  away from where  $H$  and  $\eta$  are. The discretization of concentration variables and horizontal gradients in this manner minimises the requirements for spatial averaging of velocity and elevation terms (Ji, 2008).

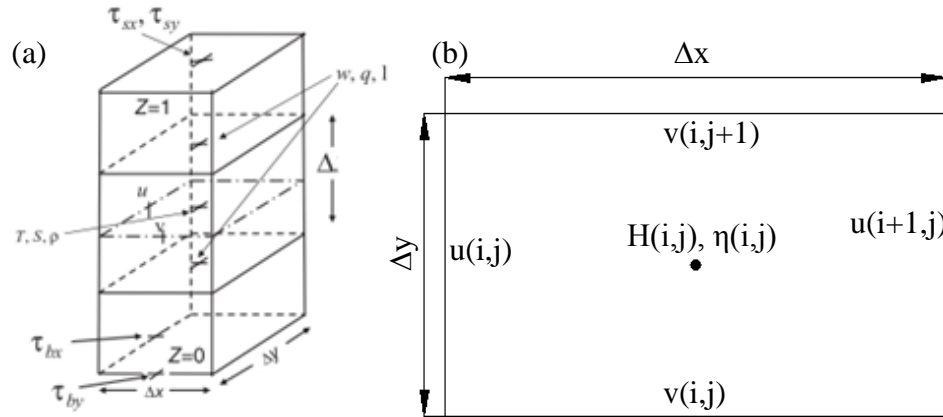


**Figure 3.10: The location of variables on the (a) sigma coordinate system and (b) the finite difference solution scheme**

### 3.3.2.4 External mode solution

The model's time integration employs a second order accurate three-time level, finite difference scheme with an internal-external mode splitting procedure to separate the internal shear or baroclinic mode from the external free surface gravity wave or barotropic mode. The external mode x-direction momentum and continuity equations are (Hamrick, 1992b):

$$\begin{aligned}
 \frac{\partial H\bar{u}}{\partial t} + \sum_{k=1}^K \left\{ \frac{\partial(H\Delta_k u_k u_k)}{\partial x} + \frac{\partial(H\Delta_k u_k v_k)}{\partial y} - f\Delta_k H v_k \right\} \\
 = -H \frac{\partial p_s}{\partial x} - Hg \frac{\partial \eta}{\partial x} + Hg \left( \bar{b} \frac{\partial h}{\partial x} - \bar{B} \frac{\partial H}{\partial x} - 0.5H \frac{\partial \bar{\beta}}{\partial x} \right) \\
 + (\tau_{xz})_K - (\tau_{xz})_0 + \bar{Q}_u
 \end{aligned} \tag{3.68}$$

$$\frac{\partial \eta}{\partial t} + \frac{\partial H\bar{u}}{\partial x} + \frac{\partial H\bar{v}}{\partial y} = 0 \tag{3.69}$$

where:

$$\bar{B} = (\sum_{k=1}^K \Delta_k \beta_k + 0.5\Delta_k(z_k + z_{k-1})b_k)$$

$$\bar{\beta} = (\sum_{k=1}^K \Delta_k \beta_k); \quad \text{with: } \beta_k = \sum_{j=k}^K \Delta_j b_j - 0.5\Delta_k b_k$$

$\Delta_k$  = vertical layer thickness; and the over bar denotes depth averaging.

Equations (3.68)-(3.69) now equate the time rate of change of the external or depth-integrated volumetric transports to the pressure gradients associated with the free surface slope, atmospheric pressure and buoyancy, the advective accelerations, the Coriolis and curvature accelerations, the free surface and bottom tangential stresses and the general source-sink terms.

Equations (3.68) and (3.69) can be expressed in finite difference format as, respectively:

$$\begin{aligned}
 \bar{p}^{n+1} = \bar{p}^{n-1} - \Delta t Hg \frac{\partial(\eta^{n+1} + \eta^{n-1})}{\partial x} - 2\theta H \frac{\partial p_s}{\partial x} \\
 + 2\Delta t Hg \left( \bar{b} \frac{\partial h}{\partial x} - \bar{B} \frac{\partial H}{\partial x} - 0.5H \frac{\partial \bar{\beta}}{\partial x} \right) \\
 - 2\Delta t \sum_{k=1}^K \Delta_k \left( \frac{\partial(p_k u_k)}{\partial x} + \frac{\partial(q_k u_k)}{\partial y} \right) + 2\Delta t \sum_{k=1}^K \Delta_k f H v_k \\
 + 2\Delta t ((\tau_{xz}^{n-1})_K - (\tau_{xz}^{n-1})_0) \\
 + 2\Delta t \sum_{k=1}^K \Delta_k \left( \frac{\partial \tau_{yx}^{n-1}}{\partial x} + \frac{\partial \tau_{xy}^{n-1}}{\partial y} + \frac{\partial \tau_{xy}^{n-1}}{\partial y} - \frac{\partial \tau_{yy}^{n-1}}{\partial x} \right)_k
 \end{aligned} \tag{3.70}$$

$$\eta^{n+1} - \eta^{n-1} + \Delta t \frac{\partial(\bar{p}^{n+1} + \bar{p}^{n-1})}{\partial x} + \Delta t \frac{\partial(\bar{q}^{n+1} + \bar{q}^{n-1})}{\partial y} = 0 \quad (3.71)$$

where  $p_k = u_k H$  and  $q_k = v_k H$ , are layer integrated volumetric flux components in the x and y direction, respectively; and all terms are understood to be evaluated at the central time level n, except those evaluated at the forward and backward time levels, n+1 and n-1, denoted by superscripts.

The discretization of the spatial differentials proceeds in a central difference formulation having the forms:

$$\frac{\partial(\phi(x, y))}{\partial x} = \frac{\phi(x + 0.5, y) - \phi(x - 0.5, y)}{\Delta x} \quad (3.72)$$

$$\frac{\partial(\phi(x, y))}{\partial y} = \frac{\phi(x, y + 0.5) - \phi(x, y - 0.5)}{\Delta y} \quad (3.73)$$

The solution scheme for equation (3.70)-(3.71) (and a corresponding y-direction momentum equation) involves first evaluating all terms in the equations at time levels n and n-1. On boundaries where the transports are prescribed, the specified values at time level n+1 are inserted into equation (3.71). Equation (3.70) (and-y-direction equations) are then used to eliminate the unknown transports at time level n+1 from equation (3.71). The result is a discrete Helmholtz type elliptic equation for the free surface displacement at time level n+1 having the general form:

$$\eta^{n+1} - g\Delta t^2 \frac{\partial H}{\partial x} \frac{\partial \eta^{n+1}}{\partial x} + g\Delta t^2 \frac{\partial H}{\partial y} \frac{\partial \eta^{n+1}}{\partial y} - \phi = 0 \quad (3.74)$$

with the term  $\phi$  containing all of the previously evaluated terms and transport boundary conditions. For cells where the free surface displacement is specified, equation (3.74) is replaced by an equation, which enforces the specified boundary condition. The system of equations corresponding to equation (3.74) is semi-implicit and is solved by a preconditioned conjugate gradient procedure (Hageman and Young, 1981). The conjugate gradient iterations continue until the sum of the squared residuals is less than a

specified value. The free surface displacements are then substituted into equation (3.70) to determine the transports at time level  $n+1$ . The model's semi-implicit external solution allows large time steps that are constrained only by the stability criteria of the explicit central difference or high order upwind advection scheme used for the nonlinear accelerations, and proceeds at the same timestep as the internal mode solution (Smolarkiewicz and Margolin, 1993).

### 3.3.2.5 Internal mode solution

The discretization of the internal mode equations proceeds by: integrating equation (3.49) with respect to  $z$  over a cell layer; dividing the resulting equation by the cell layer thickness,  $\Delta_k$ ; subtracting the equation for cell layer  $k$  from cell layer  $k+1$ ; and then dividing the result by the average thickness of the two cell layers. The internal mode momentum equations are in terms of the vertical profile of shear stress and velocity shear; the x-direction momentum equation is:

$$\begin{aligned}
 & \frac{\partial \left( H \Delta_{k+1,k}^{-1} (u_{k+1} - u_k) \right)}{\partial t} + \frac{\partial \left( H \Delta_{k+1,k}^{-1} (u_{k+1} u_{k+1,k} - u_k u_k) \right)}{\partial x} \\
 & + \frac{\partial \left( H \Delta_{k+1,k}^{-1} (v_{k+1} u_{k+1,k} - v_k u_k) \right)}{\partial y} - \Delta_{k+1,k}^{-1} (f H v_{k+1} - f H v_k) \\
 & + \Delta_{k+1,k}^{-1} \left( \Delta_{k+1}^{-1} ((wu)_{k+1} - (wu)_k) - \Delta_k^{-1} ((wu)_k - (wu)_{k-1}) \right) \\
 & = H \Delta_{k+1,k}^{-1} g (b_{k+1} - b_k) \left( \frac{\partial h}{\partial x} - z_k \frac{\partial H}{\partial x} - 0.5 H^2 \Delta_{k+1,k}^{-1} g \left( \Delta_{k+1} \frac{\partial b_{k+1}}{\partial x} + \Delta_k \frac{\partial b_k}{\partial x} \right) \right) \\
 & + \Delta_{k+1,k}^{-1} \left( \Delta_{k+1}^{-1} ((\tau_{xz})_{k+1} - (\tau_{xz})_k) - \Delta_k^{-1} ((\tau_{xz})_k - (\tau_{xz})_{k-1}) \right) \\
 & \quad + \Delta_{k+1,k}^{-1} ((Q_u)_{k+1} - (Q_u)_k)
 \end{aligned} \tag{3.75}$$

where  $\Delta_{k+1,k} = 0.5(\Delta_{k+1} + \Delta_k)$

An equivalent process is applied to the y-direction momentum equation.

Further details on the internal mode equations are provided in the next section.

### 3.3.3 Numerical representation of impeded flows

Field studies have shown that suspended canopies impacts on the flow profile in a number of ways, including, reduced velocities within the canopy and accelerated flows beneath the canopy (Blanco et al., (1994), Stroheimer et al., (2005)). These effects have important implications for aquaculture installations, such as, reduced growth rates within farms due to attenuated flow speeds (Aure et al., 2007), while the accelerated flows beneath the canopy may result in increased bed stress, and transport of detritus away from the aquaculture site.

In the area of impeded flows, little information exists on the hydrodynamic implications of suspended canopies in comparison to the more common submerged or emergent canopies; with the effects on flow often assumed to be similar to that of a submerged canopy. However, a key difference is the vertical boundary conditions: the suspended canopy has the free-surface at the top of the canopy while the free-stream flow beneath the canopy is bounded by the bottom boundary. The submerged canopy, on the other hand, is a mirror image with a solid boundary at the bottom and the free-surface boundary above the canopy. Therefore, while bottom friction may have little effect on flows within a submerged canopy, where the main impediment to flows is the canopy itself; bottom friction may have very significant implications for a suspended canopy (Plew, 2011b). Figure 3.11 illustrates the two different canopies and their associated flow profiles.

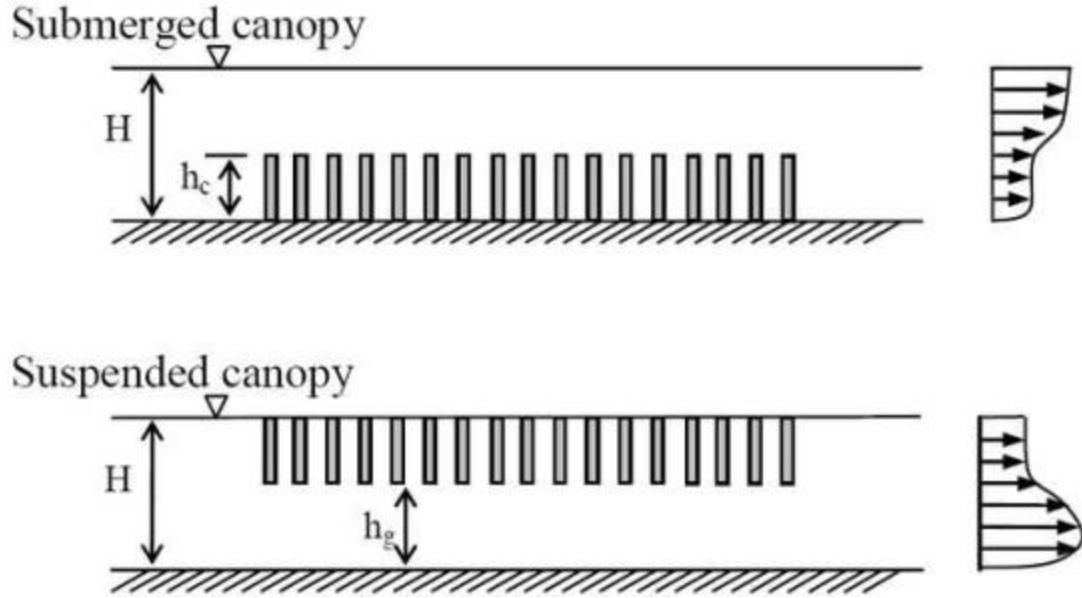


**Figure 3.11: Examples of emergent, submerged and suspended canopies with representative velocity profiles. Illustration adapted from Plew (2010).**

The EFDC model was amended to describe the effects of a suspended canopy on flows. This section presents the extended governing equations to describe canopy flows. For the purpose of this study, the water column was divided into three flow regions: free-stream flow beneath the canopy; a shear layer developing at the bottom of the canopy; and attenuated flows developing within the internal canopy region. Canopy flow processes within both the shear layer and the internal canopy layer were simulated in an amended manner in the numerical model.

As before, the effects of the mussel dropper installations were simulated as an additional drag term included in the governing equations. The additional drag term was applied to the upper portion of the water column to simulate a suspended canopy, with free-stream flow developing underneath. It describes the flow attenuation induced by the droppers within the internal canopy layer and can be expressed in a similar manner to the depth-averaged representation, equation (3.12), as:

$$F_D = \frac{a\rho_D C_D \sqrt{u^2 + v^2 + w^2}}{2} \quad (3.76)$$

Laboratory studies of flow profiles within a suspended canopy (Plew, 2011b), illustrated the development of a *canopy shear layer*, at the bottom of the canopy; as a result of interaction between the impeded canopy flows and the faster moving free-stream flow underneath. As part of this research, investigations were conducted into a number of novel methodologies of simulating these complex flow processes numerically. An analysis of laboratory results and literature led to the simulation of the shear layer by means of a *mechanical friction layer*. The author is not aware of any other research in which canopy flow processes were simulated in this way.

The mechanical friction layer was based on the assumption of boundary layer flows developing at the canopy interface. Previous studies have shown that the velocity profile above a vegetated boundary follows a logarithmic profile, with, velocity scale  $u_*$  defined by the turbulent stress at the top of the canopy, and roughness scale  $z_0$  defined by canopy morphology (Thom, (1971), Shi et al., (1995), Nepf and Vivoni, (2000), Ghisalberti and Nepf, (2004)). The shear flow profiles induced by a suspended canopy boundary are intuitively similar. By adopting this assumption, flow at the boundary exhibits a logarithmic profile of velocity and can be expressed in terms of physical elements of the canopy and flow profile (Schlichting, 1968).

$$|u| = \frac{u_*}{\kappa} \ln\left(\frac{z}{z_0}\right) \quad (3.77)$$

where,  $z$ , is the distance from the bottom of the canopy to the shear layer (i.e. mid-depth of layer),  $\kappa=0.41$ , is von Karman's constant,  $z_0$  is a roughness length quantifying the frictional resistance of the canopy interface, and the shear velocity,  $u_* =$

$\sqrt{|\tau_{xz} + \tau_{yz}|}$ . The shear stress was calculated by matching velocities with the logarithmic law of the wall, which states that, the average velocity of a turbulent flow at a certain point is proportional to the logarithm of the distance from the boundary (Blumberg and Mellor, 1987), giving:

$$(\tau_{xz})_{ML} = \frac{\kappa^2 u \sqrt{u^2 + v^2}}{\ln^2(z/z_0)} \quad (3.78)$$

$$(\tau_{xy})_{ML} = \frac{\kappa^2 v \sqrt{u^2 + v^2}}{\ln^2(z/z_0)} \quad (3.79)$$

The mechanical friction layer was incorporated into the numerical model at the interface between the canopy and free-stream flow. A single layer of the numerical model was prescribed as the mechanical friction layer. Therefore, the amended x-direction momentum equation is:

$$\begin{aligned} & \frac{\partial Hu}{\partial t} + \frac{\partial(Huu)}{\partial x} + \frac{\partial(Hvu)}{\partial y} + \frac{\partial wu}{\partial z} - fHv \\ & = -H \frac{\partial(p + g\eta)}{\partial x} + Hgb \frac{\partial h}{\partial x} - Hgbz \frac{\partial H}{\partial x} + \frac{\partial\left(\frac{v_v}{H} \frac{\partial u}{\partial z}\right)}{\partial z} + Q_u \\ & - F_D u - (\tau_{xz})_{ML} \end{aligned} \quad (3.80)$$

where,  $F_D$  represents the additional force induced by the suspended mussel droppers which is applied to the internal canopy layers; while  $(\tau_{xz})_{ML}$  represents the mechanical friction layer and is applied at the canopy interface over a single model layer.

### 3.3.3.1 Hydrodynamic solution procedure

The amended internal mode equation, (3.80) was discretized in terms of a semi-implicit fractional step scheme (Peyret and Taylor, 1983), with the first step being explicit and the second step being implicit. The computational equation for the explicit step of the x-direction momentum equation is:

$$\begin{aligned} (p_{k+1} - p_k)^{**} &= (p_{k+1} - p_k)^{n-1} \\ & - 2\Delta t \left( \frac{\partial(p_{k+1}u_{k+1} - p_k u_k)}{\partial x} + \frac{\partial(q_{k+1}u_{k+1} - q_k u_k)}{\partial y} \right) \\ & - 2\Delta t (\Delta_{k+1}^{-1}(wu)_{k+1} - (wu)_k) - \Delta_k^{-1}((wu)_k - (wu)_{k-1}) \\ & + 2\Delta t (fHv_{k+1} - fHv_k) \\ & + 2\Delta t Hg \left( (b_{k+1} - b_k) \frac{\partial(h - z_k H)}{\partial x} - 0.5H \frac{\partial(\Delta_{k+1} b_{k+1} + \Delta_k b_k)}{\partial x} \right) \end{aligned} \quad (3.81)$$

where \*\* denotes the provisional solution and all terms not having a specified time level are understood to be at the centred time level n.

An intermediary step is introduced into the governing equations at this stage to simulate the effects of the suspended canopy. The canopy effects were discretized by considering the effects of the layer-integrated formulation of the drag term, and mechanical friction layer, on the mean flow. The discretization procedure consisted of: computing the layer integrated formulation of both drag and the friction layer; dividing the resulting equation by the cell layer thickness  $\Delta_k$ ; subtracting the equation for cell layer k from cell layer k+1; and dividing the resulting equation by the thickness of the two cell layers, to give:

$$\begin{aligned} \frac{(p_{k+1} - p_k)^c}{2\Delta t \Delta_{k+1,k}} = & \frac{(p_{k+1} - p_k)^{**}}{2\Delta t \Delta_{k+1,k}} - \frac{((F_D u)_{k+1} - (F_D u)_k)}{2\Delta t \Delta_{k+1} \Delta_{k+1,k}} \\ & - \frac{(((\tau_{xz})_{ML})_{k+1} - ((\tau_{xz})_{ML})_k)}{2\Delta t \Delta_{k+1} \Delta_{k+1,k}} \end{aligned} \quad (3.82)$$

The computational equation for the implicit step of the three-time level discretization scheme is:

$$\begin{aligned} \frac{(p_{k+1} - p_k)^{n+1}}{\Delta t \Delta_{k+1,k}} = & \frac{(p_{k+1} - p_k)^c}{\Delta t \Delta_{k+1,k}} \\ & + \left[ \frac{((\tau_{xz})_{k+1} - (\tau_{xz})_k)}{\Delta_{k+1} \Delta_{k+1,k}} - \frac{((\tau_{xz})_k - (\tau_{xz})_{k-1})}{\Delta_k \Delta_{k+1,k}} \right]^{n+1} \end{aligned} \quad (3.83)$$

where the turbulent shear stresses are related to velocity by:

$$(\tau_{xz})_k^{n+1} = \left(\frac{v_v}{H}\right)_k^n \left(\frac{p_{k+1} - p_k}{H \Delta_{k+1,k}}\right)^{n+1} \quad (3.84)$$

Equation (3.84) could be used to eliminate the turbulent shear stresses from equations (3.83), to give a pair of K-1 systems of equations for the transport differences between layers, however, the resulting equations are poorly conditioned; that is small changes in the flows can induce large oscillations in the solution scheme. Instead, equation (3.84) is used to eliminate the horizontal transport differences at time level n+1 from equation

(3.83) to give a pair of K-1 (K=total number of layers) equations for the turbulent shear stresses:

$$\begin{aligned} \frac{(\tau_{xz})_{k-1}^{n+1}}{\Delta_k \Delta_{k+1,k}} + \left[ \frac{1}{\Delta_k \Delta_{k+1,k}} + \frac{(H)^{n+1}}{2\Delta t} \left( \frac{H}{v_v} \right)_k + \frac{1}{\Delta_{k+1} \Delta_{k+1,k}} \right] (\tau_{xz})_k^{n+1} - \frac{(\tau_{xz})_{k+1}^{n+1}}{\Delta_{k+1} \Delta_{k+1,k}} \\ = \frac{(p_{k+1} - p_k)^c}{2\Delta t \Delta_{k+1,k}} \end{aligned} \quad (3.85)$$

These equations are diagonally dominant and well conditioned and can be solved independently at each of the horizontal velocity location. Given the solution of equation (3.85) the K-1 transport differences,  $p_{k+1} - p_k$  are determined from equation (3.84) to form a pair of K equations for the horizontal transport differences in each cell layer, with a similar solution process applied to the y-direction momentum equation. To illustrate, the horizontal transports in the surface layer are given by:

$$p_K = \bar{p} + \sum_{k=1}^{K-1} \left( \sum_{j=1}^k \Delta_j \right) (p_{k+1} - p_k) \quad (3.86)$$

while horizontal transports at the bottom layer are given by:

$$p_1 = \bar{p} + \sum_{k=1}^{K-1} \left( 1 - \sum_{j=1}^k \Delta_j \right) (p_{k+1} - p_k) \quad (3.87)$$

where, the over bar denotes depth-averaging. Similar expressions are computed for  $q_k$  and  $q_1$

Working down from the water surface allows the remaining layer averaged volumetric flux to be determined. Solution of equation (3.85) requires specification of bottom and surface stresses at  $k=0$  and  $k=K$ , respectively. On the free surface, the surface wind stress components are specified, while the bed stress is specified at the bottom from equation (3.58). Inserting equation (3.87) and a corresponding equation for  $q_1$  into equation (3.58) allows the bottom stresses at time level  $n+1$  to be expressed in terms of the depth integrated volumetric flux components,  $\bar{p}$ ,  $\bar{q}$ . From equation (3.85), the bottom

stress  $(\tau_{xz})_{k=0}$ , can then be expressed in terms of the depth integrated volumetric flux and the internal shear stresses by:

$$(\tau_{xz})_0^{n+1} = c_b \sqrt{u_1 u_1 + v_1 v_1} \left( \frac{\bar{p}}{H} \right)^{n+1} - \sum_{k=1}^{K-1} \left( 1 - \sum_{j=1}^k \Delta_j \right) \frac{\Delta_{k+1,k} (\tau_{xz})_k^{n+1}}{\left( \frac{v_v}{H} \right)_k^n} \quad (3.88)$$

and a similar expression for the y component.

Inserting equation (3.88) and the corresponding y component equation for the bottom stress components into equation (3.85) (and corresponding y component equation) results in a nearly tridiagonal system with a fully populated first row. The system of equations can then be solved by means of a tridiagonal equation solver and a process of elimination and back substitution (Hamrick, 1992b)

### **3.3.3.2 Amended turbulence closure model**

The effects of suspended aquaculture installations on turbulent processes were also simulated in the numerical model. The turbulence model was extended to incorporate the effects of the droppers by introducing an additional term representing canopy turbulence production. The author is not aware of any other study that amended the Mellor-Yamada turbulence closure model to incorporate the canopy effects on turbulence.

As a first step in the process, the Mellor Yamada turbulence model was expressed in terms of a generic length scale (GLS) model (Warner et al., 2005). The GLS approach is a two-equation model that takes advantage of similarities in a range of two-equation turbulence formulations (Umlauf and Burchard, 2003). The first equation in the GLS model is the standard equation of transport, k, but the second equation is for a generic parameter  $\psi$  that is used to establish the turbulence length scale. The first equation is:

$$\frac{\partial k}{\partial t} + u \frac{\partial k}{\partial x} + v \frac{\partial k}{\partial y} + w \frac{\partial k}{\partial z} = \frac{\partial}{\partial z} \left( \frac{v_v}{\sigma_k} \frac{\partial k}{\partial z} \right) + P + B - \varepsilon \quad (3.89)$$

Where  $\sigma_k$  is the turbulence Schmidt number for k; and P and B represent production by shear and buoyancy respectively, as

$$P = \nu_v \left[ \left( \frac{\partial u}{\partial z} \right)^2 + \left( \frac{\partial v}{\partial z} \right)^2 \right] \quad (3.90)$$

$$B = \nu_b \frac{g}{\rho_0} \frac{\partial \rho}{\partial z} \quad (3.91)$$

Dissipation is modelled according to

$$\varepsilon = (c_\mu^0)^{3+p/n} k^{3/2+m/n} l^{-1/n} \quad (3.92)$$

where  $c_\mu^0$  is the stability coefficient based on experimental data.

The second equation in the GLS model describes the transport of a generic parameter  $\psi$  which is defined by establishing the coefficients of  $p$ ,  $m$  and  $n$  as given in Table 3-1. The equation is

$$\frac{\partial \psi}{\partial t} + u \frac{\partial \psi}{\partial x} + v \frac{\partial \psi}{\partial y} + w \frac{\partial \psi}{\partial z} = \frac{\partial}{\partial z} \left( \frac{\nu_v}{\sigma_\psi} \frac{\partial \psi}{\partial z} \right) + \frac{\psi}{k} (c_1 P + c_3 B - c_2 \varepsilon F_{wall}) \quad (3.93)$$

Where  $c_1$ ,  $c_2$  and  $c_3$  are coefficients to be determined based on experimental observations. The parameter  $\sigma_\psi$  is the turbulence Schmidt number for  $\psi$  and

$$\psi = (c_\mu^0)^p k^m l^n \quad (3.94)$$

The parameters  $p$ ,  $m$ ,  $n$ ,  $\sigma_k$ ,  $\sigma_\psi$ ,  $c_\mu^0$ ,  $c_1$ ,  $c_2$ ,  $c_3$ , and  $F_{wall}$  can then be specified to recover exact formulations of the standard Mellor-Yamada,  $k$ - $\varepsilon$  or  $k$ - $\omega$  turbulence models. Table 3-1 presents the prescribed values for each turbulence model. The specification of the equations in this manner facilitates an easy comparison between turbulence models; in addition, any theoretical or empirical developments to one model can be easily extended to other turbulence models.

**Table 3-1: Generic length scale parameters (Warner et al., 2005), where  $\kappa=0.41$  and  $E_2=1.33$ . The parameters  $d_b$  and  $d_s$  are the distances to the bottom and surface respectively.**

Parameter	Mellor Yamada $\psi = kl$	k- $\epsilon$ $\psi = (c_\mu^0)^3 k^{3/2} l^{-1}$	k- $\omega$ $\psi = (c_\mu^0)^{-1} k^{1/2} l^{-1}$
p	0.0	3.0	-1.0
m	1.0	1.5	0.5
n	1.0	-1.0	-1.0
$\sigma_k$	2.44	1.0	2.0
$\sigma_\psi$	2.44	1.3	2.0
$c_1$	0.9	1.44	0.555
$c_2$	0.5	1.92	0.833
$c_3$	1.0	1.0	1.0
$c_\mu^0$	–	0.5544	0.5544
$F_{wall}$	$1 + E_2 \left( \frac{l}{\kappa} \frac{d_b + d_s}{d_b d_s} \right)^2$	1.0	1.0

The GLS model was then extended to simulate the effects of the suspended canopy on turbulence energy and length scales. The amended models were derived based on the work of Shimizu and Tsujimoto, (1994) and Neary, (2003) on the k- $\epsilon$  and k- $\omega$  models respectively. The GLS model incorporating the additional turbulence terms describing the presence of the droppers is:

$$\frac{\partial k}{\partial t} + u \frac{\partial k}{\partial x} + v \frac{\partial k}{\partial y} + w \frac{\partial k}{\partial z} = \frac{\partial}{\partial z} \left( \frac{\nu_v}{\sigma_k} \frac{\partial k}{\partial z} \right) + P + B - \epsilon + C_{fk}(F_T u + F_T v) \quad (3.95)$$

$$\begin{aligned} \frac{\partial \psi}{\partial t} + u \frac{\partial \psi}{\partial x} + v \frac{\partial \psi}{\partial y} + w \frac{\partial \psi}{\partial z} \\ = \frac{\partial}{\partial z} \left( \frac{\nu_v}{\sigma_\psi} \frac{\partial \psi}{\partial z} \right) + \frac{\psi}{k} \left( c_1 P + c_3 B - c_2 \epsilon F_{wall} + C_{f\psi}(F_T u + F_T v) \right) \end{aligned} \quad (3.96)$$

Adopting the appropriate parameters from Table 3-1 allows the GLS transport equation for parameter  $\psi$ , be expressed in terms of the Mellor-Yamada formulation. The resulting equation is

$$\begin{aligned} \frac{\partial kl}{\partial t} + u \frac{\partial kl}{\partial x} + v \frac{\partial kl}{\partial y} + w \frac{\partial kl}{\partial z} \\ = \frac{\partial}{\partial z} \left( \frac{\nu_v}{\sigma_l} \frac{\partial kl}{\partial z} \right) + l \left( c_1 P + c_3 B - c_2 \varepsilon F_{wall} + C_{fl} (F_T u + F_T v) \right) \end{aligned} \quad (3.97)$$

The two transport equations are discretized in a similar manner to the hydrodynamic equations discussed in the previous section. The discretization of the two transport equation in (3.95) and (3.97) are then amended as follows:

*Kinetic energy transport equation*

$$\begin{aligned}
& (kH)^{n+1} - (kH)^{n-1} + \frac{2\Delta t}{\Delta x} \left[ k_{i+1/2,j}^n (uH)_{i+1/2,j}^n - k_{i,j}^n (uH)_{i-1/2,j}^n \right] + \\
& \quad \frac{2\Delta t}{\Delta y} \left[ k_{i,j+1/2}^n (vH)_{i,j+1/2}^n - k_{i,j-1/2}^n (vH)_{i,j-1/2}^n \right] \\
& \quad + \frac{2\Delta t}{\Delta_{k+1,k}} \left[ (k_{k+1/2}^n w_{k+1/2}^n - k_{k-1/2}^n w_{k-1/2}^n) \right] \\
& = \left( \frac{2\Delta t}{\Delta_{k+1,k}} \left[ \left( \frac{\nu_v}{H} \right)_{k+1}^n \frac{(k_{k+1} - k_k)}{\Delta_{k+1,k}} - \left( \frac{\nu_v}{H} \right)_k \frac{(k_{k+1} - k_k)}{\Delta_{k+1,k}} \right] \right) \\
& + \left( \frac{2\nu_v}{H} \right)_k \left[ \frac{2\Delta t}{(\Delta_{k+1,k})^2} (u_{i+1/2,j,k+1} - u_{i+1/2,j,k} + u_{i-1/2,j,k+1} - u_{i-1/2,j,k}) \right. \\
& \quad \left. + \frac{2\Delta t}{(\Delta_{k+1,k})^2} (v_{i,j+1/2,k+1} - v_{i,j+1/2,k} + v_{i,j-1/2,k+1} - v_{i,j-1/2,k}) \right]^n \\
& 4\Delta t \frac{Hk^{3/2}}{B_1 l} \Big|_{i,j}^{n+1} + \frac{2\Delta t}{4} C_T C_{fk} nD \left[ (u_{i+1/2,j}^n u_{i+1/2,j}^n + u_{i-1/2,j}^n u_{i-1/2,j}^n) (u^2 + v^2)^{\frac{1}{2}} \right]^n \\
& \quad + \left( v_{i,j+1/2}^n v_{i,j+1/2}^n + v_{i,j-1/2}^n v_{i,j-1/2}^n \right) (u^2 + v^2)^{\frac{1}{2}} \Big|_{i,j}^n
\end{aligned} \tag{3.98}$$

*Turbulence length scale transport equation*

$$\begin{aligned}
& (kHl)^{n+1} - (kHl)^{n-1} + \frac{2\Delta t}{\Delta x} \left[ (kl)_{i+1,j}^n (uH)_{i+\frac{1}{2},j}^n - (kl)_{i,j}^n (uH)_{i-\frac{1}{2},j}^n \right] + \\
& \frac{2\Delta t}{\Delta y} \left[ (kl)_{i,j+1}^n (vH)_{i,j+1/2}^n - (kl)_{i,j}^n (vH)_{i,j-1/2}^n \right] + \frac{2\Delta t}{\Delta_{k+1,k}} \left[ ((kl)_{k+1/2}^n w_{k+1/2}^n - \right. \\
& \left. (kl)_{k-1/2}^n w_{k-1/2}^n) \right] = \\
& \left( \frac{2\Delta t}{\Delta_{k+1,k}} \left[ \left( \frac{v_v}{H} \right)_{k+1}^n \frac{((kl)_{k+1} - (kl)_k)}{\Delta_{k+1,k}} - \left( \frac{v_v}{H} \right)_k \frac{((kl)_{k+1} - (kl)_k)}{\Delta_{k+1,k}} \right] \right) \\
& \left( E_1 l \frac{v_v}{H} \right)_k \left[ \frac{2\Delta t}{(\Delta_{k+1,k})^2} (u_{i+1/2,j,k+1} - u_{i+1/2,j,k} + u_{i-1/2,j,k+1} - u_{i-1/2,j,k}) + \right. \\
& \left. \frac{2\Delta t}{(\Delta_{k+1,k})^2} (v_{i,j+1/2,k+1} - v_{i,j+1/2,k} + v_{i,j-1/2,k+1} - v_{i,j-1/2,k}) \right] \\
& \frac{2\Delta t}{\Delta_{k+1,k}} (E_1 l A_b)_k^n (b_{k+1} - b_k) - 2\Delta t \frac{Hk^{3/2}}{B_1} \Big|_{i,j}^{n+1} \left[ 1 + E_2 \left( \frac{l}{\kappa H z} \right)^2 + E_3 \left( \frac{l}{\kappa H (1-z)} \right)^2 \right]^{n+1} + \\
& \frac{2\Delta t Hk^{3/2}}{4 B_1} \Big|_{i,j}^{n+1} C_T C_{fl} n D \left[ \left( u_{i+1/2,j}^n u_{i+1/2,j}^n + u_{i-1/2,j}^n u_{i-1/2,j}^n \right) (u^2 + v^2)^{\frac{1}{2}n} \right. \\
& \left. + \left( v_{i,j+1/2}^n v_{i,j+1/2}^n + v_{i,j-1/2}^n v_{i,j-1/2}^n \right) (u^2 + v^2)^{\frac{1}{2}n} \right]
\end{aligned} \tag{3.99}$$

The solution method for the partial differential equations of kinetic energy and length scale follows a similar procedure to that discussed for solving the hydrodynamic equations; with the vertical boundary conditions provided by (Ji, 2008):

$$(q^2(1), q^2 l(1)) = (B_1^{2/3} u_*^2(1), 0) \tag{3.100}$$

$$(q^2(0), q^2 l(0)) = (B_1^{2/3} u_*^2(0), 0) \tag{3.101}$$

where  $u_*$  is friction velocity and  $B_1$  is an empirical constant.

## **Chapter 4: Physical Modelling**

---

*"When dealing with water, first experiment then use judgement"*

*- Leonardo Da Vinci*

## 4.1 Introduction

The solution to a problem in hydraulics may be approached in one of three ways: by theory and design; past experience; or by investigating the problem and testing the solution on a model. However, in certain situations, past experience may be insufficient due to the complexity and uniqueness of a problem, while the nonlinear character of the governing equations of fluid motion, and our still limited analytical knowledge, may limit the viability of theory alone. In these situations, the use of physical models may be of benefit.

Research using physical models is based on the theory of similitude between the model and prototype. Munson, (2005) defined a model as a “*representation of a physical system that may be used to predict the behaviour of the system in some desired respect*”. The term encompasses physical, numerical and mathematical models. The physical system for which the predictions are to be made is called the prototype.

This chapter discusses the aims of hydraulic scale modelling and presents the conditions under which similitude may be attained. Definitions of geometric, kinematic, dynamic and mechanical similarity are presented. An assessment of model-to-prototype scale relationships is presented in Section 4.3; the primary force relationships and modelling assumptions are discussed.

Section 4.5 presents an overview of the tidal basin configuration with details on the data acquisition instrumentation. Section 4.6 and 4.7 details the validation of the tidal basin unit. Section 4.8 discusses studies conducted in the tidal basin investigating the effects of a suspended mussel dropper long-line on flows. The effects of the scaled aquaculture installations are assessed through detailed velocity measurements and dye dispersion studies. The data is adopted to validate and fine-tune a numerical model. Finally, an overview of the difficulties encountered during the physical modelling studies is discussed. Of particular interest are issues that arose due to scaling of prototype and complying with similitude conditions.

## 4.2 Similitude

The inherent requirement of any hydraulic scale-modelling endeavour is to replicate the behaviour of the situation to be modelled, in a faithful manner incorporating the chosen flow processes. The success of this depends on the accurate formulation of the problem and correctly assessing the primary forces in effect. By combining relevant experience and a theoretical assessment of the situation, a scale model allows the simplification of complex flows by emphasizing the action of some forces while eliminating or minimising others. (Novak et al., 2010) noted that a “*purely experimental approach to the problem without any theoretical analysis is likely to be a waste of effort*”. Theoretical guidelines are a necessity to produce a valid, defensible scale model that can be extrapolated to a more general solution.

The scale ratio or simply the scale denotes the relationship between model and prototype. Hughes, (1993) defined the scale as, ‘*ratio of a parameter in the prototype to the same parameter in the model*’.

Symbolically, this is represented as:

$$N_x = \frac{X_p}{X_m} = \frac{\text{Value of } X \text{ in prototype}}{\text{Value of } X \text{ in model}} \quad (4.1)$$

Where  $N_x$  is the prototype-to-model scale ratio of the parameter  $X$  and the subscripts  $p$  and  $m$  denote prototype and model respectively.

Similitude between model and prototype is achieved when all major influences on flow are in proportion while those that are not in proportion are accounted for. Requirements of similitude will vary with the problem being considered and the degree of accuracy required between model and prototype. The degree of similarity between model and prototype is often used to classify the physical model.

*Completely similar models* are models in which the relationship between all relevant parameters in the prototype is maintained in the model. A prerequisite for complete similarity is *geometric similarity* between model and prototype. Geometrically similar models, also called geometrically undistorted models, are models in which the vertical

and horizontal scales are equal. They are, therefore true, geometric replicas of the model with all dimensions reduced at the same scale. On the other hand, models in which the vertical and horizontal scales are not equal are termed geometrically distorted models or simply distorted models.

In hydraulic modelling, geometrically distorted models typically consist of horizontal scales that are larger than the vertical. This reduces the horizontal spatial area required in addition to increasing model water depth. However, it may be more difficult to extrapolate results as some flow details will not be in similitude.

*Kinematic similarity* is achieved when similarity of motion exists between model and prototype. That is, corresponding particles on the model and prototype will be at corresponding points on the model and prototype at corresponding times. A geometrically distorted model cannot be kinematically similar to the prototype. *Dynamic similarity* exists when the ratio of total forces between the model and prototype are equal. *Mechanical similarity* between model and prototype then exists if the model is in geometric, kinematic and dynamic similarity. Thus, mechanical similarity cannot be achieved in a geometrically distorted model, whereas dynamic similarity may, theoretically, be achieved if appropriate scaling of the relevant forces is applied (Novak et al., 2010).

The challenge in achieving complete mechanical similarity in a model is highlighted by considering the dual constraints of accurately representing gravity and viscous forces in a scale model. In both model and prototype, the accelerations due to gravity are identical. Similarly, when water is used in both model and prototype, then the ratio of fluid density and viscosity equal one. No scale model can simultaneously satisfy these two criteria. Therefore, the design of a valid physical model requires that similarity be achieved between those forces that dominate processes in the prototype while neglecting others. The elimination of these forces results in some discrepancy between model and prototype, known as *scale effects*. It is the duty of the physical modeller to minimise these effects by designing the physical model to the criteria of similitude and providing justification for appropriate departures from these criteria.

### 4.3 Dynamic similarity

The requirement for kinematic similarity does not incorporate the effect of prototype or model fluid properties on flow. Therefore, the kinematic similitude criteria can be satisfied with different fluid properties in model and prototype. The requirement of maintaining similitude between model and prototype fluid properties is met by the criteria of dynamic similarity. Dynamic similarity demands that the ratio of forces and masses between model and prototype are equal. The requirement for dynamic similarity stems from Newton's second law, which equates the sum of the external forces acting on a body to the body's reaction in response to these forces:

$$m \frac{dV}{dt} = \sum_n F_n \quad (4.2)$$

In the types of fluid mechanics problems typically involved in coastal engineering projects, the forces involved consist of the kinetic relations due to the inertia of an element's mass ( $F_i$ ), gravity ( $F_g$ ), viscous shear ( $F_\mu$ ), surface tension ( $F_{st}$ ), elastic compression ( $F_e$ ) and the pressure forces related to the motion ( $F_{pr}$ ).

Newton's second law then equates the vector sum of these forces to the element's mass reaction and can be written as (Hudson et al., 1979):

$$F_i = F_g + F_\mu + F_{st} + F_e + F_{pr} \quad (4.3)$$

The criterion of dynamic similarity requires that the prototype-to-model ratio of inertial forces equal the vector sum of the active forces:

$$\frac{(F_i)_p}{(F_i)_m} = \frac{(F_g + F_\mu + F_{st} + F_e + F_{pr})_p}{(F_g + F_\mu + F_{st} + F_e + F_{pr})_m} \quad (4.4)$$

where subscripts m and p stand for model and prototype respectively.

In addition, perfect similitude requires that the force ratios between prototype and model must also be equal. This can be expressed as:

$$\frac{(F_i)_p}{(F_i)_m} = \frac{(F_g)_p}{(F_g)_m} = \frac{(F_\mu)_p}{(F_\mu)_m} = \frac{(F_{st})_p}{(F_{st})_m} = \frac{(F_e)_p}{(F_e)_m} = \frac{(F_{pr})_p}{(F_{pr})_m} \quad (4.5)$$

No model fluid exists that has viscosity, surface tension and elastic compression properties that will satisfy the requirements given by equation 4.5, if the model is smaller than the prototype. However, since one or more of these forces may not significantly contribute to the particular flow phenomenon under consideration, and others may only have a slight effect; a technically defensible scale model may still be developed, provided a comprehensive understanding of the flow processes and their implications exists. The task, therefore, is to conduct a comprehensive analysis of the particular scenario and identify which forces may and may not be neglected.

Inertial forces must always be considered since the acceleration of the particles (and hence inertial forces) will determine the fluid flow pattern in almost every situation. Thus, in hydraulic modelling the assumption is made that any given problem can be reduced to the interaction of inertial forces with one of the other forces given in equation 4.5. Several well known criteria for scale modelling studies have been developed based on this assumption.

The first step in this development is expressing each of the forces in equation 4.5 in terms of their basic physical units. This is done for the relevant forces below.

$$F_i = \text{mass} \times \text{acceleration} = (\rho L^3) \left( \frac{V^2}{L} \right) = \rho L^2 V^2 \quad (4.6)$$

$$F_g = \text{mass} \times \text{gravitational acceleration} = \rho L^3 g \quad (4.7)$$

$$F_\mu = \text{viscosity} \times \frac{\text{velocity}}{\text{distance}} \times \text{area} = (\tau)A = (\mu V/L)L^2 = \mu VL \quad (4.8)$$

$$F_{st} = \text{unit surface tension} \times \text{length} = \gamma L \quad (4.9)$$

(where  $\gamma$  is a surface tension)

$$F_e = \text{modulus of elasticity} \times \text{area} = EL^2 \quad (4.10)$$

$$F_{pr} = \text{unit pressure} \times \text{area} = \rho L^2 \quad (4.11)$$

An expression relating the inertial force to each of the relevant forces can then be derived for the flow process. Requiring that the force ratios be the same in the model as the prototype provides a criterion of similitude for the model.

#### 4.4 Force relationships

Force relationships can be derived for the model based on the assumptions that

- a) two forces only dominate the flow and
- b) the force ratios in the model and prototype are equal

These assumptions describe the requirements for hydraulic similitude. Physical modelling thus reduces to mathematically equating inertial forces present in the flow problem to one other dominant forcing. This typically involves determining a relationship between inertial and gravity forces (Froude scaling) or inertial and viscous forces (Reynolds scaling) (Hughes, 1993).

##### 4.4.1 Froude criterion

In most hydraulic modelling studies with a free surface, gravity plays a dominant role in the flow process. The relative influence of gravity and inertial forces can be described by a parameter called the *Froude Number*. It is given by the square root of the ratio of inertial to gravity forces

$$\sqrt{\frac{\text{inertial force}}{\text{gravity force}}} = \sqrt{\frac{\rho L^2 V^2}{\rho L^3 g}} = \frac{V}{\sqrt{gL}} \quad (4.12)$$

This criterion describes the ratio of the force due to the acceleration of a fluid particle, to the force due to gravity (weight) (Munson, 2005). The Froude criterion of similitude requires that this ratio be equal in both model and prototype:

$$\left( \frac{V}{\sqrt{gL}} \right)_p = \left( \frac{V}{\sqrt{gL}} \right)_m \quad (4.13)$$

which gives

$$\frac{V_p}{V_m} = \sqrt{\left(\frac{g_p}{g_m}\right) \left(\frac{L_p}{L_m}\right)} \quad (4.14)$$

Assuming a gravity scale of unity, the Froude criterion can be reduced to a velocity–length scale relationship as:

$$V_m = V_p \sqrt{\frac{L_m}{L_p}} \quad (4.15)$$

Expressing in terms of scale ratios and rearranging gives

$$\frac{N_V}{\sqrt{N_L}} = 1 \text{ or } N_{Fr} = 1 \quad (4.16)$$

where  $N_V$  and  $N_L$  represent characteristic scales of velocity and length respectively.

Equation (4.16) is the Froude model criterion. It is the dominant criterion for flows in which the inertial forces are balanced primarily by gravity forces and therefore is usually the most important factor to consider when designing a coastal engineering hydraulic model.

#### 4.4.2 Reynolds criterion

In flows where viscous forces dominate the most important parameter is the ratio of inertial to viscous forces given by

$$\frac{\text{inertial force}}{\text{viscous force}} = \frac{\rho L^2 V^2}{\mu V L} = \frac{\rho L V}{\mu} \quad (4.17)$$

which is known as the *Reynolds Number*

The Reynolds number defines the ratio of the inertial forces on an element of fluid, to the viscous forces on the element (Munson, 2005). It is widely used in fluid mechanics to distinguish between laminar and turbulent flows. Model similitude is achieved when the Reynolds number is equal in both model and prototype, i.e.

$$\left(\frac{\rho LV}{\mu}\right)_p = \left(\frac{\rho LV}{\mu}\right)_m \quad (4.18)$$

which gives

$$\left(\frac{V_p}{V_m}\right)\left(\frac{L_p}{L_m}\right)\left(\frac{\rho_p}{\rho_m}\right) = \frac{\mu_p}{\mu_m} \quad (4.19)$$

In terms of scale ratios the Reynolds model criterion is

$$\frac{N_V N_L N_\rho}{N_\mu} = 1 \text{ or } N_{Re} = 1 \quad (4.20)$$

The Reynolds number plays an important role in modelling flows where viscous forces dominate, such as laminar boundary layer problems.

For the present research, the Froude criterion of similitude was adopted in the development of scale models. Nevertheless, other dynamic forces must be considered, and justifications provided for neglecting relevant forces in the scale model.

#### **4.5 Laboratory set-up**

All experimental data for this study was collected using a tidal basin facility located in the Marine Modelling Centre at National University of Ireland, Galway. The purpose of the tidal basin is to produce unsteady tidal flows and generate water circulation patterns representative of the flow features of the prototype. A three-dimensional schematic illustration is shown in Figure 4.1. The general layout with location of measuring instrumentation and equipment is presented in Figure 4.2.

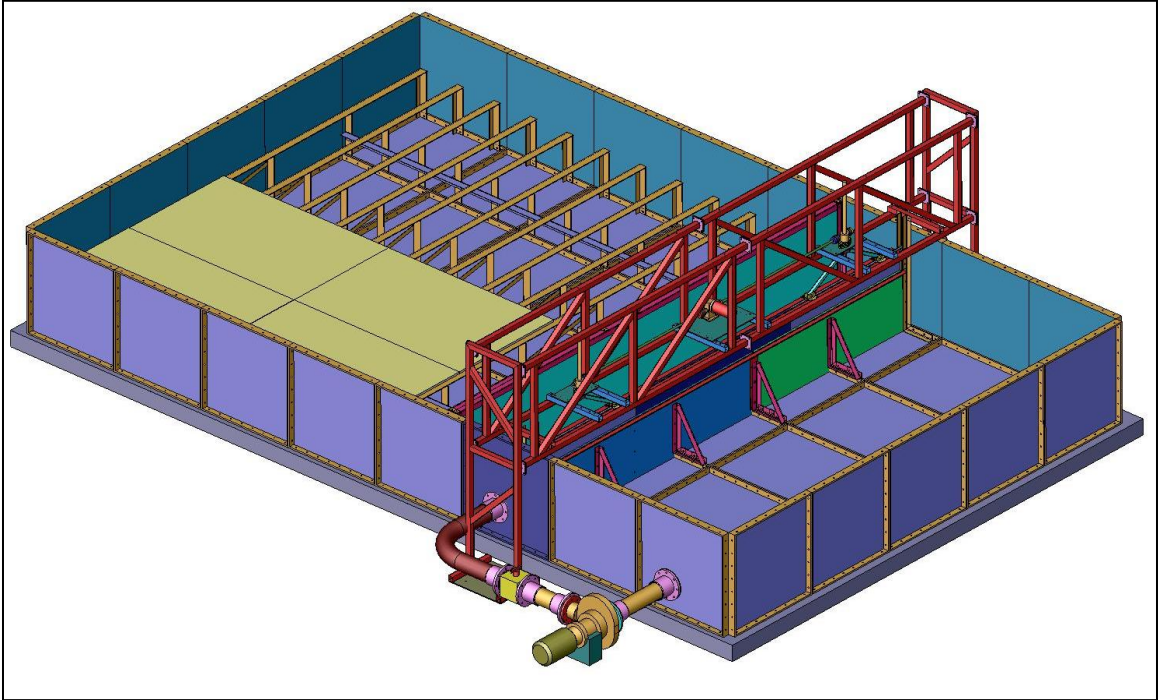


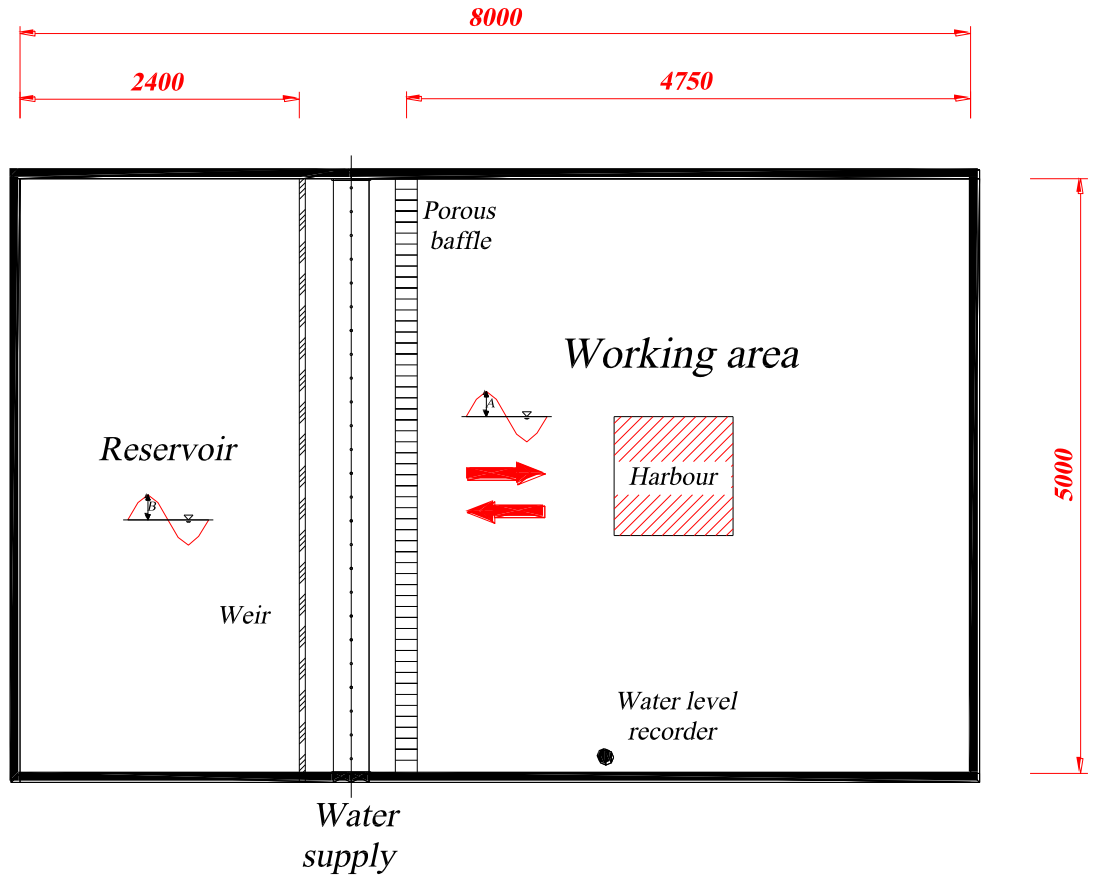
**Figure 4.1: Schematic illustration of tidal basin**



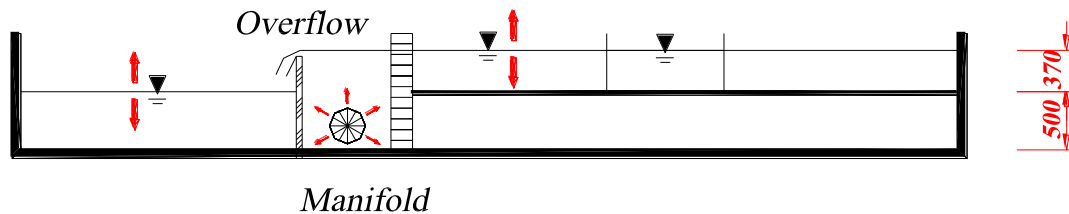
**Figure 4.2: Tidal basin arrangement**

### 4.5.1 Tidal basin specifications

The internal dimensions of the tank are 8.0m by 5.0m and the maximum depth is 1.0m. As shown in Figure 4.3 the horizontal plan is divided into three sections: reservoir, manifold chamber and working area.



(a) plan view



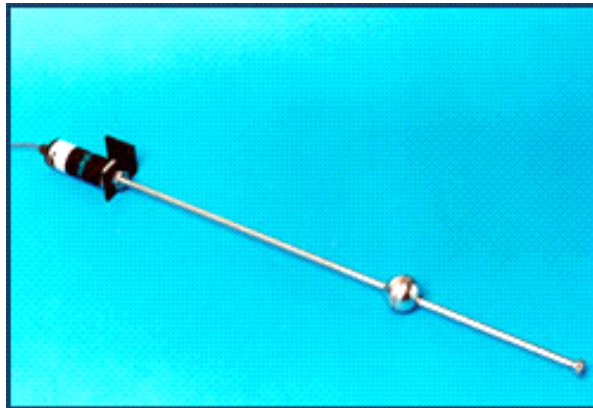
(b) cross-section

Figure 4.3: Schematic layout of tidal basin (a) plan view and (b) cross-section (Olbert, 2006)

The water reservoir of a size 2.4m by 5m and 1m depth is separated from the manifold by a variable elevation weir. The working section has dimensions of 5m by 4.75m on plan-form with the bed being raised 0.5 m above the tank floor. This reduces the maximum water level within the model to 0.37m due to the weir design. Water level in the basin is regulated by the weir that is driven by a Windows-based interface of Motion Perfect 2 software that permits the generation of realistic tides.

#### 4.5.2 Data acquisition

In the physical modelling studies, hydrodynamic processes were monitored through continuous measurements of flow-fields and elevations. In order to read water elevations accurately a water level gauge, as shown in Figure 4.4, is required. The HR Wallingford water level gauge uses a float, which moves up and down a displacement transducer. The water level is determined by accurately measuring the distance from the head of transducer to the magnetic field produced by a magnet mounted inside the float. The water level gauge has a maximum displacement of 0.3m with a specified precision of 0.5%.



**Figure 4.4: Wallingford water level gauge**

Two Nortek Acoustic Doppler Velocimeters (ADV), type Nortek 10MHz, were used to measure three-dimensional velocity fields within the working area of the tank. These velocimeters operate on the principle of the Doppler shift. The Doppler shift in frequency can be calculated using the equation:

$$F_{Doppler} = -F_{source} \frac{V}{C} \quad (4.21)$$

The NDV uses this principle to measure the velocity of water in three-dimensions. The device transmitter probe sends out a beam of acoustic wave at a particular frequency. These waves bounce off of particulate matter in the water, and three receiving probes “listen” for the change of frequency of the returned waves. The probe then calculates the velocity of the water in the x, y, and z direction. Figure 4.5 presents a general schematic of the ADV probe.

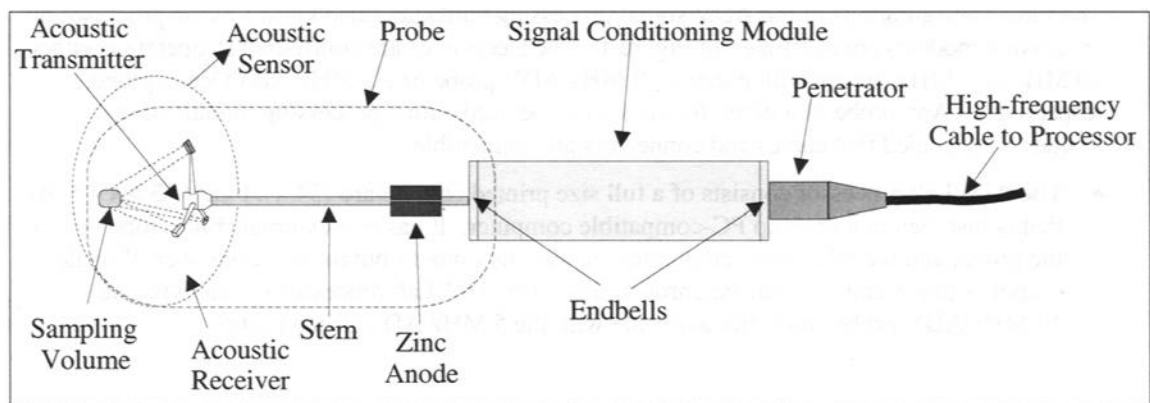


**Figure 4.5: Schematic of ADV probe**

The main element of the ADV is the probe attached to the signal conditioning module. The sensor contains an acoustic transmitter and three acoustic receivers. The instrument has the following performance characteristics

- Velocity range:  $\pm 0.03 - \pm 2.5$  m/s
- Velocity accuracy:  $\pm 1\%$
- Sampling rate: 0.1 - 25 Hz
- Random noise:  $\pm 1\%$  of velocity
- Minimum distance from sampling volume to boundary: 5mm
- Maximum operating depth: 30m

The real time data acquisition and online interfacing is done by Windows-based Collect V software.

An issue with any laboratory measurement instrument is excessive noise within results. This statistical uncertainty is an inherent property of an ADV and can be caused by a number of factors including: finite residence time for suspended particles in the sampling volume, small-scale turbulence (at scales similar to or less than the sampling volume), and beam divergence (Zedel et al., 1996). To minimize signal-to-noise ratio (SNR) a neutrally buoyant spherical seeding material of diameter 8-10 $\mu\text{m}$  was dispersed within the water. In addition, some post processing smoothing was applied to velocities based on the work of Dane, (1998). This involves the filtering of laboratory data via a first order recursive filter of the form (Olbert, 2006)

$$y_i = \alpha y_{i-1} + (1 - \alpha)x_i \quad (4.22)$$

Where:

- $x_i$  – raw data
- $y_i$  – local mean
- $i$  – sample number
- $\alpha$  – smooth parameter for low pass filter;  $\alpha = (N - 1)/N$  with  $N$  being the total number of samples within the filter width

This dual approach was found to reduce SNR to within acceptable levels. For further details on the technical specification of the tidal basin used for this research, see Olbert, (2006)

#### **4.6 Validation of tidal basin unit**

Prior to commencement of the scale modelling program, preliminary tests were conducted in the tidal basin to ensure model performance. The most important task to achieve is a uniform distribution of velocities across the working area when there isn't any scale model in-place. Due to the limited depth in the tidal basin and the numerous steps undertaken to minimise excessive swirl, depth-averaged models can ably reproduce flow structure in the basin; hence, DIVAST was used for all preliminary experiments.

As a preliminary validation step, elevations recorded in the tidal basin were compared with numerically predicted values. Tidal elevations are the easiest parameter to calibrate in a numerical model when at the open boundary water elevations are specified. All water

level recordings were measured along the side wall so as to minimise interference of the device with mean flow. Figure 4.6 displays water level recorded in the tidal basin plotted against numerical model values. As expected, both sets of data display close agreement.

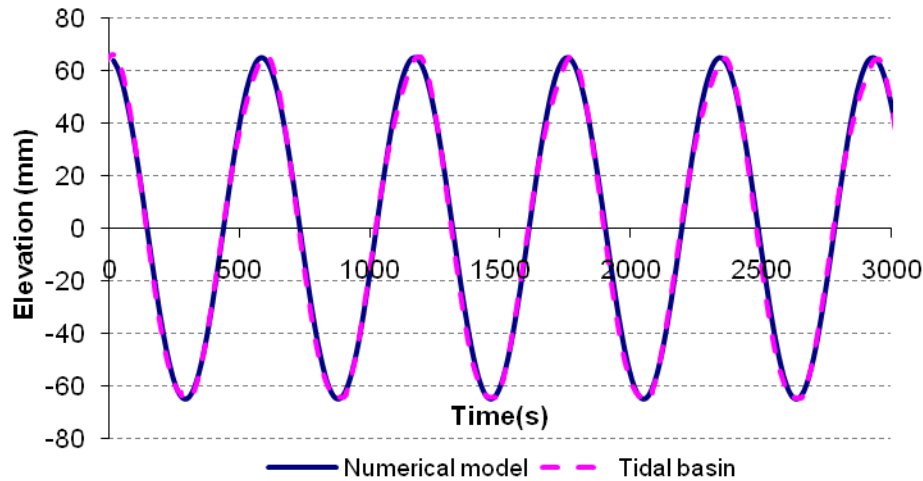


**Figure 4.6: Water levels recorded in the tidal basin plotted against those predicted by DIVAST**

The next stage is the calibration of velocities between tidal basin and numerical model predictions. Hydrodynamic data acquisition was carried out for the locations detailed in Figure 4.7 and compared with numerically predicted values. Velocity time traces were measured at a depth of  $0.4H$  from the bed based on the assumption of a logarithmic velocity profile (Wiberg and Smith, 1991). That is, in a logarithmic velocity profile, depth averaged flow occurs at a point  $H/e$  above the bottom bed or  $0.37H$ . For each sampling point, velocity time traces were recorded for five tidal cycles, and the data closely monitored for temporal discrepancies or spatial non-uniformity. Prior to the processing of velocities, the data was closely analysed for excessive noise in measurements. In many laboratory tests, signal noise can adversely affect measured velocities.

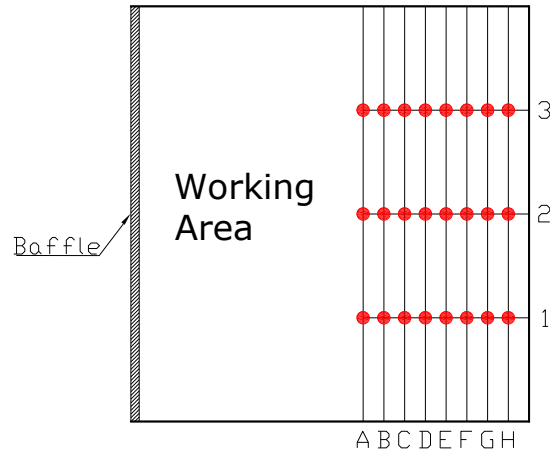


**Figure 4.7: Location of measured velocities (red circles) in working area**

The calibration of a numerical model typically involves adjusting model coefficients until reasonable agreement is achieved. For the case of velocities, this consists of adjusting the bottom bed roughness coefficient and eddy viscosity coefficient as these are the main parameters influencing the magnitude and distribution of hydrodynamic processes. The bed roughness coefficient can be calculated for the particular material properties of the basin construct from the work of Krishnappan, (1984), and for a smooth plywood bed a value of 0.8mm is often specified (Olbert, 2006).

Figure 4.8 presents experimental velocities plotted against numerically predicted values along the centreline of the tidal basin as illustrated in Figure 4.7. There is comparatively close agreement between data at points A2 and C2 within the models. The magnitude of velocities predicted by the numerical model is quite similar to those observed in the experimental study. However, as one approaches the back wall of the basin, very significant variability is present in the experimental data. This is due to a major problem encountered in the physical model studies; wave reflection off the back wall. The issue of energy reflection is an inherent property of scale model studies due primarily to tidal energy conservation and the distortion of large-scale hydraulic models. This issue will be discussed in detail in the following section.

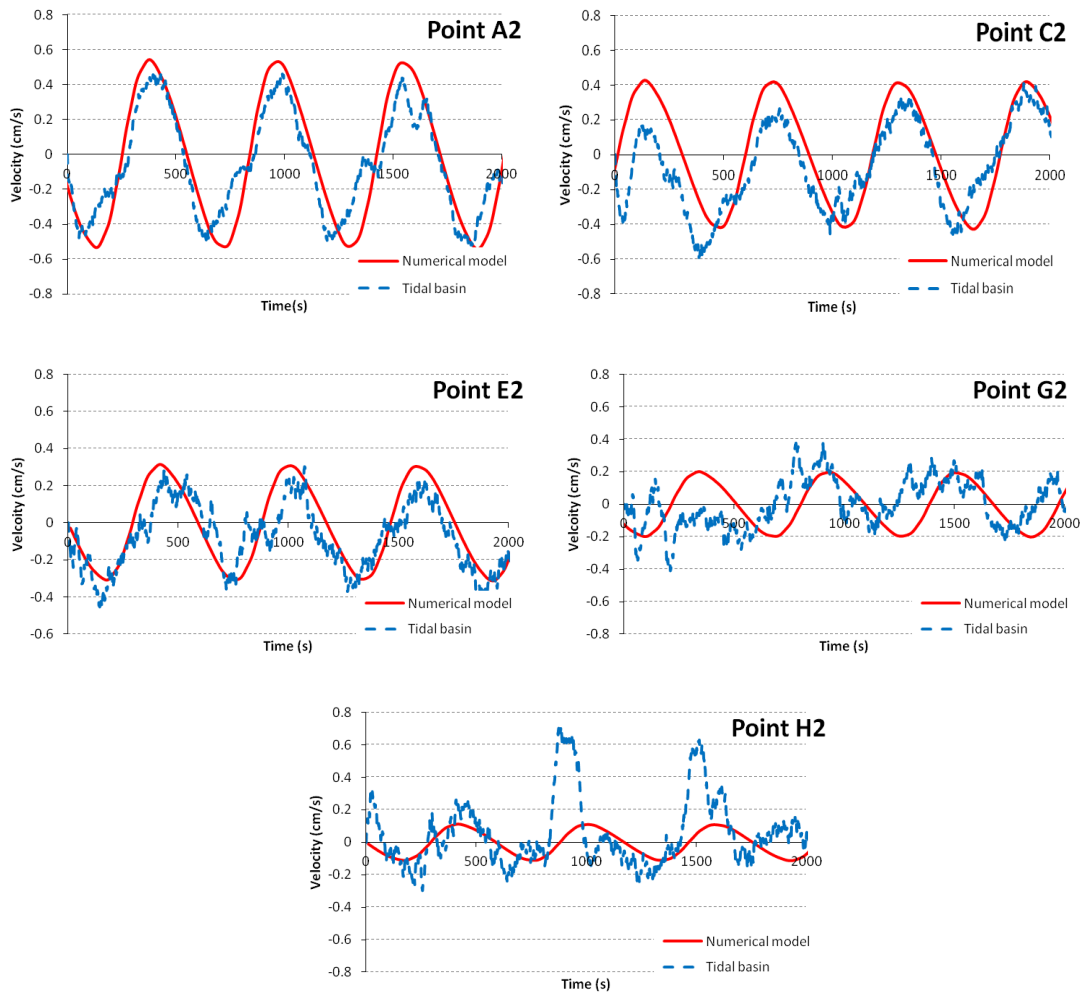


**Figure 4.8: Comparison between experimental and numerical velocities. Location of sampling points within tidal basin are illustrated in Figure 4.7 Tidal amplitude is 6.9cm and tidal period is 586 seconds**

#### 4.7 Dampening of reflected flow

Tidal energy present in any situation must eventually be dissipated. In prototype situations, this typically occurs gradually due to bed friction and vertical shear interactions within the water column. However, in model experiments the effect of bed friction is often not as great due to the effects of scaling discussed previously. Therefore, a large portion of the tidal energy remains in the flow, which then dissipates instantaneously when flow reaches the back wall of the tidal basin. This results in a

situation where tidal waves reflect back into the area of wave generation, which suppresses the generation of currents within the working area.

A number of options exist to reduce wave reflection. These include: reducing the tidal forcing in order to reduce wave energy; increasing bed roughness to induce the gradual dissipation of energy; and installing wave absorbers in the locality of reflected flow. For this study, wave absorbers were used to reduce tidal energy reflection.

A 100mm thick foam material was aligned to the back wall of the tidal basin and the effect on circulation within the basin assessed. Flow measurements were recorded at the locations detailed previously in Figure 4.7 and again compared with numerically predicted values. Figure 4.9 presents the results.

The gradual dissipation of tidal energy by the wave absorbers is quite successful in reducing reflection within the working area of the tidal basin. The generation of secondary currents, particularly in evidence near the back wall of the basin, reduces significantly, and there is much closer agreement between numerical and experimental model results. The inclusion of the tidal energy absorbers results in close agreement between experimental and numerical results even at a distance of 250mm from the back wall (point H2).

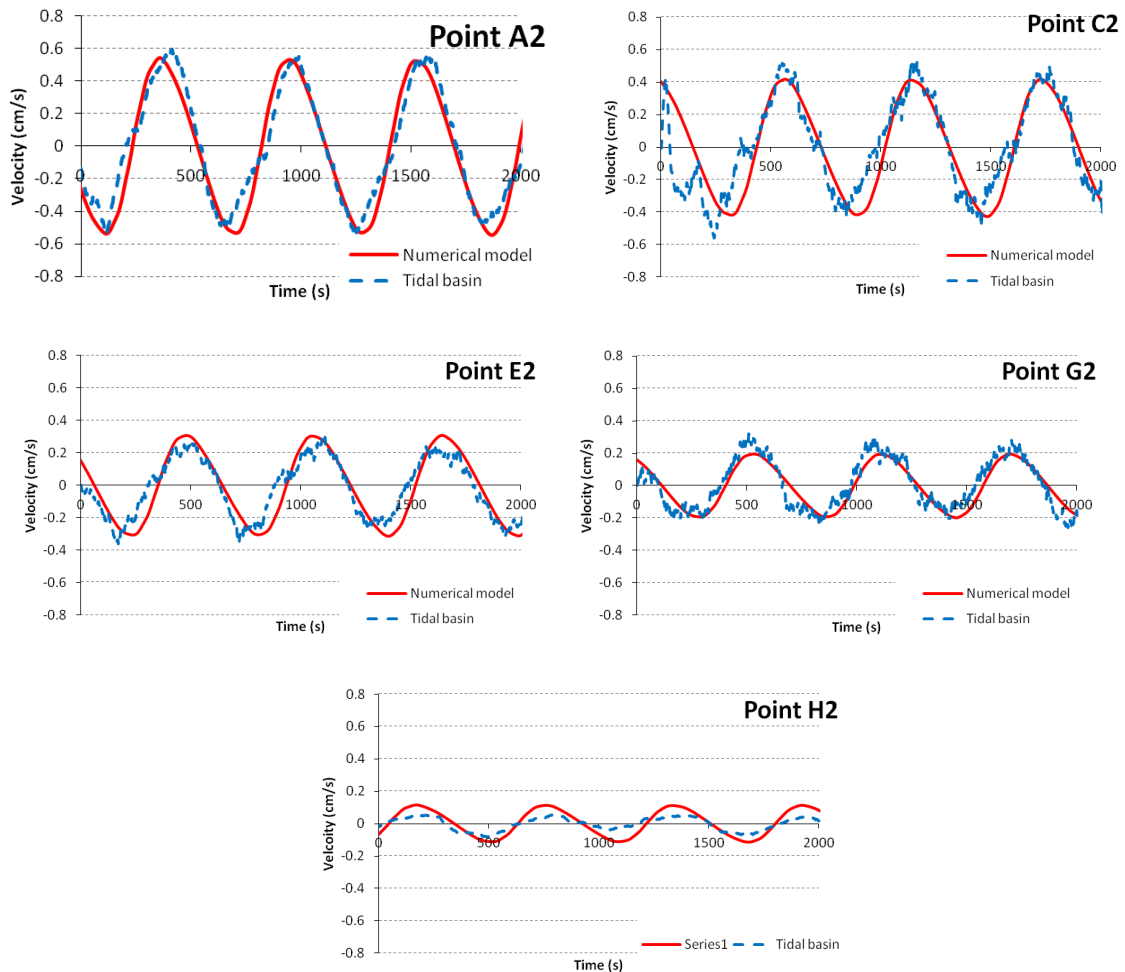


**Figure 4.9: Comparison between experimental and numerical velocities. Figure 4.7 displays location of sampling points. Tidal amplitude is 6.9cm and tidal period is 586 seconds. Foam material wave absorber installed within tidal basin**

#### 4.8 Laboratory tests and analysis

The physical modelling experiments conducted in the tidal basin involved the detailed analysis of flow through and around aquaculture structures. A Froude scaled model of a suspended mussel dropper long-line was constructed and installed in the laboratory. Flows within the model were analysed via detailed velocity measurements and solute transport experiments. This chapter presents the design and analysis of the scale model

Flows through a scaled system of bottom-feeding oyster trestles were also investigated as part of this research. A Froude scaled model of a typical bottom-culture aquaculture

structure was constructed and installed in the tidal basin; flows were again assessed by a combination of velocity measurements and tracer transport experiments. The focus of this thesis however, is physical and numerical analysis of flows through a suspended canopy. Hence, the study of bottom feeding trestles is not of relevance for this thesis, and is not discussed here; for completeness, the experiments conducted and associated numerical simulations are presented and discussed in Appendix A

The purpose of the laboratory experiments was to obtain data that could be used:

- a) To understand the hydrodynamic processes involved
- b) To assess the numerical model

The visual observation of flow processes at the laboratory scale enables one to gain a close understanding of the ‘full picture’ hydrodynamic processes that occur as flow passes through these aquaculture structures. Information can then be collected on the flow conditions that occur in prototype field conditions.

All dimensional sizing of physical and numerical models was computed using Froude law scaling relationships. Hence, the Reynolds scaling criterion could not be satisfied which resulted in a common hydraulic modelling problem; the assumption of negligible viscous forces. This assumption and its implications will be discussed in detail in subsequent sections.

As a result of the numerical modelling conducted as part of this study, the scope of the physical model experiments can be reduced to that of producing a scaled, technically defensible model of aquaculture structures that could be then reproduced at prototype scale through numerical simulation. Hence, while every effort was made to maintain physical realism when scaling the aquaculture structures; in relation to the numerical model it would have little impact, since the model would be recreating laboratory conditions. Therefore, some of the problems encountered when achieving dynamic similarity could be circumvented.

#### 4.8.1 Scale model of mussel droppers

The cultivation of shellfish via suspension feeding is carried out extensively along the West Coast of Ireland. In this cultivation methodology, shellfish are suspended via “droppers”, length of rope that hangs vertically, from longlines that are suspended from floatation device in the pelagic zone. Figure 4.10 displays a typical double longline deployment; while the vertically hanging droppers to which the cultivated mussels are attached, are presented in Figure 4.10(c). These floating structures are 110 meters long and 1.2 meters wide. Barrels act as floatation devices for the longlines, and 8 meter long droppers are suspended from them. Table 4-1 provides dimensions for a typical long-line system.

The aim of the current study was to analyse the flow through this suspended rope culture by means of laboratory studies. A mathematically correct, Froude-scaled model of an idealised mussel dropper long-line was installed in the tidal basin. A scaling factor of 30 was adopted for this study based on careful consideration of: typical deployments of long-lines, flow dynamics, and laboratory spatial limitations.





**Figure 4.10: Suspended longline showing (a) typical farm deployment, (b) flotation units and (c) vertically hanging droppers**

An important feature of mussel droppers is the surface roughness produced by the mussel shell. The surface roughness can be defined as the mean size of surface irregularities. It is commonly expressed as an equivalent sand grain roughness,  $k_s$ , and quantified as the ratio between surface roughness height and diameter  $k_s/D$ . To assess the relative importance of the surface roughness component a number of scale model simulations were investigated, namely:

- Without structures in the tidal basin (benchmark study)
- Two rows of smooth cylinders of 10mm diameter aligned parallel to the flow.
- Two rows of roughened cylinders aligned parallel to the flow with average surface roughness ratio,  $k_s/D=0.093$  (total diameter =11.86mm).

**Table 4-1: Individual long-line and scale model configuration. Scale factor = 30**

Design Element	Prototype dimension	Model dimension
Average Length	30m	1.0m
Double long-line spacing	1.9m	0.063m
Dropper Length	8m	Assumed Infinite
Dropper Diameter	0.30m	0.01m
Dropper Spacing (centreline to centreline)	0.448m	0.02m

Figure 4.11(b) details a schematic of a scaled double long-line installed in the tidal basin. Two rows of 50 cylinders were installed, with a longitudinal spacing of 20mm centre-to-centre between cylinders and a lateral spacing of 63mm centre-to-centre between rows, as described in Table 4-1. Droppers extended the entire water depth to preclude any cylindrical free-end wake interactions (Zdravkovich, 2003), and promote a more uniform flow profile in the vertical. Detailed velocity measurements were recorded at the equidistant points denoted in Figure 4.11(a). Figure 4.11(c) presents a photo of the scaled mussel dropper long-line.

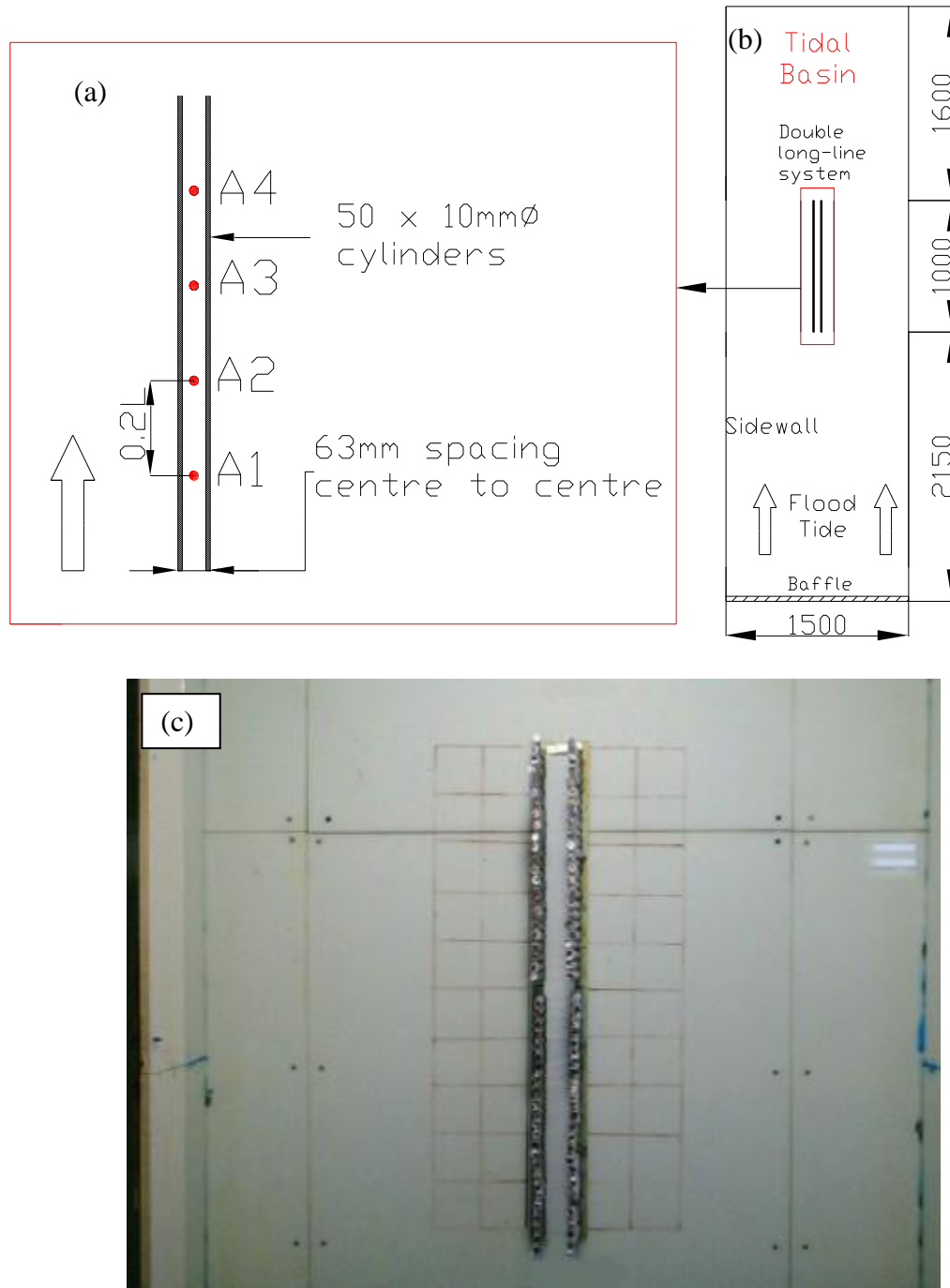


**Figure 4.11: Schematic of tidal basin scaled long-line detailing: (a) exploded view of long-line design detailing velocity measurement points A1-A4, (b) schematic detailing location of long-line in tidal basin and (c) scaled long-line installed in tidal basin.**

### 4.8.2 Smooth droppers

The objective of this laboratory study was to assess the form drag exerted by the modelled droppers on flow. A double long-line of ‘smooth’ cylinders, constructed of polished steel, was installed in the tidal basin and the effects on flows examined. The frictional resistance exerted by the cylinders was assumed minimal (relative to the roughened cylinders studied in the next section). Figure 4.11 details the location of velocity measurement points. For a ready comparison of flows, results were compared to equivalent tidal basin measurements with no structures in place (benchmark). Figure 4.12 presents the results.

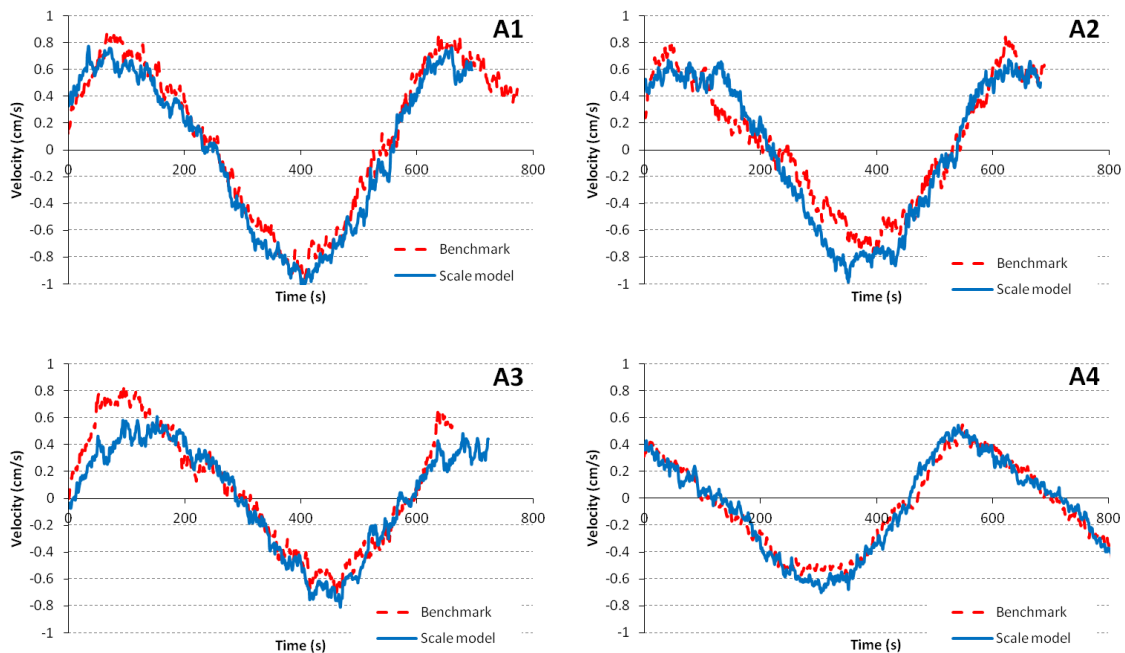


**Figure 4.12: Comparison between velocities collected in tidal basin with no structures in place (benchmark) and Froude scaled long-line installed (scale model). Figure 4.11 displays the location of sampling points.**

Figure 4.12 displays an interesting feature of observed flows through the array of smooth cylinders; results display little quantifiable difference in measured velocities within both scenarios. Velocity measurements for both cases are almost identical at points A1, A2 and A4. Point A3 displays some degree of variation; however, considering

the other data points, it seems probable that this is more a result of experimental variation, than flow attenuation due to the presence of the structures.

These results suggest that the actual influence of the structures is minimal. This is quite surprising and suggests that the spacing of droppers is such as to minimise interaction between cylinders. Studies demonstrated that at a spacing-to-diameter ratio greater than 5 (6 in this case) there is minimal interaction between cylinders and they can be assumed to essentially act independently (Zdravkovich, 2003). Another possibility is that the significant attenuation of flows induced by droppers in the field (e.g. Boyd and Heasman, (1998) is primarily a result of highly frictional flows through the rough droppers. To investigate this second hypothesis, flow profiles through a scaled model of roughened cylinders are investigated in the next section.

### 4.8.3 Roughened droppers

Mussel long-lines consist of individual droppers, which hang vertically. The vertical length of mussel-encrusted droppers represents a roughened cylinder. Figure 4.13 displays a close-up view of a mussel dropper displaying its highly irregular surface exhibiting extreme surface roughness.



**Figure 4.13: Exploded view of mussel dropper illustrating surface irregularities. Illustration adopted from (Plew, 2005)**

The effect of surface roughness on flow is something that has received a significant amount of attention in fluid dynamics. For a comprehensive review of flow past cylindrical bodies the reader is referred to Guven et al., (1980).

In this section, the effect of high surface roughness on flow around an array of cylinders is investigated. In order to investigate the effect of surface roughness on flows, the cylinders were roughened by encasing them in a wire mesh. The diameter of the cylinders was increased by 1.86mm resulting in a surface roughness-to-diameter ratio,  $k_s/D=0.093$ . The actual roughness of a long-line is quite difficult to quantify due to the extreme surface irregularities that the mussel organisms themselves present and the highly-variable temporal nature of the object as the mussels mature. However, a surface-to-diameter ratio of  $k_s/D=0.5$  has been suggested based on a consideration of the projected area of a typical mussel dropper (Plew, 2005).

The experimental methodology was equivalent to the procedure detailed in the previous section. Briefly, two rows of cylinders were arranged at a lateral spacing of 66.7mm centre-to-centre, and a stream-wise spacing of 23.7mm (spacing was increased slightly to account for diametric increase due to surface roughness). All cylinders extended from the bed to penetrate above the water surface.

Velocity measurements were carried out at four points as detailed in Figure 4.11 and again the results were compared with the case where no cylinders were placed in the basin. Figure 4.14 displays a time-series plot for the case where roughened cylinders are placed in the basin versus the benchmark case where no structures are installed in the tidal basin

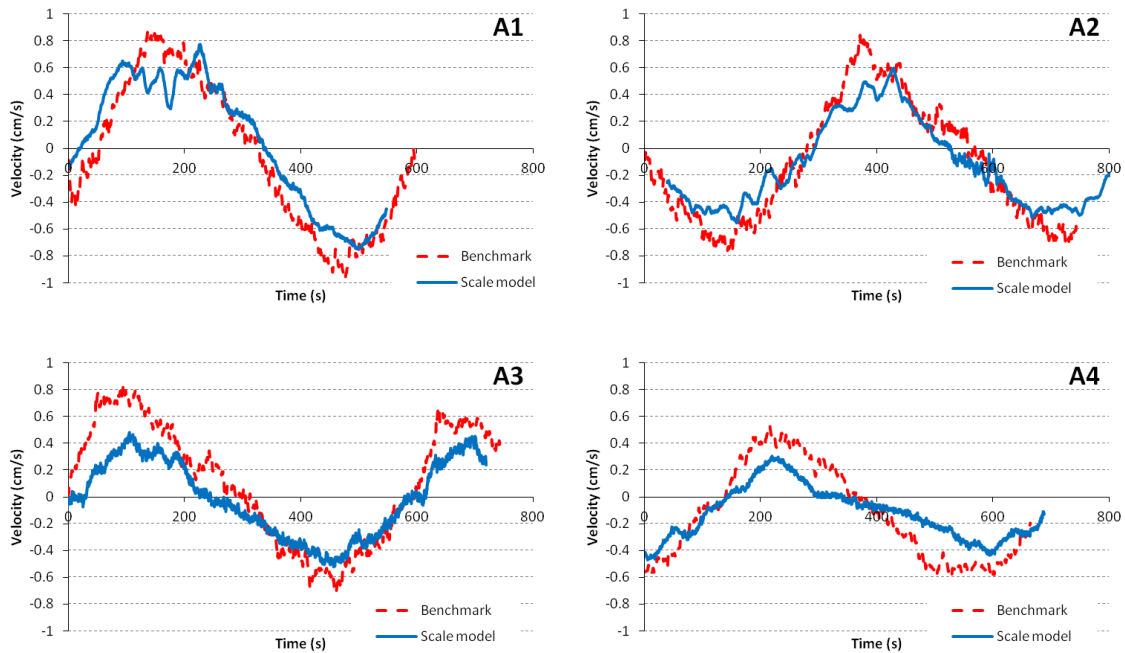


**Figure 4.14: Comparison between velocities collected in tidal basin with no structures in place (benchmark) and Froude scaled, artificially roughened, long-line installed (scale model). Figure 4.11 displays location of sampling points.ints.**

The artificially roughened cylinders appear to have a very significant effect on velocities, particularly at points A3 and A4. At all four locations there is a significant attenuation in current speed of 20-40%. This is quite interesting when one considers the almost negligible effect that the smooth cylinders had on flow. This is similar to results produced by Plew (2005), who found that drag on an array of rough cylinders was greater than drag on an array of smooth cylinders. The hydrodynamic effects and implications of both cylindrical drag and surface roughness effects will be investigated in greater detail in the next section by detailed tracer transport studies.

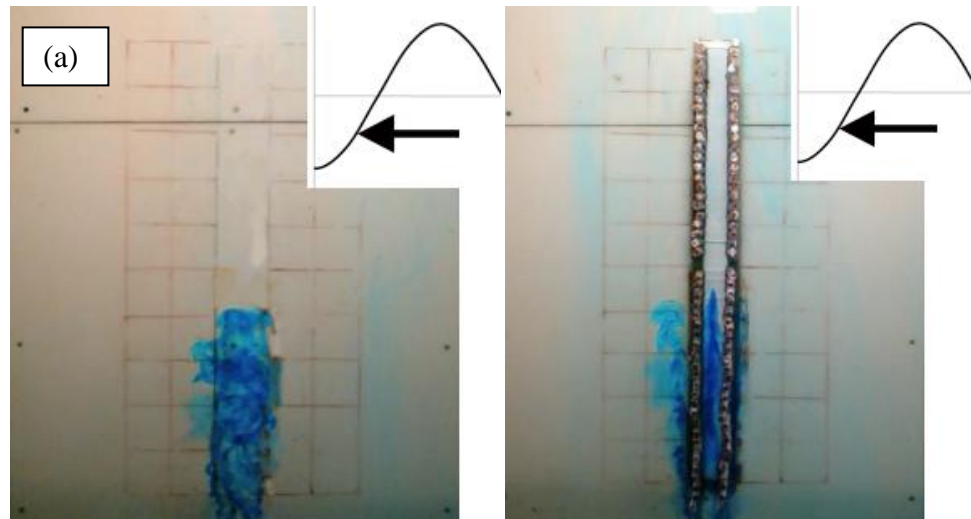
The representation of prototype surface roughness in a scale model is quite a challenging undertaking due to the large number of forcing variables that require consideration, e.g. viscous forces, surface tension effects, wake turbulence, etc. Hence, the objective of the scale modelling study of artificially roughened cylinders was not an attempt to mathematically scale actual mussel dropper roughness due to the inherent futility of attempting to scale all the system forcings. Rather, the objective of the study

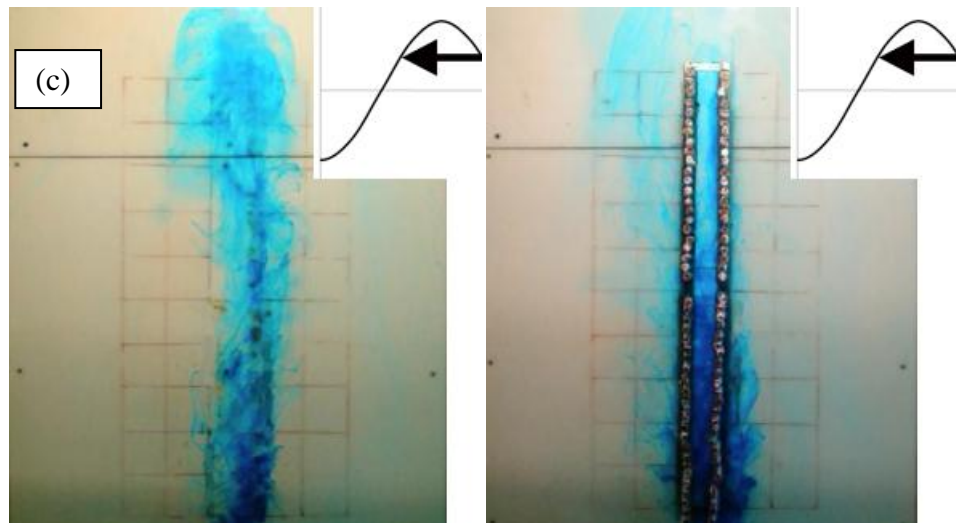
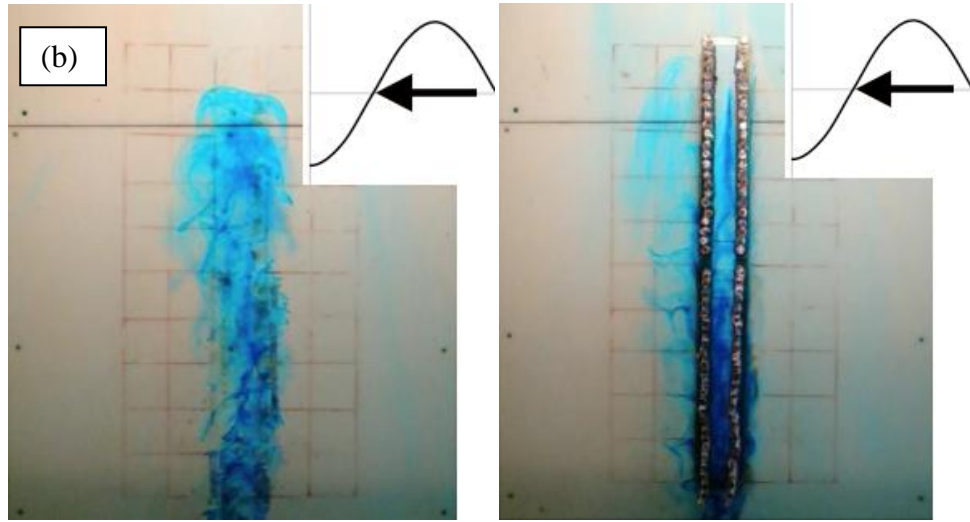
was to investigate the effect of idealised, induced surface roughness on flow patterns, wake interactions and turbulent structure.

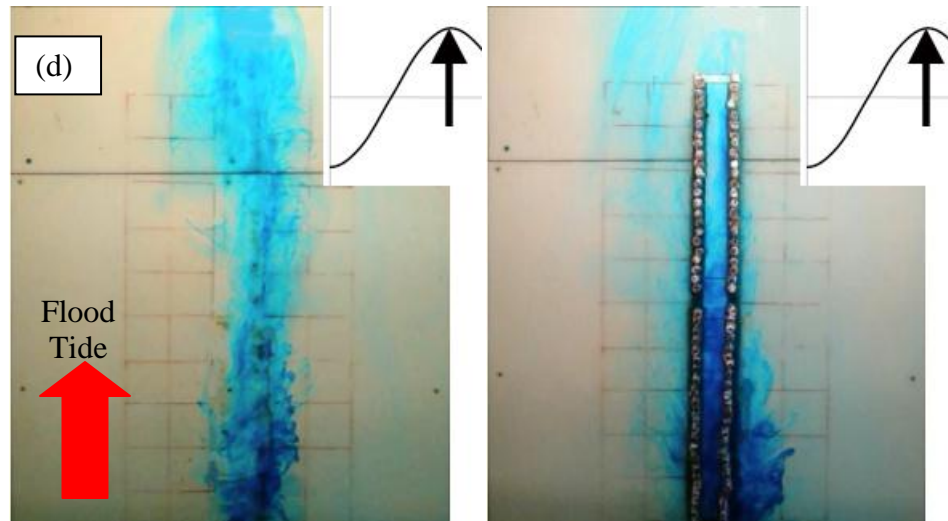
It is intuitively clear that the flow patterns observed in the scale model composed of roughened cylinders is more representative of the complex fluid-structure interactions that take place as flow passes through a canopy of suspended mussel droppers. Hence, this scale model will be referred to as the “Aquaculture Physical Model” (APM) and will be used for subsequent numerical modelling validation studies.

#### 4.8.4 Scaled mussel dropper dye tracer experiment

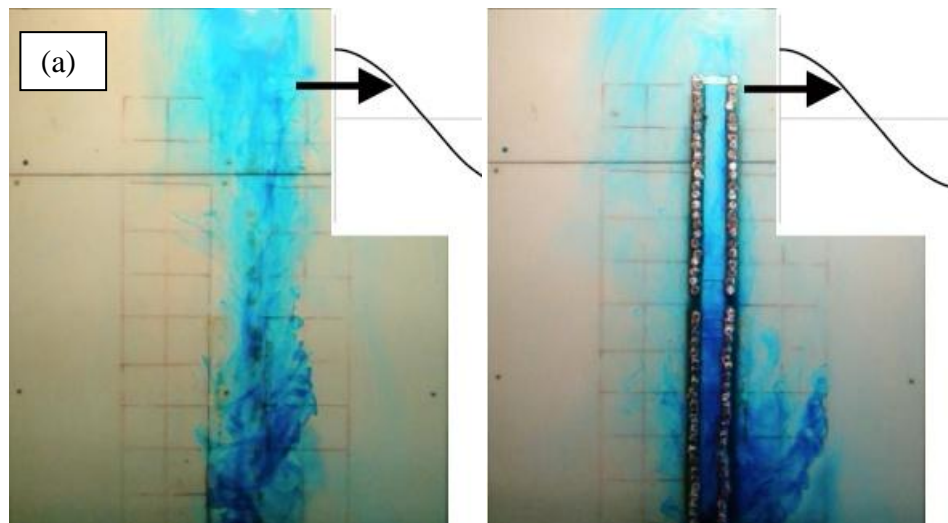
Dye tracer experiments were used to investigate the effects of a mussel dropper long-line on flow and water circulation patterns. Adopting a similar experimental process as previous material transport studies; a conservative tracer material was introduced at low water, upstream of the scaled system, and the transport observed and recorded over a full tidal cycle. The effect of the physical impediment on flows and material transport was assessed by a comparison with the benchmark system of no structures installed in the tidal basin. Figure 4.15 presents dye transport within the Froude scaled system at four different stages of the flood-tide tidal cycle; while Figure 4.16 presents dye transport at four different stages of the ebb tide, tidal cycle. Of particular interest were, the effects of the installations on the longitudinal transport of material on the flood tide; and on the flushing and removal of dye on the ebb.

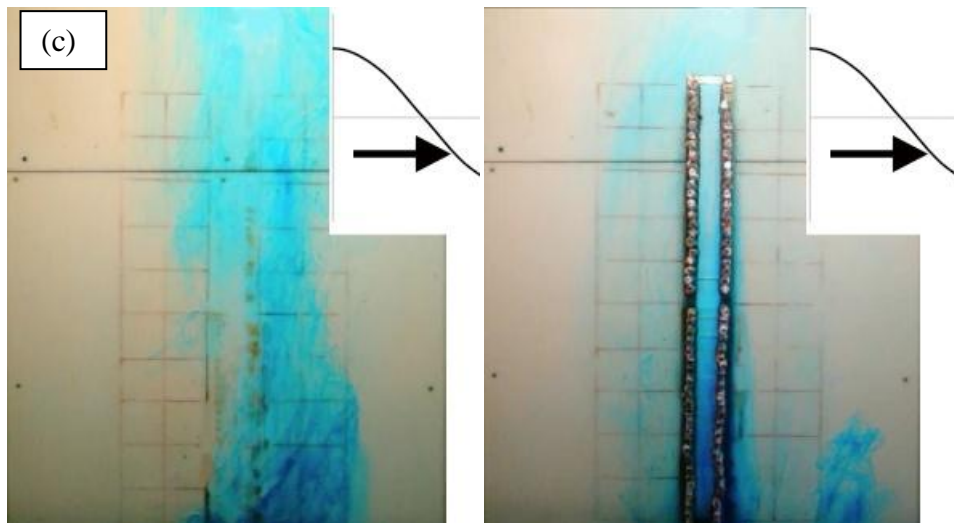
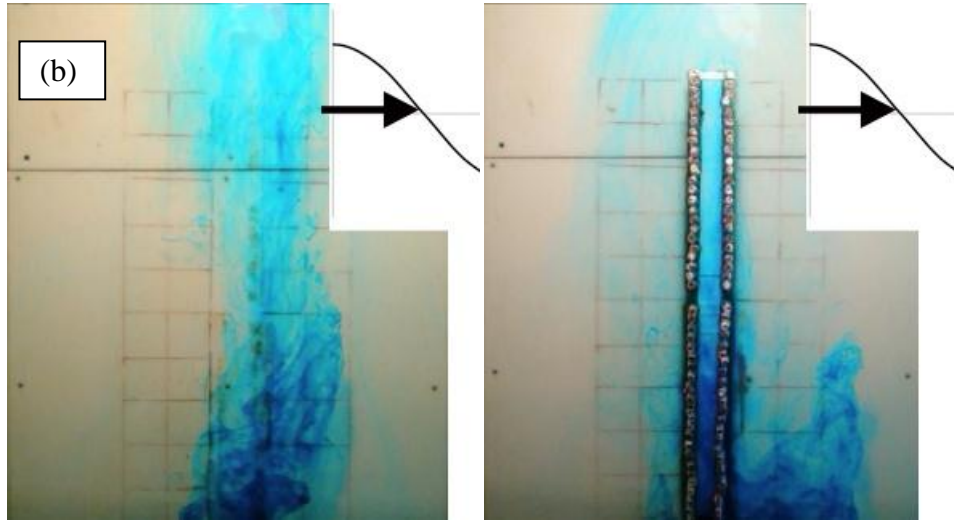






**Figure 4.15: Dye transport recorded in the tidal basin at four different stages of the flood tide tidal cycle (displayed on sinusoidal curve): (a) early-flood, (b) mid-flood, (c) late-flood and (d) high water mark. Dye transport with no impediment to flow (LHS) and through a Froude-scaled roughened long-line (RHS) are presented**





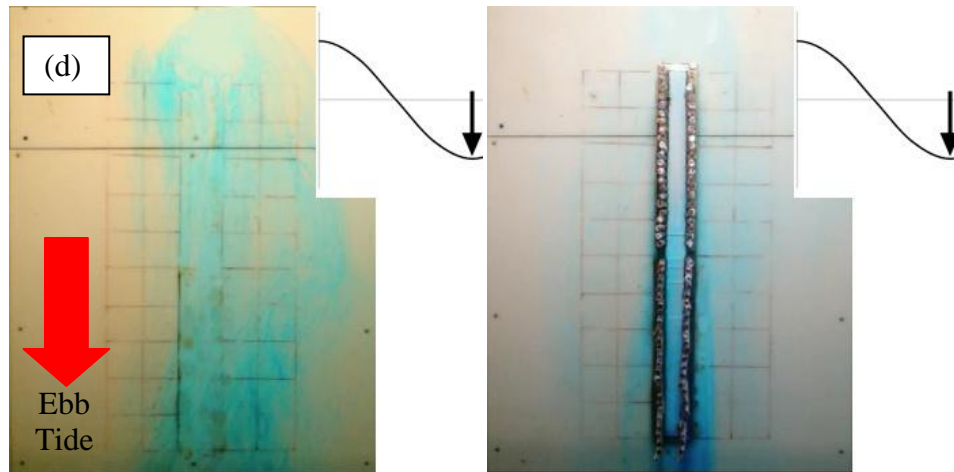


**Figure 4.16: Dye transport recorded in the tidal basin at four different stages of the flood tide tidal cycle (displayed on sinusoidal curve): (a) early-ebb, (b) mid-ebb, (c) late-ebb and (d) low water mark. Dye transport with no impediment to flow (LHS) and through a Froude-scaled roughened long-line (RHS) are presented**

The longitudinal transport of dye through the structures was significantly affected by the presence of the scaled dropper system in three ways.

1. On the flood tide, the droppers impede the transport of dye. In this simulation, the concentration of dye at the downstream extents is practically zero when the scaled mussel dropper system is in place.
2. The flow of dye on the ebb tide is also affected with some trapping of material within the system being evident. This is of utmost interest with regards supply of nutrients and the removal of pollutants. This factor will be investigated in greater detail by numerical model flushing studies.
3. The lateral transport of dye is also altered by the droppers; with a significant amount of material diverted around the structures. Again, this is of major concern from the point of view of the supply of nutrients to the bivalves and corroborates previous field studies on material transport around suspended mussel dropper long-lines, where a significant amount of the ambient flow was diverted around the system (Boyd and Heasman, 1998).

Analysing Figure 4.16 indicates some secondary circulation patterns developing within the experimental basin during lag flows, at and shortly after, the high water mark. This is particularly evident within the aquaculture scale model where a significant amount of material is diverted laterally around the structure. Comparisons with the benchmark scale model suggest that these secondary processes are a property of the experimental basin itself and are most likely due to non-uniform return flow downstream of the system. However, as the primary goal was to compare the effects of the scale installation relative to the benchmark case, these processes do not affect the viability of the results.

#### **4.9 Discussion**

This chapter presents details on the experimental studies conducted as part of this research. The fundamental theory of scale modelling is introduced and reviewed. Details are presented on the tidal basin experimental set-up, and the mathematical scaling of the scale model from prototype dimensions. Both hydrodynamic and solute transport studies conducted to assess the effects of the installations are described and discussed.

The study clearly demonstrates the significant effects a typical suspended long-line has on flows. Within the scaled long-line, we observe attenuated flow speeds; reduced material flux; and a diversion of flows around the structure. The implications for actual aquaculture developments are obvious.

In the next chapter, these results are expanded to the bay-scale level by means of numerical modelling studies. The data presented here is adopted to both assess and fine-tune numerical simulations of impeded flows. The models are then used to investigate the implications for aquacultural carrying capacity, and environmental impact studies.

#### **4.10 Scale modelling and difficulties encountered**

An inherent flaw present in any scale modelling exercise is that the model is constructed at a scale different to that of the prototype and the resulting inaccuracies that ensue. Chapter 4 discussed the necessity of balancing the requirements for similarity between inertial scales and viscous scales. The most significant sources of error in scale modelling generally fall into one of two brackets (Hughes, 1993):

- **Scale effects** are a result of the simulation of prototype flow conditions at a smaller scale. Scale effects are thus a consequence of non-similarity between model and prototype, an error arising by designing the model according to the main determining laws and neglecting others. The objective of scale modelling then is the design of the model from reality to make these errors as small as possible in the given situation. The most common example is viscous forces that are relatively larger in the model than in the prototype.
- **Laboratory effects** occur as a result of the restriction that the laboratory environment places on the simulation of field or open ocean situations. A common example is the impact model boundaries have on model simulations.

An example of a laboratory effect investigated as part of this research was reflection off the boundary walls of the tidal basin. Reflection off boundary walls is an inherent feature of physical modelling due to the reduced spatial extents and distortion of hydraulic models. In the prototype, the area of interest can be at the scale of kilometres and as a result, the dissipation of wave energy occurs more gradually over much greater distances. In the scale model, on the other hand, a large component of the wave energy must be dissipated almost instantaneously as flow hits the boundary wall of the tidal basin. On the flood tide, this results in tidal waves being reflected back into the area of wave generation.

This was investigated and addressed in this study through a detailed analysis of flows near the back wall of the tidal basin. The analysis indicated a high degree of extraneous currents being present in velocity measurements as a result of flow being reflected off the back wall of the tidal basin, which suppressed the generation of flow within the working area. This was addressed by the alignment of an absorbing foam material to the back wall of the tidal basin. This successfully resulted in a more gradual dissipation of wave energy and a significant reduction in the data scatter observed in velocity measurements.

An inherent scale effect of practically any coastal engineering physical modelling study is the discrepancy that exists between viscous forces. As discussed, when a scale model is developed using the criterion of Froude similarity, it is practically impossible to obtain

similarity between viscous forces in model and prototype. This is typically the most important scale effect to be encountered in physical modelling studies. In scale modelling, this problem is often minimised by ensuring that turbulent flow dominates in the model, i.e. (Novak et al., 2010):

$$Re_m > Re_{cr}$$

In this research, the Reynolds number for flow past a mussel dropper long-line was in the region of 3,000. To minimise the effects of turbulence it was necessary to ensure that this remained above the critical limit of laminar flow in open channel flows. The transitional Reynolds number from laminar to turbulent flows in open channel flow is not so well defined but is in the region of 1,000 to 2,000 (Henderson, 1966). Hence, flow was fully turbulent at the flooding and ebbing stages of the tidal cycle when the advective features of the flow were at their most interesting from an aquacultural development perspective.

The scale modelling of benthic inter-tidal structures such as oyster trestles poses many problems, not least the viscous and skin friction effects that result due to the flooding and drying of the system at low-tide (see Appendix A). A number of options were considered to minimise these effects. These included; the installation of a highly polished, smoothed surface and the reduction of surface roughness of the scaled oyster trestles as much as practically possible.

A difficulty encountered in this study was the porous flows that occurs through oyster trestle bags in the field. Much consideration was given to methods of simulating this in the laboratory environment. However, the mathematical consideration of Froude, Reynolds and Weber criteria for similarity precluded any modelling effort.

## Chapter 5: Two-dimensional numerical modelling

---

*“Theory cannot cover all the complications that are encountered in practise. Consequently, most major hydraulic projects are model tested to optimise design”*

*~M. S. Yalin*

## 5.1 Introduction

The main aim of this section of the research is to incorporate the effects of aquaculture farms on tidal flows and circulation patterns into an existing depth-averaged numerical model. Aquaculture farms consist of an accumulation of thousands of marine organisms placed in a waterbody. Therefore, to quantify the large-scale effects of these farms on flow, it is necessary to consider the small-scale flow interactions between the fluid and individual mussel droppers and long-lines, since the large-scale hydrodynamic effects of the farms are a direct result of flow through and around multiple arrays of these individual components. The physical effects of these structures include: reduced velocities due to enhanced drag; blockage of flows; conversion of kinetic energy to turbulence; and modified mixing patterns due to the mechanical stirring effect caused by the structures. Because of this interrelationship between the large-scale and small-scale dynamics, extensive laboratory studies were conducted to develop an understanding of flow and turbulent structure at a near-field level, which could then be extrapolated to the bay-scale level. The main objectives of the physical models were: (i) to produce a qualitative description of the flow processes involved and (ii) to calibrate and validate the numerical model.

In this section, numerical modelling studies are presented that develop and expand on these laboratory studies. A detailed assessment of the validation and application of an amended depth-averaged numerical model to simulate flows through suspended aquaculture installations is presented. The numerical model was amended to incorporate both form drag and a porosity term which describes the degree of fluid penetration throughout the farm. Both a one-equation mixing-length scheme and a two-equation  $k-\varepsilon$  turbulence closure model were considered; with the  $k-\varepsilon$  model further refined to include the production and dissipation of turbulent energy due to the presence of the structures. The previously discussed laboratory studies were used to develop appropriate coefficients, and fine-tune the hydrodynamic model to accurately simulate the complex fluid-structure interactions that occurs, both at the near-field and far-field scales of the flows. A case study investigated the applicability of the model to real coastal simulations; the model was applied to a designated aquaculture development site in the West of

Ireland, Casheen Bay. The impact of the culture leases on hydrodynamics and material transport is discussed. Flushing studies provide a time scale analysis of the effects of the aquaculture infrastructure on water circulation patterns. The viability of using relatively simple flushing studies formulae to assess the development potential and environmental impact of small scale aquaculture projects was investigated, as opposed to other relatively more expensive modelling techniques.

## **5.2 Numerical modelling**

The purpose of the numerical model is to provide an accurate method of predicting the effects of mussel dropper long-lines on flow dynamics and material transport. To achieve this, the model governing equations were amended to model the effects of the fluid passing through a dense canopy of suspended mussel droppers. Section 3.2 presents the model equations and derivation. This model will henceforth be referred to as the “aquaculture numerical model” (ANM). A refined turbulence closure model simulating the effects of the droppers on turbulence production and intensity is also examined.

As a preliminary assessment of circulation patterns within the tidal basin and the ability of the mathematical model to represent these flows, a general circulation model of the tidal basin is developed. This is used as a benchmark comparison tool for subsequent modelling efforts.

### **5.2.1 General circulation model**

A general circulation model of the tidal basin for the benchmark case was developed in DIVAST. The model was developed at the prototype scale, and described circulation patterns within the tidal basin with no aquaculture structures in place. Table 5-1 presents the bathymetric and open boundary data adopted for the numerical model. The computational domain covered a 142m x 45m area, and the grid size equalled 1.0m. This model will henceforth be termed the ‘Standard Numerical Model’ (SNM).

**Table 5-1: Dimensional values prescribed for the scale and numerical models. A scaling factor of 30 was adopted with appropriate Froude scaling laws applied**

Parameter	Physical model	Numerical model
Tidal amplitude	0.069m	2.07m
Tidal Period	586s	3210s
Bathymetry	0.255m	7.65m

Velocity data were output at the points detailed in Figure 4.12 and compared with velocity data collected at equivalent points in the tidal basin. Figure 5.1 presents the time-trace data.

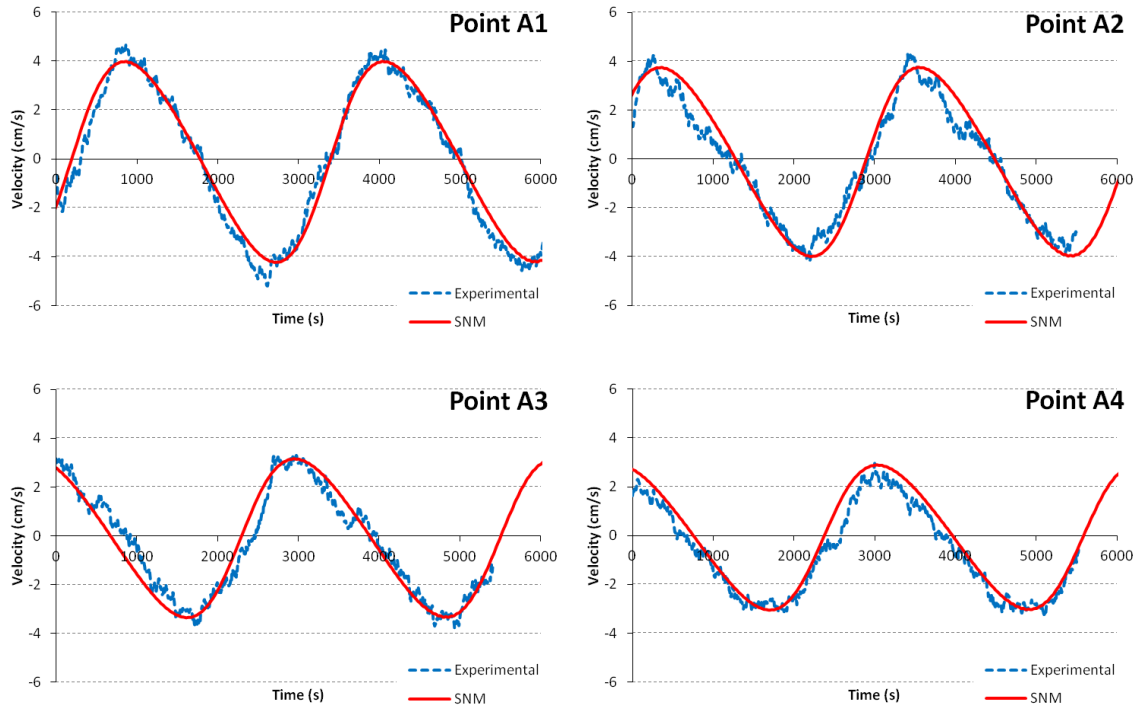


**Figure 5.1: Comparison between velocities collected in tidal basin with no structures in place (experimental) and SNM predicted velocities. Figure 4.12 displays location of sampling points.**

An analysis of the data presented in Figure 5.1 displays strong agreement between numerical and experimental data. The numerical model replicates both the magnitude and temporal profile of velocities observed in the tidal basin quite accurately. These datasets

serve both as an initial validation of tidal basin performance and, more importantly, as a benchmark for future developments of the numerical model.

### 5.2.2 APM circulation patterns

This section presents a comparison between APM and SNM results. The performance of the SNM in replicating flow patterns observed in the APM is discussed. Figure 5.2 presents SNM results plotted against APM data.

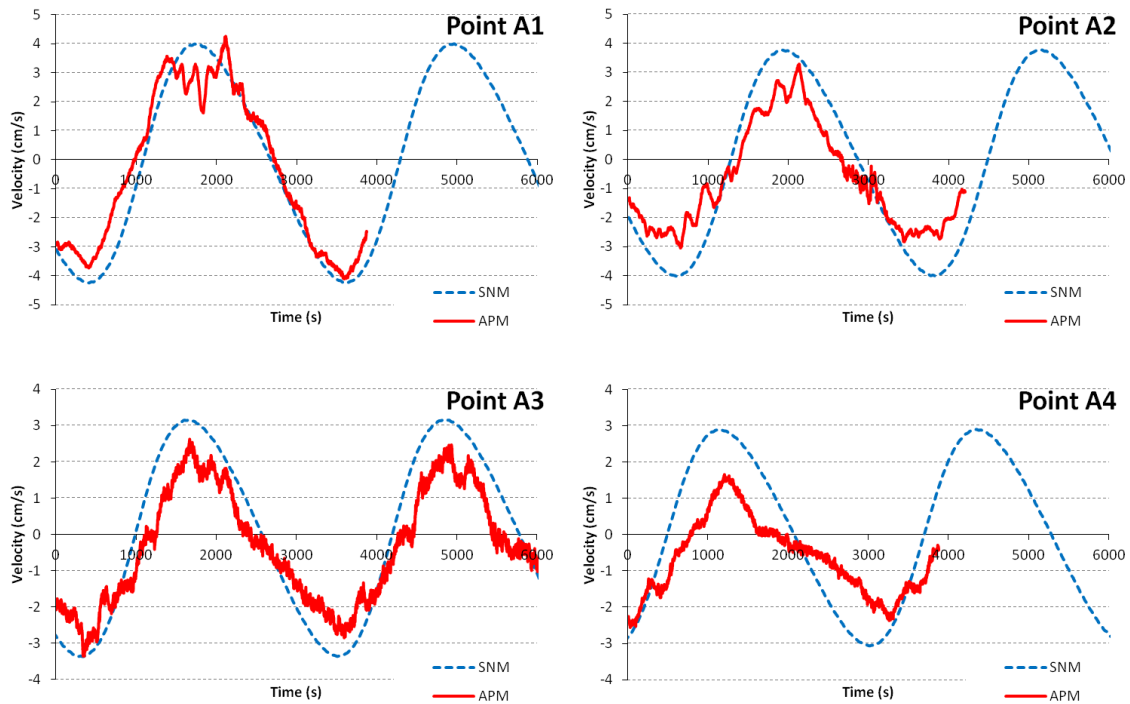


**Figure 5.2: Comparison between APM experimental velocities, and SNM predicted velocities. Figure 4.12 displays location of sampling points.**

An analysis of Figure 5.2 displays that the SNM poorly simulates the physical impediment to flow presented by the roughened long-line. The velocities observed in the APM are 20-40% less than velocities predicted by the SNM. The numerical simulation of this complex flow regime requires a significant level of modification of the governing equations of unsteady flow. As a preliminary estimate, a simple two-dimensional model of flow attenuation was developed by computing kinetic energy losses through the system.

### 5.2.3 Kinetic energy losses analysis

A comprehensive analysis of flow through mussel farms involves the solution of the Navier-Stokes equation. This can be an expensive and time-consuming undertaking, requiring a large body of information on local flow patterns and bathymetry, in addition to a detailed knowledge of the spatial density and orientation of the mussel farms. In many cases, it may be desirable to obtain a more easily accessible approximation of the impact of the mussel farms on flow. Hence, the aim of this part of the research was an order of magnitude quantification of the effect of aquaculture farms on flows. By analysing the energy losses through the farm, one may estimate the velocity attenuation throughout the farm, and determine the losses that occur due to the presence of the structures.

By developing an expression for rate of work done as flow passes through the droppers, and equating with the kinetic energy of the system, one may determine the kinetic energy dissipated from the flow due to the presence of the droppers. This process only takes into account kinetic energy losses. Evidently, energy will also be lost via additional paths such as exchanges from kinetic to potential energy. At low Reynolds numbers ( $Re < 200$ ) there will also be a significant loss due to viscous forces. However, for the current situation an analysis of kinetic energy losses gives a useful quantification of velocity attenuation through the system.

The kinetic energy lost from the system can be computed by equating the rate of work done on an individual dropper to the kinetic energy losses, assuming other minor losses can be neglected. The rate of work done on a single dropper can be calculated from the equation,  $F_D U$ , where,  $F_D$ , the drag force is given by

$$F_D = C_D \rho D L_d S_F \frac{U^2}{2} \quad (5.1)$$

where  $C_D$  is drag coefficient,  $\rho$  is water density,  $D$  is dropper diameter,  $L_d$  is dropper length,  $U$  is velocity in vicinity of dropper, and  $S_F$  is a shading factor.

The shading factor is a coefficient that accounts for the reduced drag force on downstream cylinders due to the energy dissipated by those upstream. There is some

variance in literature about a value for the shading factor. Oftentimes, a value of one is chosen (Westwater, (2001), Plew et al., (2005), Struve et al., (2003), Wu et al., (2005)). It can also be expressed as a function of cylinder diameter and spacing,  $S$ , (Naot et al., (1996), Cheng and Yong-ming, (2008)):

$$S_F = \left(1 - \sqrt{D/S}\right)^2 \quad (5.2)$$

Due to the degree of variance present in literature with regards to the parameterisation of shading factor; it was decided to assume a value of 1.0, and then calibrate the shading factor using the physical modelling results.

From the drag force equation, an expression for work done per unit area is,  $\rho_d F_D U$ , where  $\rho_d$  is the number of droppers per unit area (assuming they act independently). Assuming that only kinetic energy losses occur, the rate of change of kinetic energy per unit area farm equals the work done on the mussel farm. The kinetic energy losses through the farm can then be derived in a similar manner to (Plew et al., 2005):

Rate of change of kinetic energy

$$\frac{dk}{dt} = \frac{d(1/2 \rho L_d U^2)}{dt} \quad (5.3)$$

Work done on farm

$$F_d U = 1/2 \rho_d \rho C_D D H U^3 \quad (5.4)$$

Equating terms:

$$\frac{d(1/2 \rho L_d U^2)}{dt} = -1/2 \rho_d \rho C_D S_F D H U^3 \quad (5.5)$$

The kinetic energy losses with respect to distance can be expressed using the chain rule

$$\frac{\partial U}{\partial x} = \frac{1}{U} \frac{\partial U}{\partial t} \quad (5.6)$$

Integrating with respect to  $x$  yields an expression for velocity through the farm relative to initial velocity  $U_0$  some distance,  $x$ , upstream.

$$\frac{U}{U_0} = \exp\left(-\frac{nC_D S_F D x}{2}\right) \quad (5.7)$$

Therefore, the velocity through the farm decreases proportionally with distance as kinetic energy is lost to turbulence. This equation only considers kinetic energy, ignoring any exchange between kinetic and potential energy. This simplistic analysis can provide a preliminary estimate of energy losses through a suspended aquaculture farm. This model will henceforth be termed the Kinetic energy Numerical Model (KNM).

The objective of the KNM is to provide a preliminary estimate of flow losses and velocity attenuation throughout an aquaculture system. The SNM developed and validated previously was used to provide ambient upstream velocity boundary conditions,  $U_0$ , to be used in the KNM. The APM is used to both validate the equations and assess the ability of the model to simulate the complex flow processes.

Figure 5.3 presents velocities predicted by the KNM plotted against those measured in the APM.

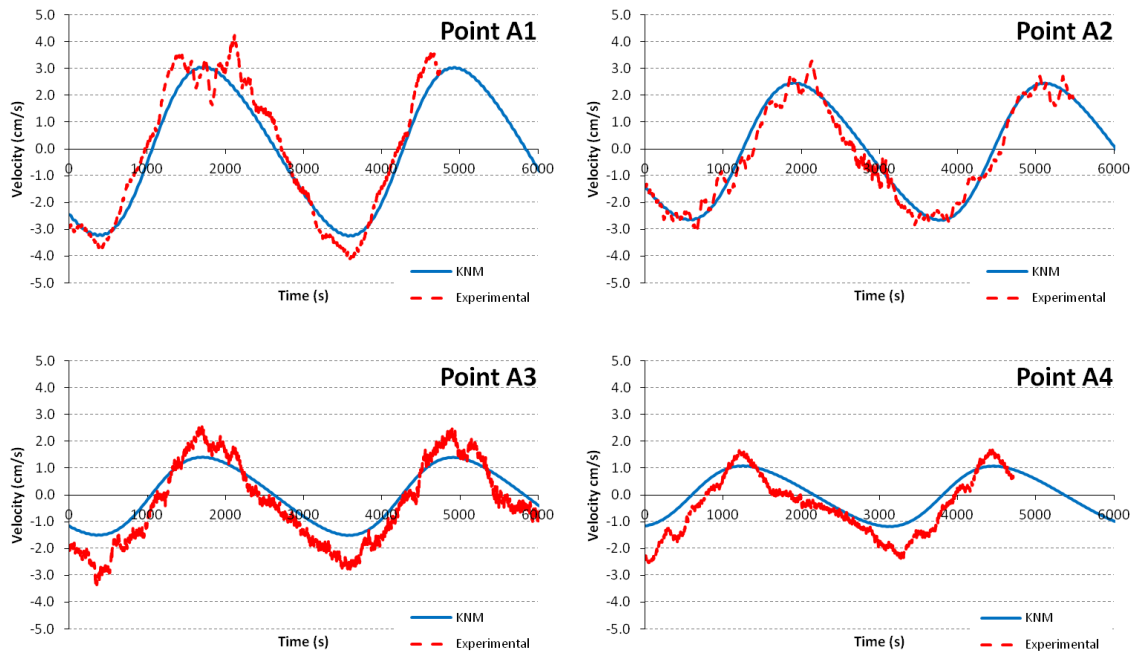


**Figure 5.3: Comparison of APM and KNM velocities. Shading factor = 1.0. Figure 4.12 displays the location of sampling points**

Figure 5.3 suggests that the KNM performs relatively poorly in predicting losses through a mussel dropper long-line. This is particularly evident at points A3 and A4. The kinetic energy model overpredicts energy losses through the farm. One reason for this may be that the chosen value for shading factor is overestimated. Since the shading factor is inversely proportional to the measure in which one dropper is affected by the other droppers, it is expected to vary considerably in any given study based on density and diameter of physical impediment (Naot et al., 1996).

For the current study, the shading factor that gave the best agreement between laboratory and mathematically predicted velocities was 0.7. Figure 5.4 presents the results.

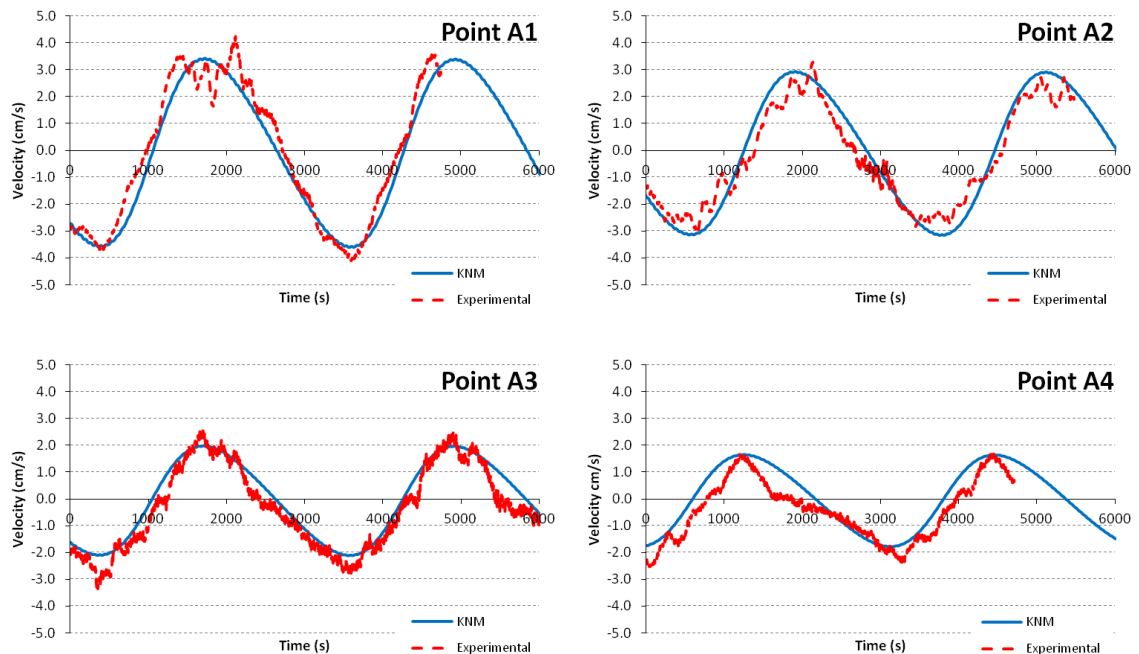


**Figure 5.4: Comparison between APM experimental velocities and KNM predicted velocities, with a shading factor of 0.7. Figure 4.12 displays the location of sampling points**

These results produce reasonable qualitative agreement between both sets of data. These results suggest that the KNM could be useful as a first estimate of energy losses within an impeded hydrodynamic system. However, certain limitations exist. The form of the equation yields a proportional decrease in velocities relative to distance throughout the farm. However, studies indicate that this is not the case for large farms, with most of

the velocity reduction occurring upstream of, or just inside of, the farm, as flow is diverted around the farm (David Plew -personal communication). This large-scale diversion of flow is not evident in the tidal basin due to the comparatively small horizontal dimensions of the system relative to in-situ farms. Therefore, the kinetic energy loss equation may be less applicable to large farms than the system considered in the tidal basin. In addition local bathymetric or topographical data and the effects of any surrounding farms are ignored.

#### 5.2.4 Numerical simulation of impeded flow

Laboratory studies of impeded flows displayed that velocities within the scaled aquaculture installation were attenuated by 20-40%. In this section, the aquaculture numerical model (ANM) developed in Chapter 3, is applied to the scale model system and fine-tuned based on laboratory results. The ANM was developed at the prototype scale; Table 5-2 presents details on both the APM and ANM design parameters.

**Table 5-2: Physical and numerical model design configurations. Scale factor = 30.**

Parameter	APM	ANM
Tidal amplitude [m]	0.069	2.07
Tidal Period [s]	586	3210
Bathymetry (uniform) [m]	0.255	7.65
Dropper diameter [m]	0.012	0.356
Dropper spacing [m]	0.02	0.6
Long-line length [m]	1.0	30
Long-line spacing [m]	0.063	1.95
Dropper density [m <sup>-2</sup> ]	1303	1.45
Porosity (area reduction) [%]	85	85

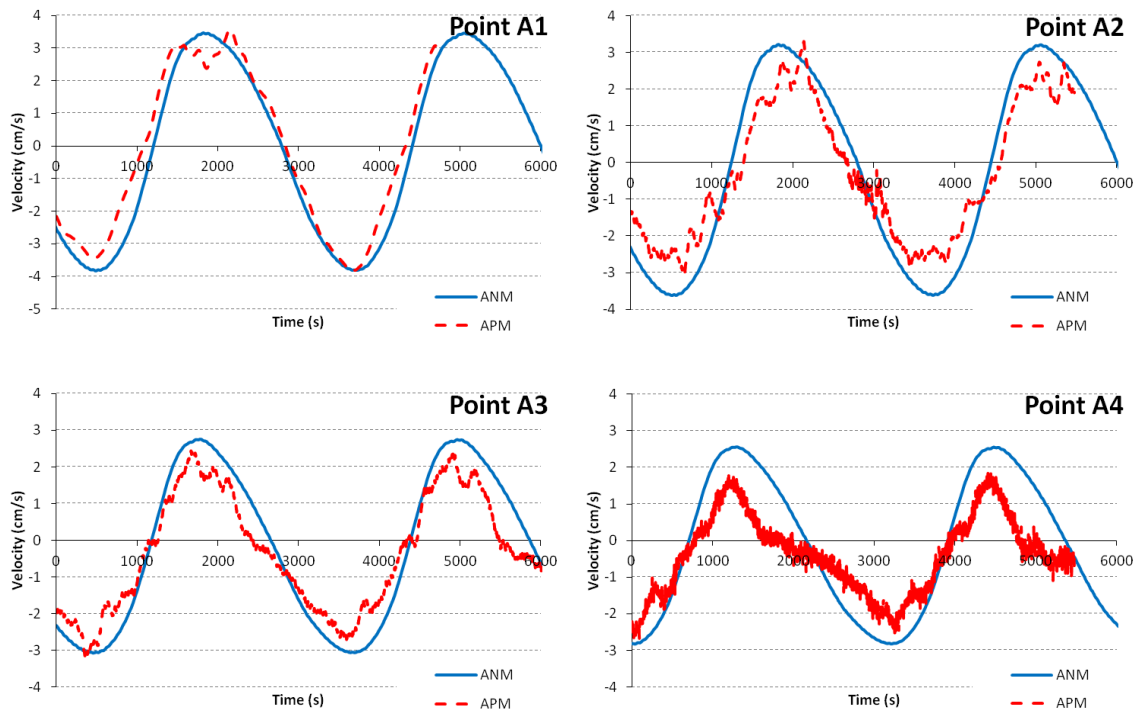
The computational domain covered a 142m x 45m area; with a grid size of 1.0m. The long-line was simulated as a distributed drag area of 30m x 3m dimensions, as denoted in

Figure 4.12(b). All cells within this region were flagged as ‘dropper cells’, with the appropriate model equations applied.

The density of droppers was computed based on APM configurations. In the APM, dropper density equalled  $1303 \text{ droppers m}^{-2}$ ; which equated to  $1.45 \text{ droppers m}^{-2}$ , at the prototype scale. Dropper diameter equalled  $0.356\text{m}$  at the prototype scale. Equivalent tidal conditions to the SNM were prescribed.

The effect of the aquaculture resistance was fine-tuned by means of the cylindrical drag coefficient. The choice of drag coefficient depends primarily on: flow conditions, dropper size and dropper density (Ghisalberti and Nepf, 2004). For this study, an initial value of 1.0 was chosen; and later fine-tuned based on laboratory data.

Velocity data were collected from the ANM and APM at the points denoted in Figure 4.12. Figure 5.5 displays velocities predicted by the ANM plotted against those observed in the physical model. With the chosen drag coefficient, the numerical model was found to overestimate flows, i.e. velocities predicted by the numerical model were greater than those observed in the tidal basin.



**Figure 5.5: Comparison of aquaculture physical model (APM) observed velocities with those predicted by the aquaculture numerical model (ANM). Drag coefficient =1.0. Figure 4.12 the location of sampling points**

These results demonstrate the effects of the user-developed modification along the length of the long-line. A significant drawback of the simple kinetic energy model developed in the previous section was the singular dependence on length of travel through the system. The mathematical model presented in this section incorporates considerably more of the parameters governing flow, namely: bathymetric data, initial effects as flow encounters impediment, turbulent structure, and areal reduction effect. The next section presents further refinement of the ANM.

### 5.2.5 Effect of drag coefficient

A preliminary analysis of ANM results presented in Figure 5.5 illustrates that the model requires further refinement. A range of modelling simulations was conducted while incrementally increasing drag coefficient. The results presented demonstrated a continuous refinement of results with the closest agreement between predicted and

measured velocities obtained with a drag coefficient of 1.8. Figure 5.6 presents a comparison of APM and ANM data with the prescribed drag coefficient.

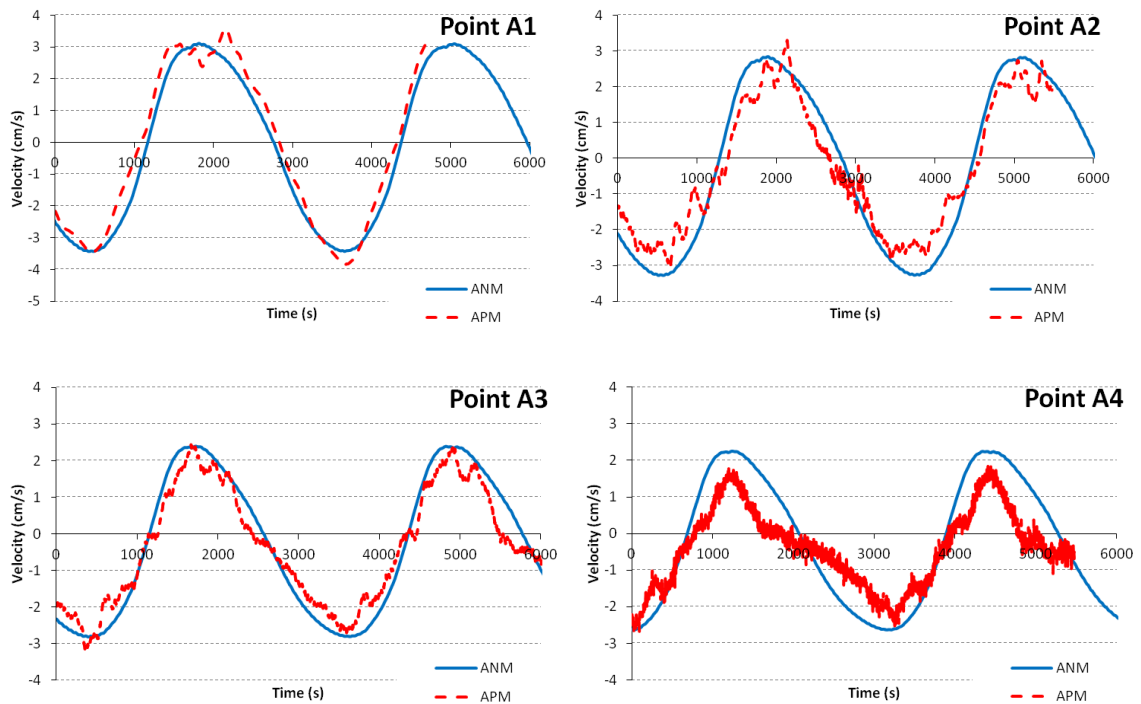


**Figure 5.6: Comparison of APM observed velocities with those predicted by the ANM. Drag coefficient =1.8. Figure 4.12 displays the location of sampling points**

These results display closest agreement with laboratory data. The model closely replicates flow attenuation observed in the APM; with both the APM and ANM displaying flow reduction of up to 30%. These findings are similar to those of Stroheimer et al., (2005) who found velocities in a commercial long-line mussel farm to be reduced by 30%, and Pilditch et al., (2001) who detected flow attenuation of 40% through suspended scallop farms. Boyd and Heasman, (1998) conducted field studies of flow within and around mussel raft culture. They observed that flows within the raft reduced by up to a factor of six depending on rope spacing and ambient flow speed.

The main consideration in the comparison of the experimental and numerical results is the choice of drag coefficient. This depends primarily on flow conditions, surface roughness and cylindrical shape factor (Souliotis and Panagiotis, 2007). In addition, the drag exerted by an array of cylinders may differ to that of a single cylinder (Blevins,

2003), and the spacing of cylinders is also significant (Zdravkovich, 2003). An increase in dropper density will result in a decrease in both flow and Reynolds number,  $Re$ , and thus, based on the relationship between drag and  $Re$ , a larger drag coefficient is required (Wu and Wang, 2004). Mazda et al., (1997) examined drag coefficients for flow through a mangrove swamp. The drag coefficient was found to increase with decreasing Reynolds number from a value of approximately 0.4 at high  $Re$  ( $>10^4$ ), to a maximum value of 10 at low value of  $Re$  ( $<10^4$ ). Wu and Wang, (2004) used laboratory flume studies of flow through model vegetation (wooden dowel with 3.2mm diameter) to verify a numerical model. A number of different vegetation densities and corresponding drag coefficients were used. The drag coefficient was set to 0.8, 1.0, 1.2, 1.8 and 3.0 for the simulations with vegetation densities of 0.04%, 0.2%, 0.6%, 2.5% and 10% respectively, to obtain acceptable agreements between the laboratory and numerical model results.

A value of 1.8 was determined for this particular research. Based on a comprehensive review of literature, this value is consistent with previous modelling efforts, particularly in the area of vegetated flow where the largest body of relevant work resides (Shimizu and Tsujimoto, (1994), Mazda et al., (1997), Nepf and Vivoni, (2000), Struve et al., (2003), Wu et al., (2005), Souliotis and Panagiotis, (2007)). Figure 5.7 presents velocities predicted by the ANM adopting a value of 1.8 plotted against SNM results.

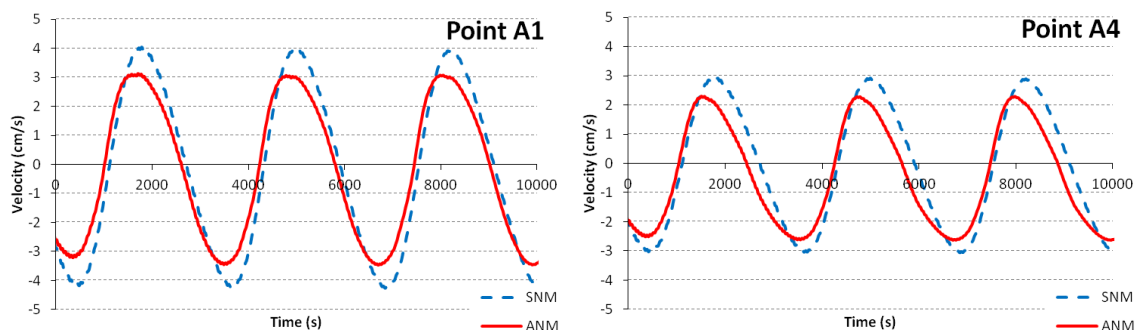


**Figure 5.7: Comparison of SNM velocities and those predicted by the ANM. ANM drag coefficient=1.8. Figure 4.12 displays the location of sampling points**

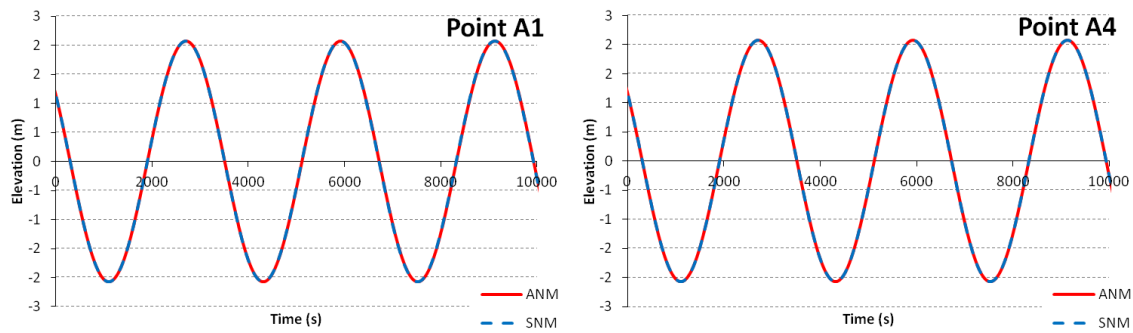


**Figure 5.8: Comparison of SNM water elevations and those predicted by the ANM. ANM drag coefficient=1.8. Figure 4.12 displays the location of sampling points**

An interesting flow feature observed in Figure 5.7 is an apparent phase shift observed in ANM predicted velocities relative to the SNM. This flow feature is not observed in Figure 5.8, with both the SNM and ANM predicting identical water elevation profiles. The temporal discrepancy seems to be a result of the aquaculture installations impeding the flows of water inducing a ‘build-up’ of flow behind the installation that affects the time-trace profile.

This mathematically derived, experimentally validated, numerical representation of flows through aquaculture installations will be used for subsequent modelling studies in this chapter.

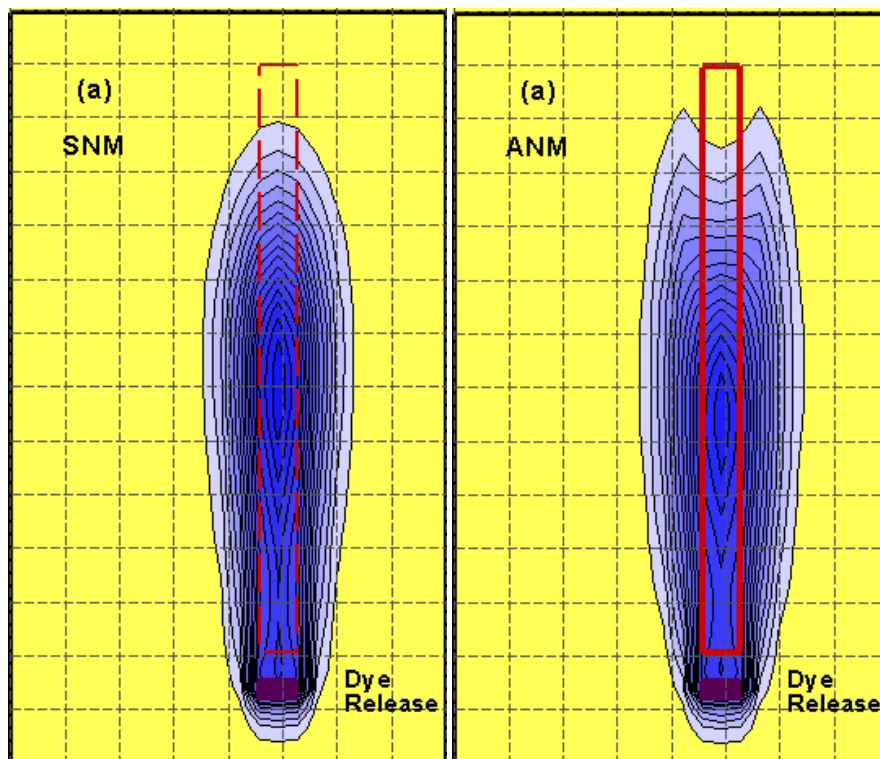
### 5.2.6 Solute transport

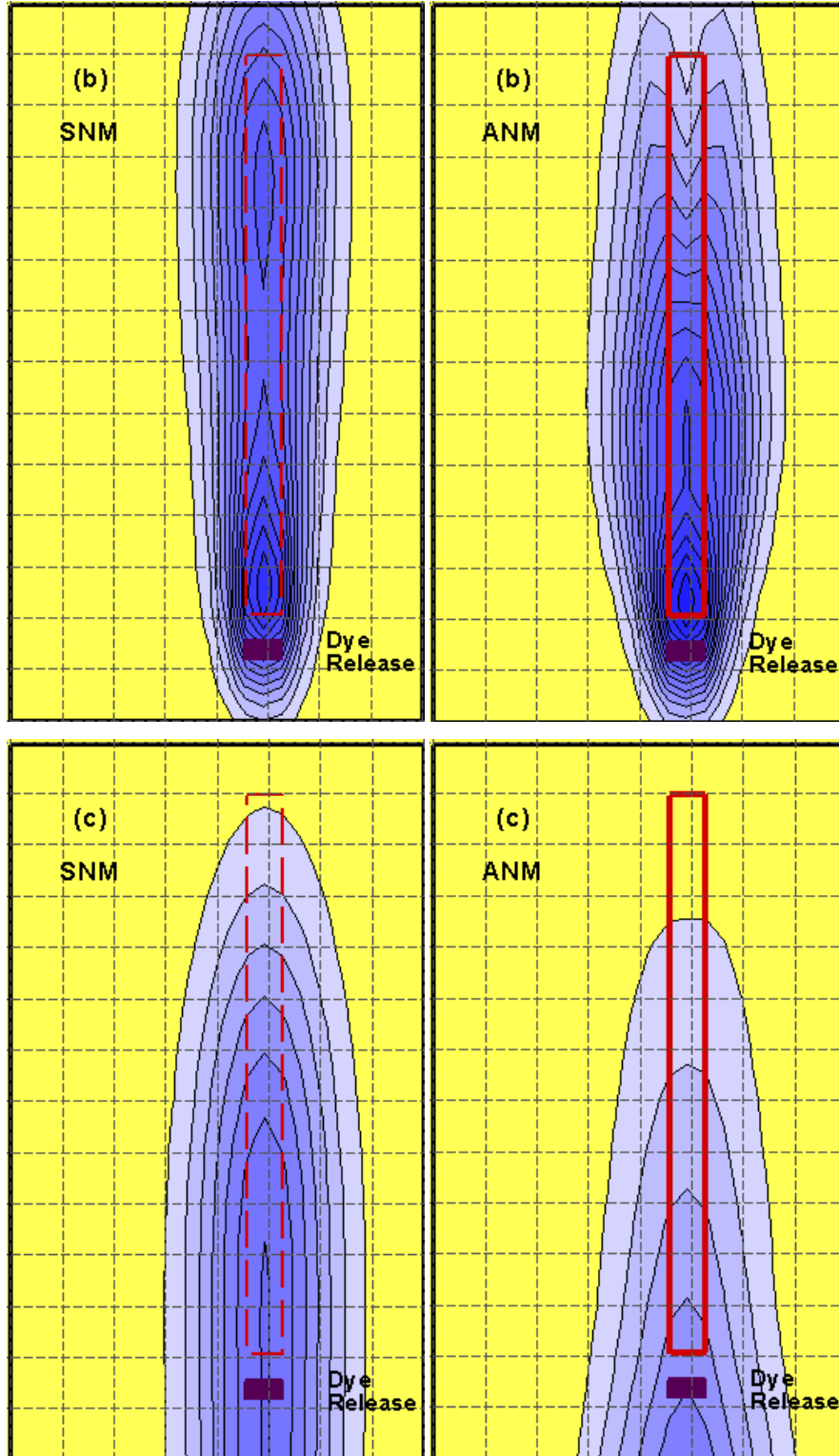
Numerical dye dispersion studies were conducted in conjunction with the laboratory tracer experiments. The numerical dye tracer experiments allow an assessment of the performance of the model in replicating dispersive and turbulent processes. The turbulent viscosity strongly influences the dispersion of a contaminant within a waterbody (Babarutsi and Nassiri, 1996); hence, tracer experiments provide a means of evaluating the ability of a model to simulate complex flow processes, in conjunction with friction dominated hydrodynamics.

For these simulations, the mixing-length turbulence closure model calculated the turbulent viscosity of the flow profile. A value of 1.0 was specified for the coefficient of eddy viscosity in all cases. No modification of the turbulence closure model was

undertaken, with the singular difference between the SNM and ANM being hydrodynamics.

An equivalent modelling procedure to that used in the physical modelling study was used to assess material transport within the long-line. A conservative tracer was introduced into the study area 2m upstream of the location of the aquaculture system at the low water mark (Figure 5.9). Simulations continued for a full tidal cycle with numerical data being output at 20-second intervals. Predicted transport in the absence of any physical impediment to flow was computed to compare against laboratory data, and provide a benchmark for further numerical tracer experiments. The ANM then assessed material transport within a long-line installation. Figure 5.9 presents numerically predicted dye transport at four different stages of the tidal cycle; the transport predicted by both the SNM and ANM is presented side-by-side for comparison. The red rectangle highlights the location of the aquaculture farm, with the location of dye release presented in purple. Within the SNM, the dashed red rectangle represents the location of the aquaculture farm, to enable easy comparison with the ANM data.





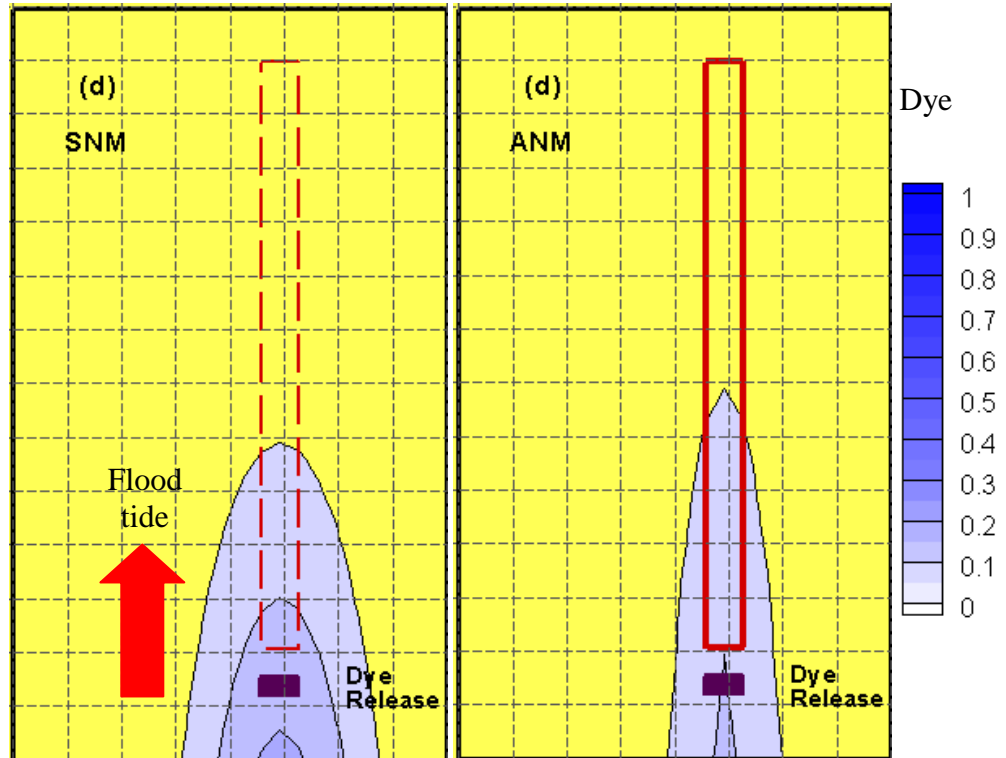


**Figure 5.9: Numerically predicted dye transport at four stages of the tidal cycle; (a) mid-flood, (b) high water mark, (c) mid-ebb and (d) low water mark. The LHS presents dye transport predicted by the SNM while the right hand side presents transport predicted by ANM. The location of the aquaculture installation is denoted by the red rectangle while the purple rectangle denotes the area of dye release.**

Analysing Figure 5.9 demonstrates that the aquaculture structure impacts on material transport in a number of ways. On the flood tide, longitudinal dye transport is reduced significantly and a slight increase in lateral spreading around the system is evident. The numerical model predicts that the longitudinal transport distance is reduced by up to 30% by the presence of the structures. These results are similar to dye studies conducted in the APM.

On the ebb tide, the concentration of material remaining in the system at the end of the tidal cycle is less in the ANM than the SNM. This is similar to results observed in the physical modelling study, and may be largely attributed to the shorter transport distance the material undergoes.

The findings of both the scale and numerical tracer experiments are very significant from a carrying capacity perspective. The reduction in material transport to the downstream extents of the system has obvious repercussions for the supply of nutrients to the bivalve feeders. In both the SPM and SNM, dye is transported to the downstream extents of the system with dye saturation evident throughout the system. On the other hand, the inclusion of the aquaculture installation in both physical and numerical modelling studies significantly impedes the transport of tracer. In fact, in both situations the concentration of dye at the downstream extents is negligible. Instead, we see an accumulation of dye at the entrance of the system and some lateral diversion of solute caused by the presence of the structures. This study demonstrates that the presence of an aquaculture farm limits nutrient supply to downstream bivalves. When one considers the effect of sequentially located farms, and intense particle consumption by suspension feeding, it is evident that ignoring these effects severely limits the viability of any analysis.

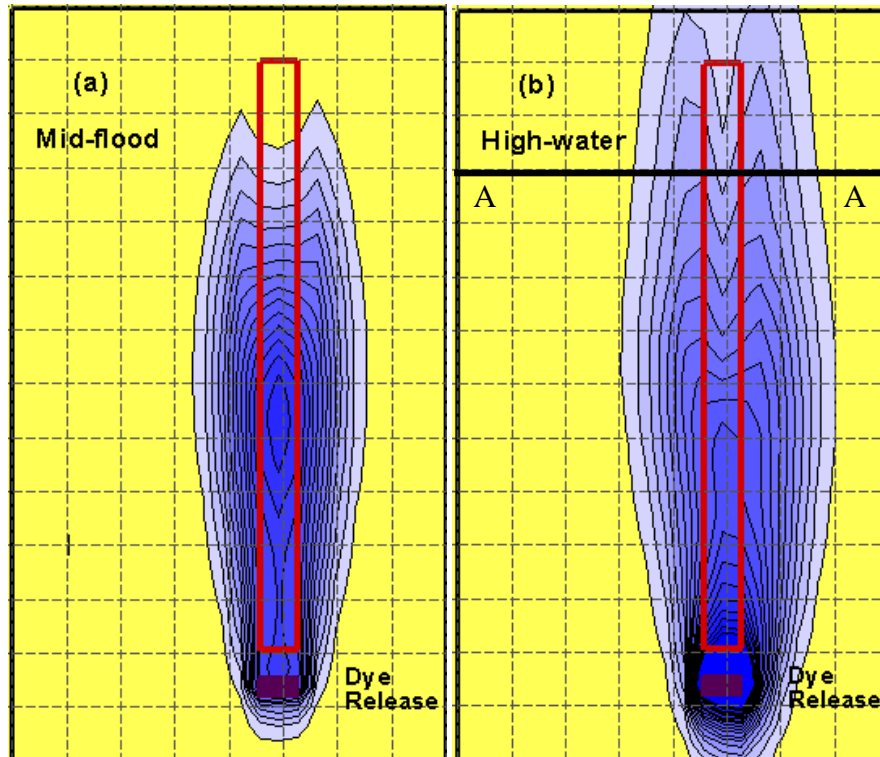
As discussed, the Reynolds Averaged Navier-Stokes equations represent random fluctuations of flow via a particular turbulence closure model of varying degrees of complexity and accuracy. This study adopted the relatively simple one-equation mixing length model. The next section examines the performance of a more complex, two-equation turbulence model in simulating flows.

### **5.3 Assessment of standard k- $\epsilon$ model**

The performance of a number of different turbulence closure models with different levels of complexity was assessed from the perspective of more accurately replicating laboratory data. Numerically predicted velocities and solute transport snapshots were output in an equivalent manner to that in the previous section, i.e. velocity datasets were output at the locations detailed in Figure 4.12, and conservative tracer transport snapshots were output at different stages of the tidal cycle.

In this section, the performance of the k- $\epsilon$  turbulence closure model was assessed. Of primary concern was the model's ability to accurately simulate tracer transport within the system. The additional complexity and accuracy of the k- $\epsilon$  turbulence closure model

comes at the cost of increased computational demands. This section assess whether the increased cost (1) provides increased accuracy and (2) is necessary to simulate flows through the aquaculture installation. Due to the additional complexity involved in simulating flows through an aquaculture installation, the focus will primarily be on the ANM. Figure 5.10 presents numerically predicted dye transport at four different stages of the tidal cycle with the  $k-\epsilon$  turbulence closure model used.



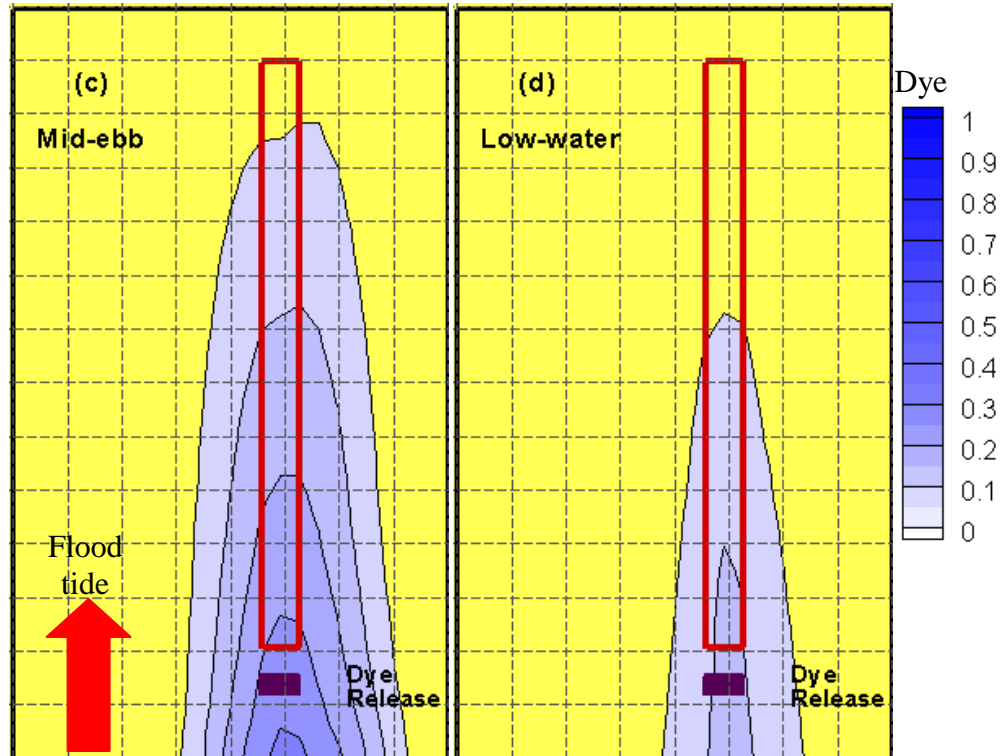


**Figure 5.10:** ANM predicted dye transport incorporating the  $k-\epsilon$  turbulence closure model at four stages of the tidal cycle: (a) mid-flood, (b) high water mark, (c) mid-ebb and (d) low water mark.

Both the two-equation and one-equation turbulence model predict quite similar dye transport plumes. However, the two-equation turbulence model predicts reduced longitudinal dye transport within the system. A cross-section of material concentration across line A-A at high water (Figure 5.10(c)) demonstrated this discrepancy. Simulations incorporating the  $k-\epsilon$  model predicted a 6% drop in concentration relative to values computed by the mixing length model.

Figure 5.11 presents time-trace velocities predicted by the ANM incorporating the mixing length model plotted against those predicted by the  $k-\epsilon$  model. Results display a slight disparity in predicted flows. The peak magnitudes of velocities are identical in both cases; however, the temporal profile of velocities is slightly different. These results demonstrate that the choice of turbulence closure model influences both hydrodynamics and solute transport. The next section examines a mathematical amendment to the  $k-\epsilon$

closure model to incorporate the effects of the aquaculture structures into the turbulence model.

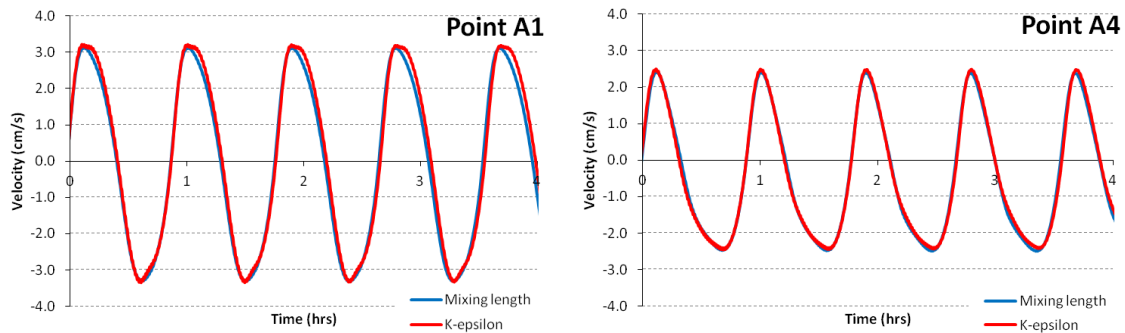


**Figure 5.11: Comparison of velocities predicted by ANM with the mixing length model and the k-epsilon model. Figure 4.12 presents the location of sampling points**

#### 5.4 Assessment of modified $k-\varepsilon$ model

A mathematical extension to the standard  $k-\varepsilon$  turbulence model was undertaken to investigate whether the widely studied, additional turbulence induced by a submerged bluff body impediment (Nepf, 1999), can be reproduced in the ANM. An additional turbulence production term was incorporated into the model equations based on the work of Shimizu and Tsujimoto, (1994), Lopez and Garcia, (2001) and Neary, (2003). The mathematical derivation and formulation was previously discussed in Chapter 3, and will not be presented here. As before, the effects of the amended equations on actual dynamics were investigated via detailed solute transport studies and to a lesser degree velocities. For a more consistent comparison, results were compared with values predicted by the standard  $k-\varepsilon$  scheme. Figure 5.12 presents tracer transport predicted by the ANM incorporating the extended  $k-\varepsilon$  closure model. As before, dye was released 2m upstream of the installation at the low water mark and transport evaluated at four different stages of the tidal cycle.

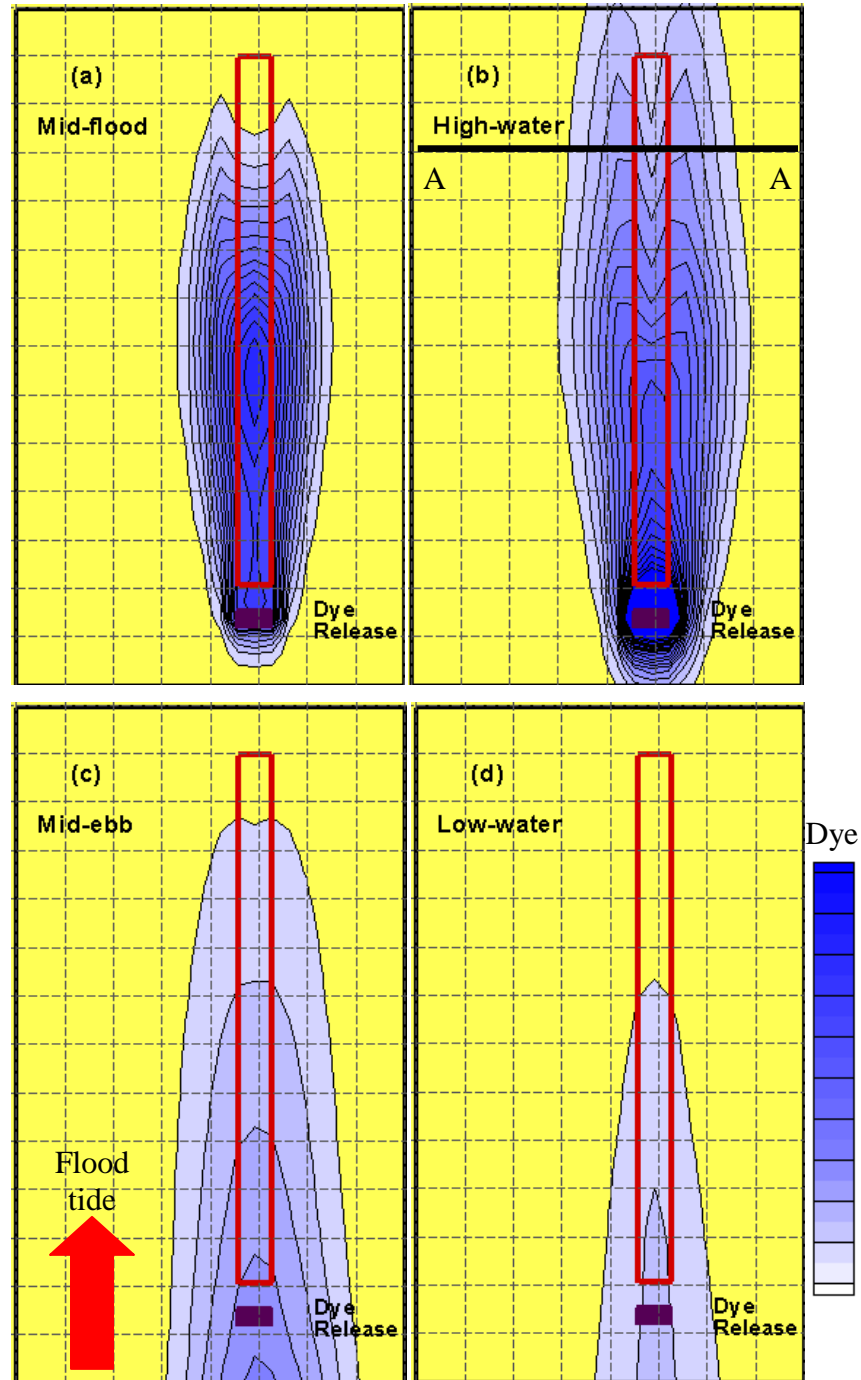


Figure 5.12: ANM predicted dye transport incorporating the user-modified  $k-\epsilon$  turbulence closure model at four stages of the tidal cycle: (a) mid-flood, (b) high water mark, (c) mid-ebb and (d) low water mark.

No significant change to the transport of dye results from the additional turbulence production term included in the numerical model. A comparison of Figure 5.10 and Figure 5.12 displays almost identical dye plume profile with no visible disparities. A traverse section across the farm at line A-A, exhibits a change in concentration of less than 1% between both simulations.

As discussed in Chapter 3, a large number of different turbulence closure models exist in computational hydrodynamics, differing in both levels of complexity and computational cost. The identification of the most efficient turbulence closure scheme to simulate a particular flow regime is a logical research question. In this case, the mixing length model performs satisfactorily in simulating flows and material transport. The material transport predicted by both closure models is quite similar with no significant improvement in model performance observed.

A point of interest however, is the greater transportability of the  $k$ - $\epsilon$  model to different modelling scenarios. The performance of the mixing length model is dependent on the prescribed value of the coefficient of eddy viscosity. For this study a value of 1.0 was prescribed based on flume studies conducted by Westwater, (2001), but the value can range from 0.1 – 1.0 (Arega and Sanders, 2004). Values are smaller for open channels and attributed to little secondary motions (Olbert, 2006). The  $k$ - $\epsilon$  model, on the other hand, typically does not require user-specified coefficients; with modelling constants instead prescribed based on empirical data. Hence, the  $k$ - $\epsilon$  closure model often performs better when extrapolating from laboratory studies to the bay scale level.

The extended turbulence model does not appear to affect results significantly, with little visible effect on material transport. A possible reason for this is the inability of a depth-averaged model to simulate elements of the three dimensional flow profiles. A similar phenomenon was observed by Katul et al., (2004), who observed no discernible difference in the performance of a one-dimensional hydrodynamic model when either a one or two-equation turbulence closure model was used. Hence, it is important to balance the complexity of the turbulence closure model with the complexity of the numerical model itself. The further extension and improvement of the modelling of turbulence will

be investigated in a subsequent chapter through more comprehensive three-dimensional modelling studies. In the next section, the validated model is applied to a proposed aquaculture development site on the West Coast of Ireland, and the far-field performance of the model investigated.

### **5.5 Case study: Casheen Bay**

Casheen Bay is a small sheltered bay on the West Coast of Ireland as shown in Figure 5.13. It was one of the first bays in Ireland designated for fish farming due to its sheltered position and open entrance, which was assumed to provide an ideal site for good tidal exchange. Currently, finfish and longline rope mussels are cultured in the bay. The refined hydrodynamic model was used to analyse the effect of the aquaculture structures at the bay scale level.



**Figure 5.13: Approximate location of Casheen Bay on the West Coast of Ireland**

#### **5.5.1 General circulation model**

A hydrodynamic model was developed by overlying a finite difference mesh on Admiralty Chart data with Cartesian grid spacing of 40m x 40m. Figure 5.14 presents a bathymetric map of the bay. Tidal conditions were specified at the western open sea boundary. All simulations were conducted under spring tide forcing of 2.2m amplitude.

Northern and southern open boundaries were assumed as streamlines and hence, all orthogonal velocities equalled zero. The tide is the main force generating currents (Gleeson, 1994), and there is no significant river inflows in Casheen Bay.

DIVAST has previously been applied to Casheen Bay on a number of occasions, primarily, Hartnett and Cawley, (1991), Gleeson, (1994), Hartnett et al., (2003) and Dabrowski, (2005). In these studies, measured data validated model hydrodynamics. Computed values of surface elevation, current speed and current direction were calibrated based on observed data. These studies validated the performance of DIVAST in replicating flows within Casheen Bay. Since model settings are principally the same as in these previous studies, and the prediction of actual bay dynamics is not of primary concern; details of the calibration process are not presented here. For further details the reader is referred to Hartnett and Cawley, (1991), Gleeson, (1994), Hartnett et al., (2003) and Dabrowski, (2005).

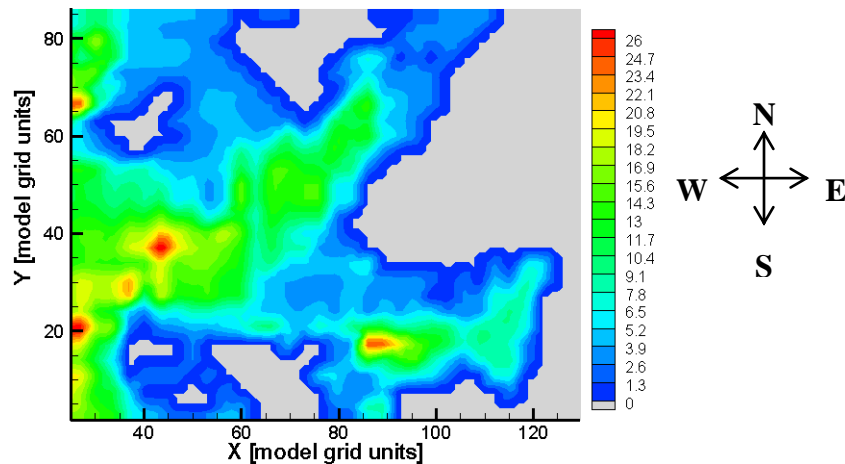
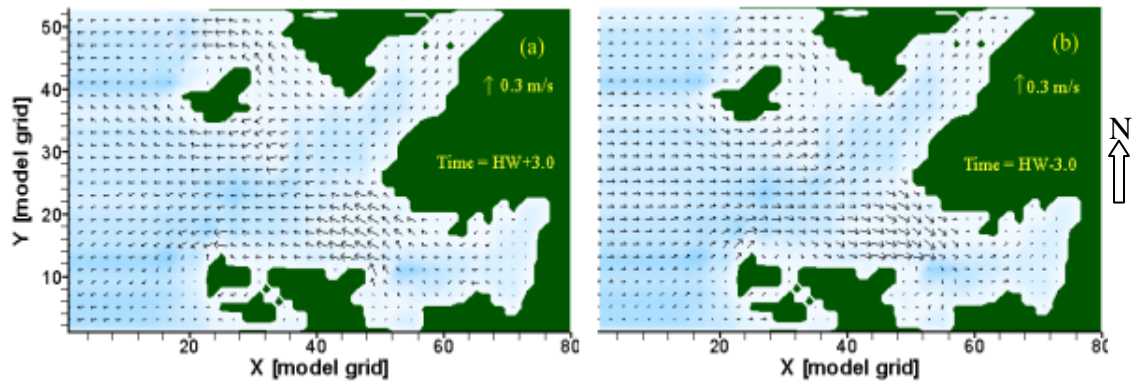


**Figure 5.14: Bathymetry map of Casheen Bay. Tidal boundary conditions were specified on the western open boundary with zero flow assumed at the northern and southern boundary**

A tidal period of 12.5hrs was specified and the model was run with a timestep of eight seconds. Table 5-3 presents a complete list of variables used for this modelling study. Figure 5.15 presents a synoptic view of flows and water circulation at different stages of the tidal cycle. Maximum tidal currents within the bay are in the region of 0.3m/s.

**Table 5-3: Variables used for Casheen Bay modelling study**

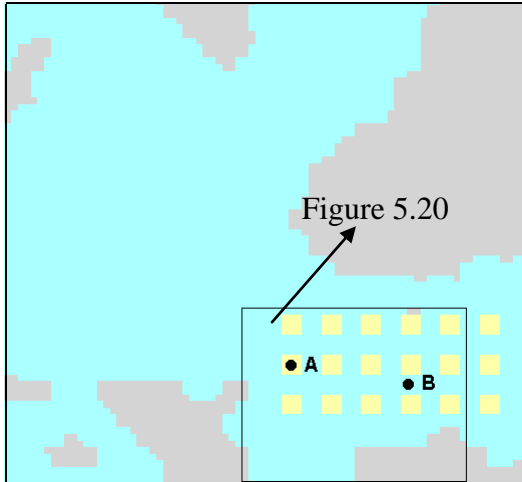
Variable	Definition	Value	Reference
I	Cells in I direction	130	-
J	Cells in J direction	86	-
$\Delta t$	Time-step [s]	12	Courant Number
$\Delta x$	Cartesian grid spacing [m]	40.0	-
$C_b$	Roughness length [m]	0.04	Literature
$C_e$	Coefficient of eddy viscosity	1.0	Literature



**Figure 5.15: Hydrodynamic snapshots of (a) mid ebb and (b) mid flood**

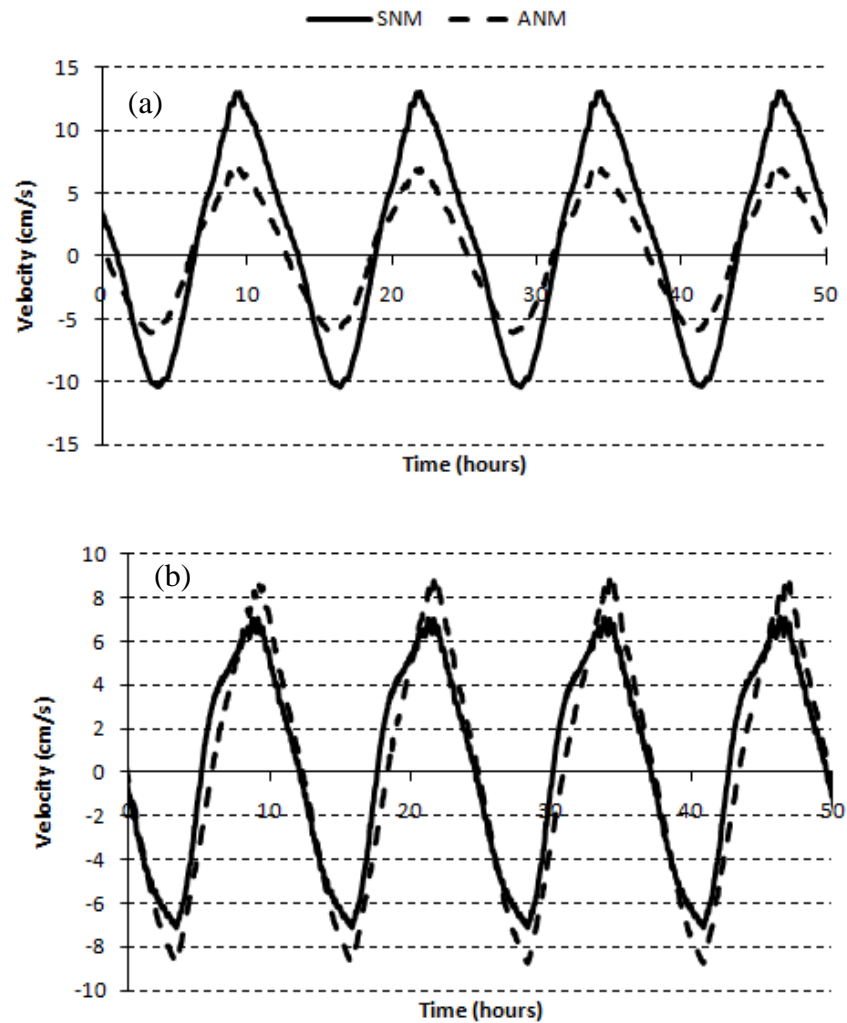
### 5.5.2 Modelling of aquaculture installations

Anecdotal evidence and preliminary hydrodynamic analysis suggested the southern embayment to be the most promising region of the bay for aquaculture developments; due to good tidal exchange and higher flow speeds. A distribution of individual farms was deployed within this embayment based on typical farm dimensions and configurations (BIM, 2002). Figure 5.16 displays the location of the modelled mussel dropper farms. Individual farms consisted of 120m long double longlines spaced 12m apart. The deployment resulted in a dropper density of  $0.33 \text{ droppers m}^{-2}$ , within the farmed regions. Twenty-one farms were installed in the bay; farms were placed 120m apart.



**Figure 5.16: Location of modelled aquaculture structures within bay (displayed in yellow), and time series locations A and B. Highlighted area denotes scale up view presented in Figure 5.20**

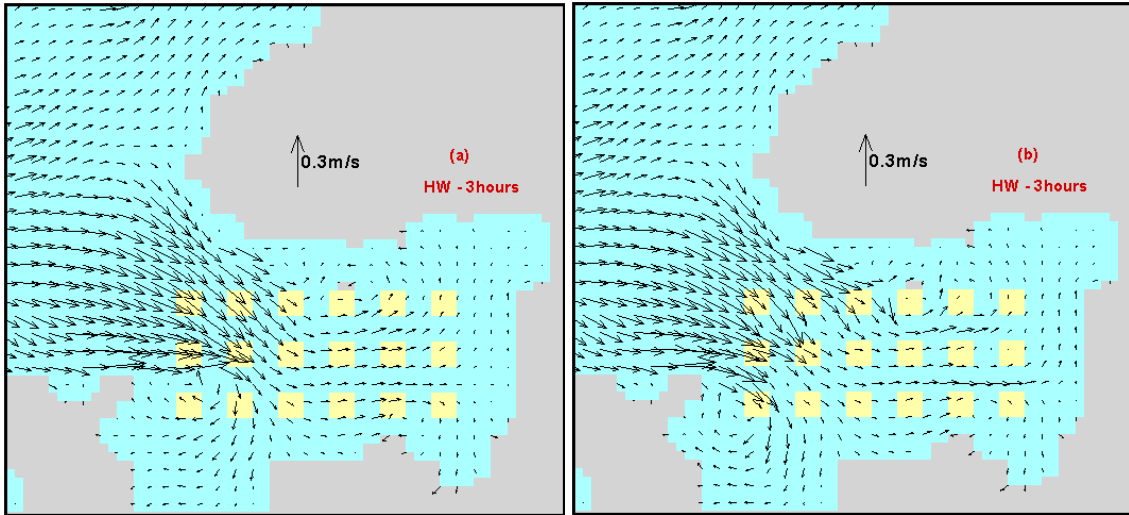
The effect of the structures on both flow fields and local hydrodynamics were analysed both spatially and temporally. Velocity time traces were plotted for the locations A and B displayed in Figure 5.16 contrasting flow within droppers (A) to flow occurring between droppers (B). A significant retardation of flow was evident within the dropper lines (Figure 5.17(a)). Interestingly, an acceleration of flows was observed between longlines, indicating that some flow was being diverted around the farms (Figure 5.17 (b)). These flow behaviours were investigated further via a synoptic bay-scale assessment of flow fields.



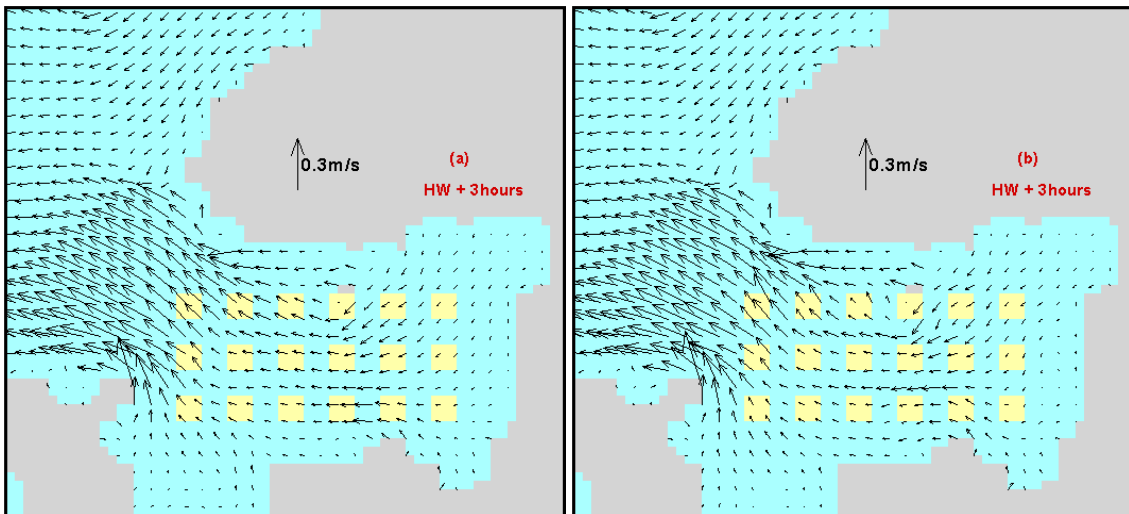
**Figure 5.17: Numerically predicted velocity time series predicted by the SNM and the ANM at, (a) location A within long-lines and, (b) location B between farms**

Figure 5.18 and Figure 5.19 presents predicted circulation patterns at mid-flood and mid-ebb. The inclusion of the droppers within the bay affects both the magnitude and direction of flow. A large-scale diminishing of flow speeds is evident throughout the aquaculture domain. This is most apparent within the first row of farms on the western side of the embayment. A significant dissipation of energy is evident after flows pass through this first row. In addition, a large-scale diversion of flows is evident at the entrance to the aquaculture farms. This is particularly evident at the southern point of the entrance, where a significant volume of flow is diverted around the system. A similar,

less pronounced diversion is apparent at the northern point of the entrance. A comparable flow feature has been reported in literature (Plew et al., 2005), where the most significant attenuation of flows occurs at the entrance to—or just before—the aquaculture structures. At a smaller scale, a change of direction is evident around individual farms. Figure 5.20 presents an expanded view of flow fields, while Figure 5.21 superimposes both velocity datasets to enable a comprehensive visual assessment.



**Figure 5.18: Hydrodynamic snapshots at mid flood (a) SNM (b) ANM**



**Figure 5.19: Hydrodynamic snapshots at mid ebb (a) SNM (b) ANM**

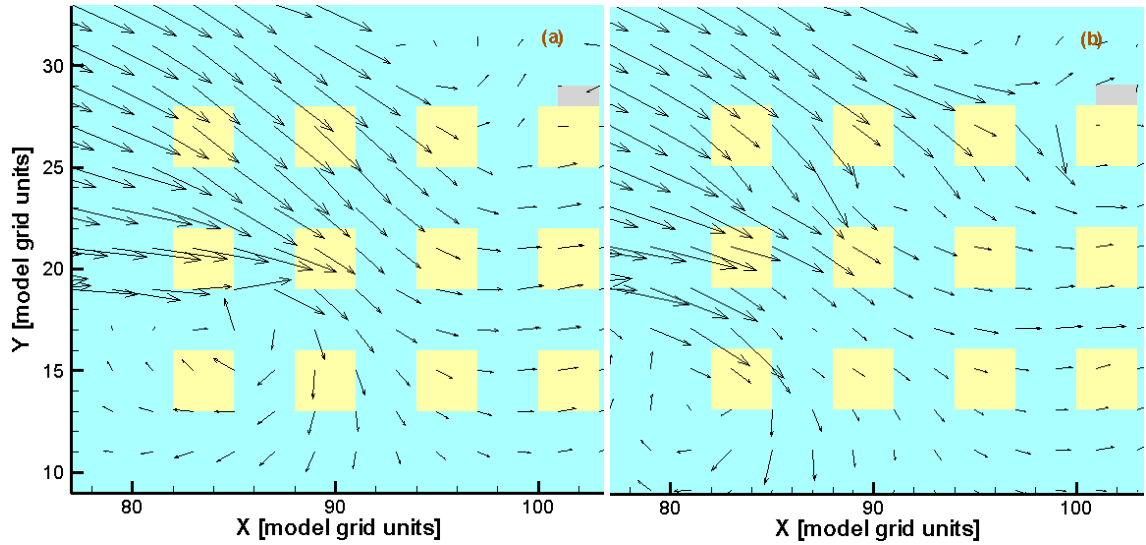


Figure 5.20: Exploded view of model predicted flow fields on flood tide (a) SNM and (b) ANM

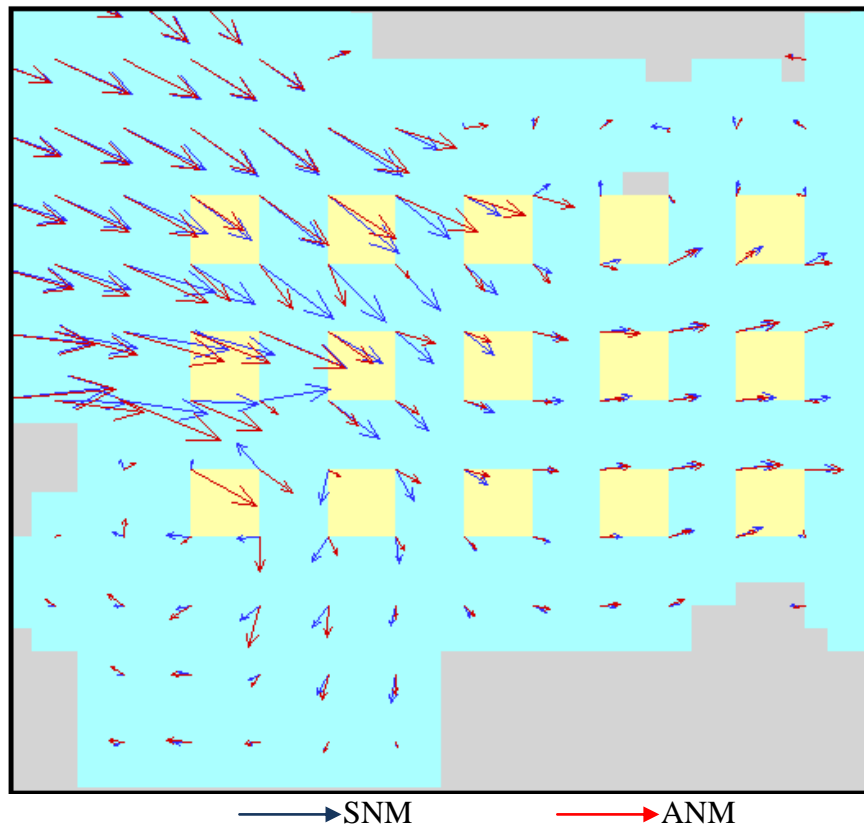


Figure 5.21: Hydrodynamic snapshots of velocities at mid-flood displaying effect of aquaculture structures.

This study produces results which corroborate the findings of a great deal of the previous work in this field which showed that aquaculture installations affected flow

patterns by retarding velocities and diverting flows around the farm (Boyd and Heasman, (1998); Plew et al., (2005)). To comprehensively assess the effects of the structures a quantifiable analysis of both flow differentials and material transport is required.

Analysis of the water circulation patterns within both the bay and the modified “aquaculture” cells proved somewhat problematic. It is apparent that the hydrodynamics in any bay vary both in space and in time. This is typically represented via a visual comparison of flow fields or a study of time series data at a specific location. Figure 5.18 presents flow field data on the flood tide. It compares ANM and SNM predicted flow fields within Casheen Bay. However, it is difficult to produce a satisfactory comparison, and in particular, a quantifiable depiction of the effects of the modified cells on water circulation based on flow fields alone; while an analysis of time series data at specific locations for an entire bay is both cumbersome and difficult to interpret. Hence, a quantitative approach to flow field patterns and velocity differentials was undertaken.

The SNM was assumed the “benchmark” model for evaluation of changes induced by the aquaculture installations. Values of computed velocity were output at each grid point in the model domain at a particular instance in time. These datasets allowed the analysis of the spatial variation of model variables, and were therefore used to calculate the spatial variation of differentials between computed velocities. This provided a representation of the effects that the modelled structures had on flows at a bay scale level. Velocity differentials were produced both at different stages of the tidal cycle, and as a *tidally-averaged* value.

Velocity data were output for all grid points of the model domain at various stages of the tidal cycle. The absolute differential, AD, and the relative differential, RE, between the respective model outputs at the same instance was then calculated according to Nash, (2010) as follows:

$$AD_{i,j}^t = |\Phi_{i,j}^t - \phi_{i,j}^t| \quad (5.8)$$

$$RD_{i,j}^t = \frac{|\Phi_{i,j}^t - \phi_{i,j}^t|}{|\Phi_{i,j}^t|} \times 100 \quad (5.9)$$

for  $i=1,2,3\dots i_{max}$ ;  $j=1,2,3\dots j_{max}$

where  $\Phi$  is the model variable computed by SNM and  $\phi$  is the model variable computed by ANM.

Figure 5.22 displays a flow field representation of the tidally averaged velocity differential caused by the presence of the aquaculture structures; while Figure 5.23 presents relative differentials. This data indicates that flow within the bay is altered by 20-60% by the presence of the droppers, with some areas displaying even greater effects.

This above algorithm provides a means of quantitatively assessing the effects of the droppers on flow magnitude over an extended period of time. This enables a ready analysis of actual bay dynamics represented via a singular plot. This can be quite useful in the preliminary planning stages of an aquaculture farm where specific areas within the bay can be pinpointed to establish where the aquaculture development has the most significant effects.

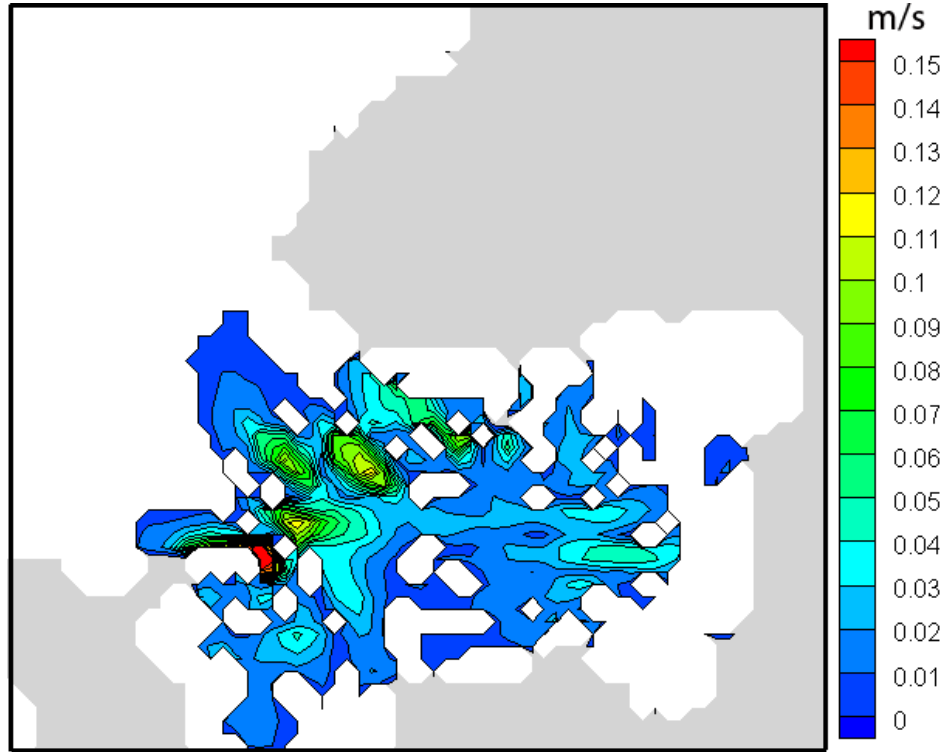


Figure 5.22: Absolute value differentials of velocity at mid-flood

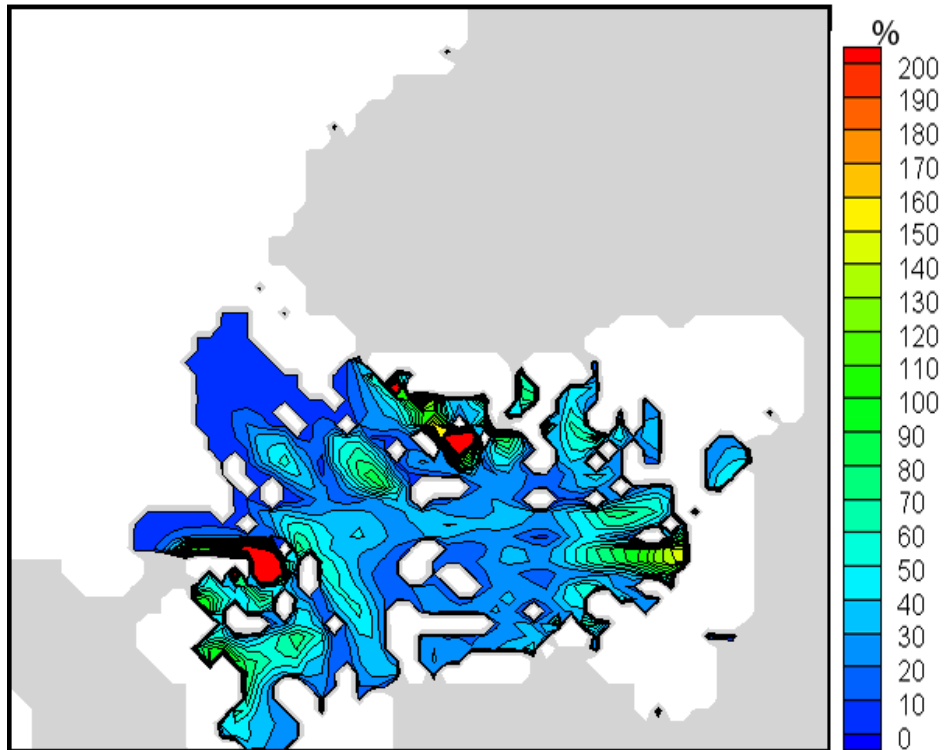
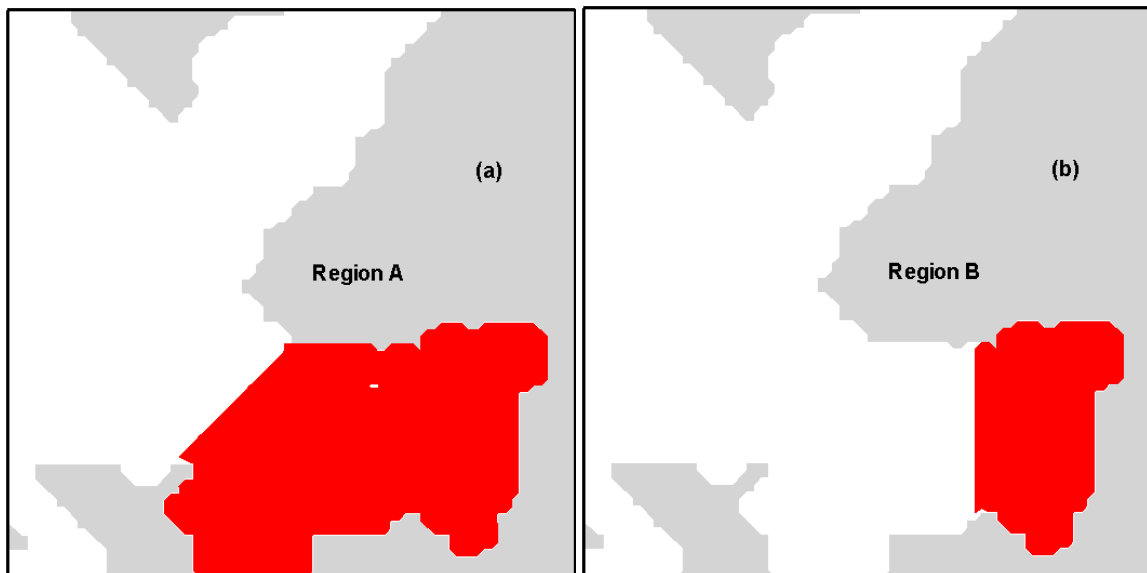


Figure 5.23: Relative differential of velocity at mid-flood

### 5.5.3 Flushing studies

The effect of the aquaculture structures on material transport was also studied. Flushing studies of the bay were carried out and the effect that the installation of the mussel droppers had on time scales of material transport was analysed. Two regions of the bay believed to have different flushing properties were chosen in order to compare relative flushing capacities of these different regions. Each region was considered separately. The chosen domains are denoted as region A and B in Figure 5.24. Region B represents a relatively deep section of the bay and the bathymetry suggests that it may behave as a stagnant backwater. Region A includes region B, to investigate potential differences in flushing between the backwater and the more open, main channel.

The solute transport module was utilized in the calculation of two characteristics, namely, the average residence time and the exchange per tidal cycle coefficient.



**Figure 5.24: Casheen Bay flushing study sub-regions**

To determine the flushing characteristics of the bay the hydrodynamic model was initially run until steady state conditions were reached (c.75.0 hrs). All node points within the specified regions were then specified as having uniform initial concentrations of trace,  $C_0$  with subsequent average spatial concentrations,  $C_n$  computed after  $n$  tidal cycles. The model was then run for a period of 300 hrs with output produced every 12.5 hrs in

order to account for the net tidally averaged dye outflow from the region. Since the primary objective is the assessment of transport differentials rather than any specific bay dynamics all simulations were driven by spring tide forcing only with no meteorological data specified. The effect of the modification of the hydrodynamic and turbulent equations on flushing was analysed. The hydrodynamic equations were amended as detailed previously. Three different turbulence closure models were also analysed, namely: a mixing length model, standard  $k-\varepsilon$  model, and an amended  $k-\varepsilon$  model. An overview of the different scenarios considered is given in Table 5-4, detailing the level of modification of the governing equations.

**Table 5-4: Summary of hydrodynamic model detailing turbulence scheme and level of user modification**

Model Name	Acronym	Details
<b>Original mixing length</b>	OMM	No modification of governing equations (original mixing length turbulence closure model used)
<b>Modified mixing length</b>	MMM	Hydrodynamic equations modified
<b>Original <math>k - \varepsilon</math></b>	OKM	No modification of governing equations ( $k - \varepsilon$ turbulence closure scheme used)
<b>Modified Hydrodynamic model</b>	MHKM	Hydrodynamic equations only modified with standard $k - \varepsilon$ turbulence closure scheme
<b>Modified <math>k - \varepsilon</math></b>	MKM	Both $k - \varepsilon$ turbulence scheme + hydrodynamic governing equations modified

Table 5-5 summarizes flushing characteristics computed based on the model. The remnant function parameters A and B were found using the least square method, from which the average residence times,  $\tau_r$ , were calculated

**Table 5-5: Flushing characteristics of Casheen Bay sub-regions**

		Model Acronym				
		OMM	MMM	OKM	MHKM	MKM
		Average Residence Times $-\tau_r$				
<b>Region A</b>	<b>A</b>	0.149	0.150	0.155	0.156	0.156
	<b>B</b>	0.787	0.701	0.779	0.694	0.694
	<b><math>\tau_r</math> days</b>	<b>6.68</b>	<b>9.92</b>	<b>6.62</b>	<b>9.67</b>	<b>9.68</b>
	<b>Exchange per tidal cycle coefficient -E</b>					
	<b>E</b>	0.074	0.058	0.075	0.059	0.059
		Average Residence Times $-\tau_r$				
<b>Region B</b>	<b>A</b>	0.132	0.153	0.131	0.164	0.164
	<b>B</b>	0.879	0.776	0.882	0.760	0.760
	<b><math>\tau_r</math> days</b>	<b>5.54</b>	<b>6.79</b>	<b>5.56</b>	<b>6.63</b>	<b>6.63</b>
	<b>Exchange per tidal cycle coefficient -E</b>					
	<b>E</b>	0.084	0.071	0.084	0.072	0.072

Decay curves of the average dye concentration in region A predicted by both the OKM and MKM simulations are presented in Figure 5.26; the computed remnant function corresponding to the OKM decay curve is also presented. Figure 5.25, in turn, shows spatial distribution of the average residence time obtained for the same model simulations, determined by the concentration drop below 1/e of the original concentration (van de Kreeke, 1983), for both regions A and B.

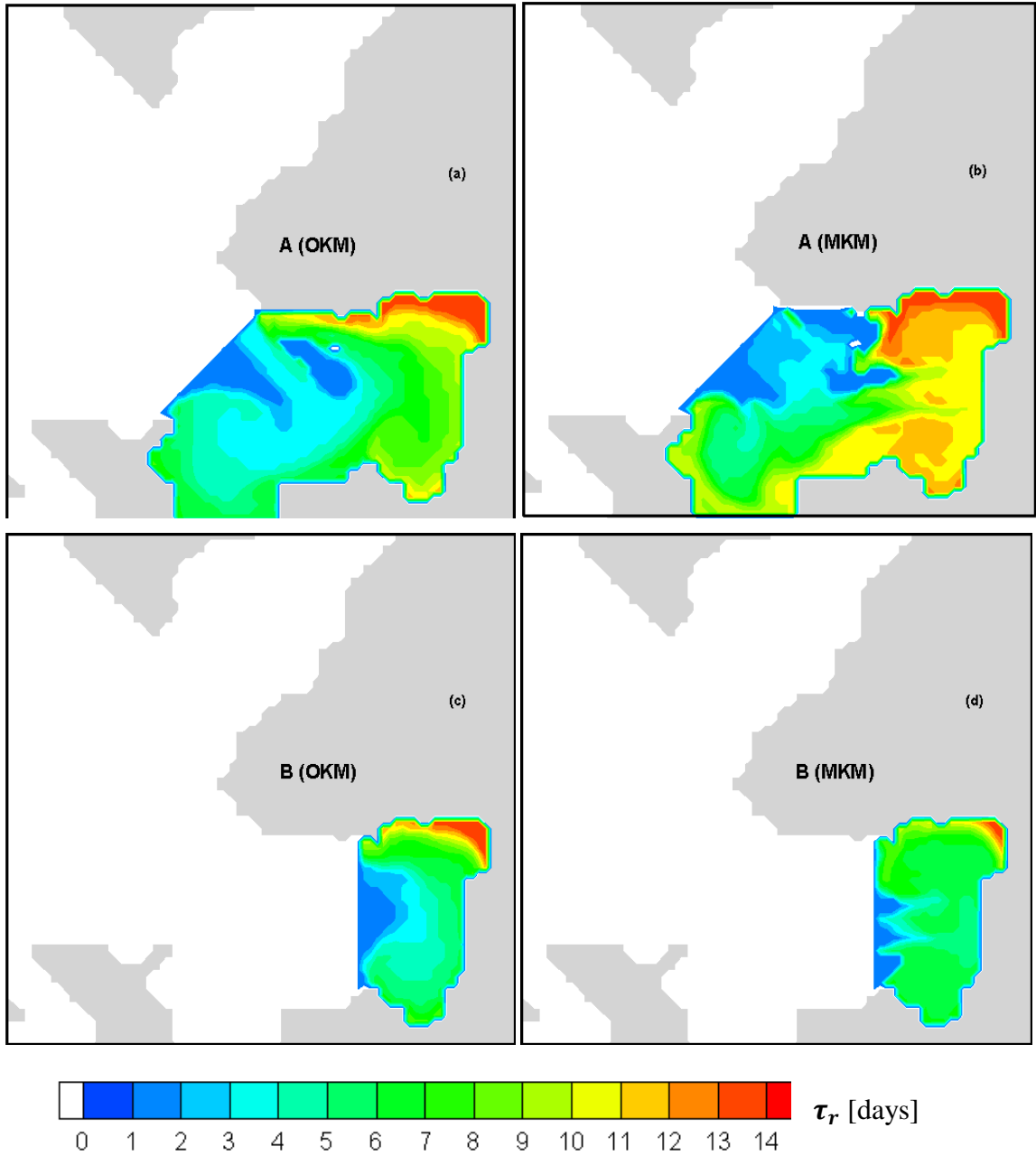
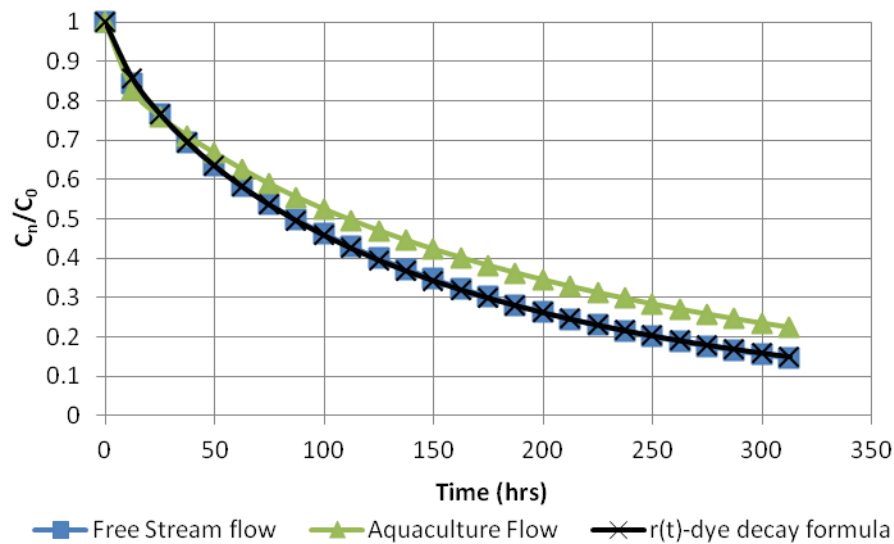


Figure 5.25: Spatial distributions of the residence time in Casheen Bay sub-regions obtained from dye studies base on DIVAST. Simulations were performed at spring tide conditions.



**Figure 5.26: Decay curves of the average dye concentration in Region A of Casheen Bay obtained from simulations based on DIVAST.**

These results demonstrate that the presence of the numerically represented aquaculture installations influence the flushing properties of the bay quite significantly. In region A, the average residence time is increased by 46%. This would have a major effect on aquaculture development capacity from both a nutrient renewal and toxin removal perspective. As one would expect the structures have a corresponding effect on the exchange per tidal cycle coefficient of the bay.

## 5.6 Discussion and conclusions

The frictional effect of suspended canopies on hydrodynamics and material transport is a much neglected area of research in aquaculture development (Grant and Bacher, 2001). Panchang et al., (1997) investigated hydrodynamics and waste transport within salmonid net-pen aquaculture developments. However, the study ignored the effects of the aquaculture installations themselves, apart from a source/sink term in the context of dispersion of food and faeces from salmon cages. Most numerical modelling studies focus on a budgeting of particulate depletion and renewal ignoring the frictional effects of the suspension feeders (Raillard and Menesguen, 1994); Pilditch et al., 2001).

In this chapter, a depth-averaged hydrodynamic model was amended to simulate the effects of these aquaculture installations on flow dynamics and material transport. A mathematically correct, Froude scaled model of a prototypical mussel dropper longline was developed which indicated these structures have significant effects on flow patterns. These datasets were used to assess and fine-tune the numerical model. The numerical model governed by the amended equations describing aquaculture structures, displayed close agreement with the velocity data collected from the physical model. The numerical model closely replicated the attenuation of velocities observed in the laboratory as flow passes through the aquaculture structures.

The main consideration in the comparison of the experimental and numerical results is the choice of drag coefficient. This depends primarily on flow conditions, surface roughness and cylindrical shape factor (Souliotis and Panagiotis, 2007). A value of 1.8 was determined for this particular research.

The most significant finding from a carrying capacity perspective was that the physical impediment presented by the droppers also significantly affected material transport in both the longitudinal and lateral direction. Dye dispersion studies displayed a substantial reduction in material supply to droppers downstream. A numerical simulation of material transport displayed similar results. Figure 5.9 presents the predicted dye cloud. Similar to the physical modelling study, we see: accumulation of material at the entrance to the system, diversion of material around the farm and a diminished supply of material to the downstream extents. This study demonstrates that the presence of an aquaculture farm limits nutrient supply to downstream bivalves. When one considers the effect of sequentially located farms and intense particle consumption by suspension feeding, it is evident that ignoring these effects severely limits the viability and reliability of any carrying capacity studies.

A numerical model of a designated aquaculture development site assessed the impact of the structures on a bay scale level. Simulations investigated the influence of the aquaculture installations on flow fields and material transport. This study indicated that the aquaculture structures influenced both flow magnitude and direction. Time trace

graphs exhibited a retardation of flow within aquaculture-designated cells, with some acceleration of flow evident between the aquaculture structures. Flow-field differentials exhibited velocity attenuation of up to 60% in large sections of the bay.

An analysis of material transport time scales examined the assimilative capacity of the bay for aquaculture development purposes. The presence of the aquaculture installations had a substantial effect on the flushing properties of the bay. The numerical model predicted an increase in average residence of 46%. Evidently, this will have significant effects on the local ecosystem in addition to limiting nutrient turnover and supply to the aquaculture installations. Carrying capacity for suspension feeders are primarily limited by the rate of renewal of available food, which is a function of phytoplankton production and water residence time (Dame and Prins, 1998). The findings of the current study are consistent with those of Grant and Bacher, (2001), who studied the effect of long-line cultures on flushing in a Chinese bay via representing the bivalve canopies as localised increases in friction. The flushing time of the bay was found to increase by 41% (from 17 to 24 hours) as a result of the aquaculture developments. They concluded that a *'disregard for the physical effects of culture structure will result in a serious overestimation of the renewal term and thus an overestimation of carrying capacity'*. Brooks et al., (1999) utilised flushing and residence time studies to investigate optimum locations for aquaculture developments in coastal Maine. The study noted the importance of adequate flushing to provide a ready supply of dissolved oxygen and flush away waste products. However, the effect of the suspension feeders themselves on flushing and residence times was not considered.

Particulate renewal versus consumption terms forms the basis for food budgets to suspension feeders (Pilditch et al., 2001) and carrying capacity studies (Grant, 1996). However, flushing studies on a bay scale level carried out as part of this study indicated that tidally driven exchange rates are reduced by up to 46% due to the retardation influence of the aquaculture canopies. Disregarding the frictional effect of the aquaculture installation may result in a serious overestimation of the assimilative capacity of a water body.

Depth-averaged hydrodynamic models provide a computationally efficient means of quantifying carrying capacity in a well-mixed waterbody, where the horizontal scales are much longer than the vertical (Duarte et al., 2003). In this chapter, the oft-neglected physical effects of aquaculture were efficiently incorporated into a numerical model in a technically defensible manner. However, the accurate simulation of flows in deep stratified bays demands the use of three-dimensional numerical models. In order to investigate these features further, the effects of aquaculture structures on the three-dimensional flow structure was examined. The validation and application of this more comprehensive model will be presented in the next chapter.

## Chapter 6: Three-dimensional numerical modelling

---

*“If we can not predict the behaviour of a simple laboratory test case, with its restricted number of variables, then we certainly can not expect to predict the behaviour of the real world prototype”*

*- R. A. Dalrymple*

## 6.1 Introduction

Previous chapters have focused on the validation of a depth-averaged hydrodynamic model against physical model data in which, nearly horizontal flows, dominate. Scale experiments conducted in the tidal basin indicated that two-dimensional simulations were sufficient for this situation due to the relatively shallow depth. However, there is a significant amount of evidence –both in literature (Plew (2005), Boyd and Heasman, (1998)), and anecdotal – to suggest that flows under and around suspended aquaculture installations in deep waters are not two-dimensional in nature. Field studies indicate that a significant retardation of flow occurs within the farm (Gibbs et al., 1991), in conjunction with a pronounced acceleration of flows occurring beneath suspended aquaculture installations (Blanco et al., 1994). The velocity shear induced between the slow moving upper layers and accelerated flow beneath the farms can have significant implications for hydrodynamic processes (Waite, 1989). Hence, this section focuses on the extension of these results to a three-dimensional model; Environmental Fluid Dynamics Code (EFDC).

Validation of the three-dimensional model requires information on the three-dimensional flow profile. Chapter 4 presented physical modelling studies conducted in a tidal basin facility where flow processes were predominantly horizontal, with negligible vertical flows. Hence, this chapter presents details on work undertaken to assess and evaluate the actual velocity profile that develops as flow passes through and around a suspended aquaculture development.

In this chapter, flow dynamics within and beneath a suspended aquaculture installation are discussed. Flow changes induced by the structures are quantified, and the effects on mixing and energy dissipation analysed. The next section presents a typical problem encountered in laboratory-based studies of hydraulic problems; that of simulating three-dimensional flow processes in a depth-limited environment. Section 6.3 presents the validation of the three-dimensional EFDC model. The remainder of the chapter focuses on the amended three-dimensional model; numerical simulations of flow processes within and beneath a suspended canopy are presented. The primary discussion points are:

- Attenuation of flows within the canopy.
- Acceleration of flows beneath the canopy.
- Flow dynamics that develop at the canopy boundary due to the induced velocity shear stresses.
- Additional turbulence and mechanical stirring within the canopy.

## **6.2 Experimental flow profile**

Chapter 4 discussed the extensive laboratory-modelling program conducted as part of this research. This scale-modelling program allowed both the qualitative analysis of impeded flow processes, and the derivation of model coefficients for the validation of the two-dimensional mathematical model. However, for the purposes of the validation of a three-dimensional hydrodynamic model, additional information on the vertical structure of impeded flows was required. A number of experiments were conducted in the tidal basin in order to observe and quantify three-dimensional flow processes. However, the limited depth of the tidal basin proved problematic in simulating three-dimensional flows.

As described previously, the MWL depth in the tidal basin equalled 0.255m; reducing to 0.186m at the low water mark. Hence, the generation of three-dimensional, fully developed, tidal flows raised concerns about laboratory effects within the study. Of particular concern was the effect of the bottom bed on the development of fully turbulent flows. The expected flow profile within a suspended canopy constitutes attenuated flows within the canopy, and increased flow speeds beneath (Figure 6.2). Within a limited depth experimental set-up, the no-slip bottom boundary constraint can affect the development of actual suspended canopy flow processes. Due to these concerns and preliminary experiments conducted in the tidal basin, it was decided that tidal basin data did not present a technically defensible means of validating a three-dimensional model. Therefore, it was decided to validate the amended numerical model from literature; based on laboratory measurements undertaken by Plew (2011b).

Plew (2011b), conducted extensive laboratory tests on flows within and beneath a suspended canopy. Acoustic Doppler Velocity measurements and particle tracking

velocimetry were used to investigate three-dimensional flow processes within the canopy. The experimental process is discussed extensively in Plew (2011b), and for convenience is briefly presented below.

The experiments were conducted in a 6m long by 0.6m wide flume. Canopies were constructed from 9.54mm diameter, aluminium cylinders, and extended the full width, and entire working length, of the experimental flume. Cylinders were arranged in rows with,  $l$ , the spacing between rows and,  $b$ , the traverse spacing between cylinders. Figure 6.1 presents a schematic of the laboratory set-up. The experimental sampling point is at a distance of 4m for the flow inlet. Figure 6.2 presents a definition diagram of the suspended canopy laboratory set-up, along with the idealised velocity profile.



**Figure 6.1: Schematic of experimental flume set-up. Cylinders were arranged in rows with  $l$  the spacing between rows and  $b$  the spacing between cylinders. Cylinders extended the full width and entire working length of the flume**

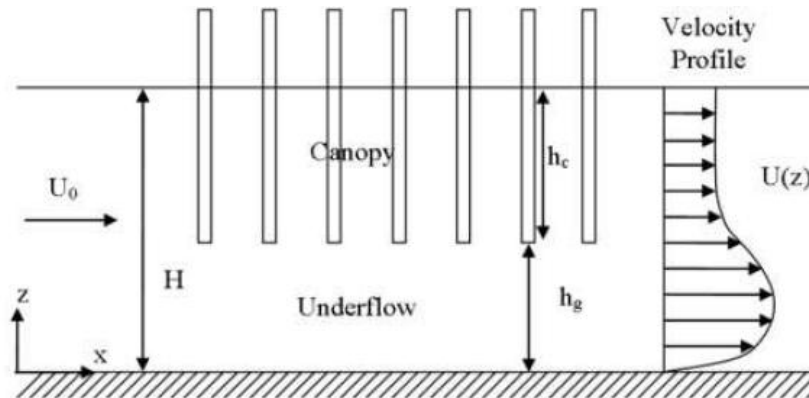


**Figure 6.2: Definition diagram for the suspended canopy laboratory experiments.  $H$  is the water depth;  $h_g$  the gap beneath the canopy;  $h_c$  the height of the canopy; and  $U_0$  the depth-averaged velocity. Illustration adopted from Plew (2011b)**

Particle Tracking Velocimetry (PTV) was used to collect information on flow. PTV measurements were made using a Dalsa 2M30 monochrome digital camera using a 2 x 2

pixel binning mode giving an effective resolution of 800 x 600 pixels, covering an area of 360mm x 200mm. Images were collected at 50Hz for 120 seconds. Images were analysed and velocity fields calculated using Fluidstream software (Nokes, 2007).

Velocity measurements were made in two vertical planes, across the flume at a distance 4m from the inlet; firstly, mid-way between cylinders, and then, in line with the cylinders. Velocity and turbulence values measured at each grid point were averaged horizontally in the x-direction over the distance between cylinder rows to give averaged vertical profiles for each plane. This enabled a vertical profile of spatially averaged velocity and turbulence statistics to be defined. Table 6-1 presents a summary of the different experiments conducted to investigate different canopy configurations. Figure 6.3 presents the velocity and turbulence profiles collected from the experiments for different canopy configurations.

**Table 6-1: Summary of experiments conducted to investigate suspended canopy effect on flows.  $H$  is the water depth,  $h_g$  the gap between the canopy and the bed,  $h_c$  the height of the canopy,  $l$  and  $b$  streamwise and cross-stream spacing between cylinders,  $a$  projected area per unit volume inside the canopy and  $Q$  is flow rate. Reproduced from Plew (2011b)**

<i>Run</i>	$H$ (mm)	$h_g$ (mm)	$h_c$ (mm)	$l$ (mm)	$b$ (mm)	$a$ (m <sup>-1</sup> )	$Q$ (L/s)
A	200	100	100	100	50	1.908	10.5
B	200	100	100	150	50	1.272	10.1
C	200	100	100	200	50	0.954	10.1
D	200	100	100	200	100	0.477	10.3

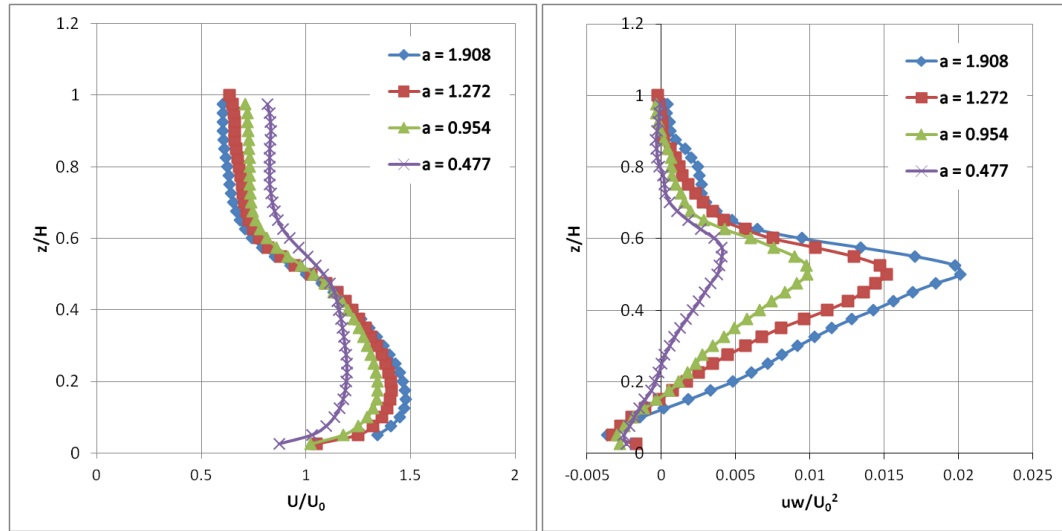


**Figure 6.3: Effect of canopy density  $a$  on profiles of (a) mean velocity and (b) turbulence. The height of the canopy  $z/H = 0.5$  and  $H = 0.20\text{m}$ , and flow rate were constant. Reproduced Plew (2011b).**

Profiles of the mean, normalised stream-wise velocity,  $U/U_0$ , presented in Figure 6.3, show three distinct regions: velocities increasing above the bed reaching a maximum at some point between the canopy and the bed; velocities decreasing into and within the canopy; and velocities approaching a constant value in the upper canopy. Increasing canopy density resulted in lower velocities within the canopy, higher velocities beneath, and stronger velocity gradients at the canopy interface. The turbulence profile increased linearly from near the bed to the underside of the canopy. Continuing upwards inside the canopy, turbulence decreased asymptotically reaching zero at the free surface Plew (2011b).

The preceding section presents data on the two-dimensional vertical flow profiles observed within a suspended canopy. The stated aim of this research was the investigation of flow processes within and beneath a suspended canopy. The experimental data shows a number of features of relevance for this study, namely: the attenuation of flow within the canopy; increased current speeds beneath the canopy; the velocity gradient observed at the canopy interface; and the distinct turbulent structure of the flow. Based on the extensive laboratory work conducted that is of relevance for this research, it provided ideal data to validate the amended three-dimensional model.

### 6.3 General circulation model

The first stage of the research was the development and validation of a three dimensional model of flows within the experimental flume used in the study. In order to preclude scaling issues, simulations were conducted at the same scale as the experiments. Hence, the computational domain encompassed an area 6m long by 0.6m wide. Grid spacing equalled 10cm, and water depth equalled 20cm. To ensure adequate resolution of the vertical flow profile 40 layers in the vertical were specified.

Open boundary conditions were prescribed based on the flow rates specified in Table 6-1. The upstream open boundary condition was specified as constant supply flow rate and the downstream end was specified as a constant water elevation maintained over a thin plate weir. The boundary elevation at the weir was based upon the weir equations as described by (Herschy, 1995), where

$$\eta_{weir} = \left( \frac{3Q}{2BC_{d,weir}\sqrt{2g}} \right)^{2/3} \quad (6.1)$$

where,  $\eta_{weir}$  is head over the weir (m),  $B$  is width of weir, and  $C_{d,weir}$  is coefficient of discharge over the weir.

The coefficient of discharge of the weir was calculated based on the Rehbock coefficient (Falvey, 2003).

$$C_{d,weir} = 0.605 + 0.08 \frac{h_w}{p_w} + \frac{1}{1000h} \quad (6.2)$$

where,  $h$  is water depth (m) and  $p$  is height above weir (m).

Model simulations were performed for 400 seconds to ensure steady state flows, with velocities output at the equivalent sampling point to the experimental studies as denoted in Figure 6.1. Velocity time series were plotted and assessed for discrepancies or model instabilities; and the vertical velocity flow profile was plotted to provide a benchmark for future simulations. Figure 6.4 presents a vertical profile of velocities and turbulent structure predicted by the numerical model. Table 6-1 presents details on model

simulations. The turbulent structure was calculated based on the velocity gradient and turbulent viscosity of the flow:

$$-\langle u'w' \rangle = \nu_v \frac{\partial u}{\partial z} \quad (6.3)$$

where,  $\langle u'w' \rangle$  are the Reynolds stresses averaged in both time and space.

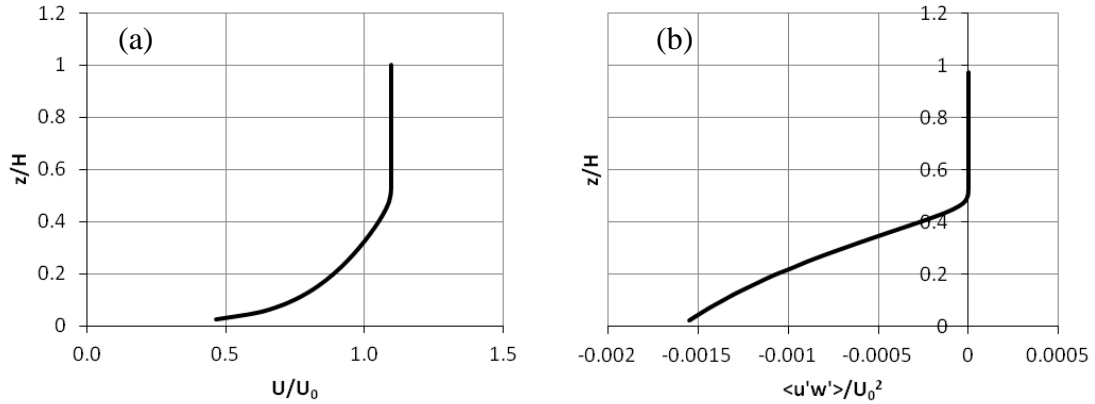


**Figure 6.4: Numerical simulation of (a) vertical velocity profile and (b) vertical turbulent structure within an experimental flume.**

#### 6.4 Amended numerical model

A numerical model was extended and refined to incorporate the effect of suspension feeding mussel droppers on hydrodynamics. The discretization of the mariculture installation into the model equations has been previously detailed in Section 3.3 and will not be presented here. Velocity data and turbulent structure within and below the suspended canopy was analysed. The results were systematically compared with experimentally collected data of flow profile through a suspended canopy conducted by (Plew, 2011b). The model was amended and fine-tuned based on the laboratory data. This section presents validation of the amended model.

In the following sections, a number of methodologies of simulating canopy flow processes are discussed, namely: an additional drag term representing flows past a bluff body; a mechanical friction layer describing flows at the bottom of the canopy as described in Section 3.3.3; and an amended turbulence closure scheme describing the

effects of the canopy on turbulence production. Table 6-2 summarises the various approaches investigated in this chapter to simulate observed canopy flow processes.

**Table 6-2: Description of methodologies used to represent canopy flow processes**

<i>Acronym</i>	<i>Name</i>	<i>Description of numerical representation</i>
CDM	Constant Drag Model	Additional drag term included
DSM	Drag and Shear Model	Drag term + mechanical friction layer describing canopy shear stress
DTM	Drag + Turbulence Model	Drag term + modified turbulence model
DSTM	Drag + Shear + Turbulence Model	Combination of CDM, DSM and DTM
DLGM	Dunn Lopez Garcia Model	Vertical variation of drag computed based on work of Dunn et al., (1996)
GNM	Ghisalberti & Nepf Model	Vertical variation of drag computed based on Ghisalberti and Nepf, (2004)
EAM	EFDC Aquaculture Model	User selected modelling coefficients to provide optimal agreement with experimental data

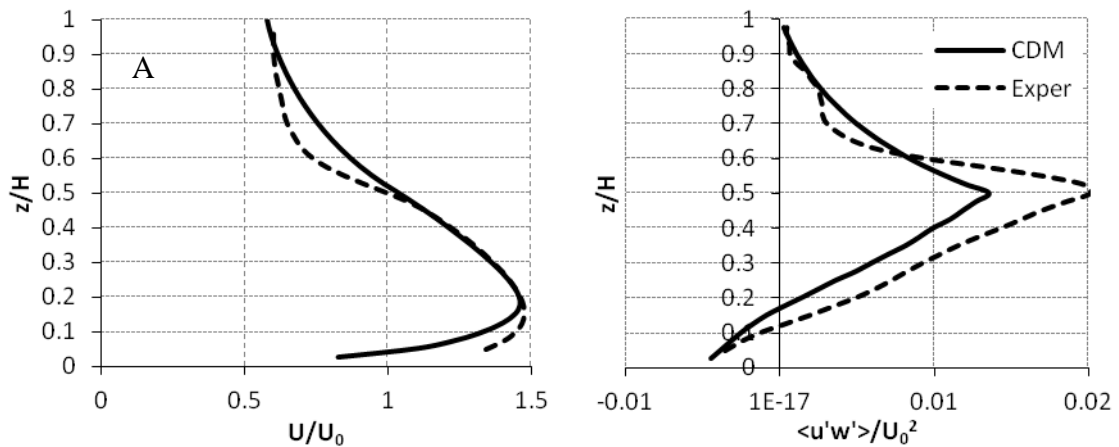
#### **6.4.1 Constant drag term model (CDM)**

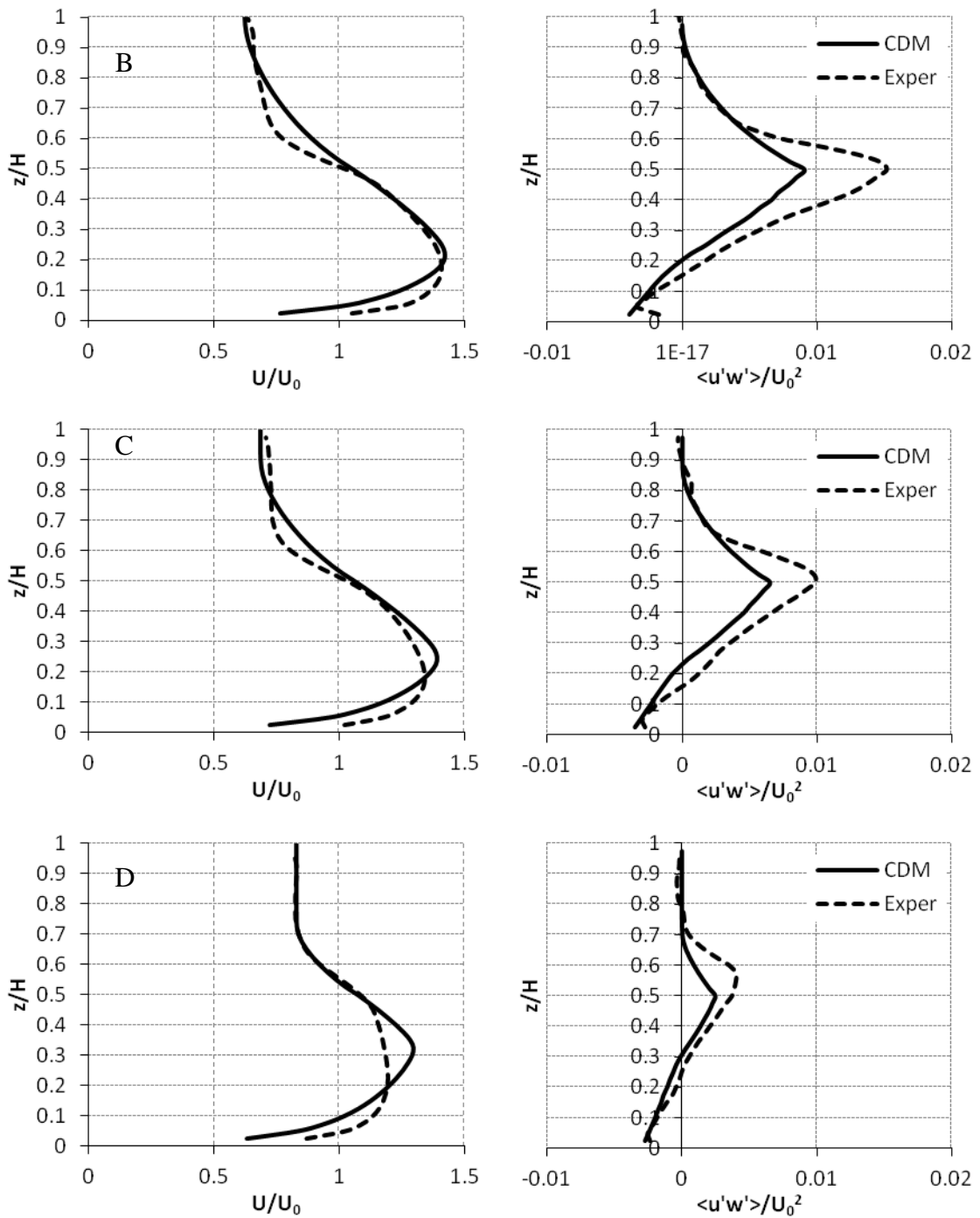
The simulation of impeded flows via an additional drag term is a frequently used method of incorporating physical obstructions into numerical models and has been discussed in much detail Chapter 3. In this section, the suspended canopy is incorporated into the numerical model via a cylindrical drag force equation as presented in equation (3.73). Table 6-1 presents dimensional data for the canopy structure. Modelled droppers were assumed to be distributed uniformly and cover the entire working area of the flume. The diameter of the droppers was 9.54mm. The droppers extend the upper portion of the water column, which corresponds to a length of 0.1m. Hence, the upper 20 layers of the computational domain were flagged as canopy layers and the specified modification

applied. Free-stream flow was computed in the lower 20 layers. Vertical profiles of both velocity and turbulence were calculated and plotted below.

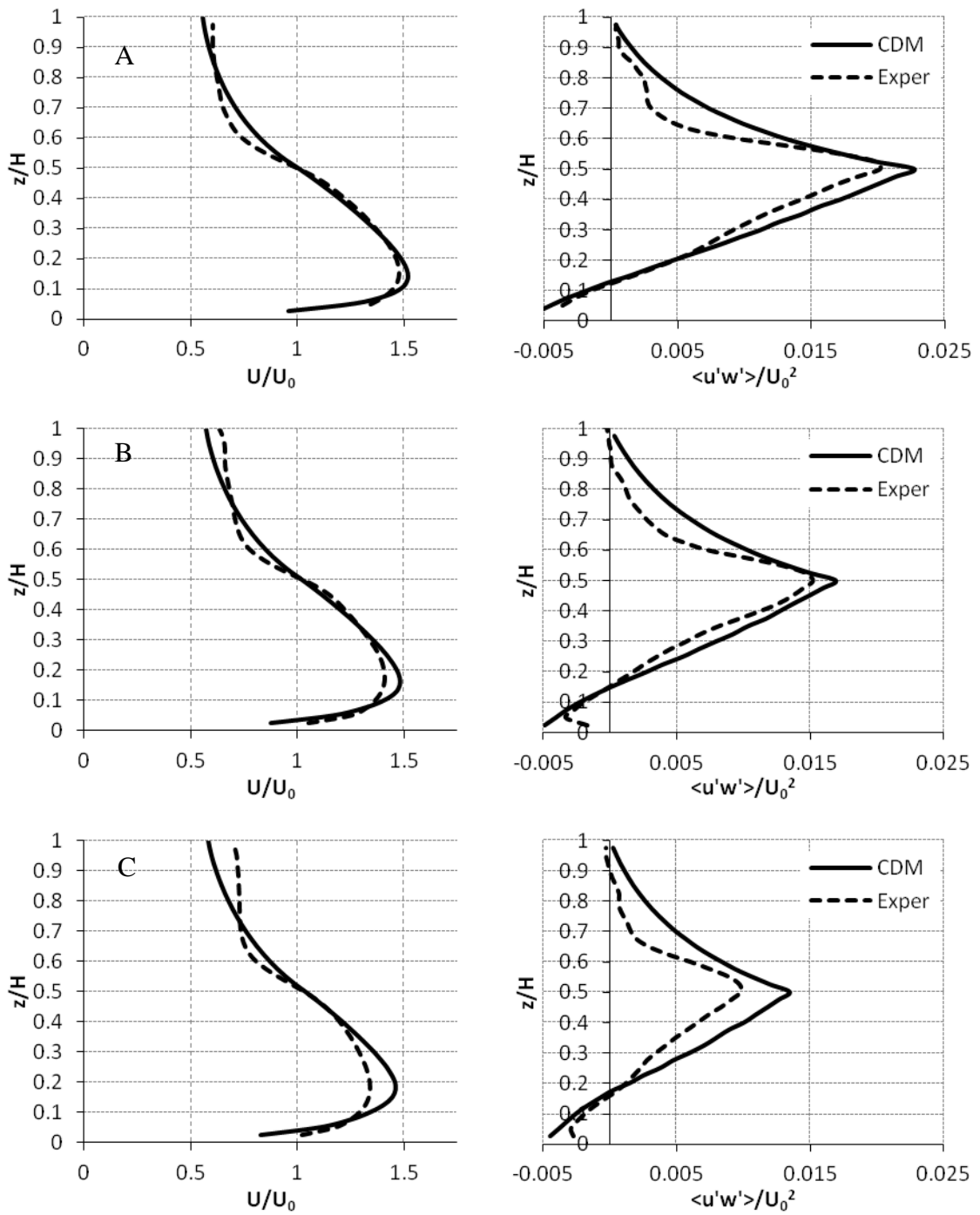
As discussed in earlier chapters, the specification of drag coefficient is a major consideration in the simulation of impeded flows. Figure 6.5 presents numerically predicted velocity and turbulent profiles plotted against experimental data for a range of different dropper densities. Table 6-1 presents details on the simulation configurations. Figure 6.5 presents numerically simulated flows with a prescribed drag coefficient of 1.0; while Figure 6.6 presents the equivalent datasets with a drag coefficient of 2.0 specified for numerical simulations. The numerical model demonstrates a number of interesting features.

In general, the model shows a marked change from Figure 6.4, and approximates the flow profiles derived from the experimental data, namely: reduced flows within the canopy, increased current speed beneath; and large turbulence production at the bottom of the canopy. A drag coefficient of 2.0 provides better agreement between numerical and experimental profiles. This is particularly true at the higher densities of distributed droppers. When a drag coefficient of 1.0 is prescribed velocity attenuation (particularly at the interface of canopy) is under-predicted by the numerical model. In addition, the turbulence production observed in the experimental study is significantly greater than that predicted by the numerical model.





**Figure 6.5:** CDM model results plotted against experimental data for mean velocity (LHS) and turbulent shear stress variance of turbulence fluctuations (RHS). Drag coefficient = 1.0. Details on model runs A-D are provided in Table 6-1



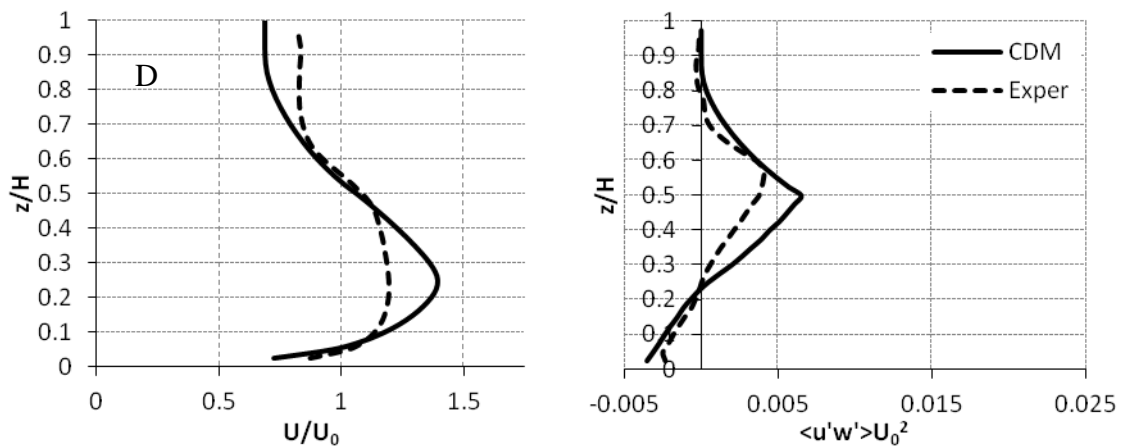


**Figure 6.6: CDM model results plotted against experimental data for mean velocity (LHS) and turbulent shear stress variance of turbulence fluctuations (RHS). Drag coefficient = 2.0. Table 6-1 presents details on model runs A-D**

The data suggests that drag coefficient may be a function of the density of cylinders, and that it may not be appropriate to prescribe a single value to describe all configurations. At a dropper density of 1.908 droppers-per-metre (run A); a drag coefficient of 2.0 provides acceptable agreement between simulated and observed flow profiles; a drag coefficient of 1.0, on the other hand, displays good model agreement at lower density of droppers (e.g. run D). Wu and Wang, (2004) reported a similar phenomenon. In that study, laboratory flume studies of flow through model vegetation (wooden dowel with 3.2mm diameter) were conducted to verify a numerical model. A number of different vegetation densities and corresponding drag coefficients were used. The drag coefficient was set to 0.8, 1.0, 1.2, 1.8 and 3.0 for the runs with vegetation densities of 0.04%, 0.2%, 0.6%, 2.5% and 10% respectively, to obtain acceptable agreements between the laboratory and numerical model results. The authors noted that, the drag coefficient depended on the density due to the inherent dependency on Reynolds Number. When the density is higher, the flow velocity and Reynolds number in the domain are smaller and thus, according to the relation of  $C_D$  and Reynolds number for single cylinder, a larger drag coefficient is required. This relationship between  $C_D$  and  $Re$  is (Schlichting, 1968):

$$C_D = \left(10^3/Re\right)^{0.25}; \text{ for } Re \leq 10^3 \quad (6.4)$$

$$C_D = \text{minimum : } 0.976 + \frac{(10^{-3}Re-2)^2}{20.5} \text{ or } 1.15; \quad \text{for } 10^3 < Re < 4 \times 10^4 \quad (6.5)$$

#### 6.4.2 Drag and shear term model (DSM)

An interesting feature of the vertical flow profile and turbulent structure observed in the laboratory is the rapid attenuation of flows observed at the canopy interface. Streamwise velocity profiles of observed data decomposed the flow into three distinct regions: velocities increasing above the bed and reaching a maximum at some point between the canopy and the bed; velocities decreasing into and within the canopy; and velocities approaching a constant value in the upper canopy. The numerical model does not accurately replicate the dissipation of velocity observed at the bottom of the canopy in the laboratory experiments. Instead, the model predicts a gradual and continuous reduction in velocities into and within the canopy. This suggests that the model is not accurately simulating the complex flow processes that develop within a suspended canopy.

Plew (2011b), classified the flow structure within the canopy into two regions based on experimental data and literature, namely, an internal canopy layer and a canopy shear layer. A canopy shear layer extended from the top of the bottom boundary layer into the canopy. This shear layer was a result of dynamic interaction between the attenuated flows within the canopy and accelerated flows beneath the canopy. An inflection point developed within the canopy shear layer (identified from a change in sign of  $\partial^2 U / \partial Z^2$ ) for all simulations.

This inflection point makes the flow susceptible to Kelvin-Helmholtz instability (Ghisalberti and Nepf, 2002). Kelvin-Helmholtz instabilities form due to the difference in velocities between attenuated flows through the canopy and flows beneath. This instability leads to the generation of large coherent vortices within the shear layer when  $C_{Dah_c} > 0.1$  (Nepf et al., 2007). Unlike free stream vortices, the vortices in a canopy shear layer do not grow continuously downstream but reach and maintain a finite scale

determined by a balance between shear production and canopy dissipation. Within submerged vegetation canopies, much attention has been given to the importance of these coherent vortices in promoting vertical transport to and from the canopy (Ghisalberti and Nepf, (2006), Gambi et al., (1990), Nepf et al., (2007)). The generation of vortex velocity greater than the mean increases vertical momentum transfer within the canopy (Ghisalberti and Nepf, 2002). Nepf and Vivoni, (2000) termed this region the “vertical transfer zone”, due to its importance in generating vertical transfer dynamics between a canopy and free stream flow. Therefore, it is imperative for the model validation process to accurately simulate actual local flow processes at the canopy interface.

As part of this research, investigations were conducted into a number of novel methodologies of simulating these complex flow processes numerically. This section discusses the introduction of a mechanical friction layer into the numerical model. The author is not aware of any other research in which canopy flow processes were simulated in this way. This model will be termed the constant Drag and Shear Model (DSM)

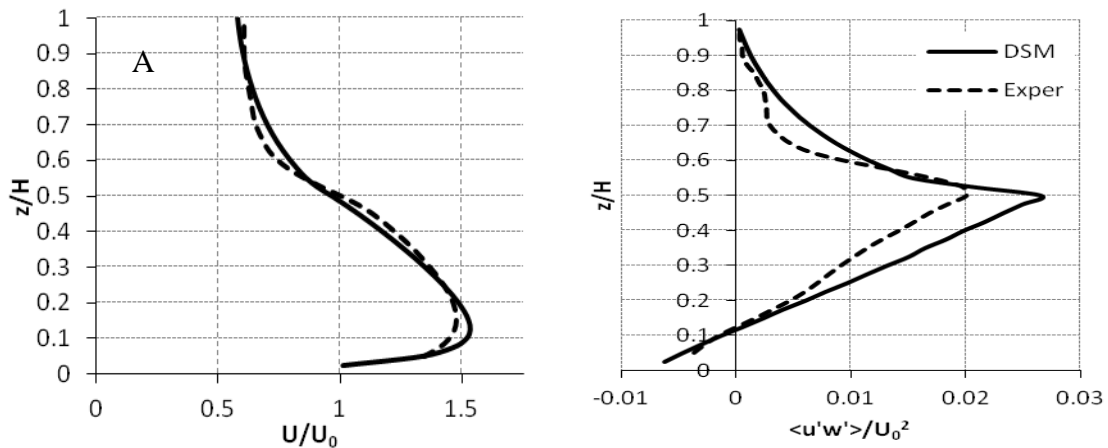
Previous studies have shown that the velocity profile above a vegetated boundary follows a logarithmic profile, with, velocity scale  $u_*$  defined by the turbulent stress at the top of the canopy, and roughness scale  $z_0$ , defined by canopy morphology (Thom, (1971), Shi et al., (1995), Nepf and Vivoni, (2000), Ghisalberti and Nepf, (2004)). The shear flow profiles induced by a suspended canopy boundary are intuitively similar. By adopting this assumption, flow at the boundary exhibits a logarithmic profile of velocity and can be expressed in terms of shear velocity  $u_*$  and a roughness length  $z_0$  as described by (Schlichting, 1968).

Section 3.3 presents the derivation of the mechanical friction layer. The layer was discretized into the numerical model at the interface between the canopy and free-stream flow, as detailed in equation (3.77). A single layer of the numerical model was prescribed as the mechanical friction layer, (i.e. layers 1-19 described free-stream flow, layer 20 represented the mechanical friction layer and layers 21-40 contained the suspended canopy).

The component of frictional shear stress was calculated based on the distributed density of droppers and a user-specified hydrodynamic roughness height. The roughness length is a function of the morphology of the suspended canopy.

Nepf and Vivoni, (2000) investigated the effects of a submerged canopy on flow structure by means of experimental studies conducted in flume. The roughness length,  $z_0$ , of the canopy was estimated by fitting the experimental data to equation (3.74), describing the logarithmic profile of the flow at the bottom of the canopy. For a submergence ratio,  $h_c/H \sim 2.0$ , a value of  $z_0=0.007\text{m}$  was computed. Hence, this value of  $z_0$  was adopted for this study.

Figure 6.7 presents vertical flow profile and turbulent structure predicted by the numerical model with the inclusion of a mechanical friction layer plotted against experimentally observed data. The numerical model better replicates the attenuation of velocities observed at the canopy interface than the CDM. The DSM induces a rapid dissipation of flow energy at the canopy interface, in conjunction with a sharp increase in the production of turbulence.



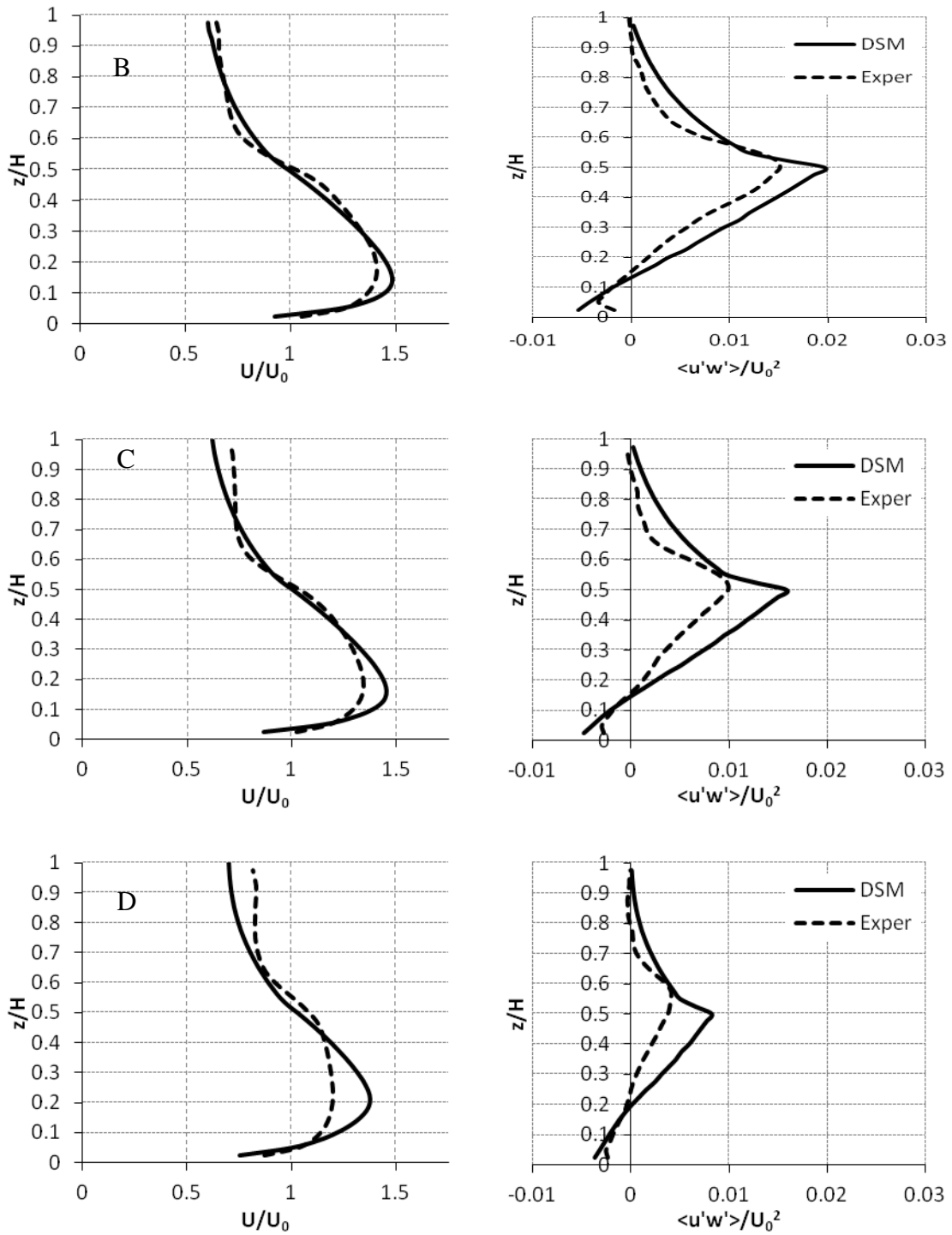


**Figure 6.7: DSM model results plotted against experimental data for mean velocity (LHS) and turbulent shear stress variance of turbulence fluctuations (RHS). Table 6-1 presents details on model runs A-D. Drag coefficient = 2.0**

An analysis of the vertical turbulent structure displays a number of interesting features. The DSM better simulates the actual *structure* of the vertical turbulence profile. Similar to laboratory measurements, the turbulence increases linearly from the bed to a maximum at the canopy interface; reduces significantly into and within the canopy; before tending to zero. The inclusion of the friction layer better reproduces the rapid production, and then dissipation of, turbulence that occurs at the canopy interface. In the absence of the mechanical friction layer (Figure 6.6), turbulence dissipates almost linearly between the canopy interface and the surface. This is not in line with the observed data.

Analysis of actual magnitudes of turbulence indicates that the model is over-predicting the production at the interface. This may be down to the prescribed roughness height being too great and the actual shearing stresses imparted by the canopy at the interface being overestimated. Another possibility is that laboratory effects impede the development of turbulence within the flume. In flows over submerged canopies, the free surface has been found to restrict vortex formation when  $C_{Dah_g} < 1.0$  (Dr. Marco Ghisalberti -personal communication). In the case of suspended canopies, such as this, the suppression of vortex formation would be even more pronounced due to the presence of the no-slip bottom boundary. It may be the case that the limited depth in the experimental flume (200mm) is suppressing some of the flow processes. This phenomenon and its implications will be discussed in more detail in later sections.

### **6.4.3 Drag and turbulence model (DTM)**

The effect of a bluff body on turbulence production and dissipation has been widely discussed in literature, particularly in relation to flows through vegetated canopies (Naot et al., (1996), Neary, (2003), Kang and Choi, (2006)). The conversion of mean kinetic energy to turbulence kinetic energy augments turbulent intensity and because the turbulence is generated at the length of the obstructing body, the dominant turbulent length scale is modified (Nepf et al., (1997), Nepf, (1999)). This section presents a numerical model incorporating an augmented turbulence closure scheme.

The effect of the suspended canopy was incorporated into the numerical model in a similar formulation to that adopted by Shimizu and Tsujimoto, (1994), Neary, (2003) and

Lopez and Garcia, (2001). The mathematical derivation and formulation was previously discussed in Chapter 3 and is presented here for convenience. The turbulence model computes values for the turbulence intensity ( $k$ ), and the turbulence length scale ( $l$ ), by the solution of a pair of transport equations, as presented below.

$$\frac{\partial k}{\partial t} + u \frac{\partial k}{\partial x} + v \frac{\partial k}{\partial y} + w \frac{\partial k}{\partial z} = \frac{\partial}{\partial z} \left( \frac{v_v}{\sigma_k} \frac{\partial k}{\partial z} \right) + P + B - \varepsilon + C_{fk}(F_T u + F_T v) \quad (6.6)$$

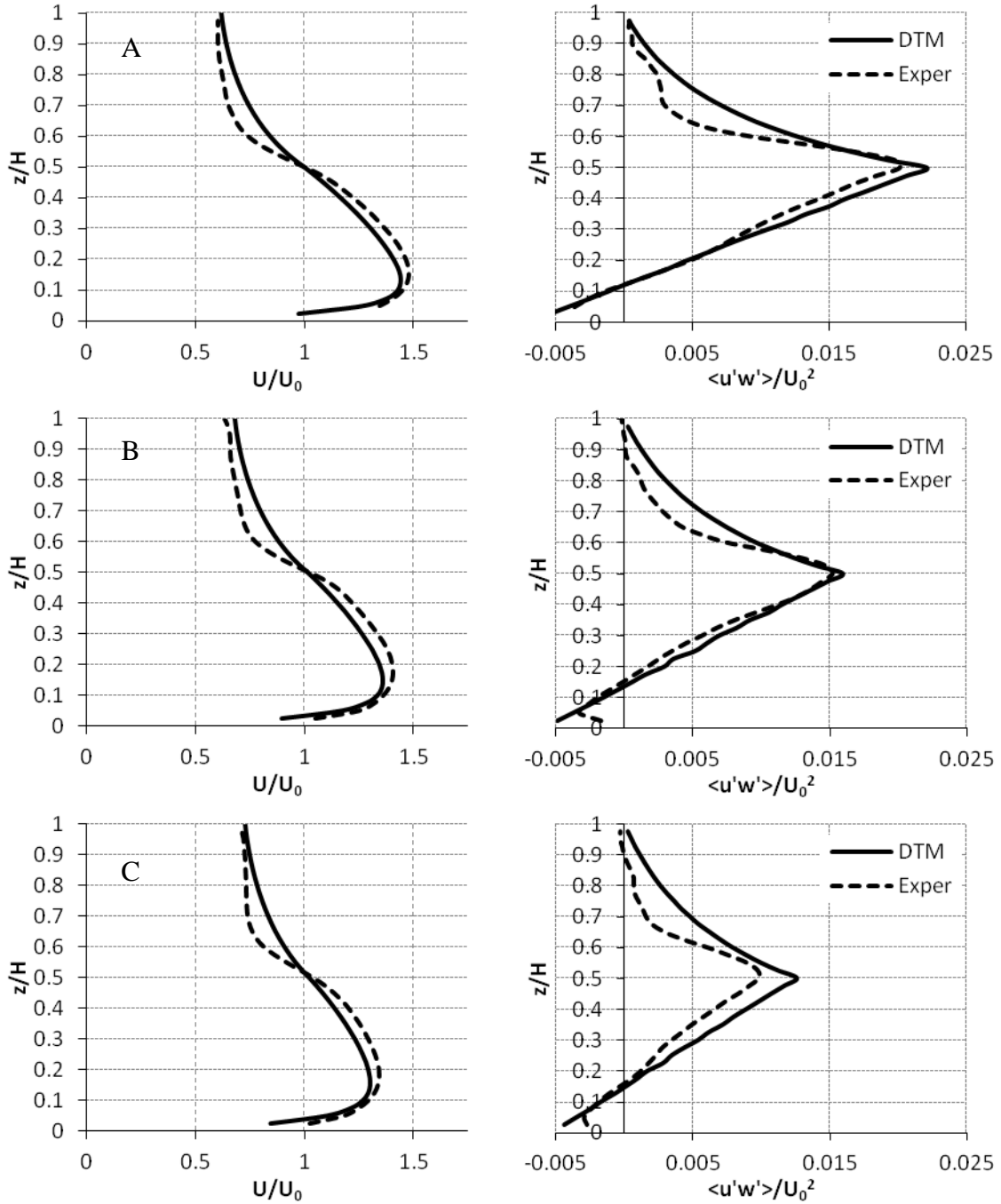
$$\begin{aligned} \frac{\partial kl}{\partial t} + u \frac{\partial kl}{\partial x} + v \frac{\partial kl}{\partial y} + w \frac{\partial kl}{\partial z} \\ = \frac{\partial}{\partial z} \left( \frac{v_v}{\sigma_\psi} \frac{\partial kl}{\partial z} \right) + l \left( c_1 P + c_3 B - c_2 \varepsilon F_{wall} + C_{fl}(F_T u + F_T v) \right) \end{aligned} \quad (6.7)$$

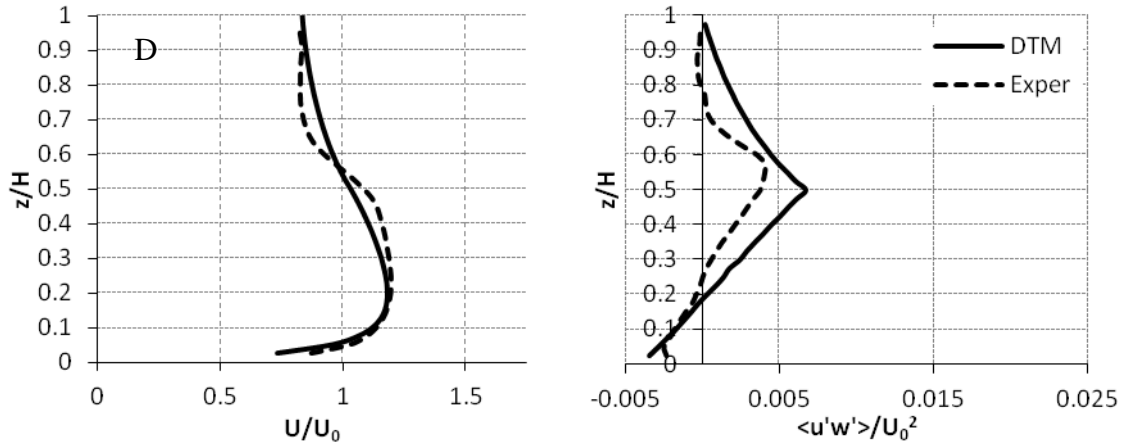
The additional turbulence induced by the presence of the droppers is represented here by an additional production term,  $F_T$ .  $C_{fk}$  and  $C_{fl}$  constitute weighting coefficients that were determined from literature and measurements of turbulence, while  $P$  and  $B$  represent turbulence production due to shear and buoyancy, respectively, as described in Section 3.3

Shimizu and Tsujimoto, (1994) adopted a  $k$ - $\varepsilon$  turbulence closure scheme to simulate flows over a vegetated canopy. The amended turbulence model incorporates the additional turbulence production induced by the vegetation. Turbulence measurements of flow over vegetated beds in a laboratory flume provided validation data for the model. Weighting coefficients of  $C_{fk} = 0.07$ , and  $C_{fl} = 0.16$  were observed to provide closest agreement between modelled and observed datasets. This is similar to research conducted by Neary, (2003), who modified a  $k$ - $\omega$  turbulence closure model to simulate vegetative resistance, in a similar manner to that adopted for this study. Best agreement with measured data was obtained when turbulence weighting coefficients of  $C_{fk} = 0.05$ , and  $C_{fl} = 0.16$  were prescribed.

Figure 6.8 presents vertical flow profile and turbulent structure predicted by the revised EFDC model incorporating the additional turbulence production term plotted against experimentally observed data. Weighting coefficients of  $C_{fk} = 0.07$ , and  $C_{fl} = 0.16$  provided best agreement with experimental data. These values are very similar to other

studies discussed above. The mechanical friction layer is neglected in this case and a drag coefficient of 2.0 is prescribed in an equivalent fashion to the CDM discussed in section 6.4.1.

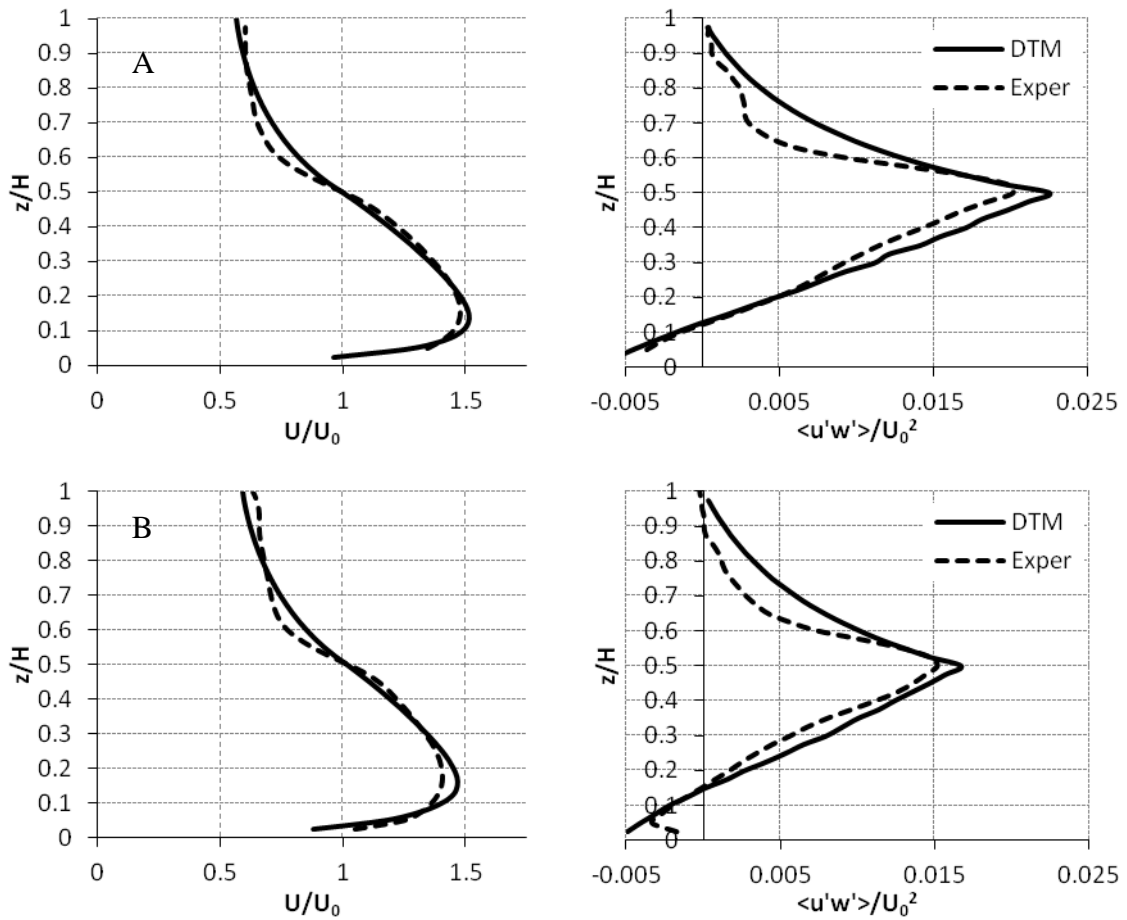




**Figure 6.8: DTM model results plotted against experimental data for mean velocity (LHS) and turbulent shear stress variance of turbulence fluctuations (RHS).  $C_{fk} = 0.07$ ;  $C_{fl} = 0.16$ . Table 6-1 provides details on model runs A-D. Drag coefficient = 2.0.**

An analysis of Figure 6.8 displays a number of interesting features of the flow profile predicted by the numerical model. The additional turbulence production term is shown not to affect turbulence production significantly at the higher densities of droppers. In fact, a slight decrease in turbulence is observed at the canopy interface for all simulations apart from Run D. However, the profiles of velocity are significantly affected; which has implications for the turbulent structure. It is apparent from equations (6.6) and (6.7) that, in addition to the turbulence transport terms on the left hand side of the equation, velocity shear,  $P$ , and buoyancy,  $B$ , are important generators of turbulence. While in this study buoyancy is negligible, since the fluid in the flume is of a constant density, shear production is of major importance due to the suspended canopy flow profile. Hence, while the additional turbulence production terms do not appear to affect turbulence significantly, the reduction in turbulence production due to shear also impacts on results. The additional turbulence reduced the magnitude of velocity shear at the canopy interface due to increased momentum transfer between layers (Nepf and Vivoni, 2000). This reduction in shear velocity reduces the production of shear turbulent energy, and hence turbulence. Therefore, the small increase in turbulence energy observed in numerical simulations is a result of the reduced turbulence production due to shear and increased turbulence production included in the extended model, negating absolute turbulence production.

To assess further the effects of the dropper-induced turbulence, numerical simulations adopted higher values of the weighting coefficients. Research conducted by Lopez and Garcia, (1997) and assessed by Neary, (2003) suggested theoretically based values of weighting coefficients to be  $C_{fk} = 1.0$  and  $C_{fl} = 1.33$ . Figure 6.9 presents model results using these coefficients.



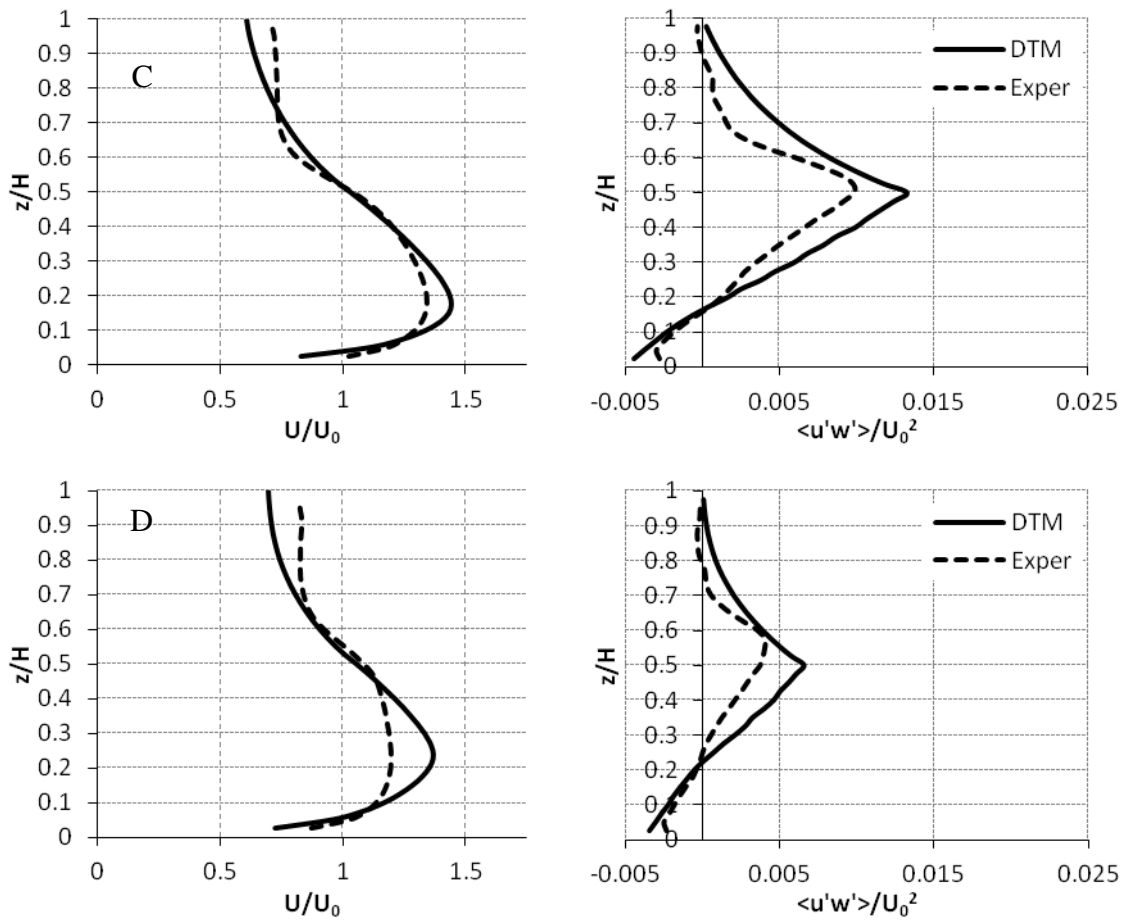


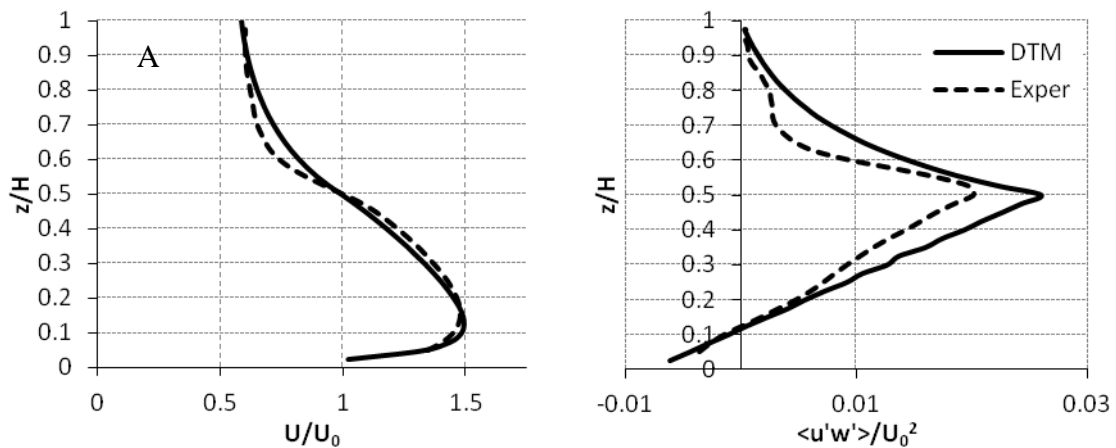
**Figure 6.9: DTM model results plotted against experimental data for mean velocity (LHS) and turbulent shear stress variance of turbulence fluctuations (RHS).  $C_{fk} = 1.0$ ;  $C_{fl} = 1.33$ . Table 6-1 provides details on model runs A-D. Drag coefficient = 2.0.**

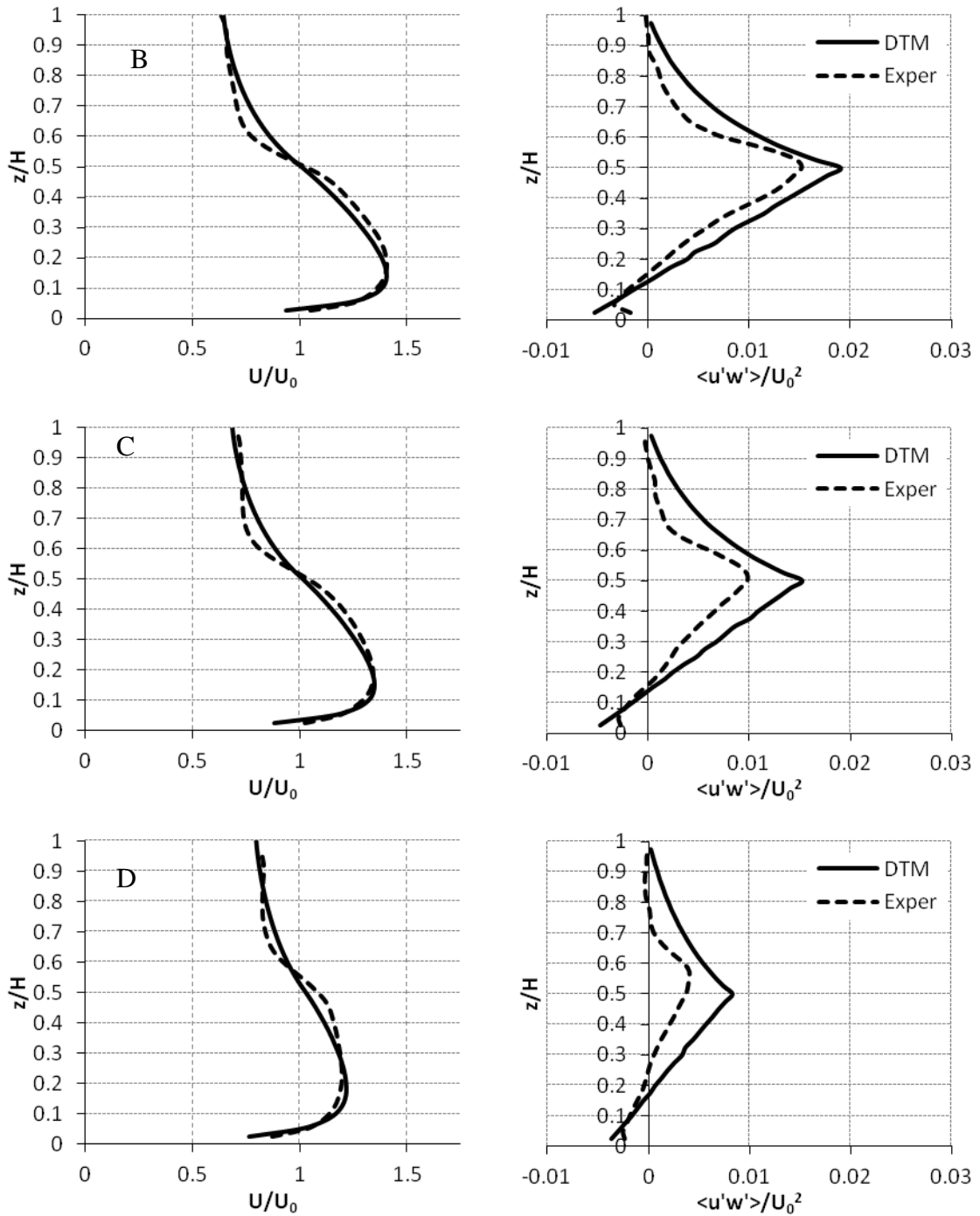
Model simulations incorporating the larger weighting coefficients do not display any significant improvement in performance compared to Figure 6.6. The turbulence structure (particularly at higher densities) is in better agreement with observed values when the prescribed coefficients,  $C_{fk} = 0.07$  and  $C_{fl} = 0.16$ , are adopted. Based on these considerations, the chosen coefficients for further model validation are  $C_{fk} = 0.07$  and  $C_{fl} = 0.16$ .

Figure 6.10 presents numerically predicted velocity profile and turbulent structure adopting an increased drag coefficient to improve correlation with velocity data. In order to achieve best agreement with velocity data a drag coefficient of 2.5 was prescribed (turbulent coefficients correspond to  $C_{fk} = 0.07$  and  $C_{fl} = 0.16$ ).

When adopting these coefficients the DTM performs significantly better in replicating observed velocity structure than the CDM. This is particularly true at the lower densities of droppers (runs C & D). In all cases, modelled and observed data exhibit improved agreement. The dependency of drag coefficient on Reynolds number and hence the density of droppers was previously discussed. These results suggest that a single drag coefficient describing all configurations of distributed cylinders may be adopted, if the vertical structure of turbulence is correctly simulated.

As might be expected, the overestimation of turbulence observed within the CDM is exacerbated by the inclusion of the additional turbulence production terms in the DTM. The reduction in the shear-induced production of turbulence observed in Figure 6.8 is not a factor here and therefore the model overestimates the production of turbulence in all model runs, to some degree. However, when one considers the observed agreement between vertical velocity profiles, and the possible suppression of laboratory production of turbulence by the bottom boundary, it was decided to investigate flow processes further before disposing of results based on the relatively poor simulation of turbulent structures.

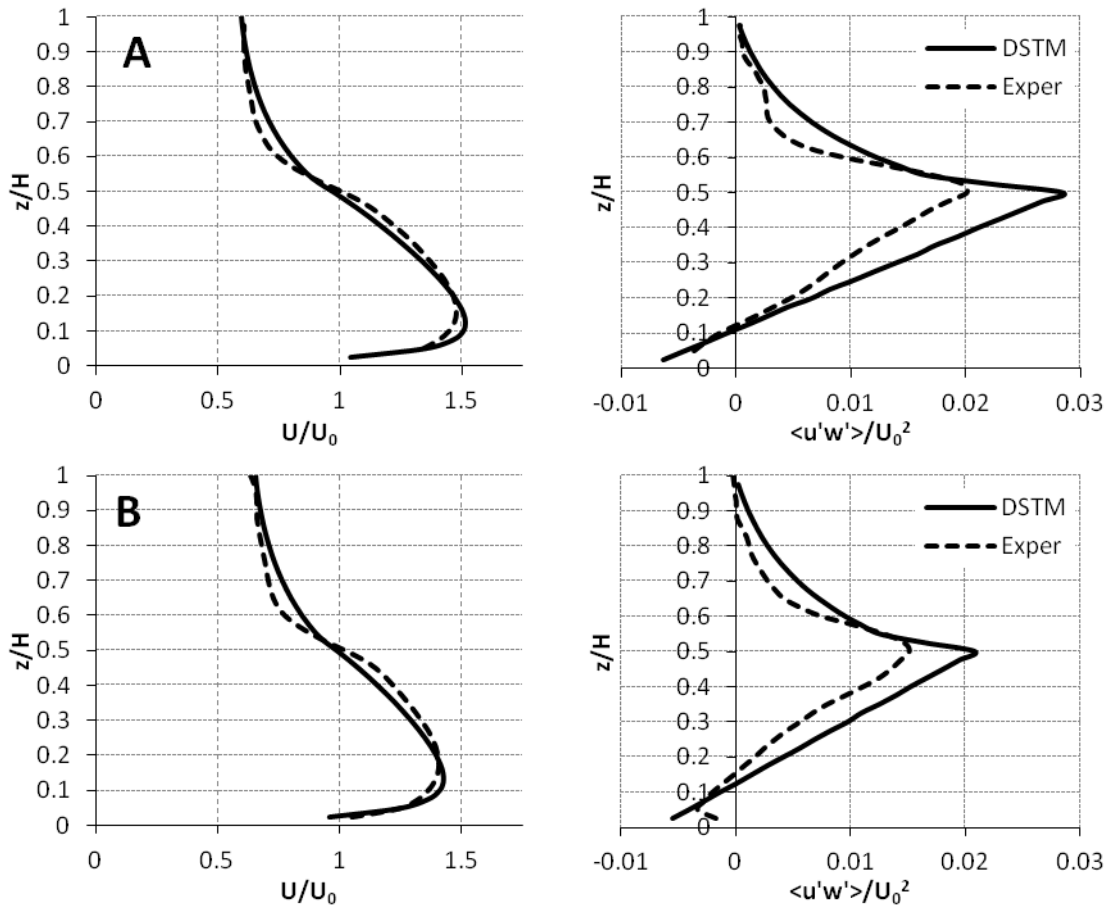




**Figure 6.10: DTM model results plotted against experimental data for mean velocity (LHS) and turbulent shear stress variance of turbulence fluctuations (RHS).  $C_{fk} = 0.07$ ;  $C_n = 0.16$ . Table 6-1 provides details on model runs A-D. Drag coefficient = 2.5.**

Model simulations were also conducted incorporating drag term, mechanical frictional layer and dropper turbulence production term into model equations. This model is termed the drag shear turbulence model (DSTM). Figure 6.11 presents vertical flow profile and turbulent structure predicted by the DSTM plotted against experimentally observed data.

The inclusion of the mechanical friction layer appears to better simulate actual flow processes. In particular, the large production of turbulence at the canopy interface alongside the rapid dissipation into and within the canopy is simulated quite well. As before, the actual magnitudes of turbulence production are overestimated. An analysis of these results suggest that actual flow processes within a suspended canopy are a complex interplay of: drag induced by the droppers; shear stresses between the attenuated canopy flows and faster free-stream flow beneath; and additional turbulence production terms induced by the droppers. The task of the modeller is to describe and quantify this complex interaction; the remainder of the chapter focuses on this issue.



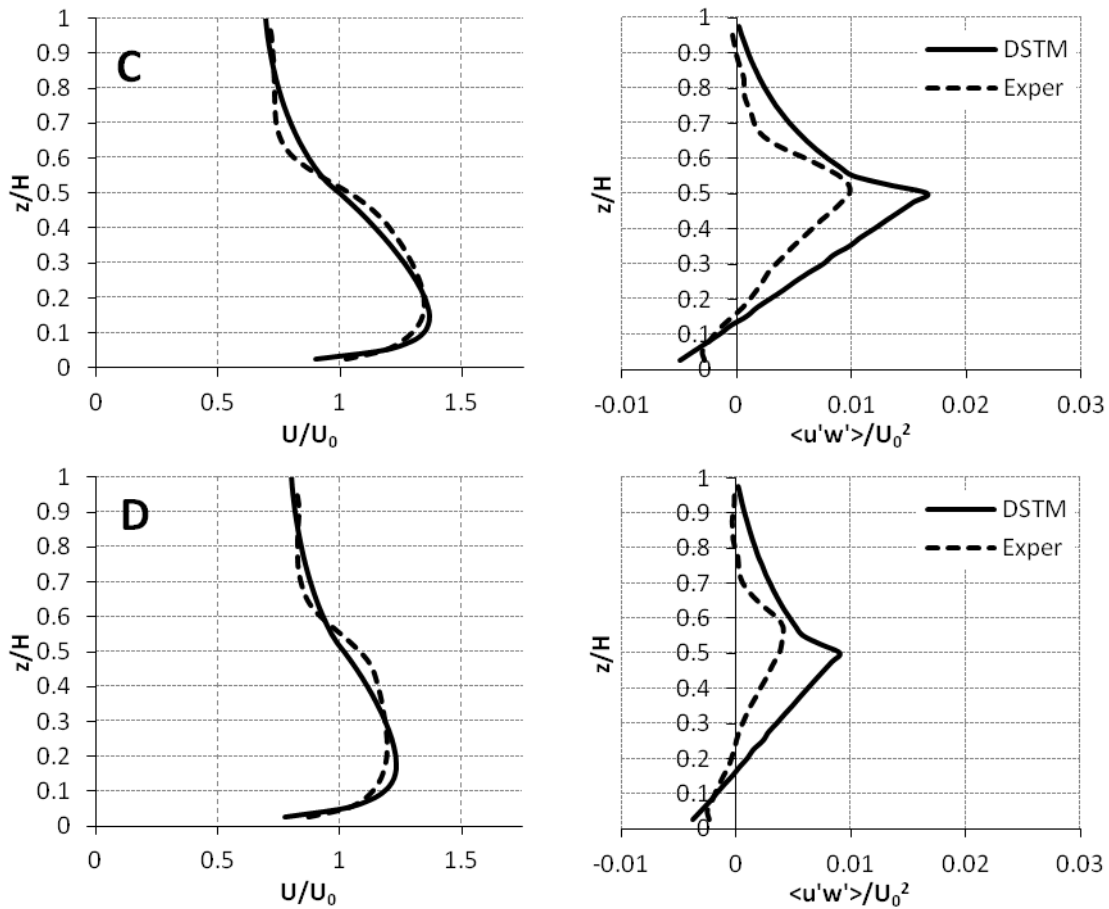


**Figure 6.11: DSTM model (incorporating mechanical friction layer) results plotted against experimental data for mean velocity (LHS) and turbulent shear stress variance of turbulence fluctuations (RHS).  $C_{fk} = 0.07$ ;  $C_{\pi} = 0.16$ . Table 6-1 presents details on model runs A-D. Drag coefficient =2.0.**

### 6.5 Variable drag coefficient

A large body of research exists to suggest that the drag on a submerged cylinder is not uniform along its length. The free end of a cantilevered cylinder generates strong vortices near the tip that causes significant disturbances to the wake structure (Ghisalberti and Nepf, 2004). The induced disturbances result in an increase in wake pressure, which leads to a reduction in drag, as compared with an infinitely long cylinder.

Dunn et al., (1996) investigated local drag coefficients within an array of rigid submerged cylinders. The computed drag coefficient was not uniform throughout the canopy, but instead typically reached a maximum within the canopy before diminishing

towards a minimum at the tip of the canopy. This section presents numerical simulations incorporating a variable drag coefficient. Appropriate profiles of drag were determined based on an extensive analysis of literature. The derived drag coefficients were analysed and validated by comparing with observed profiles of flow.

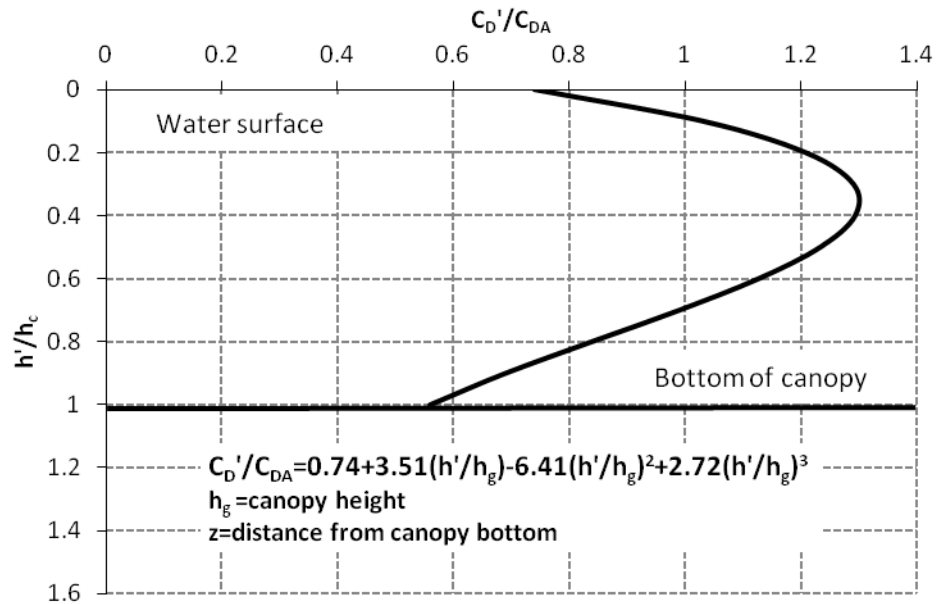
### 6.5.1 Dunn Lopez Garcia model (DLGM)

Dunn et al., (1996) investigated the flow structure above and within a canopy of rigid cylinders in an experimental study. An ADV measured velocity and turbulence characteristics in and above the cylinder canopy; appropriate drag coefficients were extrapolated from the data. The study indicated that the drag coefficient was not constant in the vertical, as many models assumed, but instead reaches a maximum at about one-third the canopy height. Data collected as part of the study conducted by Dunn et al., (1996), was used to derive drag coefficients to simulate canopy flows. This particular model will henceforth be termed the Dunn Lopez & Garcia Model (DLGM).

The experimental study undertaken by Dunn et al., (1996), was for submerged vegetation rather than a suspended canopy and obvious discrepancies exist between the two; particularly the free surface boundary condition present above the submerged canopy, and the no-slip bottom boundary present beneath the suspended type. However, as a preliminary step, the suspended canopy was assumed to behave, as an “inverted” submerged canopy and the vertical profile of drag coefficient proposed by Dunn et al., (1996), was adopted:

$$\frac{C'_D}{C_{DA}} = 0.74 + 3.51 \left( \frac{h'}{h_c} \right) - 6.41 \left( \frac{h'}{h_c} \right)^2 + 2.72 \left( \frac{h'}{h_c} \right)^3 \quad (6.8)$$

The bulk drag coefficient,  $C_{DA}$ , characterises the drag coefficient profile,  $C'_D$  within the canopy; while  $h_c$  equals the height of the canopy and  $h' = H - z$  is the distance from top of canopy (water surface). Figure 6.12 presents the vertical variation of drag coefficient inside the canopy. This drag coefficient reaches a maximum at a dimensionless distance of 0.38 from the suspended canopy top (i.e. water surface) before reducing, almost linearly, to a value of 0.56 at the bottom of the suspended canopy.

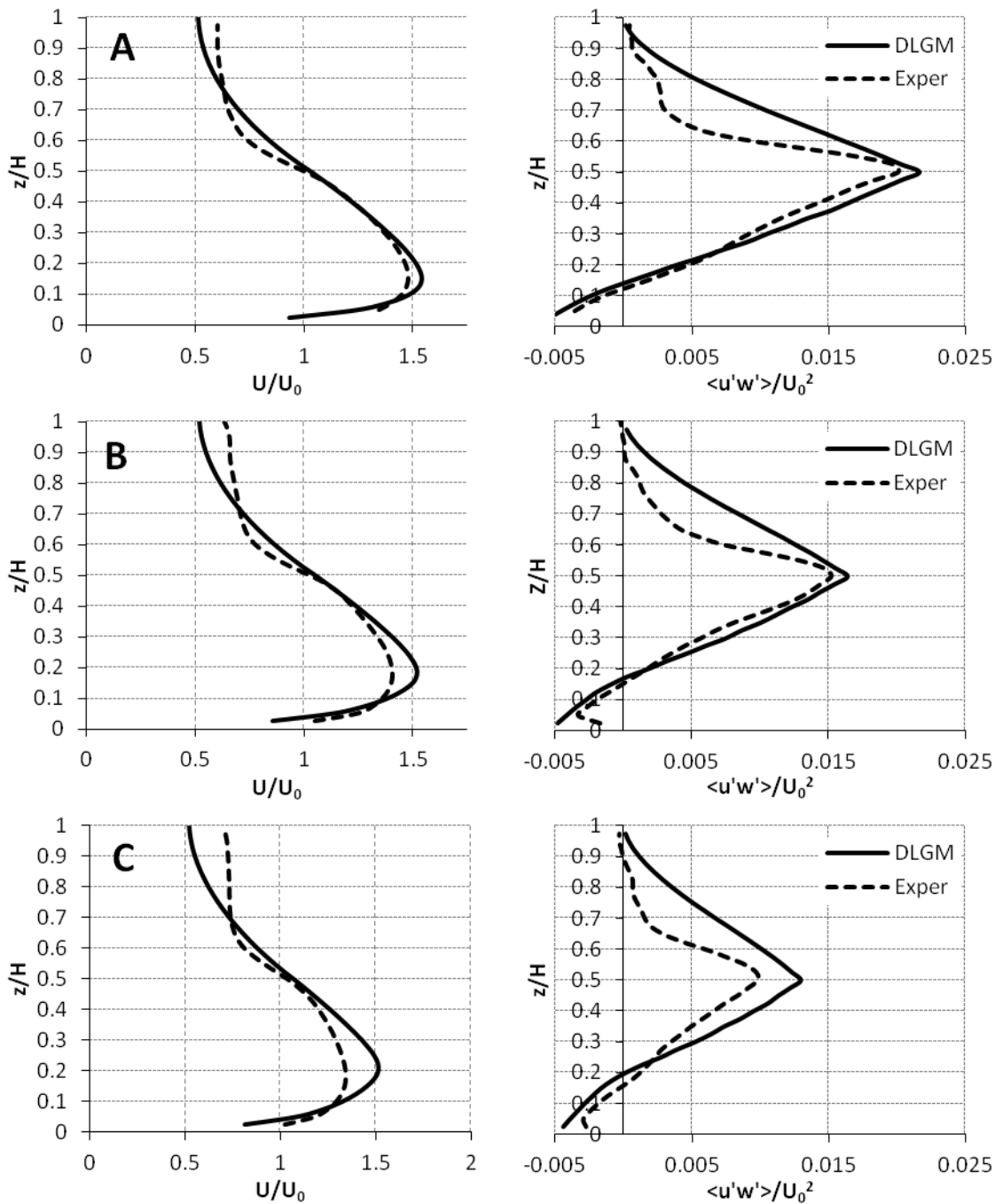


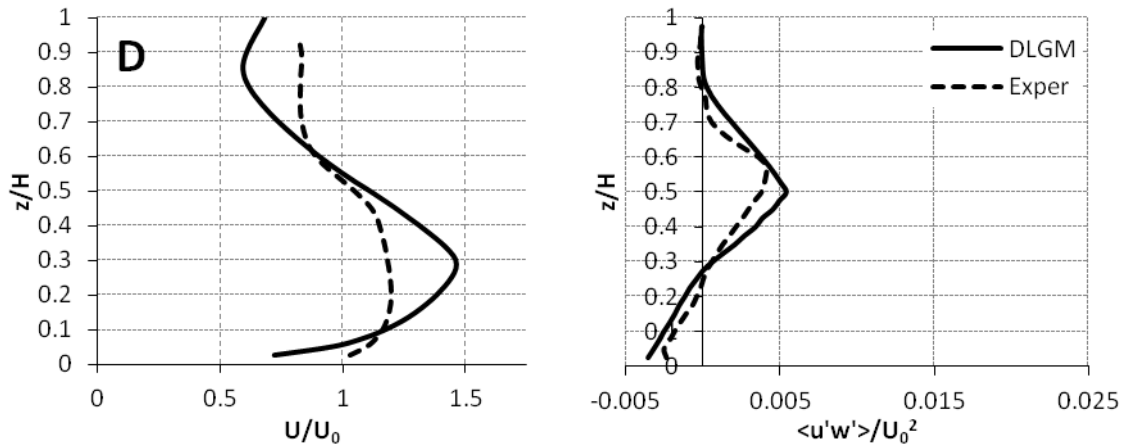
**Figure 6.12 Vertical variation of the drag coefficient inside the canopy (Dunn et al., 1996)**

Figure 6.13 presents the flow structure predicted by the DLGM model plotted against experimental data. The prescribed bulk drag coefficient was 2.0. The mechanical friction layer and additional dropper turbulence production terms were neglected for this case.

The adoption of the variable drag coefficient does not exhibit any significant improvement in the simulation of the flow processes within and below a suspended canopy structure. The predicted velocity profile is quite similar to that observed within the CDM in Figure 6.6. Velocity attenuation at the bottom of the canopy is underestimated; while at the water surface the model overpredicts flow attenuation.

The DLGM simulates observed turbulent structures quite poorly. While the actual magnitudes at the canopy interface are computed satisfactorily; the turbulence profile within the canopy is quite different from the experimental data. As previously alluded to, turbulence dissipates quite rapidly within the experimental configuration. The model, on the other hand, simulates a near linear dissipation from the canopy interface to the water surface. This does not agree with observations and constitutes a deterioration in model performance as opposed to the CDM.



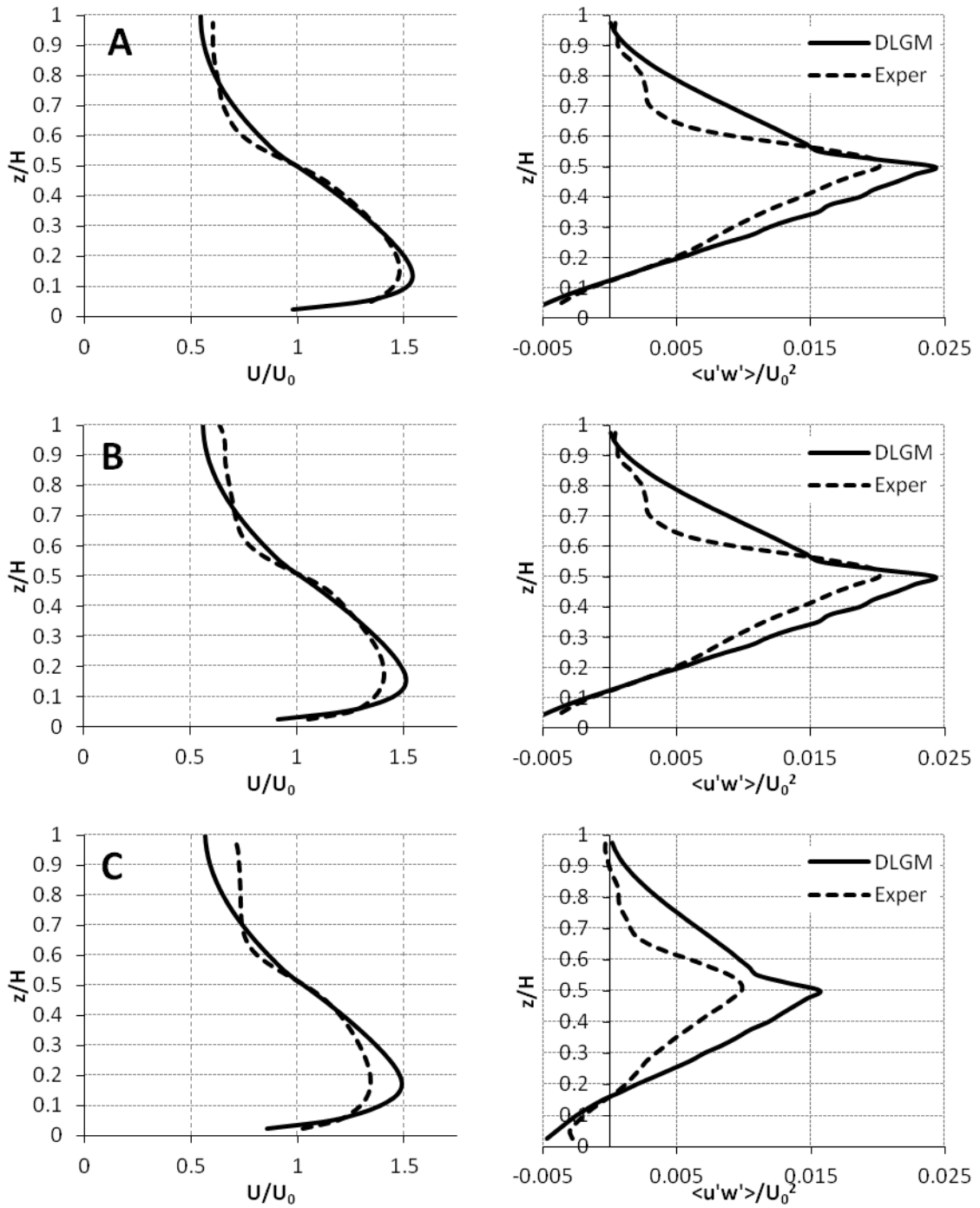


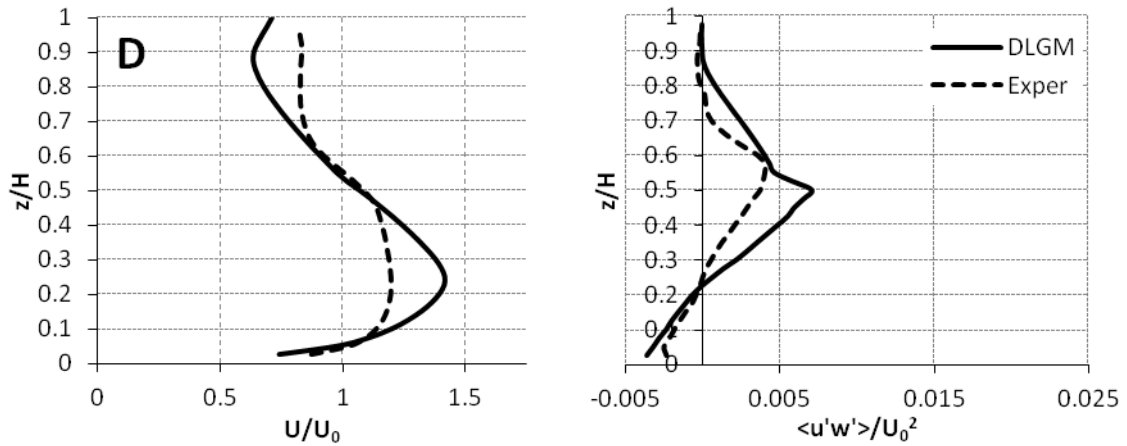
**Figure 6.13: DLGM model results plotted against experimental data for mean velocity (LHS) and turbulent shear stress variance of turbulence fluctuations (RHS). Table 6-1 provides details on model runs A-D. Drag coefficient,  $C_{DA} = 2.0$ . Details on drag coefficient provided in Figure 6.12**

The effects of incorporating the previously described mechanical friction layer, and turbulence production terms into the model were also assessed. Figure 6.14 presents DLGM predicted flow structure incorporating the mechanical friction layer plotted against experimental data. Modifications are quite similar to that observed within the DSM. The model better simulates flow profile at the canopy-free stream interface.

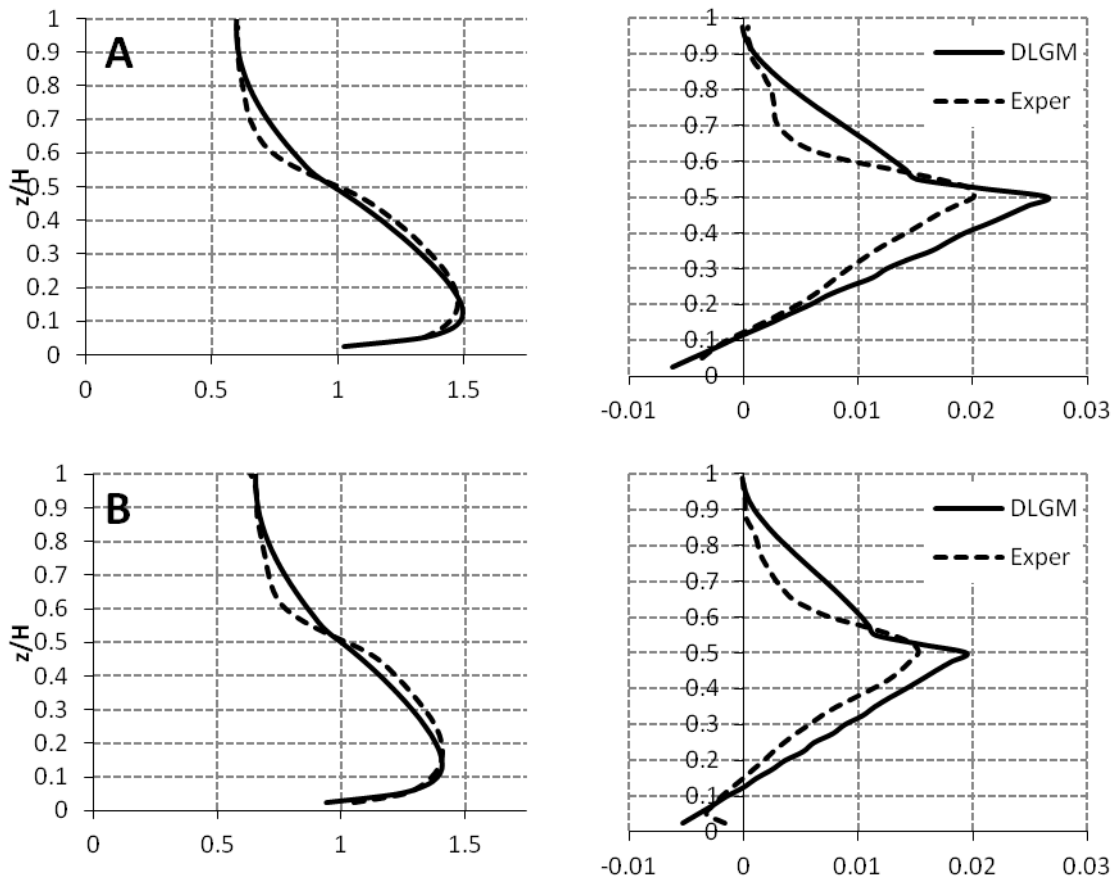
Again, the model performs poorly in simulating turbulent structure, in particular the turbulent structure within the canopy. At the bottom of the canopy, the simulation of turbulent structure, although overestimated, is acceptable. However, the performance of the model in simulating turbulent structure within the canopy is quite poor.

Figure 6.15 displays DLGM predicted flow structure incorporating the amended turbulence closure scheme describing additional production terms. Again, the model was compared to experimental data. Similar to the CDM, the amended turbulence scheme appears to better simulate vertical velocity structure within the canopy, particularly at lower densities. Again, however, the numerical model poorly computes turbulence structure.





**Figure 6.14: DLGM model results with MECHANICAL FRICTION LAYER plotted against experimental data for mean velocity (LHS), and turbulent shear stress variance of turbulence fluctuations (RHS). Table 6-1 provides details on model runs A-D. Drag coefficient,  $C_{DA} = 2.0$ .**



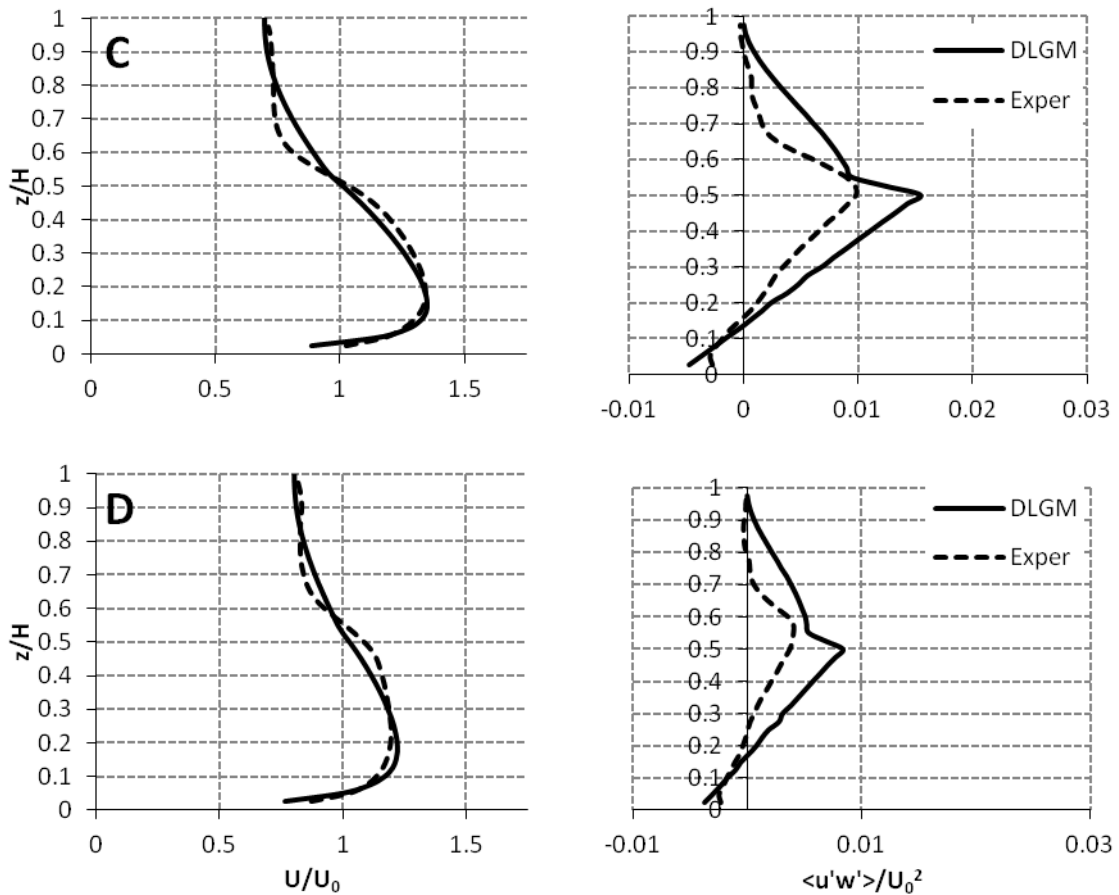


**Figure 6.15: DLGM model results with additional TURBULENCE PRODUCTION term plotted against experimental data for mean velocity (LHS) and turbulent shear stress variance of turbulence fluctuations (RHS). Table 6-1 presents details on model runs A-D.  $C_{fk} = 0.07$ ;  $C_{fl} = 0.16$ . Drag coefficient,  $C_{DA} = 2.0$ .**

An analysis of results produced by the DLGM does not exhibit any improvement in results over that produced by the CDM. Velocity profiles predicted by both are quite similar, particularly at the bottom of the canopy where the observed attenuation of flows is poorly replicated. The model shows a marked degradation in the prediction of turbulent structure. An analysis of flow profiles predicted by the DLGM illustrates two features: the drag coefficient is underestimated at the canopy interface; and the drag coefficient is overestimated within the canopy. The drag coefficient used for this modelling study (Figure 6.12) was that computed by Dunn et al., (1996), who computed a maximum value of drag occurring at a dimensionless distance of 0.38 from the water surface. These

results suggest that the peak value of drag occurs at some point closer the bottom of the canopy. This will be investigated in greater detail in the next sections, via the adoption of different profiles of the drag coefficient.

### 6.5.2 Ghisalberti and Nepf model (GNM)

Ghisalberti and Nepf, (2004) conducted laboratory flume studies of flow within and above a simulated vegetated canopy. Experimental configurations consisted of randomly distributed wooden dowels of 0.64cm diameter. Three-dimensional ADV measurements provided velocity and turbulent. The vertical profile of drag within the canopy was computed and the data used to develop a best-fit expression describing the variation of drag within the height of the canopy. Equation (6.9) presents the computed expression while Figure 6.16 displays the experimental profile plotted against that proposed by Dunn et al., for comparison.

$$\frac{C'_D}{C_{DA}} = f(x) = \begin{cases} 1.4 \left(\frac{h'}{h_c}\right)^{2.5} + 0.45, & 0 < \frac{h'}{h_g} < 0.76 \\ -4.8 \frac{h'}{h_c} + 4.8, & 0.76 \geq \frac{h'}{h_g} < 1 \end{cases} \quad (6.9)$$

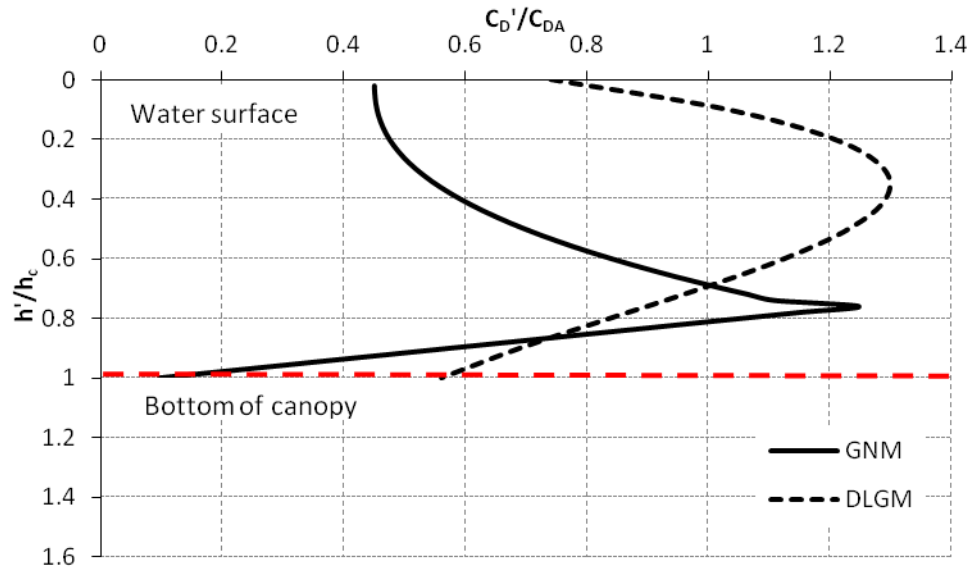
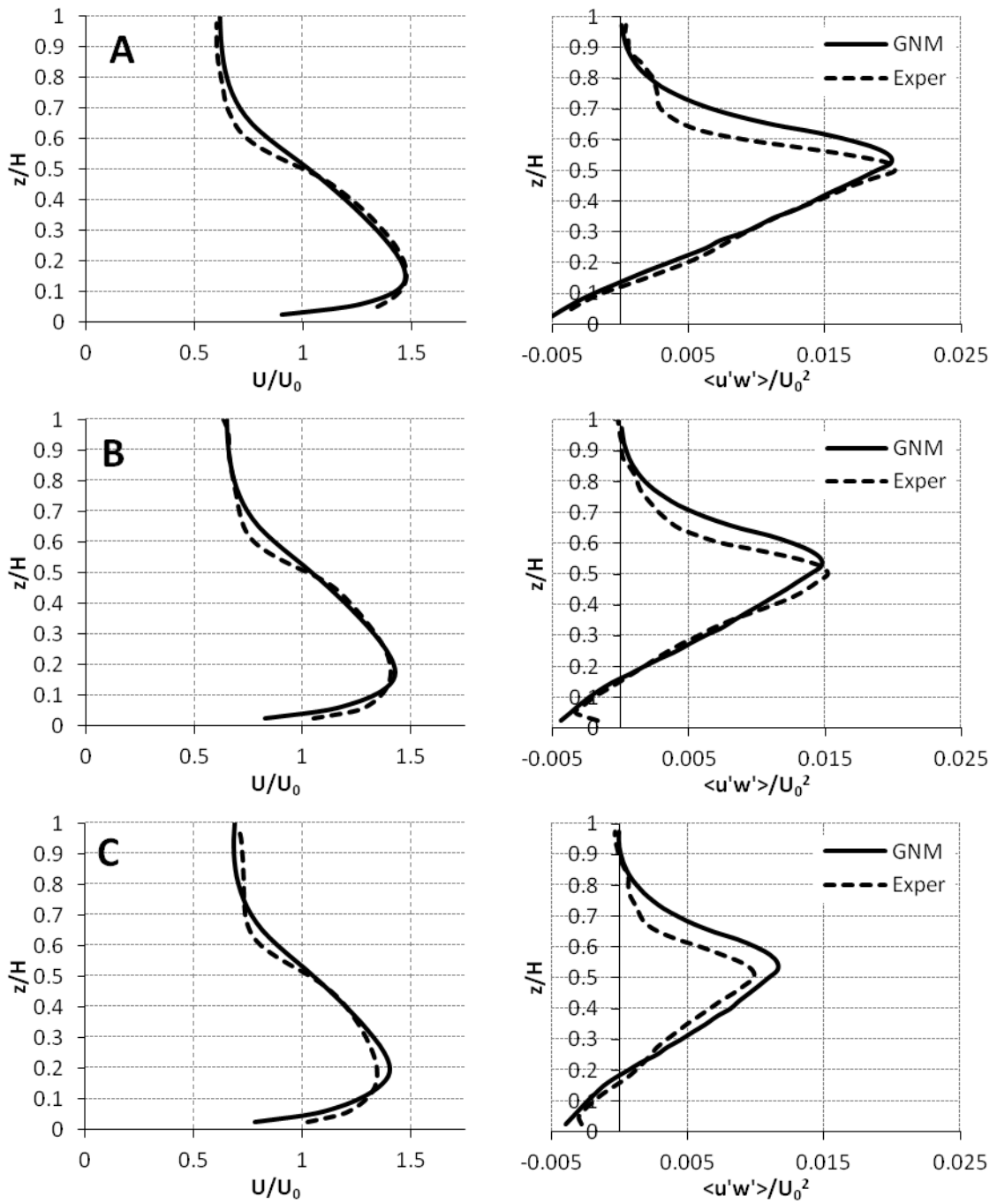


**Figure 6.16: Vertical variation of the drag coefficient inside the canopy computed by Ghisalberti and Nepf, (2004). DLGM computed profile (dashed line) presented for comparison**

The vertical profile of drag coefficient computed by Ghisalberti and Nepf, (2004), is different in many respects to that proposed by Dunn et al., (1996). Dunn et al., reported a linear increase in drag coefficient from the bed; reaching a maximum at a dimensionless distance of 0.38 from the bed to canopy surface before decreasing linearly to a minimum. Ghisalberti and Nepf, (2004), on the other hand, observed an increase in drag coefficient from a value of 0.45 at the bed, before reaching a maximum at a dimensionless distance of 0.76 from the bed to canopy surface before decreasing to zero at the canopy tip. Hence, both profiles are evidently quite different. As before (and as illustrated in Figure 6.16), the drag profile computed for a submerged canopy is assumed to apply to a suspended canopy in a mirrored format. The model, incorporating the above vertical drag profile will henceforth be termed the Ghisalberti & Nepf Model (GNM)

Figure 6.17 presents the vertical structure of velocity and turbulence computed by the GNM, plotted against experimental data. An analysis of results suggests a significant improvement in the performance of the GNM over both the CDM and DLGM. Velocity profiles are simulated quite accurately and the model replicates the vertical turbulent structure quite closely. Again, the discrepancy in results resides within the canopy shear layer at the interface. Here, velocity attenuation is underestimated, and the peak turbulence production occurs at a point within the canopy rather than at the interface between canopy and the free-stream. From Figure 6.16, we see that the computed profile of drag reduces to zero at the canopy interface. A preliminary analysis of these results suggests that this may not be the case and that increasing the flow resistance at the canopy interface may provide better agreement with observed data.

As a first attempt at representing actual resistance at the interface, and following on from previous simulations, the model incorporated a mechanical friction layer. Figure 6.18 presents the numerically simulated values plotted against experimental data.



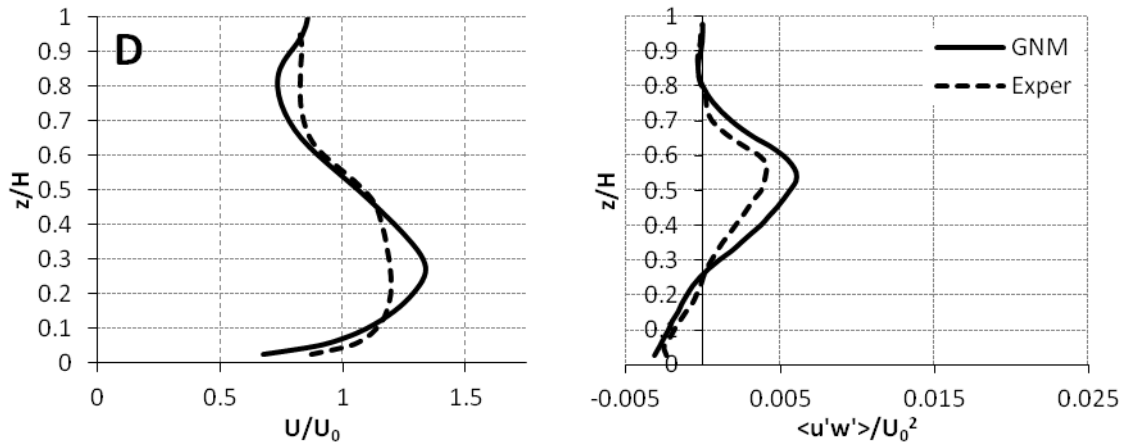
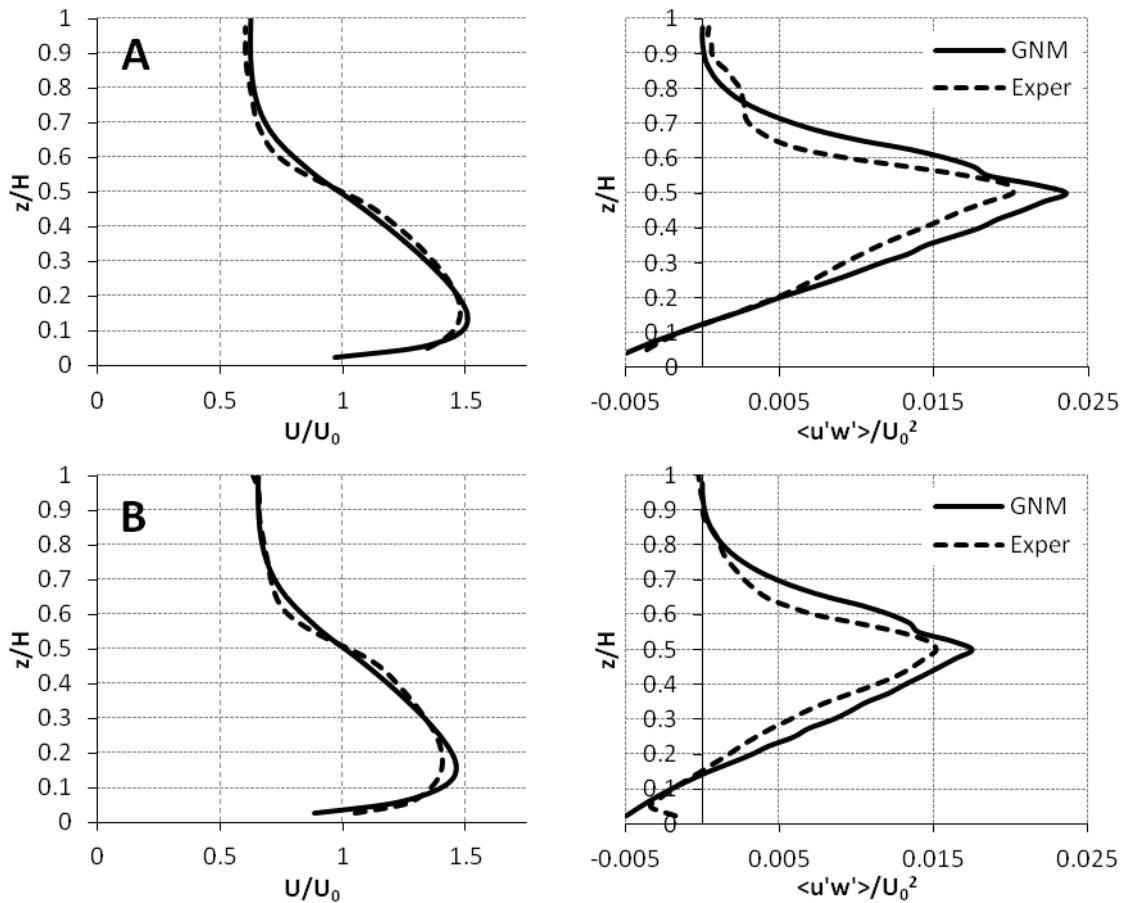
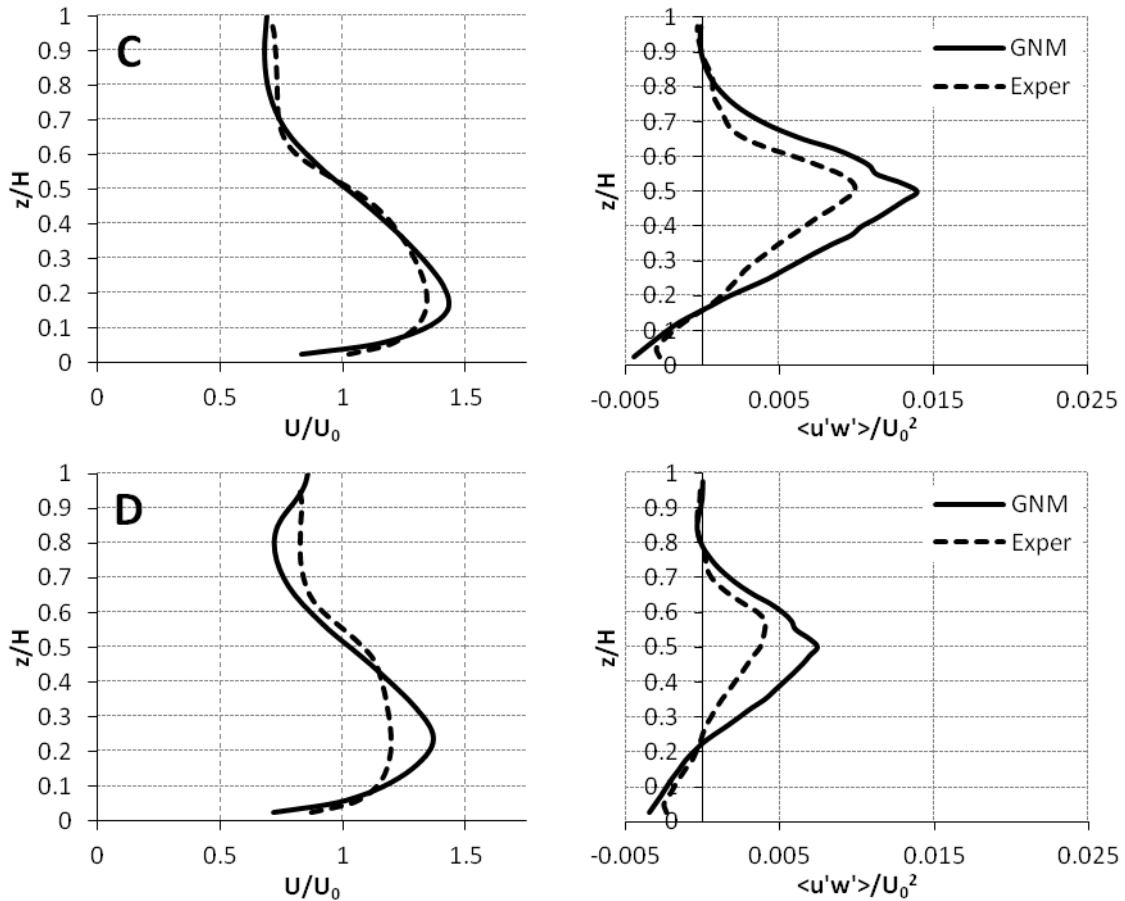


Figure 6.17: GNM model results plotted against experimental data for mean velocity (LHS) and turbulent shear stress variance of turbulence fluctuations (RHS). Table 6-1 presents details on model runs A-D. Drag coefficient,  $C_{DA} = 2.4$ .



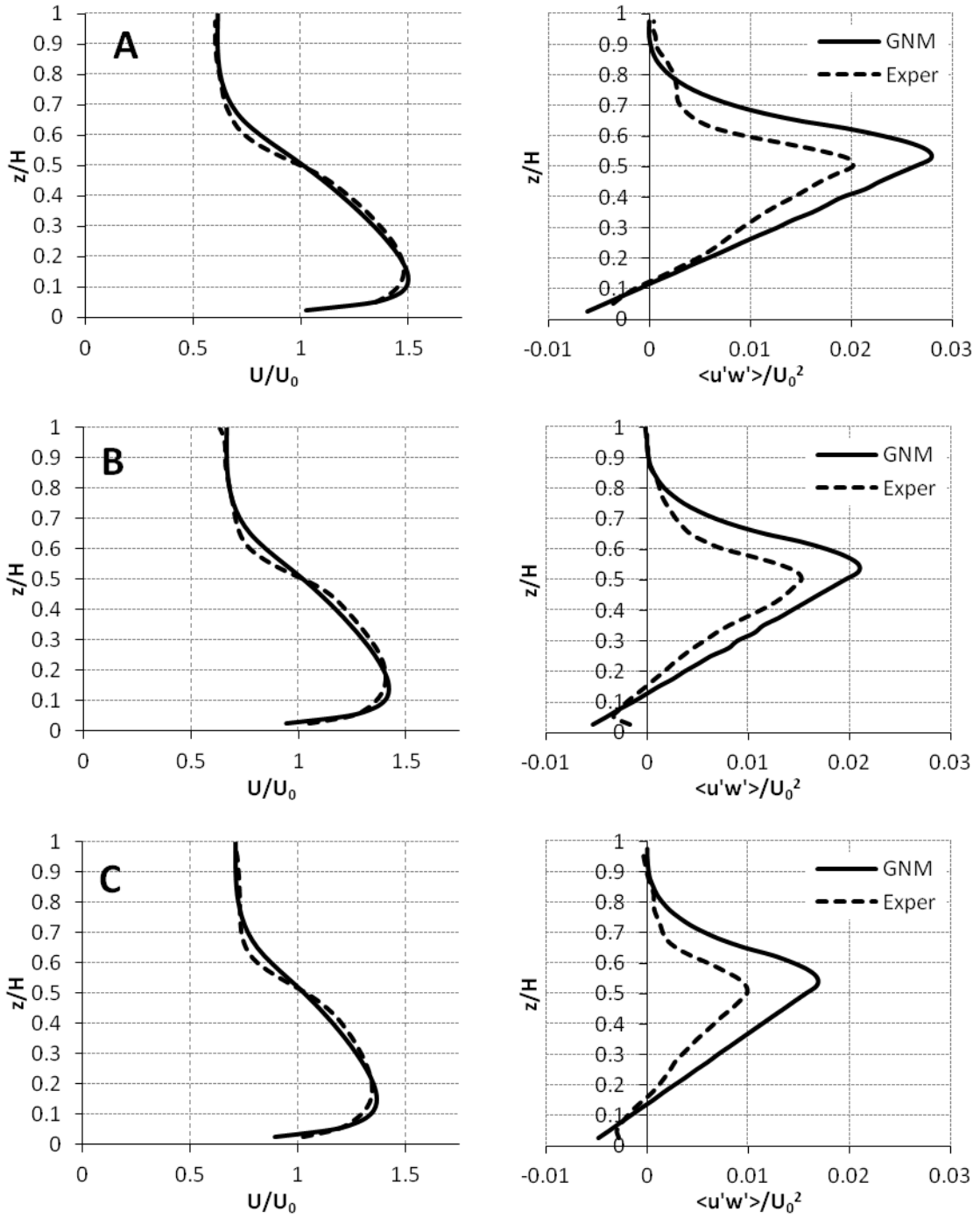


**Figure 6.18: GNM model results with MECHANICAL FRICTION LAYER plotted against experimental data for mean velocity (LHS) and turbulent shear stress variance of turbulence fluctuations (RHS). Table 6-1 provides details on model runs A-D. Drag coefficient,  $C_{DA} = 2.4$ .**

The inclusion of the mechanical friction layer improves the performance of the model in simulating the velocity profile at the canopy interface. As seen in previous studies, the high-friction shear layer better approximates the rapid attenuation in flows observed in experimental studies of flows within the canopy. However, the turbulent profile simulated by the model exhibits a significant instantaneous production component at the bottom of the canopy that does not agree with observed data.

Figure 6.19 plots GNM predicted flow structure incorporating the amended turbulence closure scheme describing additional production terms. As before, the amended turbulence model displays an improvement in the simulation of flow structure across a range of dropper configurations. Close agreement between modelled and experimental

flow profiles are observed for all simulations. However, the model does not accurately replicate observed turbulence profiles well; this represents a marked degradation in performance in this regard.



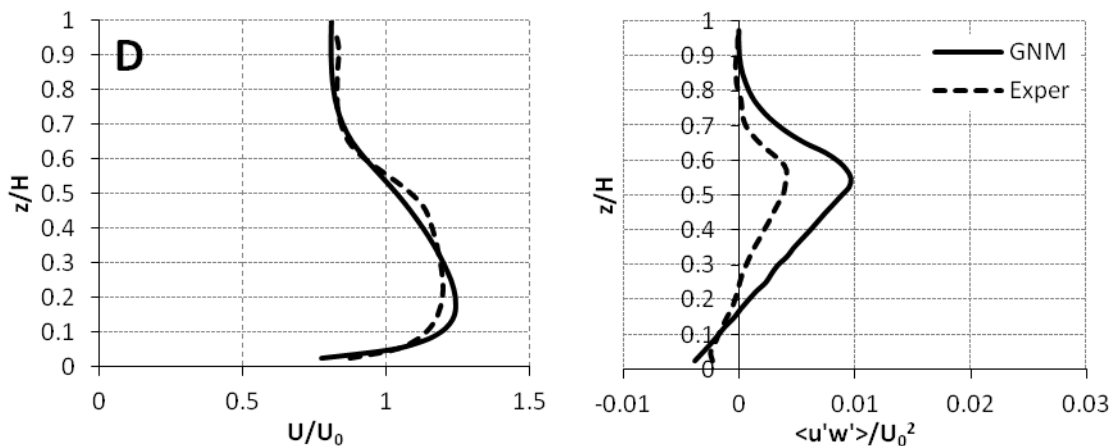


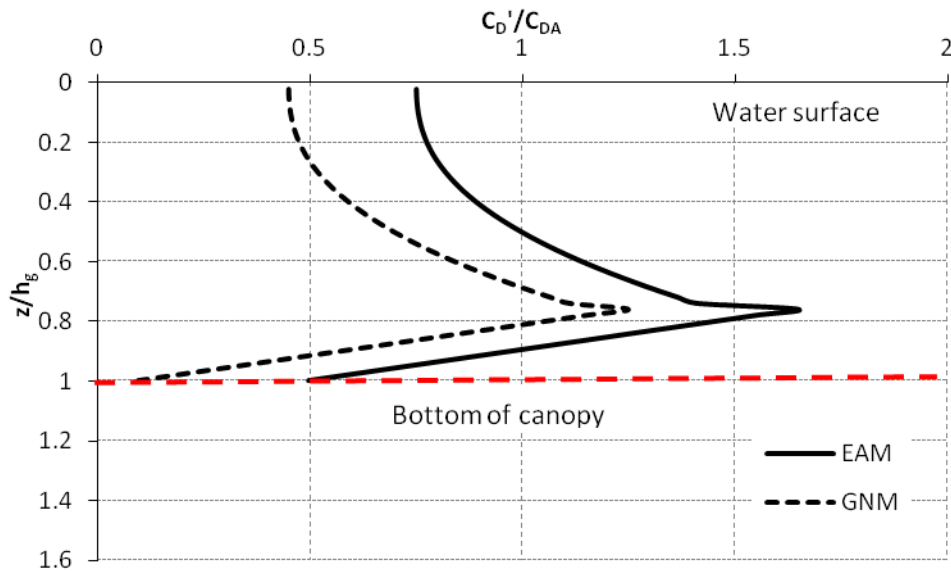
**Figure 6.19: GNM model results with additional TURBULENCE PRODUCTION term plotted against experimental data for mean velocity (LHS) and turbulent shear stress variance of turbulence fluctuations (RHS). Table 6-1 presents details on model runs A-D.  $C_{fk} = 0.07$ ;  $C_{fl} = 0.16$ . Drag coefficient,  $C_{DA} = 3.4$ .**

An analysis of flow processes computed by the GNM displays generally good agreement with observed data. A significant feature appears to be the under-prediction of velocity attenuation and turbulent production at the canopy interface. This is particularly true with regards the turbulent structure. Extensive data exists on the effects of the free end of a cantilevered cylinder on flow, and the corresponding generation of strong vortices and wake disturbances (Raupach and Thom, (1981), Gambi et al., (1990), Ghisalberti and Nepf, (2004)). The GNM predicts that peak turbulence production occurs within the canopy, rather than at the tip of the canopy as literature strongly suggests. These points raise concern over the drag profile adopted for the GNM and in particular the specification of zero-drag at the tip of the canopy. Based on these considerations, a modified drag coefficient was adopted for model simulations; this model is presented in the next section.

### 6.5.3 EFDC Aquaculture Model (EAM)

Previous sections demonstrate that a constant drag coefficient is not sufficient to accurately replicate the flow processes observed in the laboratory. In this section, a drag coefficient is chosen so as to achieve best-fit with observed data. This model will henceforth be referred to as the EFDC Aquaculture Model (EAM).

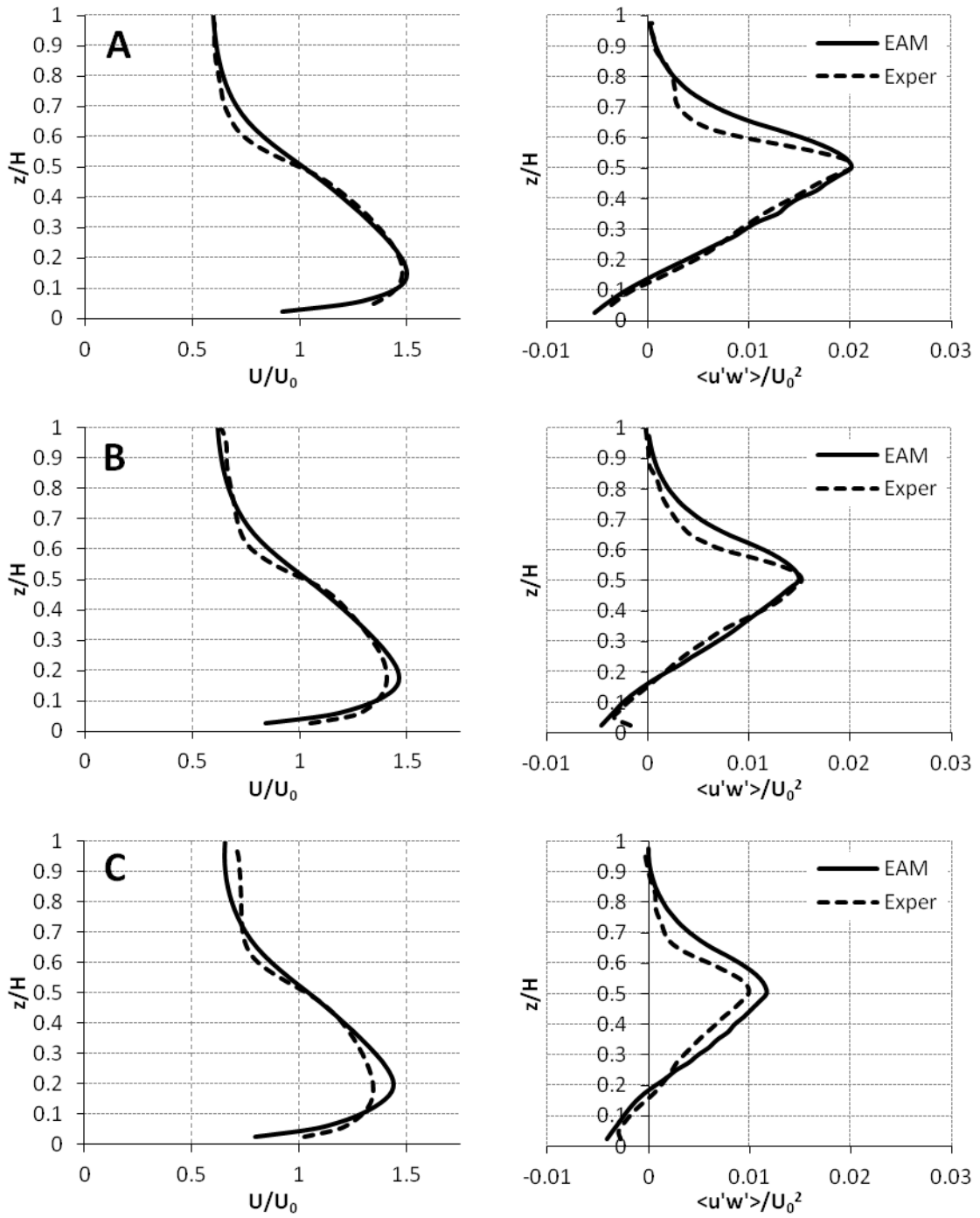
Figure 6.20 presents the drag profile that provided the best agreement with experimental data of flow and turbulence. It consists of a modified version of that proposed by Ghisalberti and Nepf, (2004), with particular emphasis on the drag exerted by the suspended canopy at the bottom. The derived drag coefficient is plotted against that proposed by Ghisalberti and Nepf, (2004), for comparison.



**Figure 6.20: Computed profile of vertical drag coefficient based on experimental data (EAM) plotted against that computed by Ghisalberti and Nepf, (2004) (GNM)**

Figure 6.21 displays EAM computed values of velocity and turbulence plotted against experimental data. Comparisons suggest that the model performs very well in simulating observed processes; particularly at the higher density of cylinders. The model accurately simulates both velocity profiles and turbulent structures. In addition, the model accurately simulates the canopy shear layer and associated processes. Good agreement is obtained between measured values of turbulence, with regards both magnitudes and structure.

The effect of the mechanical friction layer and amended turbulence model on flow structure was also investigated. Figure 6.22 presents predicted flow profile incorporating the mechanical friction layer while Figure 6.23 presents model results incorporating the amended turbulence closure model describing additional turbulence production.



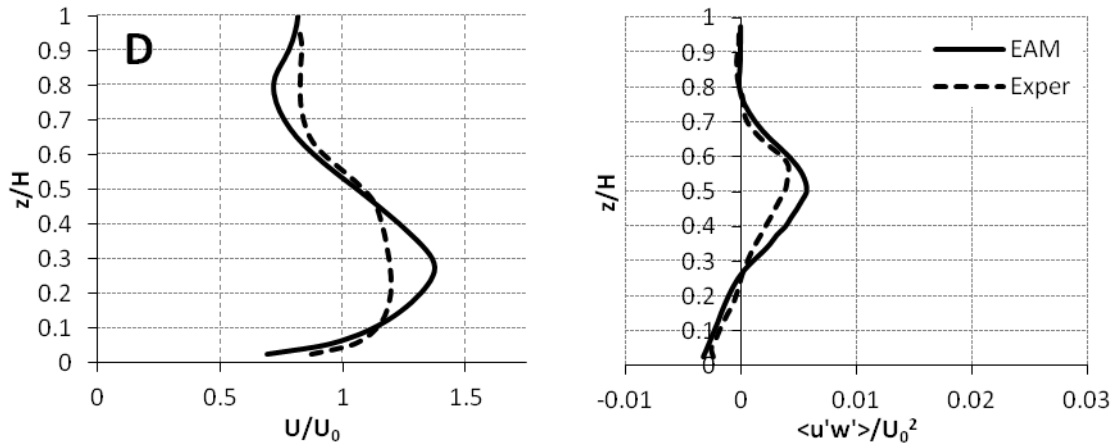
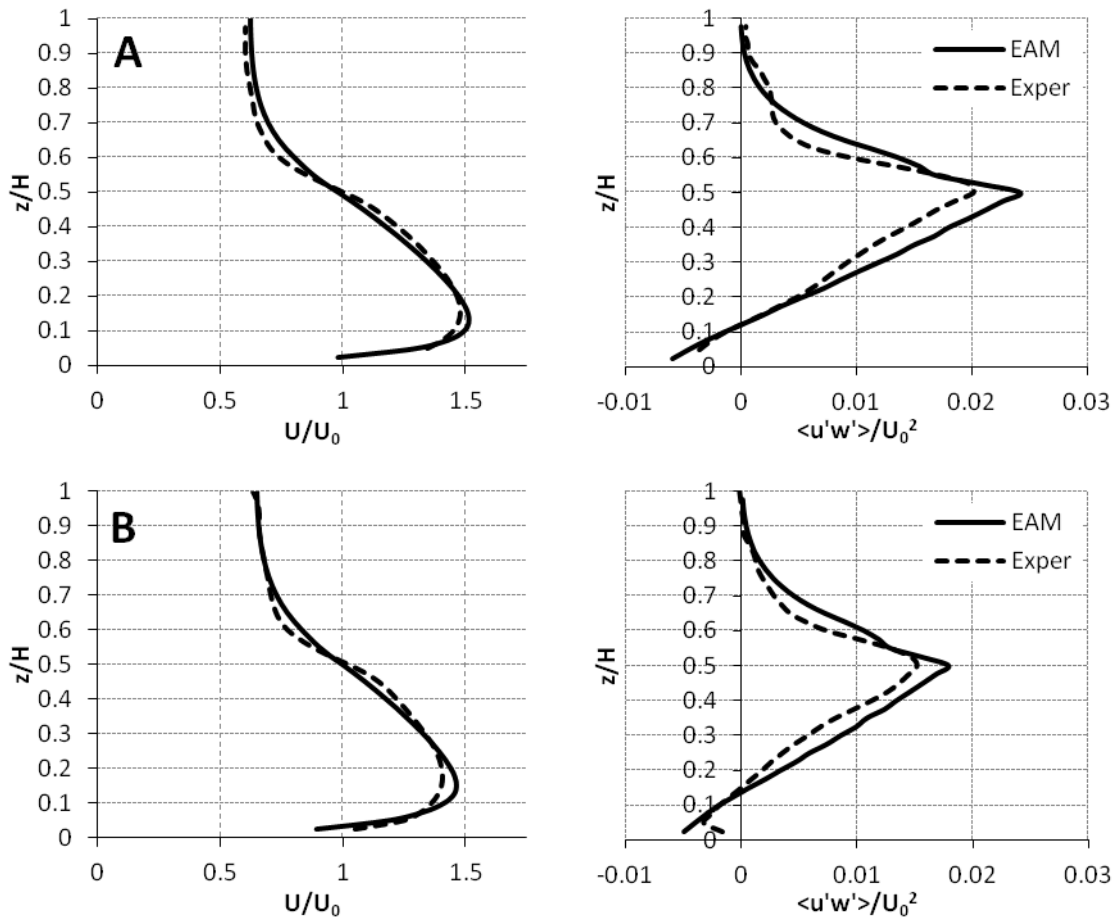
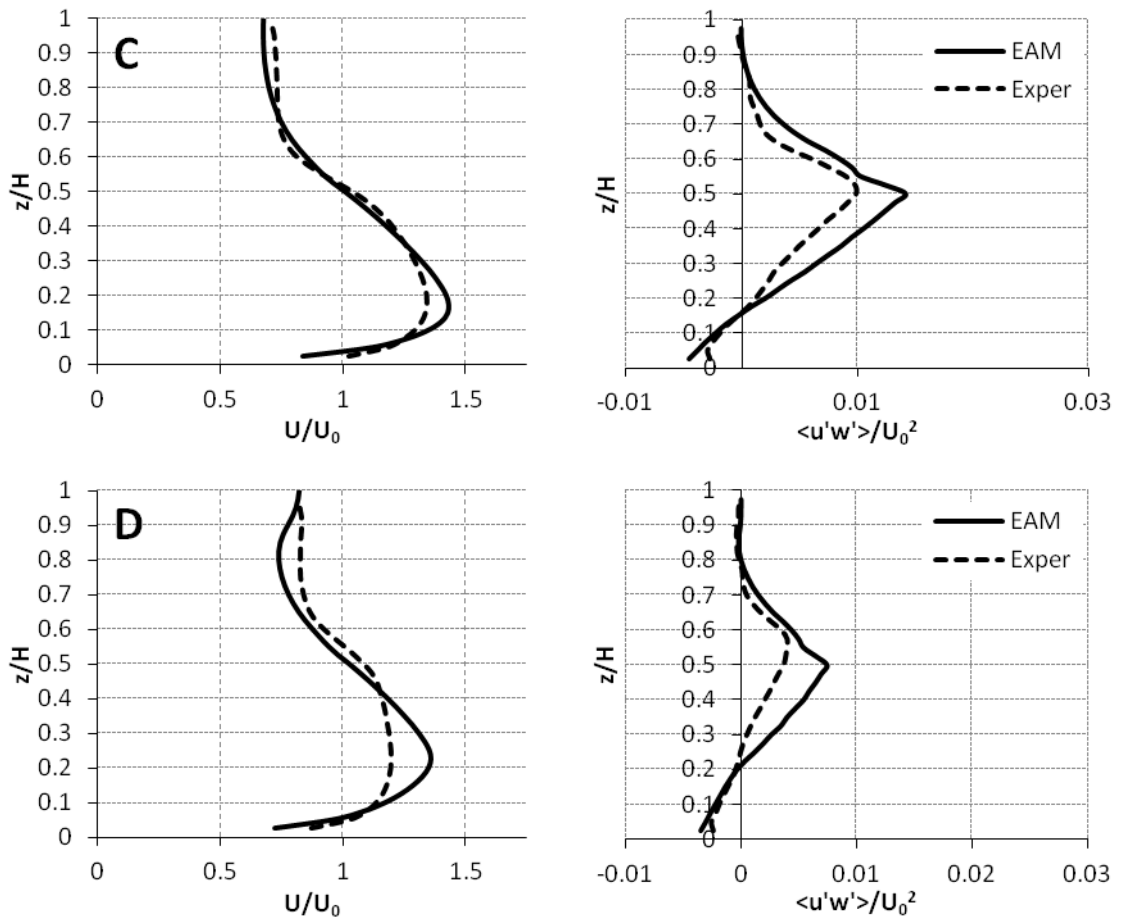
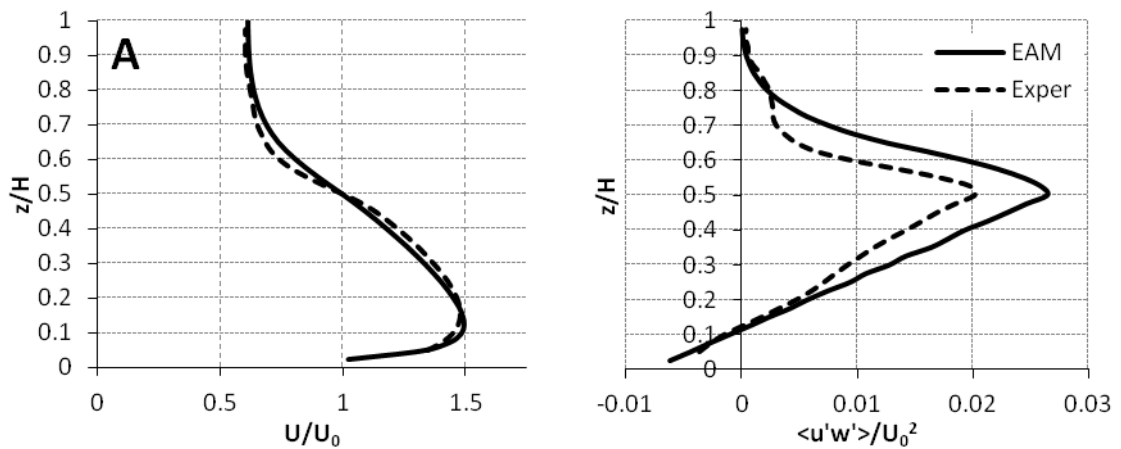


Figure 6.21: EAM model results plotted against experimental data for mean velocity (LHS), and turbulent shear stress variance of turbulence fluctuations (RHS). Table 6-1 presents details on model runs. Drag coefficient,  $C_{DA} = 1.8$ . Details on drag coefficient provided in Figure 6.20





**Figure 6.22: EAM model results incorporating MECHANICAL FRICTION LAYER plotted against experimental data for mean velocity (LHS), and turbulent shear stress variance of turbulence fluctuations (RHS). Table 6-1 presents details on model runs. Drag coefficient,  $C_{DA} = 1.8$ . Details on drag coefficient provided in Figure 6.12**



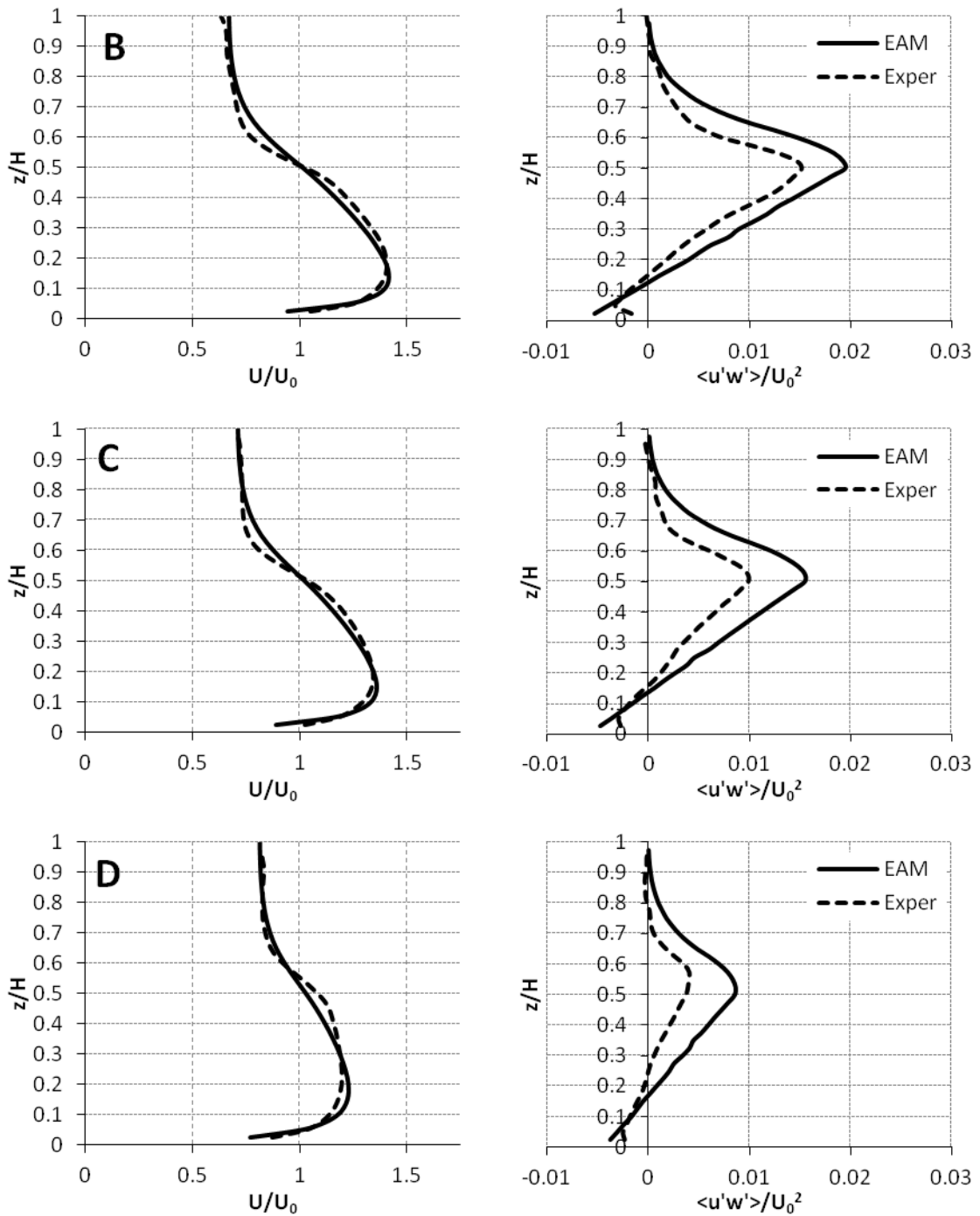


**Figure 6.23: EAM model results incorporating additional TURBULENCE PRODUCTION term plotted against experimental data for mean velocity (LHS), and turbulent shear stress variance of turbulence fluctuations (RHS). Table 6-1 presents details on model runs. Drag coefficient,  $C_{DA} = 2.4$ .  $C_{fk} = 0.07$ ;  $C_{fl} = 0.16$ . Details on drag coefficient provided in Figure 6.20**

As observed in previous sections, model simulations incorporating the mechanical friction layer adversely affect the validation process with regards the turbulent structure. Turbulent production at the canopy interface is overestimated and the predicted profile is adversely affected. On the other hand, a slight improvement in the velocity profile resulted. Better agreement with laboratory data at the canopy interface followed; where the rapid transfer of energy was better simulated by incorporating the large frictional resistance inherent.

The amended turbulence model presented in Figure 6.23 affects both the turbulent structure and the vertical transfer of momentum. As for previous studies, the amended turbulence closure model overestimates turbulence values relative to observed data. This is particularly true at the bottom of the canopy where turbulence is at its greatest.

An interesting feature of these results is the better agreement obtained between velocities, across all model simulations, when the amended turbulence closure model is adopted. All model simulations demonstrate acceptable agreement with observed data, across all cylindrical configurations (runs A-D). The original turbulence model, on the other hand, does not perform well in simulating the flow profile at the lower cylindrical densities (e.g. runs C and D). An explanation for this may be the effect of the increase in turbulence production on vertical momentum transfer. Extensive data exists in literature that describes momentum transfer within the canopy shear layer. The shear layer induces significant production of coherent vortices that dominate the vertical transfer of momentum through the layer (Ghisalberti and Nepf, 2002). These results suggest that to faithfully model observed flow profiles, the accurate quantification of the transfer of momentum between layers is a necessity. Current modelling practise demands the adoption of an appropriate turbulence closure model. The results demonstrate that the adoption of the amended turbulence closure model better simulates the vertical velocity structure. Conversely, the model performs worse in simulating observed turbulent structure. This issue, and its implications, are discussed further in the next section

## 6.6 Discussion and conclusions

This chapter presented the validation of an amended three-dimensional numerical model via laboratory data. The observed structure of flows, including: attenuated canopy flows, shear layer flows, and accelerated free-stream flows was incorporated into the numerical model. The research presented a number of techniques of describing these flow processes, including:

- A mathematical description of attenuated canopy flows via bluff body drag.
- A mathematically valid amended turbulence closure model described enhanced production and mechanical stirring induced by the cylinders.
- A novel friction layer simulated the complex flow structure and processes observed within a canopy shear layer.
- The variation of drag along the length of the cylinder was analysed via reference to literature and laboratory data.

This research presented a number of interesting features. The CDM did not perform well in simulating observed flow structure, particularly at the canopy interface. The model overestimated drag at the surface, while underpredicting the rapid attenuation of flow observed at the bottom of the canopy. The inclusion of the mechanical friction layer improved results somewhat. The model better replicated the flow profile within the canopy shear layer, with particular reference to the canopy-free stream interface. However, the model overestimated the production of turbulence within the canopy shear layer. Nonetheless, the CDM better observes complex shear layer flow structures with the inclusion of the friction layer, than via drag alone.

The research assessed a number of expressions for a varying drag coefficient within the canopy. Of particular interest was the location of maximum drag along the length of a cylinder. Dunn et al., (1996) determined the peak drag to be located at a dimensionless distance of 0.38 from the bottom while Ghisalberti and Nepf, (2004) observed drag to reach a maximum at a distance of 0.76. In this study, the profile proposed by Ghisalberti and Nepf, (2004) provided better agreement with experimental data. The profile

suggested by Dunn et al., (1996) significantly overestimated drag in the upper portions of the canopy structure. This was particularly evident with regards turbulent measurements; where the model simulations significantly overpredicted turbulent structure observed within the canopy.

The GNM performed quite well in simulating observed flow profiles. The model demonstrated good agreement with observed vertical profiles of both velocity and turbulent structure. An observed failing of the model was the simulation of velocities within the canopy shear layer. The model did not accurately simulate the complex flow structure involving a major, rapid attenuation of flow at the canopy-free stream interface. Therefore, as part of this study the laboratory profile derived by Ghisalberti and Nepf, (2004) was modified to provide optimal agreement with observed data.

The EAM provided the closest agreement between modelled and observed flows. The model accurately replicated observed profiles, of both, velocity and turbulence. The adopted profile of drag, satisfactorily computes the complex flow processes observed in the laboratory.

A large body of research exists in literature documenting the interdependency of drag and cylindrical spacing. Ghisalberti and Nepf, (2004) and Wu and Wang, (2004) investigated this interrelationship. Turbulent processes and upstream wake interactions suppress drag development within a cylinder array. This research suggests that a uniform drag coefficient does not accurately model flow processes for all cylindrical configuration. Drag coefficients adopted in this study accurately simulate canopy flow processes within a high density of distributed cylinders. On the other hand, the model performs relatively poorly in simulating processes within the lower-density of distributed cylinders. Results illustrate an interrelationship between drag coefficient and Reynolds number. When the density is higher, the flow velocity and Reynolds number in the domain are smaller and thus, according to the relation of  $C_D$  and Reynolds number for a single cylinder, a larger drag coefficient is required. Hence, to obtain greater agreement between modelled and observed data, at the lower densities of cylinders, a lower drag coefficient than that adopted in this study is required.

A feature previously alluded to, is the effect of the amended turbulence closure model on flow structure. As might be expected, the amended turbulence model simulating production by the droppers, increases turbulence within the canopy, and in particular within the canopy shear layer. A comparison with laboratory data implies that turbulence was overpredicted. However, the model performed better in simulating velocity structure across all cylindrical configurations. The improved performance appears to be a result of the model better simulating vertical transfer of momentum, particularly at the bottom of the canopy.

Within a vegetated canopy, Nepf and Vivoni, (2000), termed the upper canopy the “vertical exchange zone”. The vertical exchange between the canopy and free stream was found to be dynamically significant to the momentum balance, with turbulence production at the tip of the canopy being important. Hence, the accurate simulation of the turbulence structure at the canopy interface is of importance for describing vertical mixing processes. Within the canopy, flows are governed by canopy drag and pressure gradient, with turbulence decreasing rapidly from a peak value at the canopy interface.

An analysis of EAM model results incorporating the amended turbulence model (Figure 6.23), demonstrates a conflicting progression of model performance. Model simulations of velocity structure are in better agreement with experimental data; conversely, plots of turbulent profiles suggest decreased model accuracy. Earlier sections alluded to a possible explanation for this discrepancy. In flows over submerged canopies, the free surface has been found to restrict vortex formation when  $C_{Dah_g} < 1.0$ . In this study, the value was 0.2 for the maximum density of cylinders (run A described in Table 6-1). This data suggests that the limited depth of the flume (0.2m) may restrict the generation of actual flow processes, and in particular, turbulent flow processes. The no-slip boundary condition at the bottom exacerbates the laboratory suppression of flow processes, relative to the free-surface boundary condition for which the greatest amount of reference material exists (e.g. Raupach and Thom, (1981), Nepf et al., (2007)). Hence, laboratory effects may suppress the development of three-dimensional flow processes within the experimental flume.

The analysis of model performance demands that a number of factors be considered, namely: the accurate simulation of velocities; the accurate simulation of the vertical **profile** of turbulence; and known issues with suppression of turbulent flow processes in a depth-limited flume. To further assess the performance of the model in simulating suspended canopy flows, additional details on actual flow processes would be beneficial. The limited depth of the flume is of primary concern. It is the author's belief that increasing the depth of the flume would result in greater turbulent intensity (Dr. Marco Ghisalberti -personal communication).

Therefore, due to the many complexities inherent in the modelling of turbulent structures where boundary effects play a major role; it was decided to focus on the velocity structure for future application and assessment of the model. This chapter presents a widely-used technically-defensible model that has been amended to describe suspended canopy flow processes. Excellent agreement with experimental data was obtained. The next chapter presents the application of the EAM to a designated aquaculture development site on the West Coast of Ireland. The study focuses on the extension of the EAM from the near-field laboratory scale, to the far-field bay-scale.

## **Chapter 7:**

### **Case study: Killary Harbour**

---

*“How inappropriate to call this planet Earth when it is clearly ocean”*

*- Arthur C. Clarke*

## 7.1 Introduction

Killary Harbour is a fjord-like inlet forming part of the boundary between counties Galway and Mayo on the West Coast of Ireland. Running in a southeasterly direction, it is 13km long and approximately 700m wide throughout. With a mean depth of circa 20m, the harbour is deepest, at 42m, just inside the mouth; immediately outside, the bottom rises to some 30m with a gradient of 1 in 130 (Keegan and Mercer, 1986).

Keegan and Mercer, (1986) described the vertical structure of Killary Harbour as a partially mixed estuary with large variations in water structure, that depends on river runoff and local wind. Low-salinity water forms a surface layer above the main body of saline water with the boundary between the layers defined by a halocline. This pronounced halocline developed at a depth of 3 – 10m.

Rope mussel culture commenced in Killary Harbour in the early 1970's. Early studies indicated Killary Harbour had considerable potential for aquaculture developments due to heavy settlement of natural spat, good growth rates and little or no hard fouling. The harbour was designated for aquaculture and boundaries confining farming activities were set in 1984. Long-line cultivation is the dominant form of mussel farming. Long-lines vary in length, but the majority in use in Killary are approximately 110m. Droppers, approximately 8m in length, extend from the long-lines to collect spat and to grow mussels (BIM, 2002). Today's cultivated area is 157ha, with an annual production of 1632 ton year<sup>-1</sup> (fresh weight data; 2006) and a productivity of 10.4 ton ha<sup>-1</sup> year<sup>-1</sup> (Nunes et al., 2011).

Recent expansion of leases and suboptimal growth rates at some farms generated interest in understanding the site-specific factors, which control mussel farm productivity within Killary Harbour. This evidence suggested possible overstocking of some sites in the bay, thus leading to slower growth rates due to flow retardation and decreased phytoplankton availability.

In this chapter, a numerical model of Killary Harbour is developed. Due to the aforementioned stratification and vertical circulation processes that develop, a three-dimensional model was deemed a requirement of any modelling study. The intensive

aquaculture developments also demand consideration. Therefore, Killary Harbour presented an ideal case study site for the three-dimensional EAM (EFDC Aquaculture Model) developed and validated in the previous chapter.

This chapter presents a discussion of the physical features and hydrography of Killary Harbour; with particular attention to the implications for flows and water quality. A discussion of the collection and processing of field data follows. The remainder of the chapter focuses on the development and application of a three-dimensional baroclinic model of Killary Harbour. Data on existing and licensed aquaculture sites provided details on mariculture developments within the harbour. A number of different configurations of farms were assessed, with the focus being on analysing the effects of increased density of droppers. The model investigates both hydrodynamics and water quality parameters within the harbour. By comparison with the benchmark case of no mariculture installations, the effects of the aquaculture developments are quantified and discussed. To conclude, a discussion follows on the implications of the developments on future developments and local ecosystem.

## **7.1 Physical features and hydrography of Killary Harbour**

### **7.1.1 Geographical distribution and topography**

Killary Harbour is a fjord-like inlet on the West Coast of Ireland. Figure 7.1 details the location of Killary Harbour and the distribution of licensed aquaculture sites. The total catchment area of Killary Harbour is some 250km<sup>2</sup> and has an extreme Atlantic climate with predominantly S.W. winds and a high rainfall (2000 – 2800mm year<sup>-1</sup>). As high mountainous ground surrounds the water body freshwater runoff is a significant factor in its hydrography with the Bundorragha and Erriff rivers the principal system draining into the harbour (BIM, 2002). As a result both coastal and brackish estuarine waters are found within the water column causing stratification.

### **7.1.2 Tidal currents and general circulation**

Tidal amplitudes were measured at the locations denoted T1 and T2 in Figure 7.1, and adopted to both force and validate the numerical model. The maximum tidal amplitudes

observed in the harbour were 2.1m on the spring tide and 0.75m on the neap. Freshwater inflow has a significant effect on circulation within Killary Harbour. The principal freshwater sources are the Erriff and Bundorrigha Rivers on the northern side.

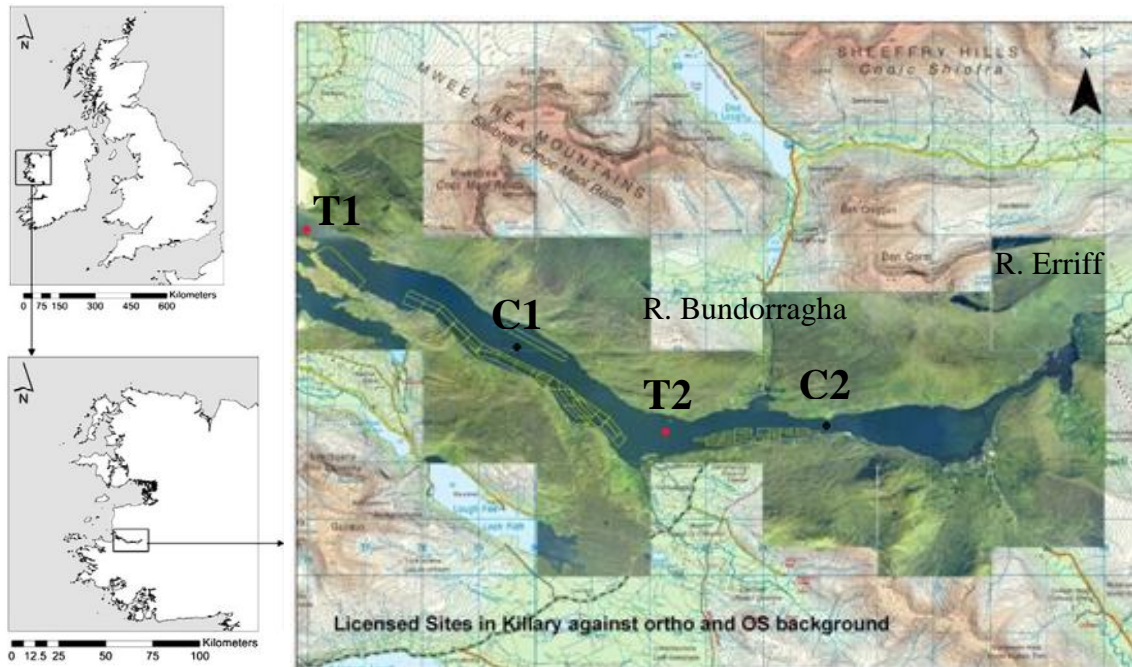


**Figure 7.1: Location of Killary Harbour (left); and detailed map of harbour detailing location of licensed sites outlined in yellow and tide gauges (T1 and T2) and current meters (C1 and C2).**

The net circulation within the harbour is estuarine, with an outflow near the surface and an inflow below. A layer of no net motion develops within the water column and coincides with the halocline at a depth of 3-10m (Keegan and Mercer, 1986). Turbulent processes induce a net vertical transport from the lower layer, through the boundary, to the upper layer (Tully, 1958).

Estuarine circulation develops within a semi-enclosed coastal body when freshwater mixes with seawater (Pritchard, 1952), resulting in the less dense freshwater rising above the saline waters. Strong velocity shear develops at the interface between salt water and fresh water that produces internal wave motion. Flow processes in the upper layer causes vertical entrainment of salt water upwards. Estuarine circulation is the net result of two processes acting simultaneously and in three dimensions; these are advection and turbulent mixing. Advection is the mass transport of water while turbulent mixing

accounts for the random fluctuations of motion and resultant intermixture of adjacent waters (Ketchum, 1952). These two processes result in complex three-dimensional circulation patterns developing within an estuary.

The evidence for estuarine circulation may have interesting geological and biological implications; during periods when vertical mixing is not significant, heavy particles, once in the lower layer, will tend to be trapped in the harbour. This can have many implications for particle residence times and material replenishment.

## 7.2 Implementation of EFDC model

### 7.2.1 Model set-up

The bathymetry data of the study area originates from the Admiralty Chart 2706, and is shown in Figure 7.2. The bathymetric data was interpolated onto a finite difference grid at spacing of 64m. Hence, the model domain was divided into 252 x 103 computational cells. In the vertical direction, 20 layers, each 5% of the total depth was used. The prescribed resolution, both in the horizontal and the vertical, was chosen so as to accurately simulate complex flow processes in a computationally efficient manner.

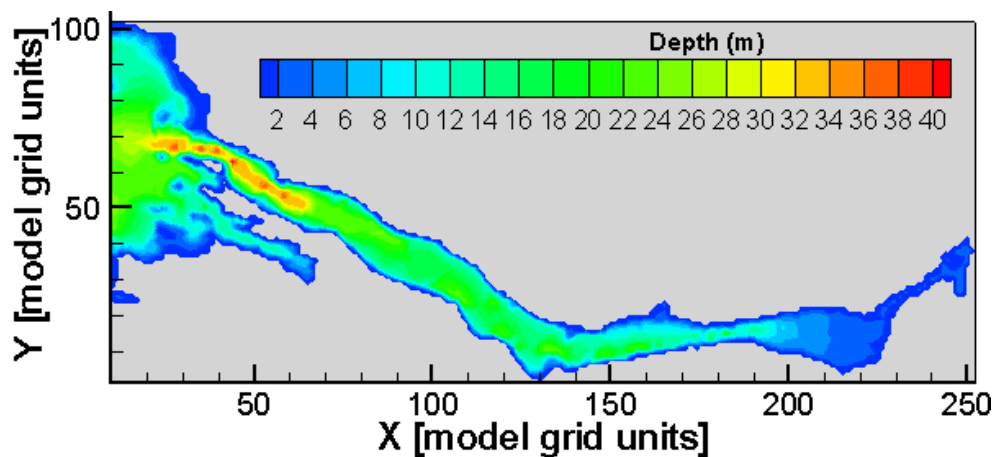
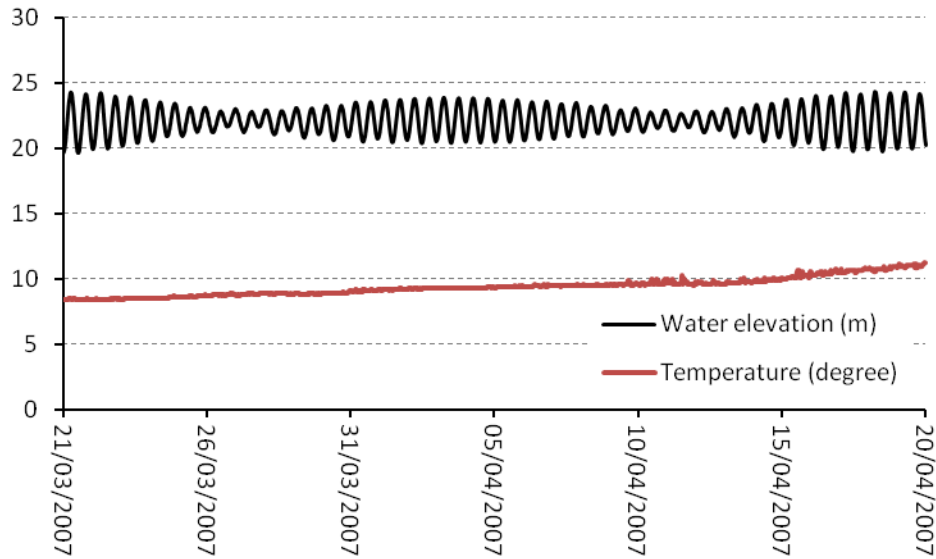


Figure 7.2: Bathymetry map of Killary Harbour

A tide gauge deployed at location T1 in Figure 7.1 provided measurements of tidal elevations and incoming temperature that were used to drive the model. The unit was deployed for a one month period from 23<sup>rd</sup> March to 24<sup>th</sup> April 2007. The tidal elevation and temperature variation with regards to time is presented in Figure 7.3. The incoming

tidal volume was prescribed a constant salinity of 35 parts-per-thousand (Keegan and Mercer, 1986).



**Figure 7.3: Water elevations and temperature recorded in outer Killary Harbour, at location T1 in Figure 7.1. Tide gauge was deployed over the course of a one month period in March 2007.**

The primary freshwater sources of interest were the River Bundorragha and Erriff detailed in Figure 7.1. Hydrological stations maintained by the Environmental Protection Agency provided details on freshwater discharges into the harbour. Due to limited data, prescribed discharges were prescribed based on long term average runoff values. Hence a constant discharge of  $8.1\text{m}^3/\text{s}$  was prescribed for the River Erriff on the eastern boundary and a value of  $2.35\text{m}^3/\text{s}$  for the River Bundorragha on the northern side of the boundary.

A Met Eireann weather station provided meteorological boundary conditions for the model simulations. A range of atmospheric parameters were measured, namely; wind, temperature, relative humidity, air pressure and rainfall. Data was obtained for the period from March-to-April 2007. The meteorological data used for this study is presented in Appendix B. Of particular interest was the effect of wind on circulation patterns. Within a stratified estuary with a pronounced halocline development, wind forcing plays a significant role in mixing the water column and may destroy the halocline if strong

enough. An oceanographic survey of Killary Harbour observed a time lag correlation between strong winds and the elimination of the halocline (Keegan and Mercer, 1986).

Model coefficients were fine-tuned based on field data. The calculation of the bottom friction stress may be the most important for a hydrodynamic model (Guo and Yanagi, 1998). In order to accurately model bed friction, first the bed roughness coefficient has to be established and then the hydrodynamic roughness height must be adjusted through model calibration. The a priori specification of bed roughness coefficient is a difficult task since the relationship between roughness coefficient and the bottom conditions are poorly understood (Fujima, 2001). The bottom stress is calculated from equations (3.55) and (3.56). The model simulates actual bottom conditions by varying the bottom roughness height  $z_0$  to provide agreement with observed flows.

Turbulence within Killary Harbour plays a significant role in vertical mixing processes. Turbulence in the top layer induces a net vertical transfer of water from the lower layers, through the halocline, to the upper layers (Tully, (1958), Keegan and Mercer, (1986)). Hence, the accurate specification of turbulent processes is a prerequisite in the simulation of the complex three-dimensional flow structure. EFDC adopts the Mellor-Yamada closure model (Mellor and Yamada, 1974) to simulate turbulent processes. The model relates turbulence mixing coefficients,  $\nu_v$  and  $\nu_b$ , in the momentum and mass transport equations to turbulence intensity ( $k$ ), turbulence length scale ( $l$ ) and the Richardson number  $R_q$ . The turbulence intensity and turbulence length scale are determined by solving a pair of transport equations for  $k$  and  $kl$  (see Chapter 3). The gradient Richardson number provides quantitative information on the stabilizing effect of buoyancy and the destabilizing effect of velocity shear. It indicates the tendency of the water column to either mix (weak stratification), or resist mixing (strong stratification), (Ji, 2008).

### **7.2.2 Hydrodynamic calibration**

Formally, model calibration has been defined as the “*estimation and adjustment of model parameters and constants to improve the agreement between model output and a dataset*” (Mazzotti and Vinci, 2007). Field data collected during a sampling program conducted during the March-April 2007 period was used to calibrate the EFDC model of

Killary Harbour. Two tide gauges were deployed at locations T1 and T2 detailed in Figure 7.1. The deployment period was from 20<sup>th</sup> March to 20<sup>th</sup> April. As discussed, water elevations measured by the tide gauge in outer Killary (T1), were used to provide boundary water levels to drive the model. The performance of the model in simulating water elevations was assessed by comparison with measured data from tide gauge T2 in middle-Killary. Figure 7.4 presents a graph of computed water elevations plotted against measured data. The model accurately simulates measured data for the 30 day simulation period. The calibration process involved adjustment of the bottom roughness coefficient to a required value. For this study a value of 0.04m proved optimal.

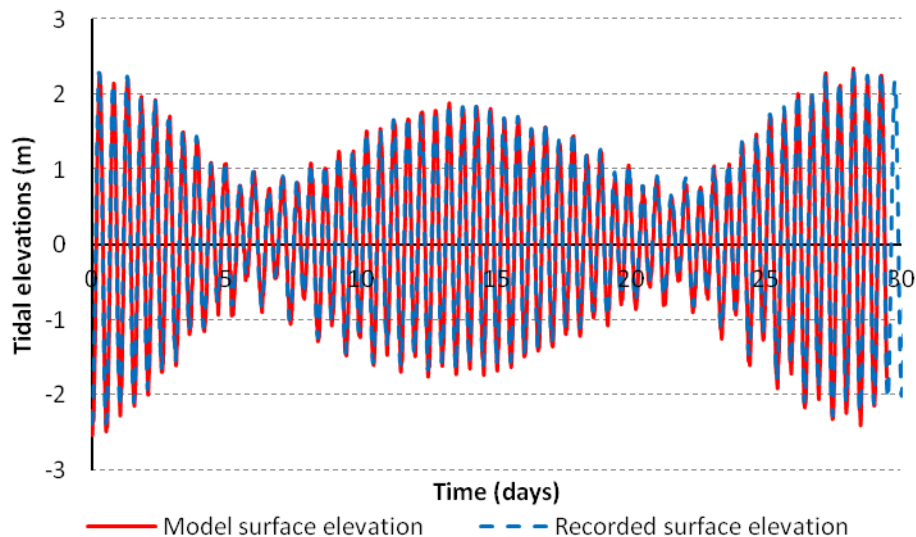


**Figure 7.4: Comparison of computed and measure water elevations at location T1 in Figure 7.1**

Two Recording Doppler Current Profilers (RDCPs) were deployed at locations C1 and C2 in Figure 7.1. The units measured current magnitude and direction at 20 minute intervals for a five-day period. This data enabled the verification of the hydrodynamic model. Figure 7.5 displays measured and computed values of both current velocity and direction in inner-Killary at location C2. Figure 7.6 plots the equivalent datasets at location C1, in outer-Killary.

The model provided satisfactory agreement with little adjustment of model parameters. As mentioned, bottom roughness and vertical mixing and turbulent structure were the

primary factors affecting flow. Bottom roughness coefficients were prescribed based on measured water level data. The turbulence model was found to adequately simulate flow processes with little user-modification required. Two-equation turbulence closure models typically do not require adjustment of coefficients unless significant field data exists on the actual turbulence structure. Empirically derived coefficients are instead prescribed. Within EFDC, the turbulence model is fine-tuned based on a background, additive, constant vertical viscosity coefficient. A nominal value of  $10^{-4} \text{m}^2/\text{s}$  was adopted for this study. Table 7-1 presents a complete list of variables used for this modelling study.

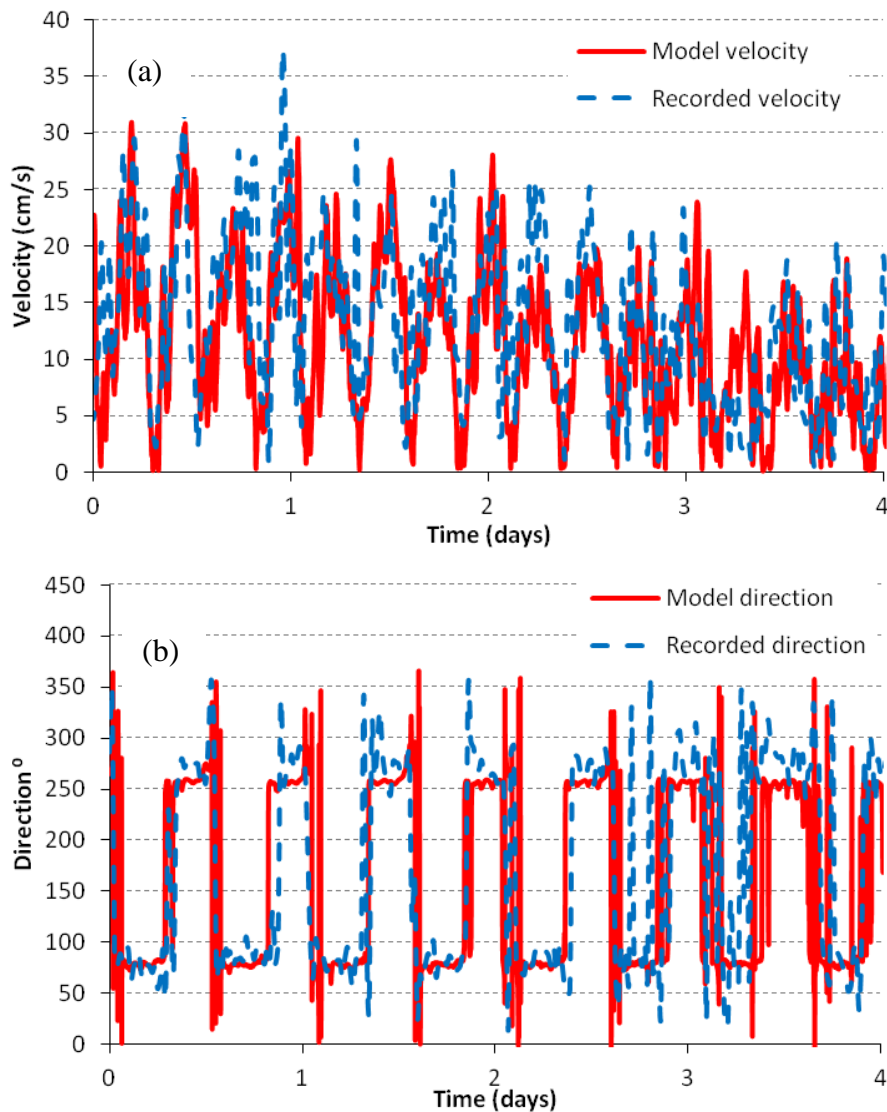


**Figure 7.5: EFDC predicted profiles of (a) current velocity and (b) current direction, plotted against RDCP current meter data recorded at location C2 detailed in Figure 7.1.**

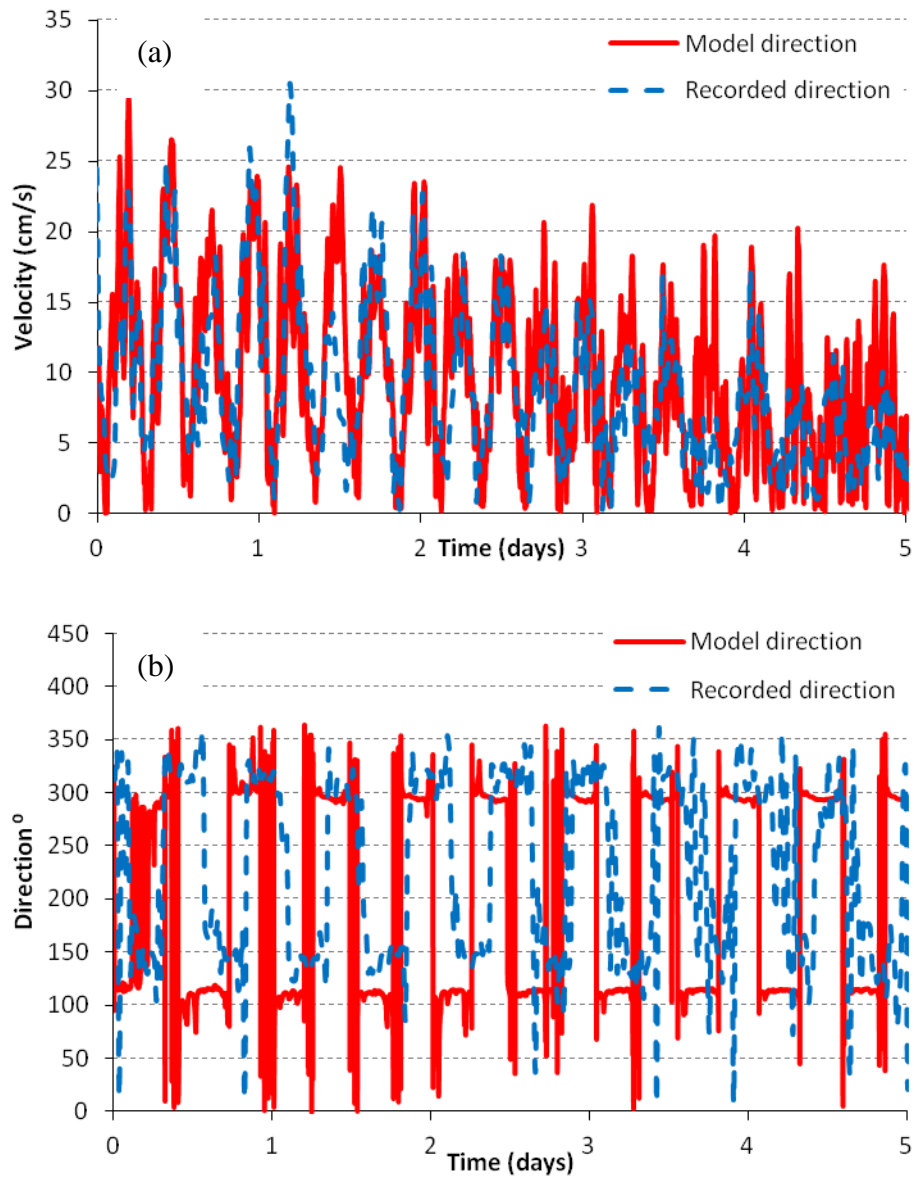


**Figure 7.6: EFDC predicted profiles of (a) current velocity and (b) current direction, plotted against RDCP current meter data recorded at location C1 detailed in Figure 7.1.**

Based on the above data, the model performed well in simulating actual field conditions. Predicted velocity magnitudes and directions were generally in good agreement with measured data. Figure 7.6, however, displays some discrepancies between measured and predicted data, particularly for current direction. Analysing Figure 7.6 shows a significant amount of variation in the current meter data. The pronounced semi-diurnal tidal flows observed in Figure 7.5 are not as distinct; a possible result of

‘noise’ in the Doppler instrumentation. The discrepancy between measured and modelled data could also be a result of the current meter measuring flow processes at scales smaller than the grid. This can be illustrated by considering that the current meter measures virtually a point measurement in space; while the model domain was obtained by overlaying a finite difference mesh on the bathymetric map with grid spacing of 64 x 64m in two mutually perpendicular directions. Hence, some bathymetric irregularities and associated flow processes measured by the current meter may not be included in the model.

**Table 7-1: Variables used for Killary Harbour modelling study**

Variable	Definition	Value	Reference
I	Cells in I direction	252	-
J	Cells in J direction	103	-
K	Number of layers	20	-
$\Delta t$	Time-step [s]	4	Courant Number
$\Delta x$	Cartesian grid spacing [m]	64.0	-
$C_b$	Roughness length [m]	0.04	Literature
$A_H$	Horizontal momentum [ $m^2/s$ ]	55.0	Literature
$\nu_v$	Vertical eddy viscosity [ $m^2/s$ ]	1.0E-04	Literature
$\nu_b$	Vertical diffusivity [ $m^2/s$ ]	1.0E-04	Literature
$W_x, W_y$	Wind speed [m]	Time varying	Weather station

Figure 7.7 presents water circulation patterns predicted by the model at mid-flood and mid-ebb.

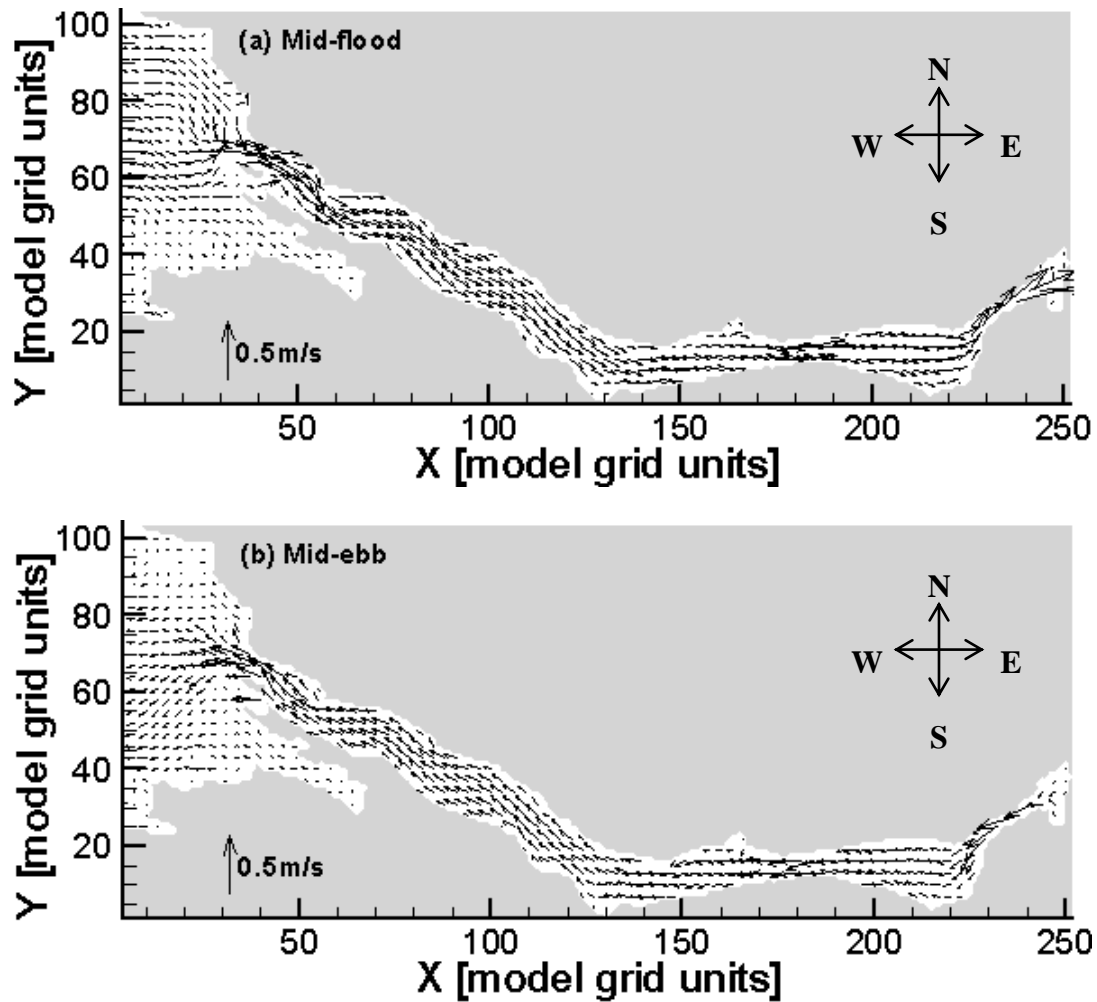


Figure 7.7: Hydrodynamic snapshots of depth-integrated velocities (a) mid-flood and (b) mid-ebb within Killary Harbour

Tidal currents within Killary Harbour are weak and fall in the region of 0.1-0.3m/s. The inlet to the harbour is partially blocked by a small island. This affects flows into, and out of the harbour. On the flood tide, water enters primarily from the northwest while on the ebb tide water exits in the form of a jet. This process may lead to the formation of recirculating eddies, having an effect on the mixing and dispersion of solutes within the estuary. If the flow out of the channel forms a dipole (product of two large counter-rotating vortices (Wells and Heijst, 2004)) having a large enough self-propagating velocity, then it moves away from the channel and is not returned on the flood tide. Otherwise, estuarine flows stays attached to the inlet and exchange is limited (Dabrowski,

2005). Flushing studies further examined mixing and tidal exchange between the harbour and the open sea.

### **7.2.3 Flushing studies**

Material residence times of the entire harbour as well as two subsections were examined. These regions are defined in Figure 7.8. Region A encompasses the entire harbour; regions B and C are believed to behave as two distinct regions and the bend in the harbour serves as a natural boundary between the inner (region B) and outer (region C) regions of the harbour. In addition, region B is nearly three times shallower than region C, and the Erriff River is believed to play a major role in flushing (Dabrowski, 2005).

To investigate the flushing properties of the harbour, the model was run until steady-state conditions were reached (c. 5 days). The specified region was then specified as having uniform initial concentrations of trace,  $C_0$  with subsequent average spatial concentrations,  $C_n$  computed after  $n$  tidal cycles. The model was then run for a period of 40 days with output produced every 12.5 hrs in order to account for the net tidally averaged dye outflow from the region. The runs were conducted adopting the tidal forcing, river inflows and atmospheric conditions previously discussed. Figure 7.8 presents the spatial distribution of residence times in Killary Harbour and its sub-regions. The model results presented include wind forcing and freshwater inflows.

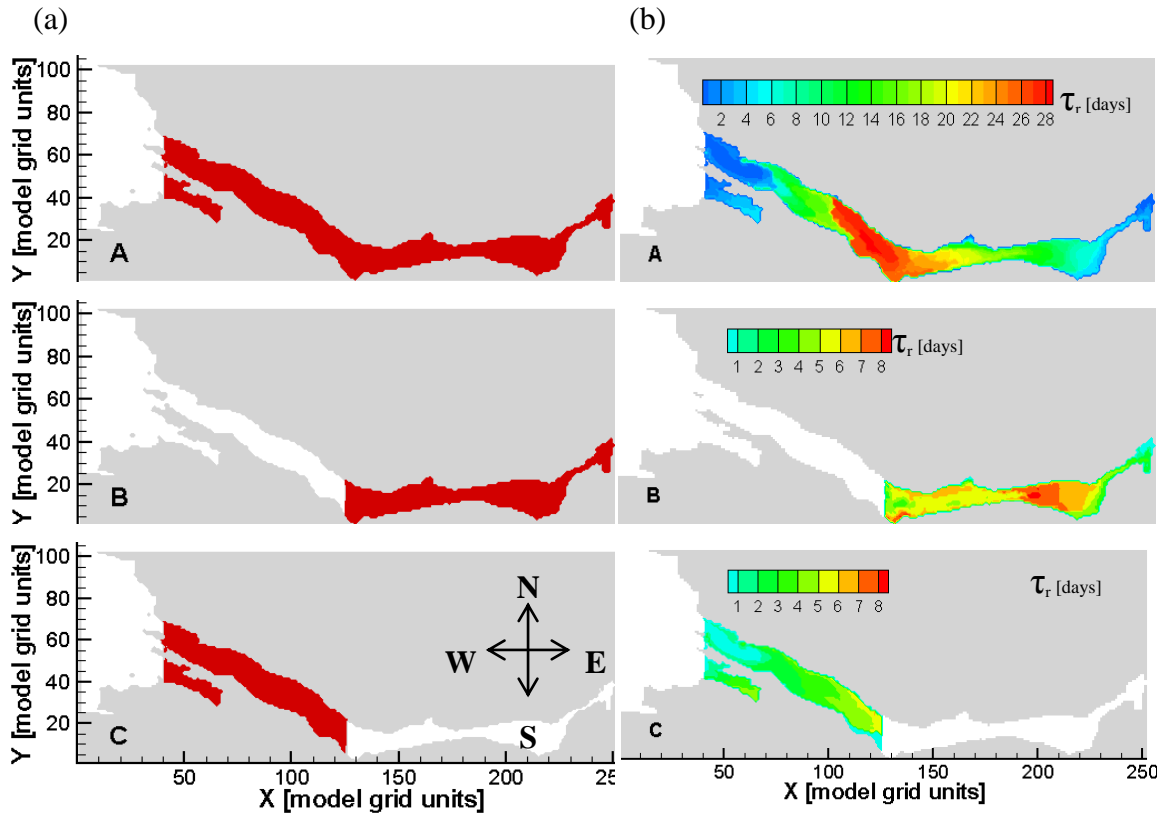


**Figure 7.8: (a)Regions of Killary Harbour selected for flushing studies and (b)spatial distribution of residence times obtained from EFDC**

Table 7-2 summarizes flushing characteristics computed based on the model. Figure 7.9 presents the dye decay curve for Killary Harbour, and its sub-regions; with the remnant function computed from equation (2.7) (corresponding to Region C) presented for comparison. The remnant function parameters A and B were found using the least square method, from which the average residence times were calculated.

**Table 7-2: Flushing characteristics of Killary Harbour sub-regions**

		Constants in the remnant function		Average residence time	Exchange per tidal cycle coefficient
Flushing parameter		A [-]	B [-]	$\tau_r$ [days]	$E \cdot 10^{-3}$ [%]
Simulation					
<b>Region A</b>	<b>No Rivers</b>	0.063	0.733	26.91	22.2
	<b>Rivers</b>	0.089	0.753	15.19	32.7
<b>Region B</b>	<b>No Rivers</b>	0.092	0.706	18.94	28.2
	<b>Rivers</b>	0.126	0.799	7.84	44.5
<b>Region C</b>	<b>No Rivers</b>	0.449	0.415	10.75	32.5
	<b>Rivers</b>	0.447	0.422	10.06	38.2

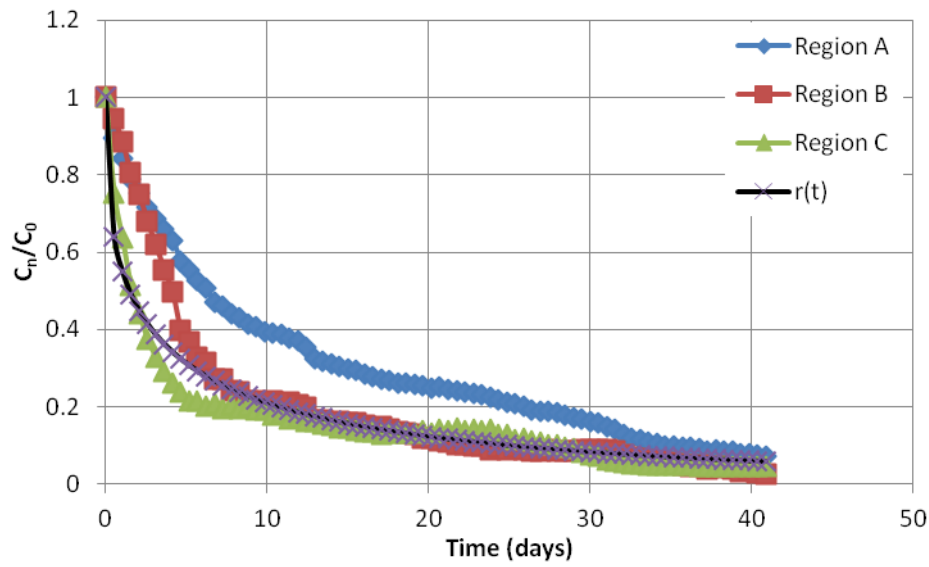


**Figure 7.9: Decay curves of the average dye concentration in region A-C in Killary Harbour**

The average residence time of Killary Harbour is 15.19 days. Table 7-3 demonstrates that river inflows play a significant role in the flushing of Killary Harbour. Model simulations, excluding river inflows, predict a 75% increase in residence times. Similar results were observed by Dabrowski, (2005) who investigated the flushing characteristics of Killary Harbour by depth-averaged, barotropic, model simulations; river inflows were found to reduce average residence times by a factor of four, relative to the benchmark case of no river inflows. Simulations conducted by Dabrowski, (2005) excluded wind forcing which limits the inter-comparison with this study.

Results observed here have implications for water quality within the harbour, particularly during the summer months, when river inflows are at their lowest. The seasonal nature of river discharge demands consideration when adopting flushing study characteristics to quantify water quality and renewal within a harbour.

### **7.3 Aquaculture effects**

The effects of aquaculture installations on Killary Harbour hydrodynamics and material transport were investigated as part of this study. Within the harbour, aquaculture activities are confined to the southern side of the harbour both inner and outer, with the dogleg, or turn of the harbour, being completely free of farms. The locations of

aquaculture farms were identified from departmental licensing data. Figure 7.1 displays the location of these aquaculture sites, while Figure 7.10 presents the farmed regions incorporated into the numerical model.

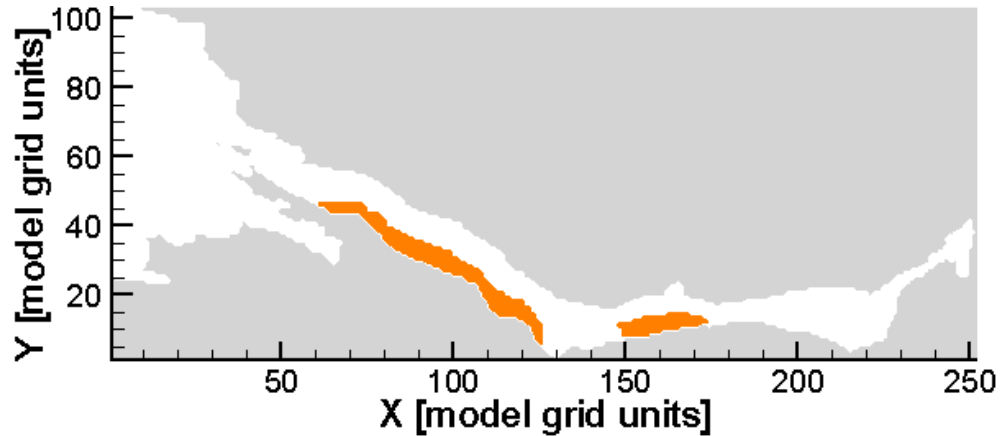


**Figure 7.10: Killary Harbour aquaculture farm locations**

The amended three-dimensional EFDC model described in the previous chapter was adopted to simulate flows within the harbour. All licensed sites were assumed to contain droppers with typical dropper densities being estimated based on line surveys conducted by BIM personnel in January 2009. Model simulations were conducted with three dropper densities, namely: high density of droppers ( $0.425 \text{ droppers m}^{-2}$ ), medium density ( $0.212 \text{ droppers m}^{-2}$ ), and low density ( $0.106 \text{ droppers m}^{-2}$ ). Densities were computed based on licensing data and a line survey conducted by BIM in 2009. Droppers were assumed to extend half the water depth, where the water depth exceeded 12m; otherwise, droppers were excluded. The choice of drag coefficient considered laboratory studies and the relatively low density of droppers. A value of 1.0 was specified. The vertical profile of drag was derived for the EAM discussed in the previous chapter. Simulations were conducted under spring tide conditions (tidal amplitude = 1.74m) with no freshwater inflows.

Figure 7.11 presents flow-fields on the flood tide, while Figure 7.12 presents flow-fields on the ebb. Flow-fields are for layer 15 of the numerical model which is at mid-height of the suspended canopy. The effects of the aquaculture farms are demonstrated in

Figure 7.11(b) and Figure 7.12(b). These simulations incorporate a dropper density of  $0.425\text{m}^{-2}$  within the highlighted areas.

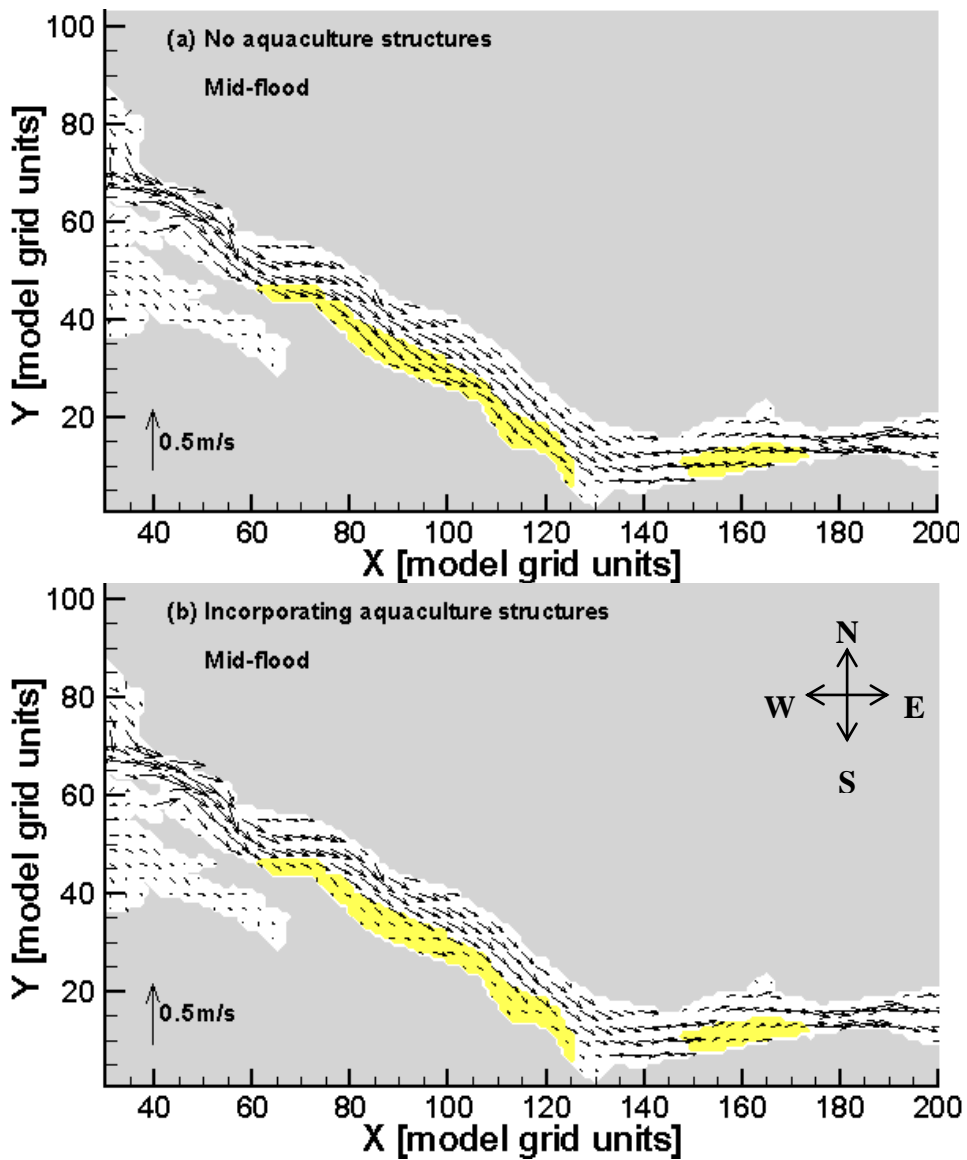


Figure 7.11: Hydrodynamic snapshots at mid flood for (a) no aquaculture structures and (b) aquaculture structures included. The yellow cells represent the location of the farms.

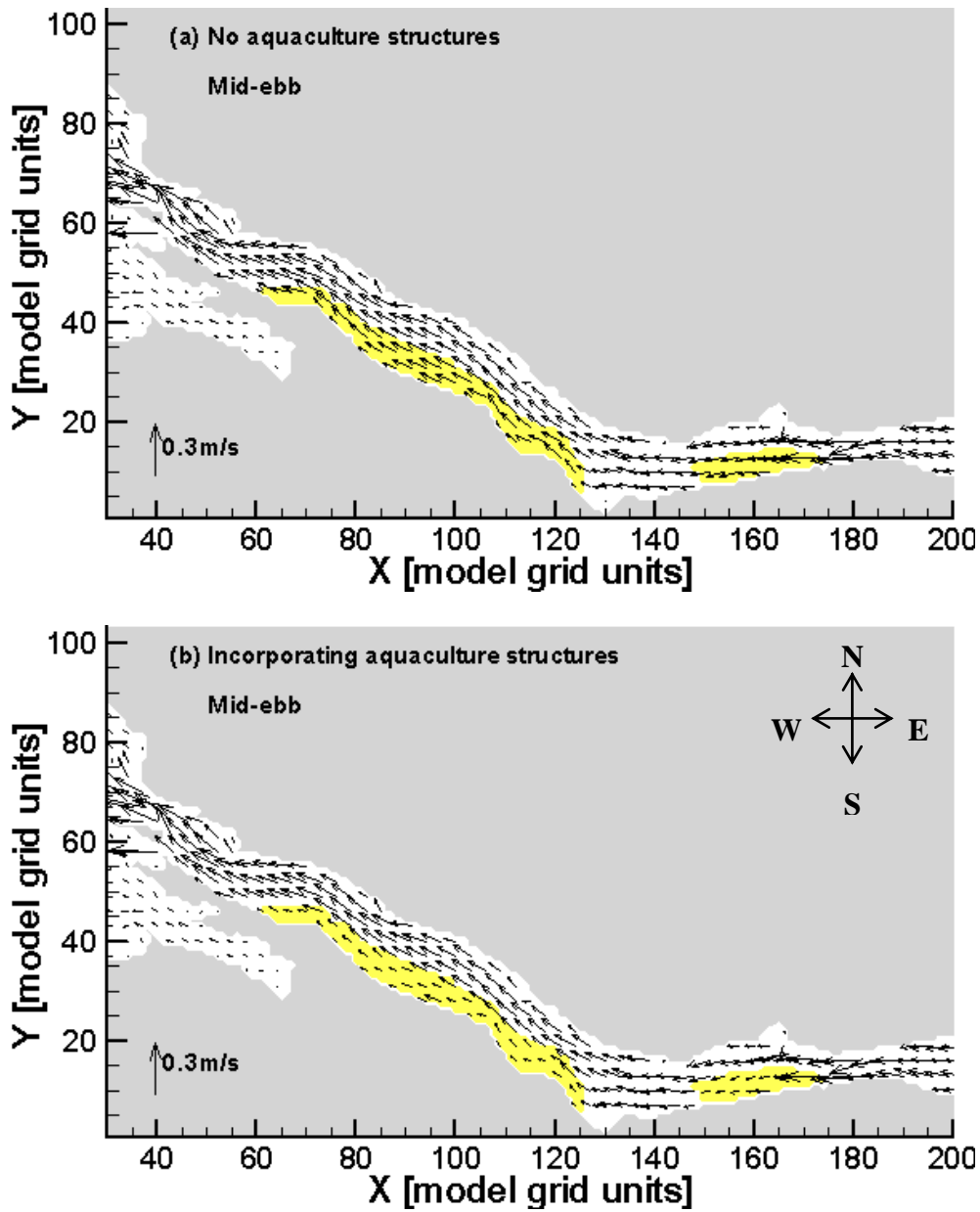


Figure 7.12: Hydrodynamic snapshots at mid ebb for (a) no aquaculture structures and (b) aquaculture structures included. The yellow cells represent the location of the farms

A significant attenuation of flows is evident within both the inner and outer farms. Some diversion around the farms is observed with the dominant flow assumed to be under the farms. Flow dynamics were quantified in terms of velocity differentials of velocity and relative velocity. Differentials were computed by the equation

$$AD_{i,j} = \Phi_{i,j} - \phi_{i,j} \quad (7.1)$$

$$RD_{i,j} = \frac{(\Phi_{i,j} - \phi_{i,j})}{\Phi_{i,j}} \times 100 \quad (7.2)$$

for  $i=1,2,3\dots i_{max}$ ;  $j=1,2,3\dots j_{max}$

where,  $\Phi$  is the model variable with no modification,  $\phi$  is the model variable with aquaculture installations included AD is the velocity differential and RD is the relative velocity percentage differential.

Figure 7.13 presents the velocity differential computed within the harbour while Figure 7.14 presents the relative percentage differentials. Differentials (a) within the dropper layers and (b) at mid-distance between the bottom of the canopy and the bed are presented. Differentials are presented relative to unimpeded flows. Hence, a positive value signifies a decrease in flows; while negative values indicate an increase in flows.

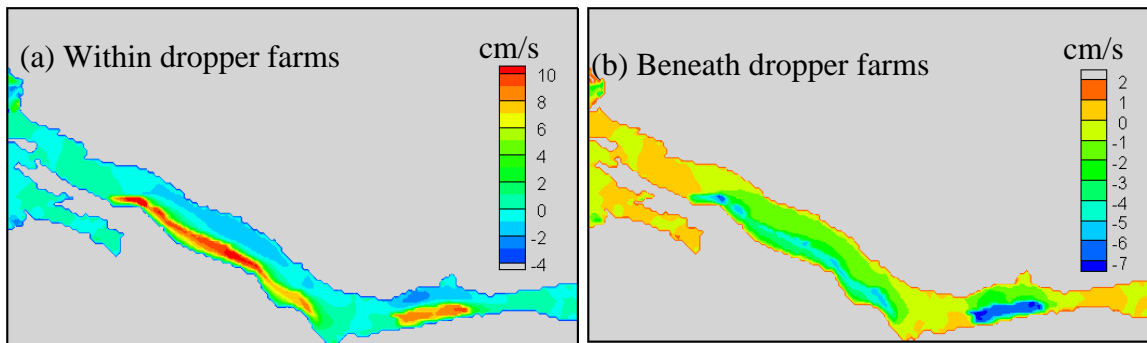


**Figure 7.13: Absolute differentials of velocity (a) within the mussel dropper farms and (b) beneath the mussel dropper farms.**

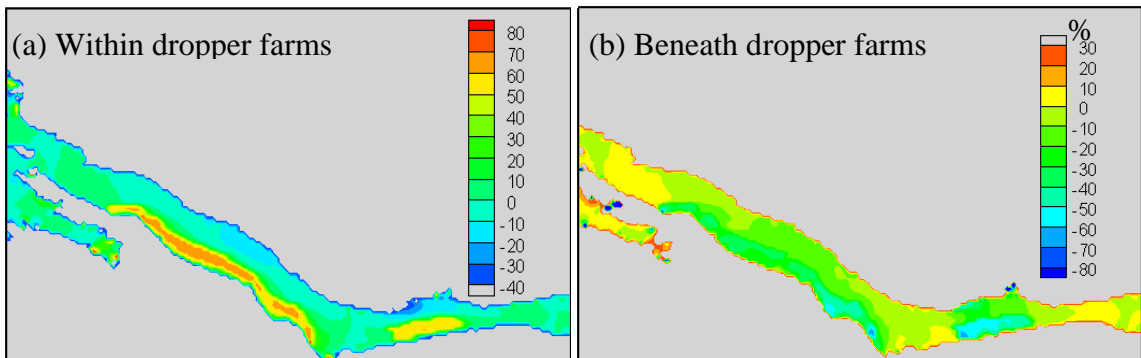


**Figure 7.14: Relative percentage differentials of velocity (a) within mussel dropper farms and (b) beneath mussel dropper farms.**

These figures illustrate the highly significant attenuation of flows induced by the aquaculture installations. Flows within the farm are reduced by up to 70% with a similar increase in flows observed beneath the farms. Some diversion of flow around the farms is observed, with flows increased by circa 10%.

Effects of different dropper densities were also examined. Figure 7.15 presents velocity differentials calculated incorporating a medium density ( $0.212\text{m}^{-1}$ ), and low density ( $0.106\text{m}^{-1}$ ) of droppers. As expected, the effect of the structures decreases with decreased densities. At the maximum density of droppers (Figure 7.13), flow attenuation of circa  $10\text{cm/s}$  was observed; while at the lowest density flows were reduced by circa  $6\text{cm/s}$ .

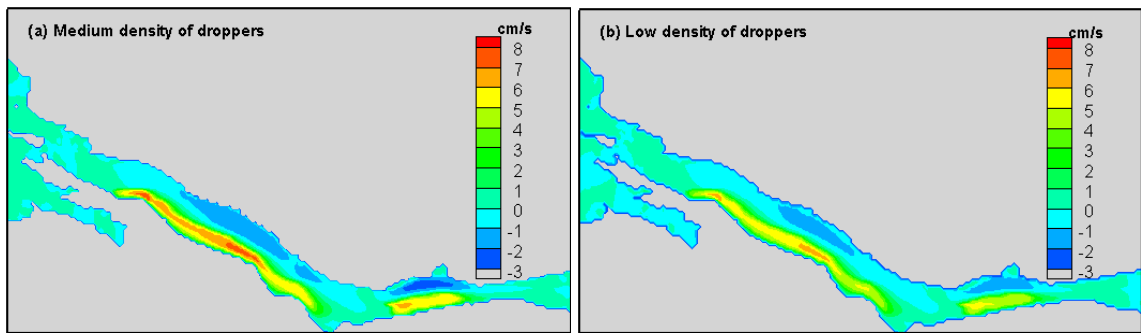


**Figure 7.15: Absolute differential of velocity at different dropper densities (a) medium density of droppers and (b) low density of droppers.**

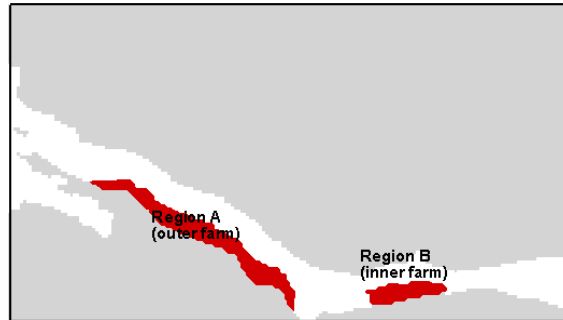
These studies demonstrate the highly significant effects of the aquaculture installations on flow dynamics. In the next section, the implications on water quality are considered.

#### **7.4 Flushing time scales**

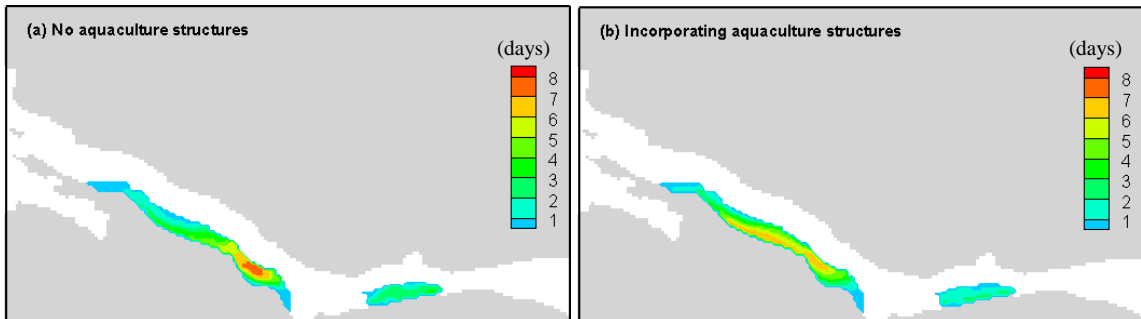
The effect of the aquaculture structures on material transport and residence times was examined. The primary focus was on material transport time scales within the actual aquaculture farms. All cells containing aquaculture installations were coded as having uniform initial concentrations of trace,  $C_0$  with subsequent spatial concentrations,  $C_n$ , computed after  $n$  tidal cycles. Figure 7.16 presents the location of the dye release regions. Spring tide conditions forced the model with no river inflows included.

The flushing studies focused on the *pulse residence times* (PRT) of the farmed sites as opposed to the average residence times of the entire harbour discussed in the previous section. Miller and McPherson, (1991) defined the pulse residence times as the time to

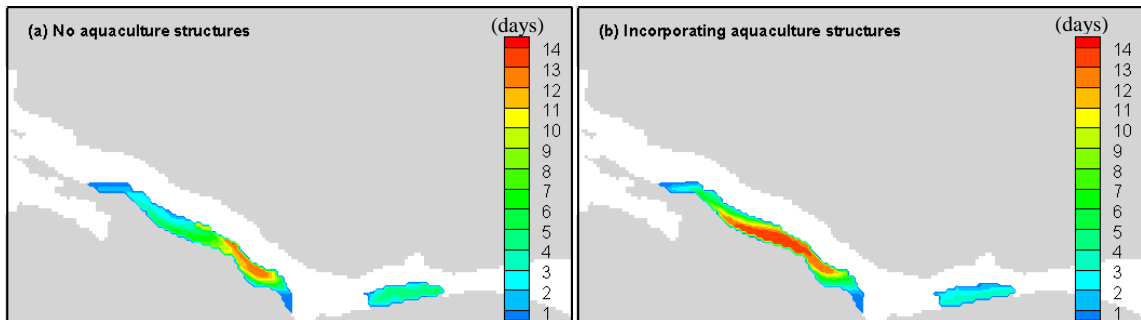
flush a given fraction (e.g. 90%) of a conservative constituent from an estuary if it is introduced at a certain location. Section 2.4 presents additional details on residence time formulae. Figure 7.17 presents a spatial distribution of the time required to flush 63% of a conservative constituent; Figure 7.18 presents the time to flush 75% of the tracer.



**Figure 7.16: Regions of Killary Harbour selected for flushing studies. Region A corresponds to farmed area in outer Killary and Region B corresponds to farmed area in inner Killary.**



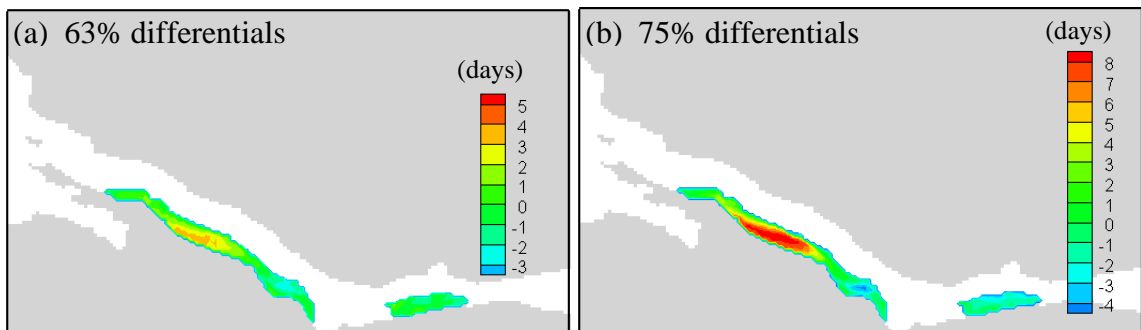
**Figure 7.17: PRT 63% (the time to flush 63% of conservative tracer) for (a) no aquaculture structures included and (b) aquaculture installations included.**



**Figure 7.18: PRT 75% (the time to flush 75% of conservative tracer) for (a) no aquaculture structures included and (b) aquaculture installations included.**

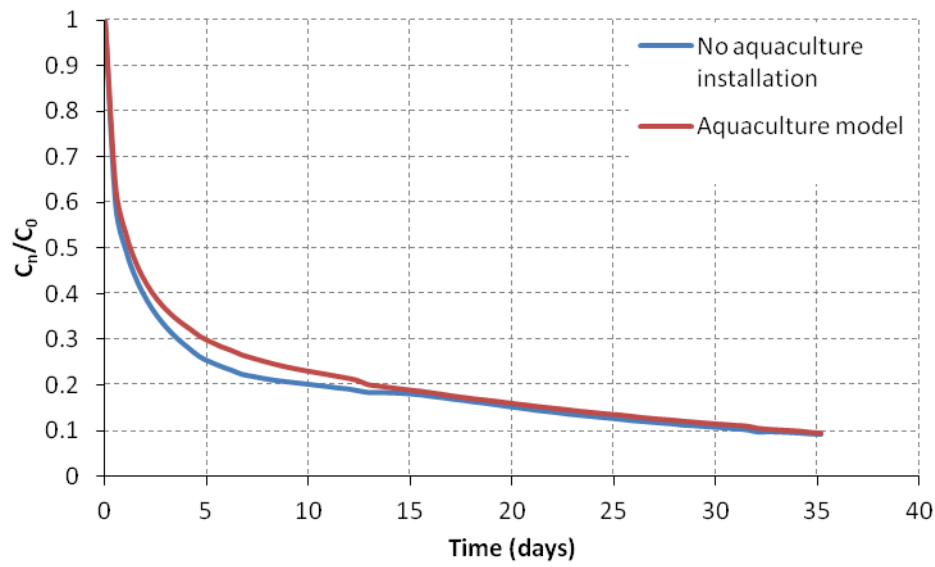
The inclusion of the aquaculture structures affects the removal of materials from the farms. For both 63%, and 75% removal of tracer, the flushing times are significantly increased. These effects were quantified in terms of a simple differential calculation in a similar fashion to the velocity differentials calculated in equation (7.1).

Figure 7.19 presents the computed residence time differentials. The farms increased residence times quite significantly; an order of magnitude increase is observed in large sections of the domain. In the central region of the farms, residence times were increase by up to eight days (Figure 7.19(b)).



**Figure 7.19: Pulse residence times differentials. Increase in residence times induced by the presence of the droppers. (a) 63% of material removed and (b) 75% of material removed**

Decay curves of the average dye concentration within the outer farm (Region A) predicted by EFDC are presented in Figure 7.20. Residence times were estimated for 50, 63, 75 and 90% constituent replacement, in an equivalent manner to Miller and McPherson, (1991). Table 7-3 summarizes the results obtained.



**Figure 7.20: Decay curves of the average dye concentration in Region A of Killary obtained from simulations based on EFDC.**

**Table 7-3: Pulse residence times within the aquaculture farms.**

Pulse Residence Times	Region A		Region B	
	No Aquaculture	Aquaculture	No Aquaculture	Aquaculture
PRT 50% [days]	0.98	1.2	0.7	0.9
PRT 63% [days]	2.2	2.8	1.3	1.8
PRT 75% [days]	5.3	8.0	2.6	3.8
PRT 90% [days]	34	34	21.5	21.5

The aquaculture installations significantly extend residence times within both regions A and B. The model predicts a 50% increase in the time it would take to flush 75% of the original water from region A with a similar, 46%, increase predicted for the flushing of region B. The simulations neglected river inflow, which based on flushing studies conducted in the previous section, were not expected to significantly affect residence times in these regions of the harbour.

An interesting feature observed, is that the time to remove 75% of the material is increased by circa 50% when aquaculture structures are included for both regions, while the aquaculture structures do not influence the 90% PRT of the harbour. This suggests that different flow processes affects flushing of material at different time-scales. The reduced flow rate affects material exchange rates for time scales <20 days (Figure 7.9), however, for time scales greater than this, the attenuated flows do not significantly affect residence times. A similar flushing characteristic was observed in another study involving the author; the effects of tidal turbines on the flushing characteristics of an estuary were investigated (Hartnett et al., 2011). In that study, the reduced flows induced by the tidal turbines initially hindered the removal of material, thereby increasing residence times relative to the unimpeded flow situation; however residence times for 90% removal of a hypothetical constituent converged to an identical value for both modelled scenarios. These results are qualitatively equivalent to this study.

## **7.5 Discussion**

This chapter examined the effects of aquaculture installations on flow dynamics and water quality within an actual aquaculture site. The EFDC hydrodynamic model was applied to Killary Harbour, on the West Coast of Ireland. An extensive field-monitoring program provided data to force and calibrate the hydrodynamic model, namely: current meter, tide gauge and weather station data. The model provides information on hydrodynamics and material residence times within the harbour. Simulations assessed time scales of transport of two distinct regions of the harbour, and the harbour as a whole.

The average residence time within Killary Harbour for mean annual river runoff equals 15.19 days. This value increases to 29.61 days, if simulations neglect river discharges completely. From Figure 7.8, it can be seen that the inner regions of Killary Harbour are efficiently flushed by river discharge from the Erriff. Outer Killary also exhibits quick and efficient flushing of material with strong tidal exchange promoting good mixing and low residence times. However, residence times within the central regions of Killary Harbour are significantly longer. The region characterized by maximum residence times is approximately 5km upstream from the harbour mouth, before the ‘dogleg’. These areas

are of importance from an aquaculture development point of view with a large number of farms contained in this area. This has implications for the supply of nutrients and removal of toxins from the fish farms.

The amended model, described in the previous chapter, was adopted to simulate flows and material transport within the farmed regions of the harbour. Line survey data provided information on typical density of droppers within farms. Figure 7.11 and Figure 7.12 presents modelled flow-fields within the harbour. Based on a typical configuration and density of droppers, within-farm flows were reduced by up to 70% from ambient. Some flow diversion around the farms (circa 10%) was observed, with the greater portion being diverted under the suspended farms. Flows beneath the farms increased by 40-60% due to the effects of the farms. These results are comparable to field studies conducted by Boyd and Heasman, (1998); current meter measurements within suspended aquaculture farms displayed a decrease in flows of up to 80%, with diversion around and underneath the farms observed. Plew et al., (2005) investigated flows within and underneath a suspended mussel dropper farm. ADP measurements demonstrated a 36-63% reduction in average currents within the farm, while flows beneath the farm were an order of magnitude greater. For filter feeders such as mussel droppers, lower current speeds within farmed areas reduce the supply of seston and increase the risk of seston depletion, both of which may limit production (Hawkins et al., (1999), Pilditch et al., (2001)), and limit the dispersal of waste (Weise et al., 2009). Any assessment of the impact of marine farms on carrying capacity should therefore account for the reduction of currents caused by the farms themselves (Plew, 2011a).

Flushing studies were conducted to quantify the effects of reduced currents on material transport. Figure 7.20 presents the predicted dye decay curve for the outer farm. Model simulations examined the flushing times to remove 50, 63, 75 and 90% of a conservative tracer from the farmed regions. Table 7-3 summarizes the results, while Figure 7.17 and Figure 7.18 present the spatial distribution of residence times for the removal of 63% and 75% of trace material, respectively. These datasets illustrate the impacts of the aquaculture installations on material transport and flushing. Local residence times are

increased by a factor of two in large sections of the farmed regions (Figure 7.19). The average residence time within both farms, and in particular, the larger outer farm, is significantly increased. The farms increase the time it would take to flush 75% of a conservative material by 50% in region A, and 46% in region B.

Neglecting these implications poses significant risk for the carrying capacity and production capacity of an aquaculture farm. Dame and Prins, (1998) expressed aquaculture carrying capacity in terms of the primary production of phytoplankton and water mass residence times. A number of studies have adopted flushing studies as a means to investigate aquaculture carrying capacities. Brooks et al., (1999) investigated optimum locations of aquaculture farms by developing bay-scale maps of mean tidal residence times. Lee et al., (2003) linked farm-scale and bay-scale residence times in an attempt to incorporate the effectiveness of mass exchange with the surrounding waters and the open sea into carrying capacity studies. However, both studies ignored the effects of the aquaculture installations themselves. These studies demonstrate the potential of applying relatively simple flushing study techniques in the planning stages of aquaculture developments. However, as demonstrated, neglecting the frictional effect of the aquaculture installation may result in a serious overestimation of the calculated assimilative capacity of a water body.

This chapter presented the application of a validated three-dimensional hydrodynamic model to a bay with significant aquaculture developments. The aquaculture installations themselves were incorporated into the model in a technically defensible manner. Model simulations investigated hydrodynamic changes and water quality implications within the harbour. The author is not aware of any other study of aquaculture developments in which a three-dimensional numerical model was amended to simulate actual flow profiles within and around the actual farms. This has significant potential for aquaculture management studies; where a range of farm configurations can be quickly and easily investigated through numerical modelling simulations, and an optimum configuration identified.

## Chapter 8: Summary and conclusions

---

*“The correct interpretation of a set of measurements from an engineering or scientific experiment is often more difficult than performing the tests and obtaining the observations”*

*- Robert Y. Hudson*

## 8.1 Summary

This thesis is concerned with the effects of aquaculture installations on hydrodynamics and mixing patterns at both the near-field farm-scale, and the far-field bay-scale level. While there has been large amounts of research carried out on the growth and feeding patterns of marine bivalves most carrying capacity studies focus on budgeting of particulate food depletion and renewal. The effects that frictional resistance of mariculture structures have on flows has often been almost ignored. This is particularly true of numerical modelling studies on the subject (McKindsey et al., 2006). The primary objectives of this thesis were twofold: firstly to develop a numerical model describing flows through a cultivated mariculture region, and secondly, to assess the performance of the model by comparison with experimental data, and application to real marine environments. In order to address demands for both computational efficiency and comprehensive modelling capabilities, two numerical models were adopted, namely, the depth-averaged DIVAST model, and the three-dimensional EFDC model.

The first stage of the research consisted of a review of the literature, presented in Chapter 2. A number of significant implications of aquaculture installations were noted, including: flow attenuation of up to 87% (Boyd and Heasman, 1998), increased material residence times (Grant and Bacher, 2001), modified mixing and circulation patterns (Plew, 2011b), depletion of nutrients (Pilditch et al., 2001), reduced farm productivity (Stroheimer et al., 2005) and adverse environmental implications (Milewski, 2001). The need for a comprehensive modelling package to simulate the complex flow features induced by an aquaculture installation, and assist in environmental impact assessments was undeniable.

Chapter 3 presents the development of the numerical models, along with a discretization of the governing equations, and a description of the solution scheme. Depth-averaged models are applicable to well-mixed coastal and estuarine waterbodies, where the flow profile is essentially two-dimensional. It may seem counterintuitive to adopt a depth-averaged model to simulate flows through a suspended aquaculture canopy, where flows beneath the canopy can be an order of magnitude greater than within the

canopy (Gibbs et al., 1991). However, studies have demonstrated that within stratified waterbodies, where, critically, the canopies extend over most of the water depth, diversion of flows is predominantly around the farms, and can be described as nearly horizontal. Hence, DIVAST provides a computationally efficient option to simulate the effects of aquaculture structures within many such waterbodies.

The model was amended to simulate flows through a typical idealised aquaculture installation. The effect of an individual mussel dropper on flow dynamics was parameterised in terms of a bluff body drag force, and an areal reduction coefficient. A number of turbulence closure models were also assessed, namely: a simple mixing length model, a two-equation  $k$ - $\epsilon$  model and an extended  $k$ - $\epsilon$  scheme to simulate canopy flow turbulence production processes. The mixing length model is an empirically based model that relates the eddy viscosity to the mean velocity gradients and a mixing length parameter. The performance of the model is highly dependent on the specification of an appropriate value for the coefficient of eddy viscosity. The  $k$ - $\epsilon$  closure model accounts for the transport and history effects of turbulence by solving a pair of transport equations for the turbulent kinetic energy,  $k$ , and the rate of dissipation,  $\epsilon$ . The extended  $k$ - $\epsilon$  model simulated the direct contribution of the droppers to the production of turbulence energy.

The second approach used in this thesis was to look at small-scale flow features through laboratory experiments discussed in Chapter 4. The large-scale effects of the structures on currents and mixing result from the combined interactions of the flow around a multi-array deployment of suspended long-lines. The laboratory experiments provide an insight into the effects of a single long-line on flows; while eliminating extraneous forcing such as wind and wave action. Results indicated a reduction in velocities of 20-40% within the long-line, and a corresponding reduction in material transport flux. The laboratory study also provided data to fine-tune and validate the amended models.

Chapter 5 discusses the validation of the extended DIVAST model. The performance of the hydrodynamic and solute transport modules were assessed by comparison with experimental data. Appropriate model coefficients were derived and the model was fine-

tuned as part of the validation process. The numerical model, governed by the amended equations describing aquaculture structures, displayed close agreement with the velocity data collected from the physical model.

A case study applied the amended model to a designated aquaculture development site on the West Coast of Ireland. Simulations investigated the influence of the aquaculture installations on flow fields and material transport. This study indicated that the aquaculture structures influenced both flow magnitude and direction. Time trace graphs exhibited a retardation of flow within farm, with some acceleration of flow evident between the aquaculture structures. Flow-field differentials exhibited velocity attenuation of up to 60% in large sections of the bay. An analysis of material transport time scales examined the assimilative capacity of the bay for aquaculture development purposes. The presence of the aquaculture installations had a substantial effect on the flushing properties of the bay, with an increase of 46% in average residence times predicted.

As mentioned, DIVAST is an appropriate choice for certain modelling scenarios. However, to accurately simulate the complex flow regimes and velocity gradients that develop within and beneath a suspended canopy, a three-dimensional model of impeded aquaculture flows was required. This study adopted the EFDC hydrodynamic model. Chapter 3 describes the derivation of the mathematical equations describing impeded flows, along with the discretization of the governing equations. The amended model simulates canopy flows extending over a user-specified region of the water column, with free-stream flow developing beneath. Within the canopy, both the hydrodynamics and turbulent structure were modified to simulate the effects of the suspended droppers. The distinct shear layer that develops between the impeded canopy flows, and faster, free-stream flow below, was simulated by means of a mechanical friction layer. This layer describes the rapid attenuation of flows that develops at the bottom of the suspended canopy, as free-stream flow and the physical impediment interact.

Chapter 6 presents the validation of the amended EFDC model against published experimental data. The research presented a number of novel techniques of describing suspended canopy flow processes, including:

- A mathematical description of attenuated canopy flows via bluff body drag.
- A mathematically valid, amended turbulence closure model described enhanced production and mechanical stirring induced by the cylinders.
- A novel friction layer simulated the complex flow structure and processes observed within a canopy shear layer.
- The variation of drag along the length of the cylinder was analysed by reference to literature and laboratory data.

The specification of a constant drag coefficient in the vertical proved unsatisfactory in simulating observed flow processes. An examination of the data demonstrated that, the model underestimated drag at the bottom of the canopy. This research assessed a number of expressions for a varying drag coefficient within the canopy. Empirical profiles of drag derived by Dunn et al., (1996) and Ghisalberti and Nepf, (2004) were investigated. In this study, the profile proposed by Ghisalberti and Nepf, (2004) provided closest agreement with experimental data. The profile suggested by Dunn et al., (1996) significantly overestimated drag in the upper portions of the canopy structure. This was particularly evident with regards turbulent measurements; where the model simulations significantly overpredicted turbulent structure observed within the canopy.

The GNM performed quite well in simulating observed flow profiles. The model demonstrated good agreement with observed vertical profiles of both velocity and turbulent structure. An observed failing of the model was the simulation of velocities within the canopy shear layer. The model did not accurately simulate the complex flow structure involving a rapid attenuation of flow at the canopy-free stream interface. Therefore, as part of this study, the laboratory profile derived by Ghisalberti and Nepf, (2004) was amended to provide optimal agreement with observed data. The EAM provided the closest agreement between modelled and observed flows. The model accurately replicated observed profiles, of both, velocity and turbulence. Based on the close agreement with laboratory data, the EAM was adopted for subsequent modelling studies.

The EFDC model and the amended EAM model were both tested in a real coastal environment, Killary Harbour on the West Coast of Ireland. A three-dimensional model was required to represent the water circulation patterns in the relatively deep, highly stratified harbour (Keegan and Mercer, 1986). An extensive field-monitoring program provided data to force and calibrate the hydrodynamic model, namely, current meter, tide gauge and weather station data. The model provides information on hydrodynamics and material residence times within the harbour. Simulations assessed time scales of transport of two distinct regions of the harbour, and the harbour as a whole.

The average residence time within Killary Harbour for mean annual river runoff equals 15.19 days. This value increases to 29.61 days, if simulations neglect river discharges completely. Different regions of the harbour exhibit different flushing properties, with the inner harbour highly dependent on river inflows, while tidal exchange dominates flushing in the outer harbour.

The amended model simulated flows and material transport within the farmed regions of the harbour. Based on a typical configuration and density of droppers, within-farm flows were reduced by up to 70% from ambient. Some flow diversion around the farms (circa 10%) was observed, with the greater portion being diverted under the suspended farms. Flows beneath the farms increased by 40-60% due to the effects of the farms. Flushing studies quantified the effects of reduced currents on material transport. Model simulations examined the flushing times to remove 50, 63, 75 and 90% of a conservative tracer from the farmed regions. The average residence time within both farms, and in particular, the larger outer farm, was significantly increased. The presence of farms increase the time it would take to flush 75% of a conservative material by 50% in the outer farm, and 46% in the smaller, inner farm.

## **8.2 Discussion and Conclusion**

Several important findings and observations were reported in this study. The main conclusions that have emerged from this research are summarized and discussed below. Laboratory experiments of flows through a scaled double long-line installation lead to the following conclusions:

- The near-field effects of an aquaculture structure are significant. In this study, flows through the long-line were attenuated by 25-40%, at all points. This suggested a significant diversion of flows around the system. Comparing flows at the entrance to the system (point A1) to further downstream (point A4); we see that the current speed reduction is quite similar at both points. This suggests that rather than a gradual reduction in flows due to friction as water passes the roughened droppers, the greatest portion of energy loss occurs at the entrance to, or just upstream of the long-line.
- An inter-comparison of observed flow profile within smooth and roughened droppers, demonstrated that surface roughness has a significant effect. Little attenuation of ambient flows was observed within the double long-line of smooth cylinders; as opposed to the highly significant flow attenuation observed in the latter case. The results suggest that there is a greater interaction between the rough cylinders, resulting in greater energy dissipation and drag. A similar feature was observed by Plew (2005), who conducted laboratory experiments of flows past an array of both smooth and rough cylinders. The drag imparted by the roughened cylinders ( $k_s/D = 0.09$ ) was 10-15% greater than the drag imparted by the smooth cylinders.
- Solute transport studies demonstrated a significant reduction in dye flux to the downstream extents of the scaled system. The concentration of dye at the downstream extents of the system was almost negligible with a reduction of up to 50% in the longitudinal transport distance, relative to the default case of no aquaculture structure included. In addition, a significant amount of material flux diverts around the long-line. These results have significant implications for nutrient supply and carrying capacity studies; particularly when one considers the effect of sequentially located farms and intense particle consumption by feeding.

The amended depth-averaged model was fine-tuned and validated by comparison with the experimental data. This model was then extrapolated to the bay-scale level. This

allowed an assessment of the effects of an aquaculture installation on both local and far-field flow dynamics. Several effects on flows and material transport were observed:

- An inter-comparison between numerical and experimental results displayed close agreement between both datasets. The numerical model closely replicates the attenuation of velocities, and modified dye plume, observed in the laboratory. The main consideration in the comparison of the experimental and numerical results is the choice of drag coefficient. A value of 1.8 was determined as appropriate for this research. This is comparable with previously used values for similar studies (Shimizu and Tsujimoto, (1994), Mazda et al., (1997), Nepf and Vivoni, (2000), Struve et al., (2003), Wu et al., (2005)).
- Extending the model to the bay scale level demonstrated that flows were reduced within aquaculture farms; and that the effects extended beyond the farm boundaries. Time trace graphs exhibited a retardation of flow within aquaculture-designated cells, with some acceleration of flow evident between the aquaculture structures. Flow-field differentials exhibited velocity attenuation of up to 60% in large sections of the bay. Despite farms covering only a small portion of the embayment, simulations predicted that water speeds were reduced over most of the bay.
- Flushing studies assessed the impacts of aquaculture installations on time scales of transport within the embayment. The average residence time and the exchange per tidal cycle coefficient were computed. Simulations predicted that the inclusion of the aquaculture structures increased average residence times by up to 46% within the bay. Evidently, this will have significant effects on the local ecosystem, in addition to limiting nutrient turnover and supply to the aquaculture installations. A large number of studies have utilised numerical models to assess the carrying capacity of a waterbody (Carver and Mallet, (1990), Bacher et al., (1998), Bacher et al., (2003)). McKindsey et al., (2006) classed the production capacity of a waterbody as being dependent on, primary production within the area of interest, and the importation of organic matter from the surrounding waterbody. However,

this study demonstrates that tidally driven exchange rates are significantly reduced by the inclusion of the aquaculture installations. Disregarding the frictional effect of the aquaculture installation may result in a serious overestimation of the assimilative capacity of a water body, and consequently carrying capacity.

- An extended material residence times also has very serious implications for the ecological carrying capacity of a waterbody. McKindsey et al., (2006) defined ecological carrying capacity as the '*maximum level of production which is possible without having an unacceptable ecological impact*'. Aquaculture installations can affect the ecological health of a water body by producing elevated nutrient levels and strong organic deposition in the neighbourhood of culture sites (Weise et al., 2009). This addition of organic matter can overwhelm the assimilative capacity of the local environment, thus sometimes changing the physical, chemical and biological structure of the waterbody. The removal of matter from the waterbody is dependent on exchange rate with the surrounding waters. Hence, an aquaculture installation can adversely affect the local ecosystem by incurring elevated nutrient levels in conjunction with reduced exchange rates.

Investigations into the three-dimensional flow structure leads to several observations:

- Simulations were conducted at the laboratory scale investigating the effects of a suspended canopy on flows within an experimental flume. Profiles of the normalized stream wise velocity,  $U/U_0$ , where  $U_0$  is the depth-averaged velocity, show three distinct regions of flow: velocities increasing above the bed reaching a maximum at some point between the canopy and bed; velocities decreasing into and within the canopy; and velocities reaching a constant value in the upper canopy. Based on laboratory studies conducted by Plew (2011), three flow regions were identified: a bottom boundary layer, a canopy shear layer and an internal canopy layer.
- The thickness of the bottom boundary layer (BBL) can be estimated by a number of methods such as, the distance from the bed to maximum  $U$ , or zero  $\langle u'w' \rangle$ . Both methods give very similar estimates of BBL thickness, when compared for

different model simulations, and generally falls within the range of  $0.1-0.2h$ . BBL thickness was found to be dependent on canopy density with an increased density serving to decrease the layer thickness.

- The amended numerical model closely replicated the canopy shear layer observed in experimental studies conducted by Plew. An inflection point in the vertical flow profile defines the canopy shear layer, which has been associated with the development of large coherent vortices (Nepf and Vivoni, 2000). Unlike free stream vortices, the vortices in a canopy shear layer do not grow continuously downstream but reach and maintain a finite scale determined by a balance between shear production and canopy dissipation. This balance defines the length scale of vortex penetration into the canopy. The shear layer was observed to extend from the top of the BBL, some distance into the canopy. Plew identified the depth of penetration into the canopy as the height above the canopy where  $\langle u'w' \rangle$  reached 10% of its peak value (Nepf et al., 2007). Inter-comparing experimental and numerically predicted profiles of both velocity and turbulence demonstrated that the model slightly overestimated the depth of penetration into the canopy; a result of a discrepancy between the relative velocity gradients. However, the EAM provided the closest agreement with experimental data and was deemed the most appropriate for this study. The location of the canopy shear layer and the point of development above the BBL (either by measurements of  $U$  or  $\langle u'w' \rangle$ ) are very closely replicated by the model.
- The internal canopy layer is the region above the canopy shear layer based on the 10% of maximum  $\langle u'w' \rangle$  threshold. This region is defined by highly attenuated velocities and reduced production due to turbulence shear. The model closely replicates observed profiles of both velocity and turbulence within the canopy layer, provided an appropriate drag coefficient is adopted. For this study, a constant drag profile performed quite poorly in simulating laboratory flows, with closest agreement provided by a user-modified version of the drag profile proposed by Ghisalberti and Nepf, (2004). Another factor worthy of consideration

is the effect of dropper density on drag coefficient. This research suggests that a uniform drag coefficient does not accurately model flow processes for all cylindrical configuration. Results illustrate an interrelationship between drag coefficient and Reynolds number. When the density is higher, the flow velocity and Reynolds number in the domain are smaller and thus, according to the relationship between drag and Reynolds number for a single cylinder (Schlichting, 1968); a larger drag coefficient is required.

- The different flow regions observed within and beneath a canopy have several implications for suspended aquaculture developments. Nepf and Vivoni, (2000) divided a submerged canopy of aquatic vegetation into two distinct zones, namely: a vertical exchange zone and a longitudinal exchange zone. In the upper canopy, vertical exchange between the canopy and free stream is dynamically significant to the momentum balance; with turbulence production at the tip of the canopy being important. The lower canopy, on the other hand is called the longitudinal exchange zone because the dominant exchange mechanism with the surrounding waters is longitudinal advection. The vertical exchange zone was not observed in emergent vegetation demonstrating the importance of the canopy shear layer for vertical mixing. Extending the results to a suspended canopy has a number of important implications for aquaculture developments. In the lower regions of the canopy, vertical turbulent exchange is an important mechanism of transport. The thickness of this vertical exchange zone can be approximated to the depth of penetration of the canopy shear layer as discussed above. This depth of penetration is dependent on both canopy density and the distance between the suspended canopy and the top of the BBL. Hence, increasing canopy density, and decreasing the free-stream gap beneath the canopy, decreases the depth of penetration of the vertical exchange zone. Within a submerged canopy, the depth of penetration is reduced due to a depth-induced restriction on eddy length-scales when  $H/h_c < 2$ ; where  $h_c$  is the canopy height. This effect would be even more pronounced within a suspended canopy, where the no-slip boundary condition at the bottom presents a greater restriction to eddy formations than the free-surface boundary condition for the

submerged case. This is an important factor to consider when designing suspended aquaculture installations. Extending the droppers over too great a depth of the water column can suppress or eliminate vertical exchange between the farm and surrounding waters; thereby reducing exchange mechanisms to longitudinal advection alone. This can have important implications for aquaculture carrying capacity; field studies have demonstrated the importance of boundary-layer flows in supplying phytoplankton to suspension feeders (Frechette et al., 1989)

- The vertical exchange of nutrients between the nutrient-depleted aquaculture-containing zone, and the adjacent nutrient-rich layer has been shown, has been demonstrated to be of importance for bottom-feeding
- The study of Killary Harbour provided an invaluable opportunity to investigate three-dimensional flow and circulation patterns for a tidally inundated region, as opposed to a scaled hydraulic flume. The study provided a number of important insights. Flushing studies conducted in section 7.3 gives some insight into flow processes in the Harbour. The flushing of the domain is highly dependent on river discharges into the harbour. Neglecting river discharges results in an order of magnitude increase in average residence time. An analysis of flushing properties of different regions of the harbour exhibit different flushing characteristics; inner Killary is efficiently flushed by river discharge from the Erriff, while outer Killary also exhibits quick and efficient flushing of material, due to strong tidal exchange promoting good mixing and low residence times. A hugely significant observation for aquaculture development is the poor flushing characteristics observed in middle-Killary; an area of intensive aquaculture cultivation. This has implications for the supply of nutrients and removal of toxins from the fish farms.
- The amended EFDC model simulated flows within licensed aquaculture sites in the harbour. Based on a typical configuration and density of droppers, within-farm flows were reduced by up to 70% from ambient. Some flow diversion around the farms (circa 10%) was observed, with the greater portion being diverted under the suspended farms. Flows beneath the farms increased by 40-60% due to the effects

of the farms. Flow attenuation within the suspended canopy was described by a mathematical formulation describing bluff body drag force. However, the relative diversion of flows beneath or around aquaculture farms is a matter of some debate; many studies have reported accelerated flows beneath farms (Gibbs et al., (1991), Plew et al., (2005)) while horizontal diversion dominates in other situations (Plew et al., 2006). Therefore, further investigation of actual flows in the field is necessary to validate the amended model.

- Flushing studies were conducted to quantify the effects of reduced currents on material transport. Model simulations examined the flushing times to remove 50, 63, 75 and 90% of a conservative tracer from the farmed regions. Results demonstrate that the farms affect exchange rates quite significantly; with local residence times increased by a factor of two in large sections of the farmed regions. Neglecting these results poses significant risk for the carrying capacity and production capacity of an aquaculture farm. This is particularly true in regions with relatively poor exchange rates. Flushing studies of the harbour conducted in section 7.3 demonstrated that both inner and outer Killary had good exchange rates and low residence times. However, parts of middle-Killary displayed relatively poor flushing characteristics, and extended material residence times. Coupled with intensive aquaculture development that retards flushing further, it is apparent that adverse effects associated with prolonged material residence times may become an issue in this region. For mariculture purposes, these effects include reduced production capacity within the farms and increased organic content near the farms that may result in disturbances in natural balance, and harmful algal blooms.

In conclusion, the results of this research have a number of important implications for the design of mussel farms and for the assessment of their effects. Both the laboratory and numerical data demonstrates that there is a significant reduction of current speed within farms. As a consequence of the lower velocities, reduced material flux was also observed through the farms. This has obvious implications for nutrient supply to the farms, and in particular to sequentially located farms. Hence, consideration of ambient

nutrient supply to the feeders should account for the fact that water velocities will be lower within the farms.

Another result of reduced water velocities is extended material residence times within the domain. A number of studies have applied time scale formulae to assess the carrying capacity of a bay for mariculture. However, this study has demonstrated that the farms themselves reduce exchange rates quite significantly. Disregarding the frictional resistance of the farms themselves will result in a serious overestimation of the renewal term and thus an overestimation of carrying capacity.

An assessment of three dimensional flow structure and literature has demonstrated that vertical exchange between the suspended canopy and the underlying water is dynamically significant to the momentum balance. This mixing layer can be significant in transporting nutrients into the canopy; while the thickness of the mixing layer itself is dependent on dropper density and the free-stream gap beneath the canopy. Hence, studies suggest that when the droppers extend greater than half the depth of the water column, the bottom bed impacts on the depth of penetration of the mixing layer into the canopy. This may have implications for the supply of nutrients into the canopy.

Simulations at both the laboratory-scale and bay-scale demonstrated significant acceleration of flows beneath the farms. This can have significant implications for sediment transport and erosion beneath the farms. The bed shear stress is dependent on both the density of droppers and the gap between the bed and the canopy. Increased canopy density will increase bed shear stress because of faster velocities beneath the canopy. Reducing the gap between the canopy and the bed will reduce bed shear stress, since a greater portion of the flow is diverted around, rather than under, the farms.

This study presents a comprehensive numerical modelling approach to investigate the aforementioned effects. The model can be adopted to investigate a wide range of flow features, including: reduced flow speeds within the farm, increased flows beneath and around the farms, increased turbulent shear production, modified tidal exchange mechanisms, and increase material residence times. The amended model has huge

potential in the planning stage of aquaculture developments; particularly in determining optimum farm locations and bay carrying capacity.

### 8.3 Recommendations for Future Work

From the study presented in this thesis, it can be seen that aquaculture installations have quite significant implications, and that numerical models may provide very beneficial information in assessing these implications. The thesis presents amended versions of both DIVAST and EFDC. The following are recommendations for future research which would, in the author's opinion, enhance the functionality and reliability of the model. Both models are discussed in turn:

- Chapter 5 presents the validation of the DIVAST model against laboratory data. The model was developed on the assumption that the suspended canopy extends the full depth of the water column. However, this is generally not the case. Extensive data exists on the idealized flow profile that develops within and beneath a suspended canopy. This makes it possible to derive an analytical expression for the drag profile of the suspended canopy in terms of the ratio of the canopy height to the total water depth. Incorporating such a drag profile (validated by appropriate experimental data) into the numerical model may better replicate actual canopy flow profiles in the numerical model.
- In this study, the drag was varied along the length of the dropper; however, drag also depends on dropper density and flow speeds (due to the inherent dependency on Reynolds number). Further laboratory experiments are required to quantify this dependency. An example is work conducted by Nepf, (1999), who derived an expression relating bulk drag coefficient,  $C_{DA}$ , and cylinder densities ( $ad$ ) in a study of emergent vegetation:

$$C_{DA} = \frac{C}{1.16} \{1.16 - 9.31(ad) + 38.6(ad)^2 - 59.8(ad)^3\} \quad (8.1)$$

- The focus of the amended EFDC model was to investigate flows within and beneath the canopy. The laboratory data, which validated the model, was collected in a flume where droppers extended across the entire horizontal domain. However,

in reality, flow is diverted both under and around the canopy. Further laboratory experiments are required to investigate flow diversions under and around the canopy; which can be used to validate the model

- A comprehensive field-monitoring program is also required to validate the model at the bay-scale level. This consists of measurements of flows, within a suspended canopy, beneath the canopy, and beside the canopy.
- Vertical exchange between the canopy and the underlying waters can be significant to the nutrient balance of a farm. In flows over submerged canopies the free surface has been found to restrict vortex formation when  $C_{Dah_g} < 1.0$ . In this study, the maximum value was 0.2. Canopy shear and mixing layer processes may be better simulated in a deeper flume, where the effects of the bottom bed would be more easily discounted (Dr. Marco Ghisalberti, - personal communication).
- Studies have indicated that stratification of the water column has a significant effect on canopy flows, by restricting vertical diversion under the canopy, and limiting the effectiveness of the shear generated mixing layer. A baroclinic model, validated by field measurements of salinity and temperature, can be used to investigate the effects of stratification on canopy flows. Killary Harbour is an ideal site for such a study due to its classification as a partially stratified estuary.
- Increased flow speeds beneath the canopy have obvious implications for bed stress and erosion. The sediment transport module in EFDC can be adopted to investigate these effects.
- This thesis presents the amended models applied to simulate suspended canopy flow processes; however, the models can also be applied to a wide range of other impeded flow scenarios. Natural and man-made structural arrangements like kelp and sea grass beds, float breakwaters and wave and offshore wind energy extraction arrays will all influence local currents.

## **Bibliography**

---

- Aiba, S., Tsuchida, H., Ota, T., 1982. Heat transfer around tubes in in-line tube banks. *Bulletin of the JSME* 25, 919–926.
- Aiguo, Q., 2003. Three-dimensional modelling of hydrodynamics and tidal flushing in deep bay (M.Sc.). University of Hong Kong
- Andersen, K.H., Mork, M., Nilsen, J.E.Øi., 1996. Measurement of the velocity-profile in and above a forest Of *Laminaria hyperborea*. *Sarsia* 81, 193–196.
- Arakawa, A., Lamb, V.R., 1977. Computational design of the basic dynamical processes of the UCLA general circulation model. *Methods in Computational Physics* 17, 173–265.
- Arega, F., Sanders, B.F., 2004. Dispersion Model for Tidal Wetlands. *Journal of Hydraulic Engineering* 130, 739.
- Aure, J., Stroheimer, T., Strand, O., 2007. Modelling current speed and carrying capacity in long-line blue mussel (*Mytilus edulis*) farms. *Aquaculture Research* 38, 304–312.
- Babarutsi, S., Nassiri, M., 1996. Computation of shallow recirculating flow dominated by friction. *Journal of hydraulic engineering* 122, 367–372.
- Bacher, C., Duarte, P., Ferreira, J.G., Heral, M., Raillard, O., 1998. Assessment and comparison of the Marennes-Oleron Bay (France) and Carlingford Lough (Ireland) carrying capacity with ecosystem models. *Aquatic Ecology* 31, 379–394.
- Bacher, C., Grant, J., Hawkins, A.J.S., Fang, J., Zhu, M., Besnard, M., 2003. Modelling the effect of food depletion on scallop growth in Sungo Bay (China). *Aquatic Living Resources* 16, 10–24.
- Bai, S., Lung, W.-S., 2005. Modeling sediment impact on the transport of fecal bacteria. *Water Res* 39, 5232–5240.
- Batteen, M.L., Han, Y.-J., 1981. On the computational noise of finite-difference schemes used in ocean models. *Tellus* 33, 387–396.
- BIM, 2002. Killary Co-ordinated local aquaculture management system. Bord Iascaigh Mhara.
- Blanco, J., Zapata, M., Morono, A., 1994. Some aspects of the water flow through mussel rafts. *Scientia Marina* 60, 275–282.
- Blevins, R.D., 2003. *Applied fluid dynamics handbook*. Krieger Publishing Company, New York.
- Blumberg, A.F., Mellor, G.L., 1987. A description of a three-dimensional coastal ocean circulation model. *Three-dimensional coastal ocean models, Coastal and Estuarine Science* 4, 1–16.
- Bolin, B., Rodhe, H., 1973. A note on the concept of age distribution and transit time in natural reservoirs. *Tellus* 25, 58–62.
- Boyd, A.J., Heasman, K.G., 1998. Shellfish mariculture in the Benguela System: water flow patterns within a mussel farm in Saldanha Bay, South Africa. *Journal of Shellfish Research* 17, 25–32.

- Bradshaw, P., Huang, G.P., 1995. The Law of the Wall in Turbulent Flow. *Proceedings: Mathematical and Physical Sciences* 451, 165–188.
- Brooks, D.A., Baca, M.W., Lo, Y.-T., 1999. Tidal Circulation and Residence Time in a Macrotidal Estuary: Cobscook Bay, Maine. *Estuarine, Coastal and Shelf Science* 49, 647–665.
- Burke, R.W., 1983. Free surface flow through salt marsh grass (PhD). Massachusetts Institute of Technology
- Burke, R.W., Stolzenbach, K.D., 1983. Free surface flow through salt marsh grass (Technical No. R/C-21). Massachusetts Institute of Technology, Cambridge, MA.
- Carver, C.E.A., Mallet, A.L., 1990. Estimating the carrying capacity of a coastal inlet for mussel culture. *Aquaculture* 88, 39–53.
- Cea, L., Pena, L., Puertas, J., Vázquez-Cendón, M.E., Peña, E., 2007. Application of Several Depth-Averaged Turbulence Models to Simulate Flow in Vertical Slot Fishways. *Journal of Hydraulic Engineering* 133, 160–173.
- Chanson, H., 2004. *The hydraulics of open channel flow: An introduction; basic principles, sediment motion, hydraulic modelling, design of hydraulic structures*. Butterworth-Heinemann.
- Cheng, L., Yong-ming, S., 2008. Flow structure and sediment transport with impacts of aquatic vegetation. *Journal of Hydrodynamics* 20, 461–468.
- Costa-Pierce, B.A., 2002. The 'Blue Revolution' - Aquaculture must go green. *World Aquaculture* 33, 4–5.
- Dabrowski, T., 2005. A flushing study analysis of selected Irish waterbodies (PhD). National University of Ireland, Galway
- Dabrowski, T., Hartnett, M., 2008. Modelling travel and residence times in the eastern Irish Sea. *Marine Pollution Bulletin* 57, 41–46.
- Dame, R.F., Prins, T.F., 1998. Bivalve carrying capacity in coastal ecosystems. *Aquatic Ecology* 31, 409–421.
- Dane, H.J., 1998. Ultrasonic measurement of unsteady gas flow. *Flow Measurement and Instrumentation* 8, 183–190.
- Drapeau, A., Comeau, L.A., Landry, T., Stryhn, H., Davidson, J., 2006. Association between longline design and mussel productivity in Prince Edward Island, Canada. *Aquaculture* 261, 879–889.
- Duarte, P., Meneses, R., Hawkins, A.J.S., Zhu, M., Fang, J., Grant, J., 2003. Mathematical modelling to assess the carrying capacity for multi-species culture within coastal waters. *Ecological Modelling* 168, 109–143.
- Dunn, C., Lopez, F., Garcia, M., 1996. Mean flow and turbulence in a laboratory channel with simulated vegetation, *Hydraulic Engineering Series No. 51*. University of Illinois at Urbana-Champaign, Department of civil engineering.
- El Kasmi, A., Masson, C., 2008. An extended k-epsilon model for turbulent flow through horizontal-axis wind turbines. *Journal of Wind Engineering and Industrial Aerodynamics* 96, 103–122.

- Eriksson, E., 1961. Natural reservoirs and their characteristics. *Geofisica International* 1, 67–84.
- Eriksson, E., 1971. Compartment models and reservoir theory. *Annual Review of Ecology and Systematics* 2, 67–84.
- Falconer, R., 1994. An introduction to nearly-horizontal flows, in: *Coastal, Estuarial and Harbour Engineer's Reference Book*. Chapman & Hall, Oxford, p. 736.
- Falconer, R.A., 1976. Mathematical modelling of jet-forced circulation in reservoirs and harbours (PhD). University of London
- Falconer, R.A., Lin, B., 2001. DIVAST model reference manual (user manual). Cardiff University, Hydro-Environmental Research Centre.
- Falvey, H.T., 2003. Hydraulic design of labyrinth weirs. ASCE Publications.
- FAO, 2006. The state of World Fisheries and Aquaculture 2006. Food and Agriculture Organization of the United Nations.
- FAO, 2010. The state of World Fisheries and Aquaculture 2010. Food and Agriculture Organization of the United Nations.
- Fischer, H.B., 1979. Mixing in inland and coastal waters. Academic Press.
- Folke, C., Kautsky, N., Troell, M., 1994. The costs of eutrophication from salmon farming: implications for policy. *Journal of Environmental Management* 40, 173–182.
- Frechette, M., Butman, C.A., Geyer, W.R., 1989. The importance of boundary-layer flows in supplying phytoplankton to the benthic suspension feeder, *Mytilus edulis* L. *Limnology and Oceanography* 34, 19–36.
- Fujima, K., 2001. Long wave propagation on large roughness, in: ITS 2001, Proceedings Session 7. pp. 891–895.
- Galperin, B., Kantha, L.H., Hassid, S., Rosati, A., 1988. A quasi-equilibrium turbulent energy model for geophysical flow. *Journal of the Atmospheric Sciences* 55–61.
- Gambi, M.C., Nowell, A.R.M., Jumars, P.A., 1990. Flume observations on flow dynamics in *Zostera marina* (eelgrass) beds. *Marine Ecology Progress Series* 61, 159–169.
- Ghisalberti, M., Nepf, H., 2006. The structure of the shear layer in flows over rigid and flexible canopies. *Environ Fluid Mech* 6, 277–301.
- Ghisalberti, M., Nepf, H.M., 2002. Mixing layers and coherent structures in vegetated aquatic flows. *Journal of Geophysical Research* 107, 1–11.
- Ghisalberti, M., Nepf, H.M., 2004. The limited growth of vegetated shear layers. *Water Resources Research* 40, 1–12.
- Gibbs, M.M., James, M.R., Pickmere, S.E., Woods, P.H., Shakespeare, B.S., Hickman, H.W., Illingworth, J., 1991. Hydrodynamic and water column properties at six stations associated with mussel farming in Pelorus Sound. *New Zealand Journal of Marine and Freshwater Research* 25, 239–254.

- Gibbs, M.M., James, M.R., Pickmere, S.E., Woods, P.H., Shakespeare, B.S., Hickman, H.W., Illingworth, J., 1992. Nutrient and chlorophyll a variability at six stations associated with mussel farming in Pelorus Sound. *New Zealand Journal of Marine and Freshwater Research* 26, 197–211.
- Gleeson, F., 1994. A flushing study analysis of Casheen Bay (M. Sc). Trinity College, Dublin
- Goldburg, R., Naylor, R., 2005. Future seascapes, fishing, and fish farming. *Frontiers in Ecology and the Environment* 3, 21–28.
- Gowen, R., Bradbury, N., 1987. The ecological impact of salmonid farming in coastal waters: a review. *Oceanography and Marine Biology: an annual review* 25, 563–575.
- Grant, J., 1996. The relationship of bioenergetics and the environment to the field growth of cultured bivalves. *Journal of Experimental Marine Biology and Ecology* 200, 239–256.
- Grant, J., Bacher, C., 2001. A numerical model of flow modification induced by suspended aquaculture in a Chinese bay. *Canadian Journal of Fisheries and Aquatic Sciences* 58, 1003–1011.
- Guo, X., Yanagi, T., 1998. Three-dimensional structure of tidal current in the East China Sea and the Yellow Sea. *Journal of Oceanography* 54, 651–668.
- Güven, O., Farrell, C., Patel, V.C., 1980. Surface-roughness effects on the mean flow past circular cylinders. *Journal of Fluid Mechanics* 98, 673–701.
- Hageman, L.A., Young, D.M., 1981. *Applied Iterative Methods*. Academic Press.
- Hamrick, J.M., 1992a. Estuarine environmental impact assessment using a three-dimensional circulation and transport model. *Estuarine and Coastal Modeling* 2, 292–303.
- Hamrick, J.M., 1992b. A three-dimensional environmental fluid dynamics computer code: Theoretical and computational aspects (Special Report in Applied Marine Science and Ocean Engineering). Virginia Institute of Marine Science, College of William and Mary.
- Hamrick, J.M., 1996. User manual for the environmental fluid dynamics computer code (Special Report in Applied Marine Science and Ocean Engineering No. 331). College of William & Mary, Virginia Institute of Marine Science.
- Hamrick, J.M., Wu, T.S., 1997. Computational design and optimization of the EFDC/HEM3D surface water hydrodynamic and eutrophication models, in: *Next Generation Environmental Models and Computational Methods*. Society for Industrial and Applied Mathematics, Philadelphia, pp. 143–156.
- Harlow, F.H., 1972. The marker-and-cell method. In *Von Karman Inst. for Fluid Dyn. Numerical Methods in Fluid Dyn.*
- Hartnett, M., Cawley, A., 1991. Mathematical modelling of the effects of marine aquaculture developments on certain water quality parameters. Presented at the First International Conference on Water Pollution: Modelling, Measuring and Prediction, Computational Mechanics Publications/ Elsevier Press, Southampton, UK, pp. 279–299.

- Hartnett, M., Gleeson, F., Falconer, R.A., Finegan, M., 2003. Flushing study assessment of a tidally active coastal embayment. *Advances in Environmental Research* 7, 847–857.
- Hartnett, M., Nash, S., O Donncha, F., O'Brien, N., Olbert, A., 2011. Effects of tidal stream turbines on material transport, in: 30th International Conference on Offshore Marine and Arctic Engineering. Presented at the OMAE, Rotterdam Netherlands.
- Hawkins, A.J.S., James, M.R., Hickman, R.W., Hatton, S., Weatherhead, M., 1999. Modelling of suspension-feeding and growth in the green-lipped mussel *Perna canaliculus* exposed to natural and experimental variations of seston availability in the Marlborough Sounds, New Zealand. *Marine Ecology Progress Series* 191, 217–232.
- Helsey, C.H., Kim, J.W., 2005. Mixing downstream of a submerged fish cage: a numerical study. *IEEE Journal of Oceanic Engineering* 30, 12–18.
- Henderson, F.M., 1966. *Open Channel Flow*, 1st ed. Prentice Hall.
- Herschy, R.W., 1995. *Streamflow measurement*, 2nd ed. Spon Press.
- Hinze, J.O., 1975. *Turbulence*. McGraw-Hill.
- Hudson, R.Y., Herrmann, F.A., Sager, R.A., Whalin, R.W., Keulegan, G.H., Chatham, C.E., Hales, L.Z., 1979. *Coastal Hydraulic Models (No. 5)*. U.S. Army, Corps of Engineers, Coastal Engineering Research Center.
- Hughes, S.A., 1993. *Physical model and laboratory techniques in coastal engineering*, Advanced Series on Ocean Engineering. World Scientific Publishing.
- Igarashi, T., 1986. Characteristics of the flow around four circular cylinders. *The Japan Society of Mechanical Engineers* 29, 751–757.
- Igarashi, T., Suzuki, K., 1984. Characteristics of the flow around three circular cylinders arranged in line. *The Japan Society of Mechanical Engineers* 27, 2397–2404.
- Inglis, G., Hayden, B.J., Ross, A.H., 2000. An overview of factors affecting the carrying capacity of coastal embayments for mussel culture. Report for Ministry for the Environment No. MFE00505.
- Jackson, G.A., Winant, C.D., 1983. Effect of a kelp forest on coastal currents. *Continental Shelf research* 2, 75–80.
- Ji, Z.-G., 2008. *Hydrodynamics and water quality: modeling rivers, lakes, and estuaries*. John Wiley & Sons.
- Jones, W., Launder, B., 1972. The prediction of laminarization with a two-equation model of turbulence. *International Journal of Heat and Mass Transfer* 15, 301–314.
- Kang, H., Choi, S.-U., 2006. Turbulence modeling of compound open-channel flows with and without vegetation on the floodplain using the Reynolds stress model. *Advances in Water Resources* 29, 1650–1664.
- Katul, G.G., Mahrt, L., Poggi, D., Sanz, C., 2004. One- and two-equation models for canopy turbulence. *Boundary Layer Meteorology* 113, 81–109.

- Kautsky, N., Berg, H., Folke, C., Larsson, J., Troell, M., 1997. Ecological footprint for assessment of resource use and development limitations in shrimp and tilapia aquaculture. *Aquaculture research* 28, 753–766.
- Kawamura, T., Hiwada, M., Hibino, T., Mabuchi, I., Kumada, M., 1984. Flow around a finite circular cylinder on a flat plate. *Bulletin of JSME* 27, 2142–2151.
- Keegan, B.F., Mercer, J.P., 1986. An oceanographical survey of Killary Harbour on the west coast of Ireland, in: *Proceedings of the Royal Irish Academy. Section B: Biological, Geological, and Chemical Science*. pp. 1–70.
- Ketchum, B.H., 1952. Circulation in Estuaries, in: *Proceedings of the International Conference on Coastal Engineering*. Cambridge, MA, p. 6.
- Khangaonkar, T., Zhaoqing, Y., Degasperi, C., Marshall, K., 2005. Modeling hydrothermal response of a reservoir to modifications at a high-head dam. *Water International* 30, 378–388.
- Kobus, H., 1980. *Fundamentals in hydraulic modelling*. Verlag Paul Parey, Hamburg/London.
- Kolmogorov, A., 1942. Equations of turbulent motion of an incompressible fluid. *Izv. Akad. Nauk SSSR, Ser. Fiz* 6.
- van de Kreeke, J., 1983. Residence Time: Application to Small Boat Basins. *J. Wtrwy., Port, Coast., and Oc. Engrg.* 109, 416–428.
- Krishnappan, B.G., 1984. Laboratory verification of turbulent flow model. *Journal of hydraulic engineering* 110, 500–514.
- Lauder, B.E., Spalding, D.B., 1974. The numerical computation of turbulent flows. *Computer Methods in Applied Mechanics and Engineering* 3, 269–289.
- Lee, J.H.W., Choi, K.W., Arega, F., 2003. Environmental management of marine fish culture in Hong Kong. *Marine Pollution Bulletin* 47, 202–210.
- Lenihan, H.S., Peterson, C.H., Allen, J.M., 1996. Does flow speed also have a direct effect on growth of active-suspension feeders: An experimental test on oysters. *Limnology and Oceanography* 41, 1359–1366.
- Leonard, L.A., Luther, M.E., 1995. Flow hydrodynamics in tidal marsh canopies. *Limnology and Oceanography* 40, 1474–1484.
- Liang, D., Falconer, R.A., Lin, B., 2007. Coupling surface and subsurface flows in a depth averaged flood wave model. *Journal of Hydrology* 337, 147–158.
- Liang, D., Lin, B., Falconer, R.A., 2007. A boundary-fitted numerical model for flood routing with shock-capturing capability. *Journal of Hydrology* 332, 477–486.
- Lopez, F., Garcia, M., 1997. Open-channel flow through simulated vegetation: Turbulence modeling and sediment transport (Technical Report No. WRP-CP-10). University of Illinois at Urbana-Champaign.
- Lopez, F., Garcia, M.H., 2001. Mean Flow and Turbulence Structure of Open-Channel Flow through Non-Emergent Vegetation. *J. Hydr. Engrg.* 127, 392–402.

- Mazda, Y., Wolanski, E., King, B., Sase, A., Ohtsuka, D., Magi, M., 1997. Drag force due to vegetation in mangrove swamps. *Mangrove and Salt Marshes* 1, 193–199.
- Mazzotti, F.J., Vinci, J.J., 2007. Validation, verification, and calibration: Using standardized terminology when describing ecological models (Technical Report No. WEC216). University of Florida, Wildlife Ecology and Conservation Department.
- McKindsey, C.W., Thetmeyer, H., Landry, T., Silvert, W., 2006. Review of recent carrying capacity models for bivalve culture and recommendations for research and management. *Aquaculture* 261, 451–462.
- Mellor, G.L., Yamada, T., 1974. A hierarchy of turbulence closure models for planetary boundary layers. *Journal of the Atmospheric Sciences* 31, 1791–1806.
- Mellor, G.L., Yamada, T., 1982. Development of a turbulence closure model for geophysical fluid problems. *Reviews of Geophysics and Space physics* 20, 851–875.
- Milewski, I., 2001. Impacts of salmon aquaculture on the coastal environment: A review, in: *Marine Aquaculture and the Environment: A Meeting for Stakeholders in the Northeast*. Cape Cod Press, Falmouth, Massachusetts. pp. 166–198.
- Miller, R.L., McPherson, B.F., 1991. Estimating Estuarine Flushing and Residence Times in Charlotte Harbor, Florida, Via Salt Balance and a Box Model. *Limnology and Oceanography* 36, 602–612.
- Mirto, S., Bianchelli, S., Gambi, C., Krzelj, M., Pusceddu, A., Scopa, M., Holmer, M., Danovaro, R., 2010. Fish-farm impact on metazoan meiofauna in the Mediterranean Sea: Analysis of regional vs. habitat effects. *Marine Environmental Research* 69, 38–47.
- Moustafa, M.Z., Hamrick, J.M., 1994. Modelling circulation and salinity transport in the Indian River Lagoon, in: *3rd International Conference on Estuarine and Coastal Modeling*. Presented at the American Society of Civil Engineers, M. L. Spaulding (ed), New York, pp. 381–395.
- Munson, B.R., 2005. *Fundamentals of fluid mechanics*, 5th ed. John Wiley & Sons.
- Murakami, K., 1991. Tidal exchange mechanism in enclosed regions, in: *2nd International Conference on Hydraulic Modelling of Coastal Estuaries and River Waters*. pp. 110–120.
- Naot, D., Nezu, I., Nakagawa, H., 1996. Hydrodynamic behaviour of partly vegetated open channels. *Journal of Hydraulic Engineering* 122, 625–633.
- Nash, S., 2010. A development of an efficient dynamically-nested model for tidal hydraulics and solute transport (PhD). National University of Ireland, Galway
- Naylor, R.L., Goldburg, R.J., Primavera, J.H., Kautsky, N., Beveridge, M.C.M., Clay, J., Folke, C., Lubchenco, J., Mooney, H., Troell, M., 2000. Effect of aquaculture on world fish supplies. *Nature* 405, 1017–1024.

- Neary, V.S., 2003. Numerical solution of fully developed flow with vegetative resistance. *Journal of Engineering Mechanics* 129, 558–563.
- Nece, R.E., Falconer, R.A., 1989. Hydraulic modelling of tidal circulation and flushing in coastal basins, in: *Proceedings of the Institution of Civil Engineers*. pp. 913–935.
- Neori, A., Troell, M., Chopin, T., Yarish, C., Critchley, A., Buschmann, A.H., 2007. The need for a balanced ecosystem approach to blue revolution aquaculture. *Environment: Science and Policy for Sustainable Development* 49, 36–43.
- Nepf, H., Ghisalberti, M., White, B., Murphy, E., 2007. Retention time and dispersion associated with submerged aquatic canopies. *Water Resources Research* 43, 10.
- Nepf, H.M., 1999. Drag, Turbulence and Diffusion in Flow through Emergent Vegetation. *Water Resources Research* 35, 479–489.
- Nepf, H.M., Sullivan, J.A., Zavistoski, R.A., 1997. A model for diffusion within emergent vegetation. *Limnology and Oceanography* 42, 1735–1745.
- Nepf, H.M., Vivoni, E.R., 2000. Flow structure in depth-limited, vegetated flow. *Journal of Geophysical Research* 105, 28547–28557.
- Nikuradse, J., 1933. *Strömungsgesetze in rauhen Röhren*, vdi-forschungsheft 361 (English translation: *Laws of flow in rough pipes*). (Technical Report), NACA Technical Memo 1292. VDI-Verl., National Advisory Commission for Aeronautics, Washington, DC.
- Nokes, R., 2007. *FluidStream 7.0–System Theory and Design* (Technical Report). University of Canterbury, Christchurch, New Zealand.
- Novak, P., Guinot, V., Jeffrey, A., Reeve, D.E., 2010. *Hydraulic modelling-an introduction Principles, methods and applications*, 1st ed. Taylor & Francis Ltd.
- Nunes, J.P., Ferreira, J.G., Bricker, S.B., O’Loan, B., Dabrowski, T., Dallaghan, B., Hawkins, A.J.S., O’Connor, B., O’Carroll, T., 2011. Towards an ecosystem approach to aquaculture: Assessment of sustainable shellfish cultivation at different scales of space, time and complexity. *Aquaculture* 315, 369–383.
- Olbert, A., 2006. *Investigations into turbulence processes in tide-induced flows - scale and numerical modelling* (PhD). National University of Ireland, Galway
- Panchang, V., Cheng, G., Newell, C., 1997. Modelling hydrodynamics and aquaculture waste transport in Coastal Maine. *Estuarine Research Federation* 20, 14–41.
- Peterson, C.H., Beal, B.F., 1989. Bivalve Growth and Higher Order Interactions: Importance of Density, Site, and Time. *Ecology* 70, 1390–1404.
- Peyret, R., Taylor, T.D., 1983. *Computational methods for fluid flow*. Springer-Verlag.
- Phillips, N.A., 1957. A coordinate system having some special advantages for numerical forecasting. *Journal of Meteorology* 14, 184–185.

- Pilditch, C.A., Grant, J., Bryan, K.R., 2001. Seston supply to sea scallops (*Placopecten magellanicus*) in suspended culture. *Canadian Journal of Fisheries and Aquatic Sciences* 58, 241–253.
- Plew, D.R., 2005. The hydrodynamic effects of long-line mussel farms (PhD). University of Canterbury
- Plew, D.R., 2011a. Shellfish farm-induced changes to tidal circulation in an embayment, and implications for seston depletion. *Aquaculture Environment Interactions* 1, 201–214.
- Plew, D.R., 2011b. A depth-averaged drag coefficient for modelling flow through suspended canopies. *Journal of Hydraulic Engineering* 137, 234–247.
- Plew, D.R., Spigel, R.H., Stevens, C.L., Nokes, R.I., Davidson, M.J., 2006. Stratified flow interactions with a suspended canopy. *Environmental Fluid Mechanics* 6, 519–539.
- Plew, D.R., Stevens, C.L., Spigel, R.H., Hartstein, N.D., 2005. Hydrodynamic implications of large offshore mussel farms. *IEEE Journal of Oceanic Engineering* 30, 95–108.
- Prandtl, L., 1945. Über ein neues Formelsystem für die ausgebildete Turbulenz., *Nachr. Akad. Wiss. Gottingen* 6–19.
- Pritchard, D.W., 1952. *Estuarine Hydrography: Advances in Geophysics I*. Academic Press, New York.
- Rahman, M., Chaudhry, M.H., 1998. Simulation of dam-break flow with grid adaptation. *Advances in Water Resources* 21, 1–9.
- Raillard, O., Menesguen, A., 1994. An ecosystem box model for estimating the carrying capacity of a macrotidal shellfish system. *Marine Ecology Progress Series* 115, 117–130.
- Rastogi, A.K., Rodi, W., 1978. Predictions of Heat and Mass Transfer in Open Channels. *Journal of the Hydraulics Division* 104, 397–420.
- Raupach, M.R., Thom, A.S., 1981. Turbulence in and above Plant Canopies. *Annu. Rev. Fluid Mech.* 13, 97–129.
- Richardson, J., 2009. BIM UISCE carrying capacity (Technical). BIM.
- Rodi, W., 1993. Turbulence models and their application in hydraulics : a state-of-the art review, 3rd ed. ed. International Association for Hydraulic Research., Rotterdam Netherlands; Broofield Vermont.
- Rodi, W., 1993. Elements of the Theory of Turbulence, in: *Coastal, Estuarial and Harbour Engineer's Reference Book*. Chapman & Hall, London, pp. 46–59.
- Rosenberg, R., Loo, L.O., 1983. Energy-flow in a *Mytilus edulis* culture in western Sweden. *Aquaculture* 35, 151–161.
- Sachs, J., 2007. The promise of the Blue Revolution. *Scientific American Magazine* 297, 37–38.
- Schlichting, H., 1968. *Boundary layer theory*. McGraw Hill Book Co., New York.

- Sequeira, A., Ferreira, J.G., Hawkins, A.J.S., Nobre, A., Lourenço, P., Zhang, X.L., Yan, X., Nickell, T., 2008. Trade-offs between shellfish aquaculture and benthic biodiversity: A modelling approach for sustainable management. *Aquaculture* 274, 313–328.
- Shen, H.H., 2002. *Environmental fluid mechanics: theories and applications*. ASCE Publications.
- Shen, J., Boon, J.D., Kuo, A.Y., 1999. A modeling study of a tidal intrusion front and its impact on larval dispersion in the James River Estuary, Virginia. *Coastal and Estuarine Research Federation* 22, 681–692.
- Shi, Z., Pethick, J.S., Pye, K., 1995. Flow Structure in and above the Various Heights of a Saltmarsh Canopy: A Laboratory Flume Study. *Journal of Coastal Research* 11, 1204–1209.
- Shimizu, Y., Tsujimoto, T., 1994. Numerical analysis of turbulent open-channel flow over a vegetation layer using a k-e turbulence model. *Journal of Hydroscience and Hydraulic Engineering* 11, 57–67.
- Simpson, J.H., Berx, B., Gascoigne, J., Saurel, C., 2007. The interaction of tidal advection, diffusion and mussel filtration in a tidal channel. *Journal of Marine Systems* 68, 556–568.
- Smagorinsky, J., 1963. General circulation experiments with the primitive equations, Part I: the basic experiment. *Monthly Weather Review* 91, 99–164.
- Smolarkiewicz, P.K., Margolin, L.G., 1993. On forward-in time differencing for fluids: Extension to curvilinear framework. *Monthly Weather Review* 1847–1859.
- Sokolnikoff, I.S., Redheffer, R.M., 1966. *Mathematics of Physics and Modern Engineering*, 2nd ed. McGraw-Hill College.
- Soto, D., Aguilar-Manjarrez, J., Brugère, C., Angel, D., Bailey, C., Black, K., Edwards, P., Costa-Pierce, B., Chopin, T., Deudero, S., 2008. Applying an ecosystem-based approach to aquaculture: principles, scales and some management measures, in: *Building an Ecosystem Approach to Aquaculture*. Food and Agriculture Organization, pp. 15–35.
- Souliotis, D., Panagiotis, P., 2007. 3D numerical experiments on drag resistance in Vegetated flows, in: *International Association for Hydraulic Research*. Presented at the IAHR, Spain.
- Stelling, G.S., Wiersma, A.K., Willemse, J.B.T.M., 1986. Practical Aspects of Accurate Tidal Computations. *Journal of Hydraulic Engineering* 112, 802.
- Stewart, J.A., 1995. *Assessing sustainability of aquaculture developments* (PhD). University of Stirling
- Streeter, V.L., 1962. *Fluid Mechanics*, 3rd ed. McGraw-Hill Book Company, New York.
- Stroheim, T., Aure, J., Duinker, A., Castberg, T., Svardal, A., Strand, O., 2005. Flow reduction, seston depletion, meat content and distribution of diarrhetic shellfish toxins in a long-line blue mussel (*Mytilus Edulis*) farm. *Journal of Shellfish Research* 24, 15–23.

- Struve, J., Falconer, R.A., Wu, Y., 2003. Influence of model mangrove trees on the hydrodynamics in a flume. *Estuarine, Coastal and Shelf Science* 58, 163–171.
- Sumer, B.M., Fredsoe, J., 1997. *Hydrodynamics around cylindrical structures*. World Scientific, London.
- Sumner, D., Heseltine, J.L., Dansereau, O.J.P., 2004. Wake structure of a finite circular cylinder of small aspect ratio. *Experiments in Fluids* 37, 720–730.
- Sumner, D., Wong, S.S.T., Price, S.J., Paigdoussis, M.P., 1999. Fluid behaviour of side-by-side circular cylinders in steady cross-flow. *Journal of Fluids and Structures* 13, 309–338.
- Takeoka, H., 1984. Fundamental concepts of exchange and transport time scales in a coastal sea. *Continental Shelf Research* 3, 311–326.
- Tennekes, H., Lumley, J.L., 1972. *A First Course in Turbulence*. The MIT Press.
- Thom, A.S., 1971. Momentum absorption by vegetation. *Quarterly Journal of the Royal Meteorological Society* 97, 414–428.
- Tuckey, B.J., Gibbs, M.T., Knight, B.R., Gillespie, P.A., 2006. Tidal circulation in Tasman and Golden Bays: implications for river plume behaviour. *New Zealand Journal of Marine and Freshwater Research* 40, 305–324.
- Tully, J.P., 1958. On structure, entrainment, and transport in estuarine embayments. *Journal of Marine Research* 17, 523–535.
- Umlauf, L., Burchard, H., 2003. A generic length-scale equation for geophysical turbulence models. *Journal of Marine Research* 61, 235–265.
- Vallentine, H.R., 1959. *Applied hydrodynamics*. Butterworths Scientific Publications.
- Vinokur, M., 1974. Conservation equations of gas dynamics in curvilinear coordinate systems. *Journal of Computational Physics* 14, 105–125.
- Waite, R.P., 1989. *The nutritional biology of Perna canaliculus with special reference to intensive mariculture systems (PhD)*. University of Canterbury
- Walters, R.A., 2005. Coastal ocean models: two useful finite element methods. *Continental Shelf Research* 25, 775–793.
- Warner, J.C., Sherwood, C.R., Arango, H.G., Signell, R.P., 2005. Performance of four turbulence closure models implemented using a generic length scale method. *Ocean Modelling* 8, 81–113.
- Weise, A.M., Cromey, C.J., Callier, M.D., Archambault, P., Chamberlain, J., Mckindsey, C.W., 2009. Shellfish-DEPOMOD: Modelling the biodeposition from suspended shellfish aquaculture and assessing benthic effects. *Aquaculture* 288, 239–253.
- Wells, M.J., Heijst, G.J.F. van, 2004. Dipole formation by tidal flow in a channel. Presented at the International Symposium on Shallow Flows, Balkema Publishers, Delft, The Netherlands, pp. 63–70.
- Westwater, D., 2001. *Modelling hydrodynamic and Shallow water processes over vegetated floodplains (PhD)*. Cardiff University

- White, K., O'Neill, B., Tzankova, Z., 2004. At a Crossroads: Will Aquaculture Fulfill the Promise of the Blue Revolution? SeaWeb Aquaculture Clearinghouse.
- Wiberg, P.L., Smith, J.D., 1991. Velocity Distribution and Bed Roughness in High-Gradient Streams. *Water Resour. Res.* 27, 825–838.
- Wilcox, D., 1998. Turbulence modeling for CFD. American Institute of Aeronautics and Astronautics, Reston Va.
- Williamson, C.H.H., 1996. Vortex dynamics in the cylinder wake. *Annual Review Fluid Mechanics* 28, 477–539.
- Wu, W., Shields Jr., F.D., Bennett, S.J., Wang, S.S.Y., 2005. A depth-averaged two-dimensional model for flow, sediment transport, and bed topography in curved channels with riparian vegetation. *Water Resources Research* 41, 1–15.
- Wu, W., Wang, S.S.Y., 2004. A depth-averaged two-dimensional numerical model of flow and sediment transport in open channels with vegetation, in: *Riparian Vegetation and Fluvial Geomorphology*. American Geophysical Union.
- Zdravkovich, M.M., 1997. *Flow around circular cylinders, volume 1: Fundamentals*. Oxford University Press, Oxford.
- Zdravkovich, M.M., 2003. *Flow around circular cylinders volume 2: Applications*, 1st ed. Oxford University Press.
- Zdravkovich, M.M., Stonebanks, K.L., 1990. Intrinsically nonuniform and metastable flow in and behind tube arrays. *Journal of Fluids and Structures* 4, 305–319.
- Zedel, L., Hay, A.E., Cabrera, R., Lohrmann, A., 1996. Performance of a single-beam pulse-to-pulse coherent Doppler profiler. *IEEE Journal of Oceanic Engineering* 21, 290–297.
- Zimmerman, J.T.F., 1976. Mixing and flushing of tidal embayments in the western Dutch Wadden Sea part I: Distribution of salinity and calculation of mixing time scales. *Netherlands Journal of Sea Research* 10, 149–191.

**Appendix A**  
**Scale modelling and 2D numerical modelling:**  
**bottom trestles**

---

## A.1 Flow through scaled oyster trestles

Trestles are used to grow oysters in many locations, including Dungarvan Harbour on the East Coast of Ireland. Bags containing oysters are placed on top of the trestles and the trestles themselves are deployed in long rows in inter-tidal waters. Table A-1 provides dimensions for an individual trestle and pictures of a typical deployment are shown in Figure A-1.

Typically oyster trestle systems used in Dungarvan Harbour measure 3m in length and 1m in width and are raised approximately 0.4m above the seabed. A typical inter-tidal farm can consist of up to 20 of these trestle systems arranged in a row with up to ten rows side-by-side. Typical tidal ranges are from 3.6m on a spring tide to 2m on a neap tide with predicted values of 3.4m and 2.3m given in admiralty tide tables. Current speeds in Dungarvan typically lie in the range of 5-40cm/s.



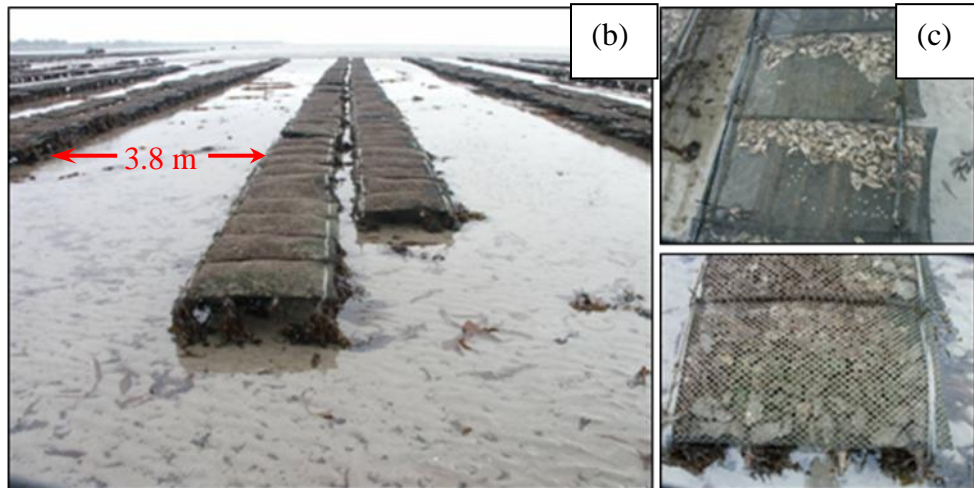


**Figure A-1: Typical oyster trestle farm; (a) oyster trestle farm, (b) double trestle configuration and (c) oyster bag**

**Table A-1: Individual Trestle Configuration**

Design Element	Dimension
Average Length	2.5m
Number of Bags per Trestle	5
Bag Dimensions	0.76m x 1.2m x 0.2 m
Trestle Height	0.303m
Trestle Width	0.787m
Spacing Between Double Trestle Rows	3.785m
Nominal Deployment Scheme	Double Rows of 20 trestles

#### **A.1.1 Tidal basin circulation patterns**

One of the problems associated with hydraulic modelling of comparatively fine-scale objects such as oyster trestles is determining the appropriate scaling parameters to use. In the scaling of the oyster trestles, it was desirable to maximize the physical dimensions so as to ensure that frictional and viscous forces did not dominate. This was particularly true of the vertical dimensions since a typical trestle system has a length to height ratio of up to 200 (Richardson, 2009). Therefore, it was decided to construct a geometrically distorted physical model of a prototypical oyster trestle system.

Distorted models are physical models in which the horizontal length scale and the vertical length scale are different. The use of a distorted model is suitable in situations where a hydrostatic pressure distribution in the vertical can be assumed and vertical flow motion is relatively small, as is the case in tidal flow (Novak et al., 2010). There are certain flow processes that cannot be modelled in a distorted model. These include: the modelling of eddies, spreading of jets, the flow around some bodies where separation may occur in the model but not in the prototype (Kobus, 1980). A distorted model also results in vertical velocity scale that is different to the horizontal. For distorted models, the vertical velocities in the scale model are  $(L_x/L_z) \cdot 1/\sqrt{L_z}$  times faster than in the prototype. Nevertheless, once the implications are understood, a distorted model can be used very successfully (Hughes, 1993).

The preliminary design consideration in the construct of a distorted scale model is the distortion factor. Hughes, (1993) recommended a distortion factor less than 5 be used for long-wave hydraulic models. Based on considerations of a range of factors; primarily a marriage between, maximizing observable flow processes, and ensuring viscous forces didn't dominate in a miniscule scaled system; a scaling factor of 40 in the horizontal and 15 in the vertical was decided on for this study. This corresponded to a distortion factor of 2.7; within the limit suggested by Hughes, (1993).

Appropriate tidal forcing constituents were prescribed based on a comprehensive consideration of actual field dynamics and previous scale modelling studies conducted in the tidal basin; the objective being to strike a balance between realistic tidal conditions and laboratory limitations. The calculated values were a tidal range of 138mm and tidal period of 586 seconds.

In order to simulate the positioning of oyster trestles in the inter-tidal marine environment, it was considered important to ensure that the scaled system be exposed to inter-tidal flow conditions. In order to achieve this, a 175mm high raised platform was placed in the basin extending 2.5m from the back wall and across the width of the basin as detailed in Figure A-2. This placed the model within the range of tidal motions. The modification of the tidal basin to simulate inter-tidal flow conditions raised concerns regarding the effects the platform may have on flow circulation. Hence, this stage of the study required that the basin be compared against numerical model data to assess any discrepancies. Table A-2 presents bathymetric and open

boundary data adopted for both the physical and numerical model. Of primary concern was whether the raised platform induced significant wave reflection within the basin and whether flow currents over the inter-tidal surface were subjected to noticeable viscous forces. Flow measurements were recorded at the locations detailed in Figure A-2 and again compared with numerically predicted values.

The inter-tidal simulation conditions of the tidal basin resulted in the ADV probe being exposed for a portion of the tidal cycle. Hence, gaps exist in the data as the tidal cycle approaches the low water mark. However, as currents are negligible for all practical purposes at this stage of the tidal cycle, this gap in data was not of concern for this study.

**Table A-2: Dimensional values prescribed for the scale and numerical models. A scaling factor of 40 in the horizontal and 15 in the vertical was adopted with appropriate Froude scaling laws applied**

Parameter	Physical model	Numerical model
Tidal amplitude	0.069m	1.035m
Tidal Period	586s	6052s
Bathymetry	0.085m	1.275m

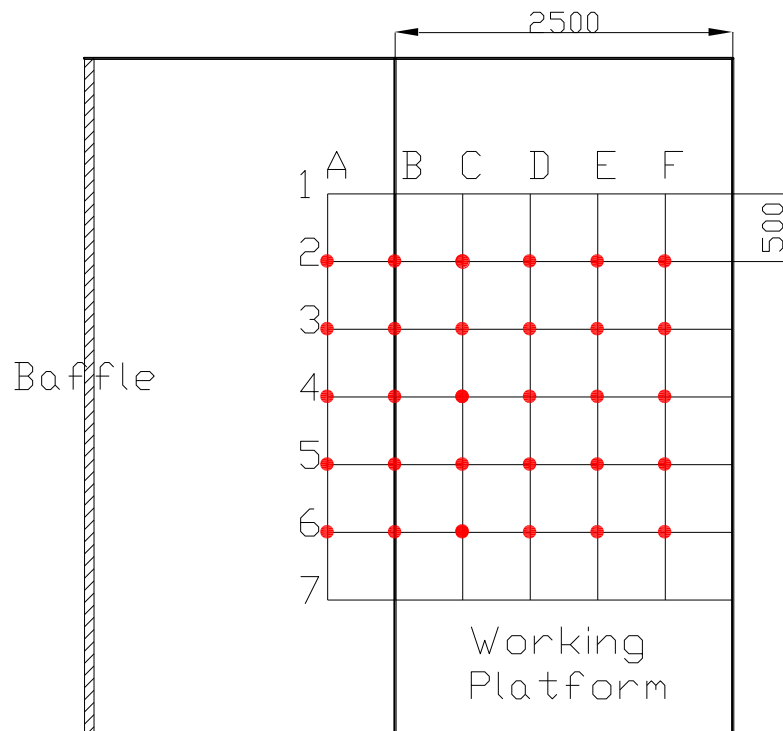


**Figure A-2: Tidal basin schematic detailing location of raised platform (2500mm from back wall) and velocity testing points (red circles)**

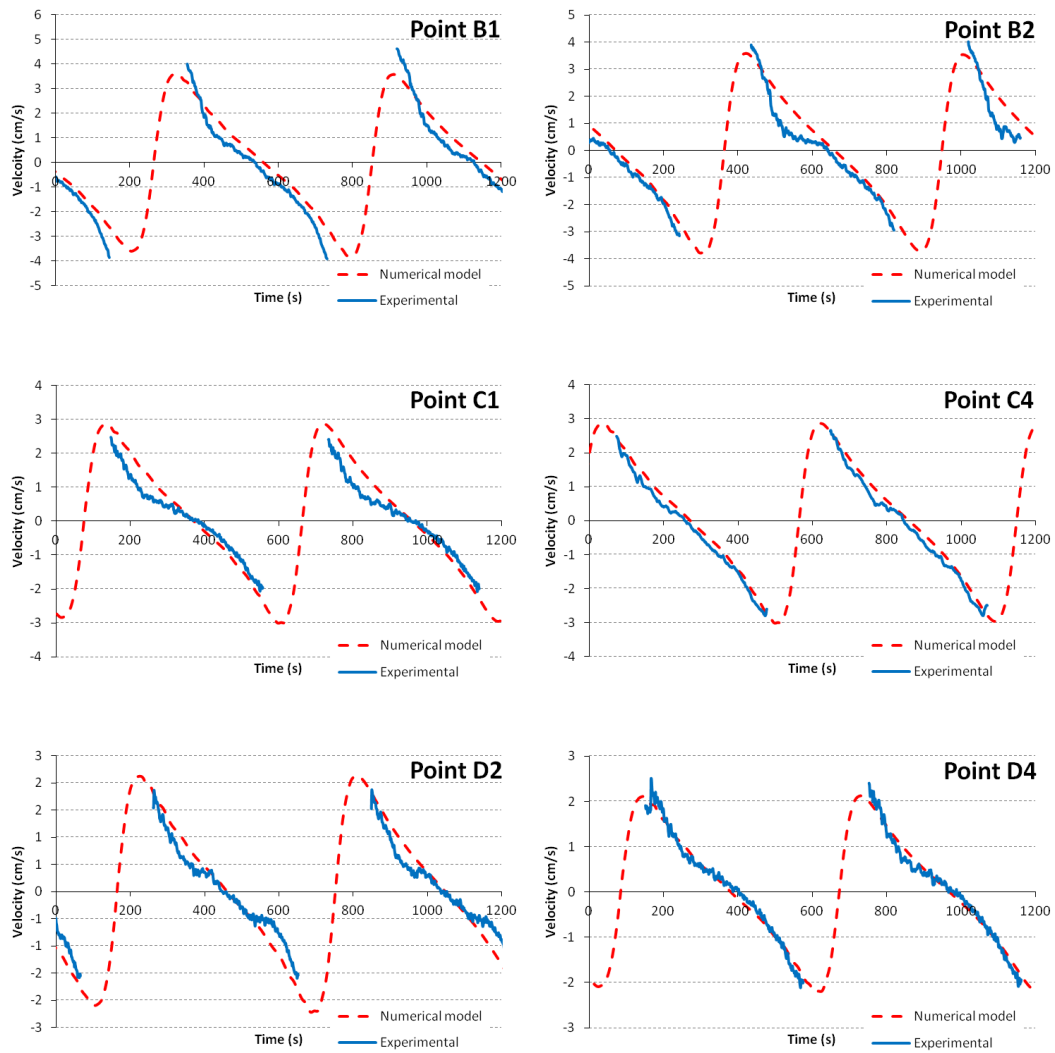


**Figure A-3: Comparison between experimental and numerical velocities Location of sampling points within tidal basin are illustrated in Figure A-2**

The primary issue in this validation exercise was that the numerical model replicated the velocities observed in the laboratory. We generally see quite good agreement between both sets of data. Velocity magnitudes are replicated quite well and there is no discrepancy in the predicted profile of flow over time. The model appears to overestimate velocities at some points; notably peak ebb-tide velocities at points C1 and D2. However, the accuracy of the ADV probe at this stage of the tidal cycle is questionable due to the water level falling below the level of the probe for part of the ebb-tide. Hence, the agreement between experimental and numerical results was deemed satisfactory. Subsequent sections investigate the effects of scaled trestles on tidal flows and circulation patterns.

### A.1.1 Scaling of trestles

To analyse flows through oyster farms, a scaled trestle system was installed in the tidal basin. The scaled model trestle system, constructed for the tidal basin experiments, was based on the prototype dimensions collected in the field and a review of photographs taken in Dungarvan Harbour. The prototype trestle configuration had 8 double rows; each 50 metres long (Figure A-4).



**Figure A-4: Trestles in Dungarvan Harbour**

Based on scaling factors and the prototype configuration detailed previously, Table A-3 presents dimensional information on the scaled trestle system. Eight trestles were placed in the basin to represent a typical oyster farm layout.

**Table A-3: Prototype and model design configuration**

Design Element	Physical model	Numerical model
Trestle Height	0.27m	0.403m
Trestle Width	0.04m	1.6m
Trestle Length	1.25m	49.6m
Trestle spacing	0.1m	4m
Tidal Range	0.14m	2.1m
Tidal Period	586s	6052s
Bathymetry	0.085m	1.275m

The porous nature of an oyster trestle system posed a problem for the physical modelling studies. This porosity, applied at the scale model level, undermines the assumption that inertial forces only dominate. Instead, any flow through the trestle system would be highly viscous and dominated by frictional effects. Richardson, (2009), conducted high resolution CFD modelling studies of flow distribution within an oyster trestle system. Figure A-5 presents a snapshot from the predicted flow regime within and around an oyster trestle system. The study found that flows through the trestles were practically zero. Therefore, based on these considerations, it was decided to neglect flows through an individual trestles, and instead, the trestles were modelled as solid blocks.

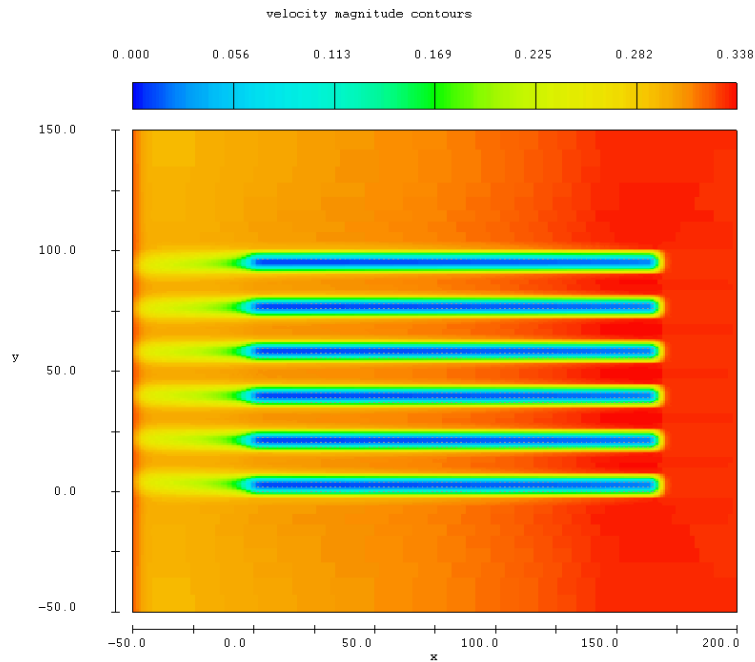


**Figure A-5: Predicted flow distribution within a typical oyster trellis system. Average values of approach flow speed and water depth were used as boundary conditions. Adopted from Richardson, (2009)**

### A.1.2 Numerical model

A numerical model of the scaled trellis system was developed in DIVAST at the prototype scale. The objectives of the numerical model study were twofold: to investigate the interactions between the modelled aquaculture installations and flows, and to extend the laboratory simulations to the bay-scale level.

Two methods have been widely adopted to model physical impediments in hydrodynamic simulations. The first is to treat the impediments as solid blocks, whose configurations are included in the bathymetry of the computational domain. The second method is to specify a very high local roughness values to represent the drag effects acting on the flow in the vicinity of the installation, while the shape of the actual impediment is not included in the domain topography. Liang, et al., (2007) investigated a third method, whereby the physical impediment was treated as a porous medium. In this analysis, the flows through the impediment were computed based on mass conservation and the hydraulic conductivity properties of the medium. The study assessed the performance of the three methods in predicting flood flows around buildings. Namely, the buildings were simulated as: (1) solid blocks, (2) a local increase in roughness and (3) as a porous medium. Despite the differing

hydrodynamics principles involved, the results were quite similar. All three methods accurately predicted the complex shock waves that occur in close proximity to the buildings. Due to the similarities in reported performance, it was decided to represent the prototype-scale oyster trestles as solid objects for the purposes of this study. Hence, the numerical model represented the trestles as an additional element of the computational domain and included them in the model bathymetry.

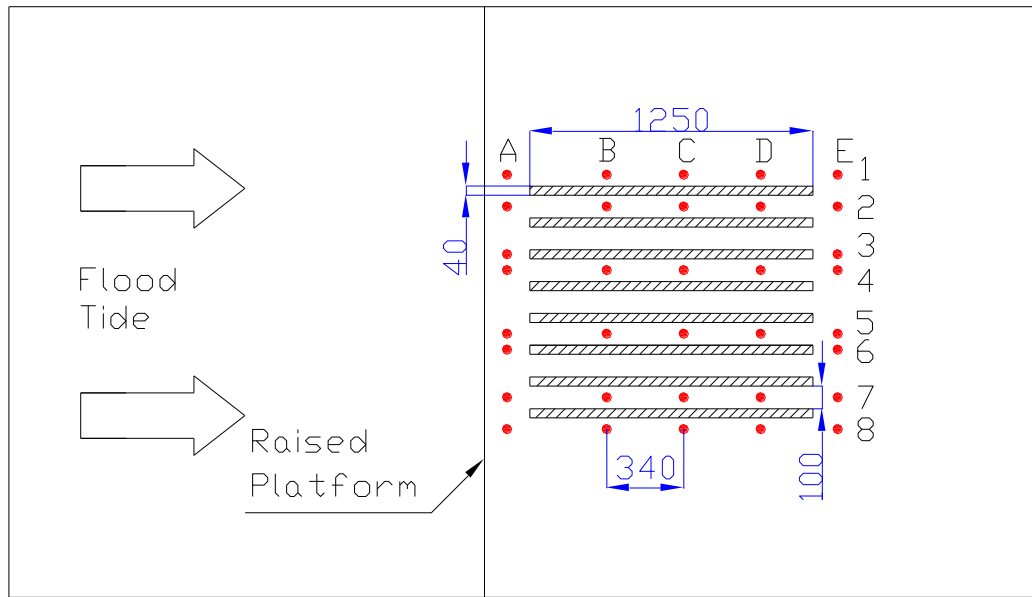
Table A-3 presents details on the numerical model. Briefly, the oyster trestles were dimensioned based on typical measured field data (Figure A-4), with tidal conditions based, not on typical tidal conditions occurring in the field, but rather a scaled representation of the tidal parameters specified in the tidal basin. The scaling of bathymetry resulted in a computational domain of 1.275m depth, with this reduced to 0.87m in cells containing modelled trestles. This equated to an instantaneous jump in bathymetry of 30% in a domain that also included extensive wetting and drying processes during the inter-tidal period.

The simulation of dynamics near sharp bathymetric irregularities can induce spurious high-frequency oscillations (Rahman and Chaudhry, 1998). This is particularly true when wetting and drying occurs (Liang, Lin, et al., 2007), as is the case for flow over the modelled oyster-trestles during the inter-tidal period. Hence, the performance of the model with regards both stability and the accurate simulation of wetting and drying processes was of interest in this study.

### **A.1.3 Flows parallel to trestles**

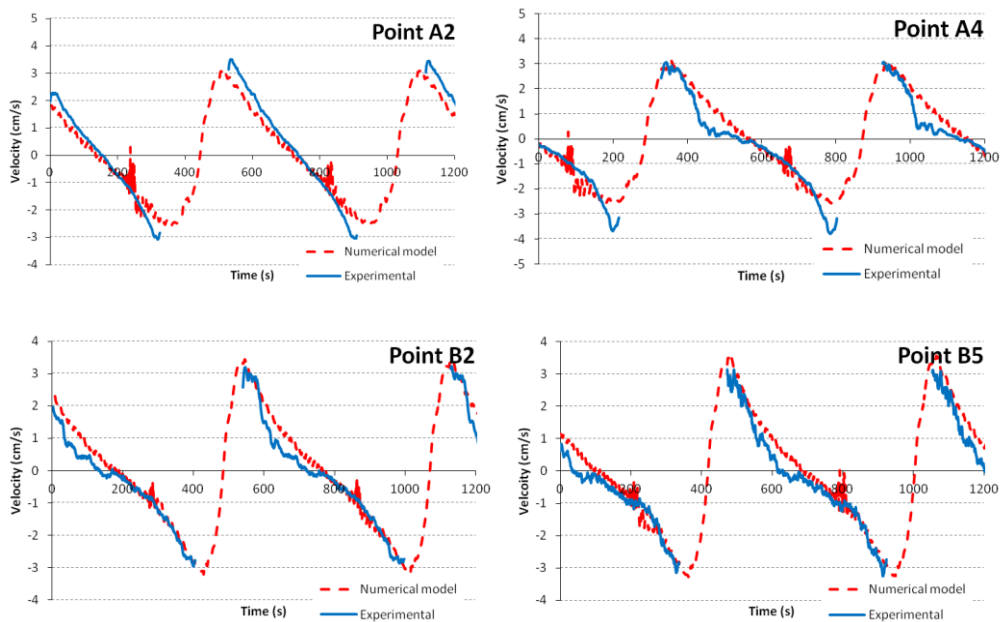
Initially the trestles were aligned to the direction of flow as detailed in Figure A-6. This is the most common orientation for oyster trestles in the field (BIM 2006, pers. comm.). One of the research objectives was to assess whether this is the optimal arrangement.

Velocity measurements were recorded at the points detailed in Figure A-6 and compared with the numerical model. Results were analysed to investigate whether the trestles induced any attenuation of flow, and in particular, whether this retardation effect was exacerbated in the downstream extents of the installations.



**Figure A-6: Tidal basin schematic detailing location of scaled trestle system (hatched) and velocity testing points (red circles)**

Figure A-7 presents velocity data collected at the relevant points in the tidal basin plotted against numerically predicted output. To compare physical and numerical data, a scaling factor of  $L_x/\sqrt{L_z}$  was applied to the time measurement and a factor of  $1/\sqrt{L_z}$  to velocity measurements in accordance with Froude law similitude criteria discussed previously.



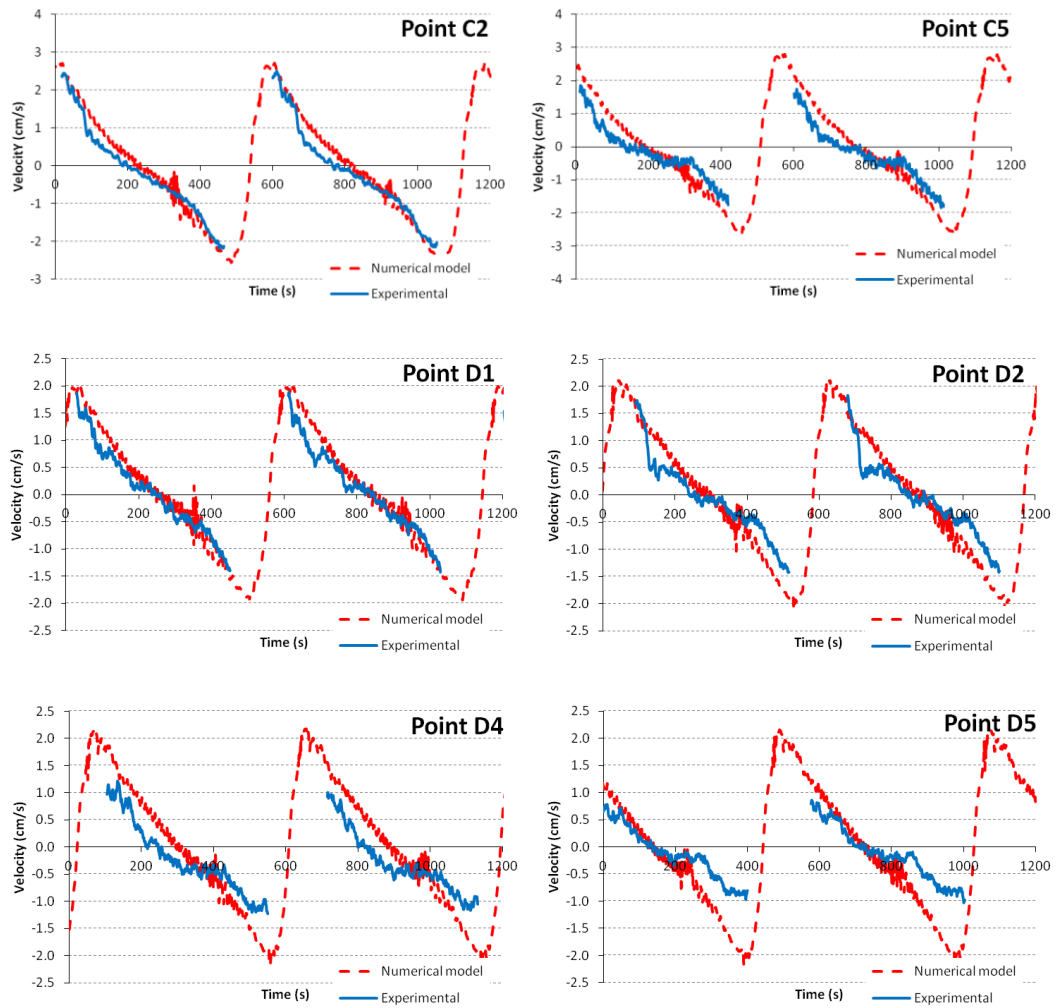


**Figure A-7: Comparison between experimental and numerical velocities. Figure A-6 details location of sampling points**

An analysis of velocities at all data points displays a number of interesting features. In general, the numerical model replicated both the velocity profile and magnitudes observed in the tidal basin quite well. However, a number of measurement points display significant inconsistencies between observed and predicted data. Observed velocities within the physical model are consistently lower in magnitude along the centreline (primarily axis 4 and 5) of the scale model than the numerical model. At other observation points, there is generally good agreement with the numerically predicted results. This is particularly evident along axis D. On the outer extents of the physical model (D1, D2) there is good agreement between experimental and numerical data output. However, at points D4 and D5 the numerical model significantly overestimates velocities. It appears that the numerical model is under predicting the local frictional resistance of the installation. A local increase in

frictional drag may be required to accurately simulate the actual dynamics of the system. This will be discussed in detail in subsequent sections.

#### A.1.4 Flow at 15 degree to trestles

One of the main objectives of this part of the research was to investigate whether changing the orientation of the aquaculture installation affects flow patterns within the system, and in particular, whether there is an optimal orientation of trestles. In this section, we look at the effect of orientating the trestle system at an angle of  $15^\circ$  to the direction of flow. Figure A-8 details a schematic of the physical model.

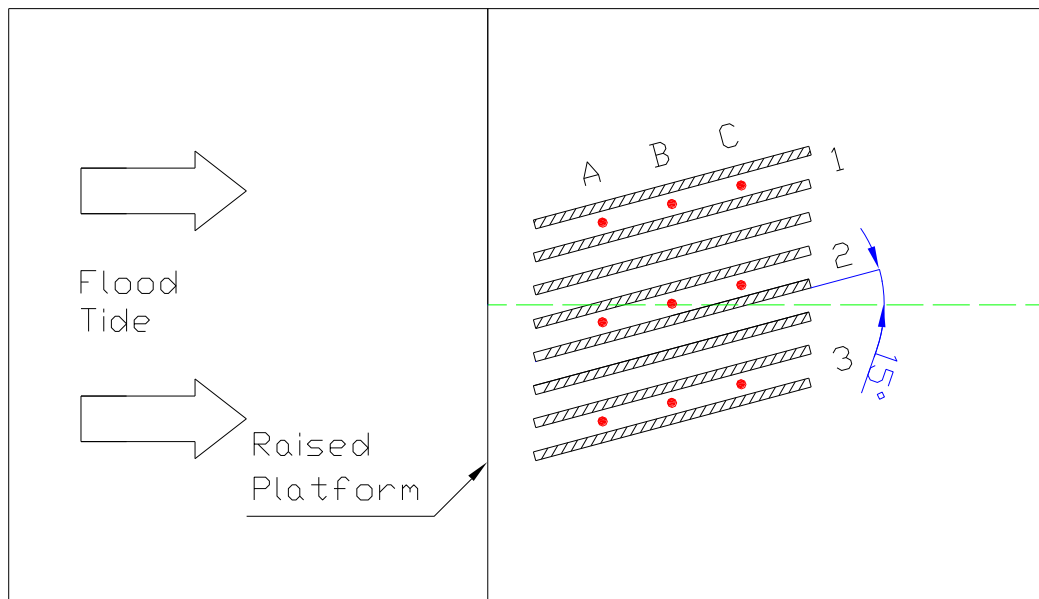


**Figure A-8: Tidal basin schematic detailing location of scaled trestle system (hatched) and velocity testing points (red circles). Trestles system aligned at  $15^\circ$  to direction of flow**

Detailed velocity measurements were collected at the points detailed in Figure A-8 and again compared with numerical model output. As before, the main objectives of this study were, to assess the numerical model performance, and to determine the degree of attenuation of flow that may occur within the system.

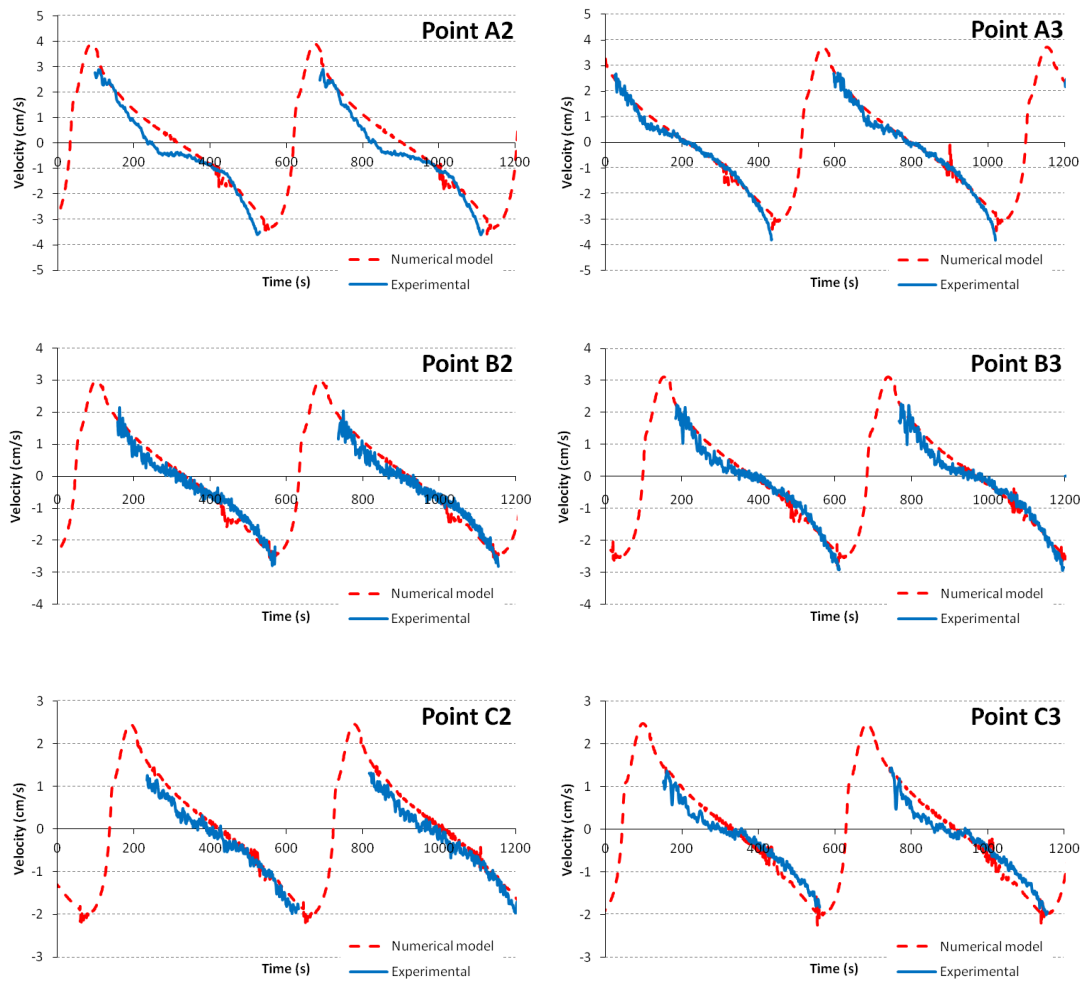


**Figure A-9: Comparison between experimental and numerical velocities. Figure A-8 presents location of sampling points within tidal basin.**

Figure A-9 displays a significant attenuation of flow within the physical model, particularly at the downstream extents. Axis A produces generally good agreement between numerical and physical model data; while the numerical model significantly overpredicted velocities along axis C. Analysis of the data suggests that this is again a result of the numerical model underestimating the frictional resistance of the physical model.

The total drag exerted on the fluid by the physical model can be reduced to a combination of form drag and frictional resistance (Chanson, 2004). As flow enters the system, the main impediment is form drag provided by the physical presence of the structure, that induces separation of flow and corresponding loss of momentum. The numerical model simulates this quite accurately as displayed by velocity data collected along axis A. Subsequently, skin drag becomes the dominant force

component retarding flow due to the viscous shearing that develops between the surface and the layer of fluid just above it. The frictional resistance of the scale model was underestimated by the numerical model as displayed by comparison of results along axis C. This is particularly evident on the flood tide where flows were reduced by up to 50%. A localised, experimentally derived increase in bed roughness may be required to simulate the flow processes observed in the laboratory.

#### A.1.5 Trestles at 45 degree to direction of flow

The effect of a further increase in the angle of orientation to the direction of flow was investigated by a similar procedure. Figure A-10 presents a schematic of the experimental situation. A primary feature of interest in this study was whether the flow attenuation observed in the previous section (trestles at 15° to flow), were exacerbated by the increase in angle. Velocity data was recorded at the points denoted in Figure A-10 and results were assessed vis-à-vis numerically predicted output. Of particular interest was whether the numerical model again underestimated the frictional resistance that is exerted on the flow. Figure A-11 displays a plot of numerically predicted velocities plotted against experimental results.

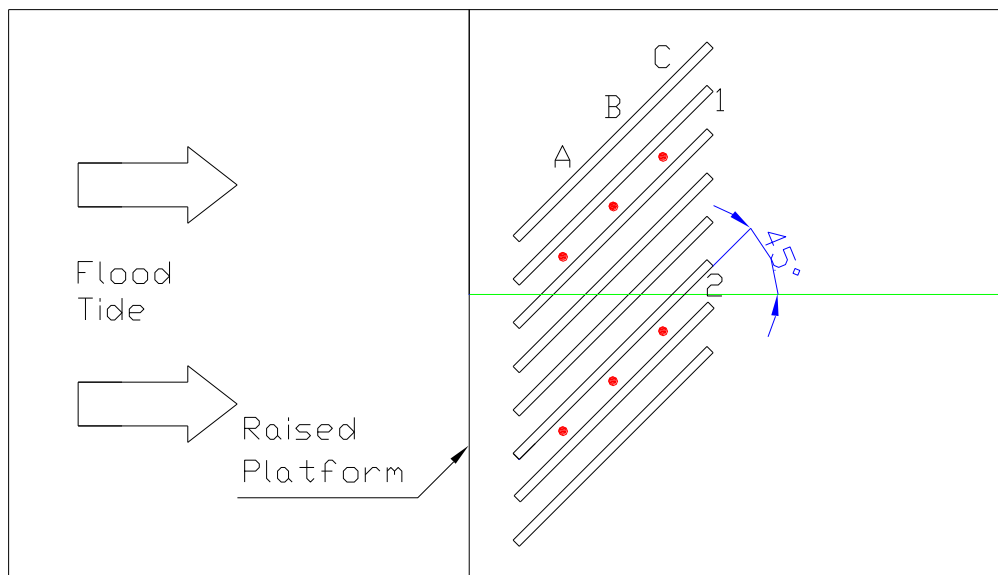


**Figure A-10: Tidal basin schematic detailing location of scaled trestle system (hatched) and velocity testing points (red circles). Trestles system aligned at 45° to direction of flow**

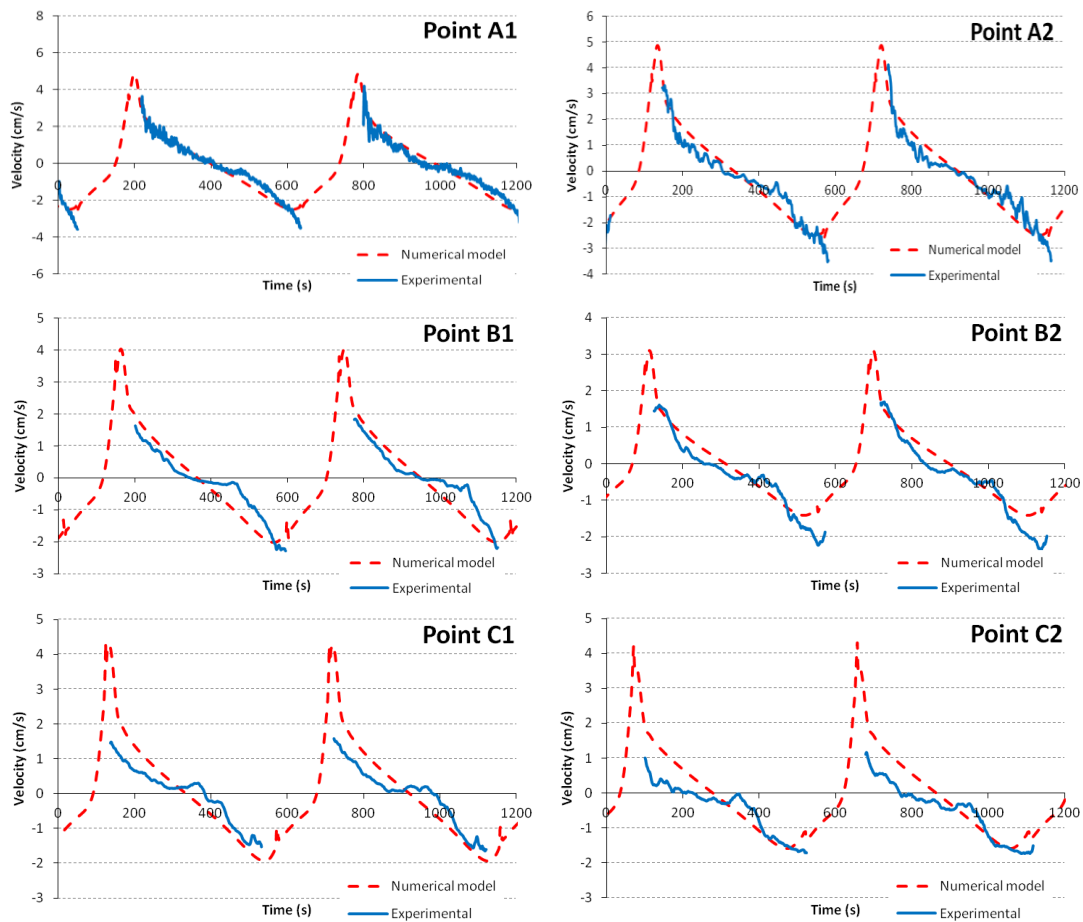


**Figure A-11: Comparison between experimental and numerical velocities. Figure A-10 displays location of sampling points.**

An interesting flow phenomenon predicted by the numerical model was an apparent ‘channelling’ of flows between the trestles. During the inter-tidal, flooding-and-drying period of the tidal cycle, the trestles ‘dry out’ and are removed from the computational domain; resulting in a greater portion of the flow being diverted between the trestles. This results in a large velocity peak developing on the flood tide. As the water level continues to rise, the trestles are ‘flooded’ again, and the local velocity between trestles reduces rapidly to an ambient mid-flood level of circa 2cm/s as flow returns to the trestle-containing region. (A similar ‘channelling’ effect was observed in solute transport studies carried out as part of this study (Section A.2). Tracer experiments demonstrated greater transport occurring between the trestles with material transport being directed in the direction of trestle orientation. This will be discussed in greater detail in later sections.)

This velocity peak was not observed in the tidal basin. Instead, mid-flood and mid-ebb peak tidal flows are both circa 2cm/s. A reason for this discrepancy may be the differing positions in the water column at which velocity measurements are recorded. In the physical model, the ADV was positioned at a level with the top of the trestles, as a result of a trial and error analysis of the optimum location for measuring tidal velocities. In the numerical model, on the other hand, depth-averaged velocity measurements were output at a point that coincides with a depth 0.36H. Figure A-12 demonstrates this discrepancy between the physical and numerical model sampling depths. In this case, at a hypothetical water depth of 40mm, the numerical model samples at approximately mid-height of the trestle system (0.36 of the water depth), while the ADV probe measures currents at the top of the trestle system. At particular stages of the tidal cycle, this will result in discrepancies between physical and numerical model results.

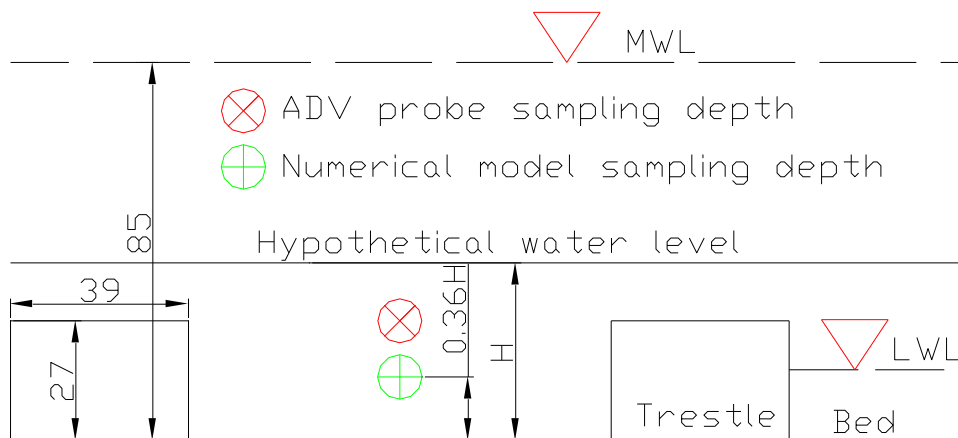


**Figure A-12: Schematic detailing sampling locations of physical and numerical model sampling depth at the low water mark**

## A.2 Dye tracer experiments

Flow circulation patterns and solute transport within an aquaculture system was analysed via dye tracer experiments conducted within both the physical and numerical models. Of particular interest were:

1. Longitudinal and lateral dimensions of solute travel within the system; primarily whether the concentration of dye at the downstream extents of the farm was reduced or altered in anyway (this is of considerable interest concerning the supply of nutrients within an aquacultural system).

- Whether the time that the tracer spends within the system is affected. This has significant consequences for the removal of pollutants from a waterbody.

#### A.2.1 Scale model solute transport studies

A detailed assessment of dye tracer transport within the scaled oyster trestle system was conducted. Dispersion of malachite green dye was recorded by a camcorder mounted above the centre of the system. Dye was released 0.2m upstream of the scaled system. Simulations always began at the low water mark and continued for a full tidal cycle. Of particular interest was the effect that varying the orientation of the trestle system had on flow and water circulation patterns. Figure A-13, Figure A-14 and Figure A-15 presents dye transport through the scaled oyster trestle system at three different orientations; trestles aligned parallel to direction of flow, trestles aligned at a 15° angle to the direction of flow and trestles aligned at a 45° angle to the direction of flow.

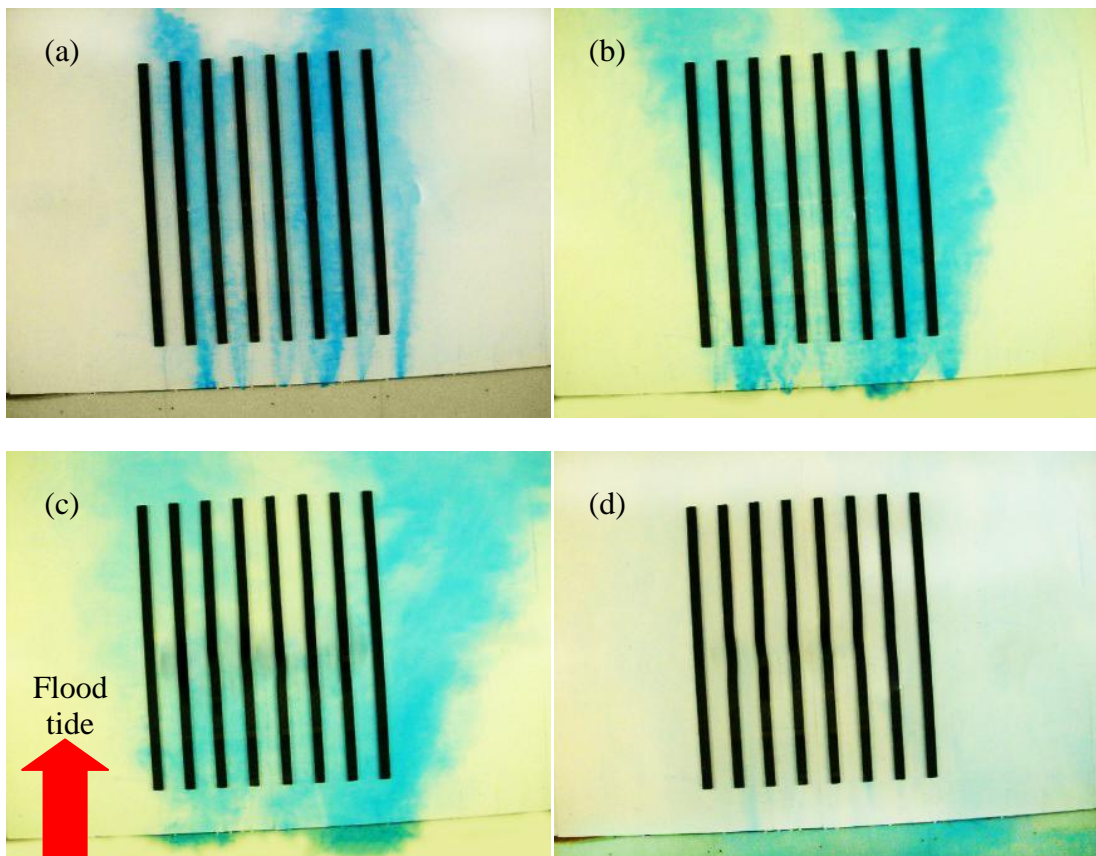


**Figure A-13: Dye transport recorded in the tidal basin with trestles orientated parallel to the direction of flow at four different stages of the tidal cycle; (a) flood tide, (b) high water mark, (c) ebb tide and (d) low water mark**

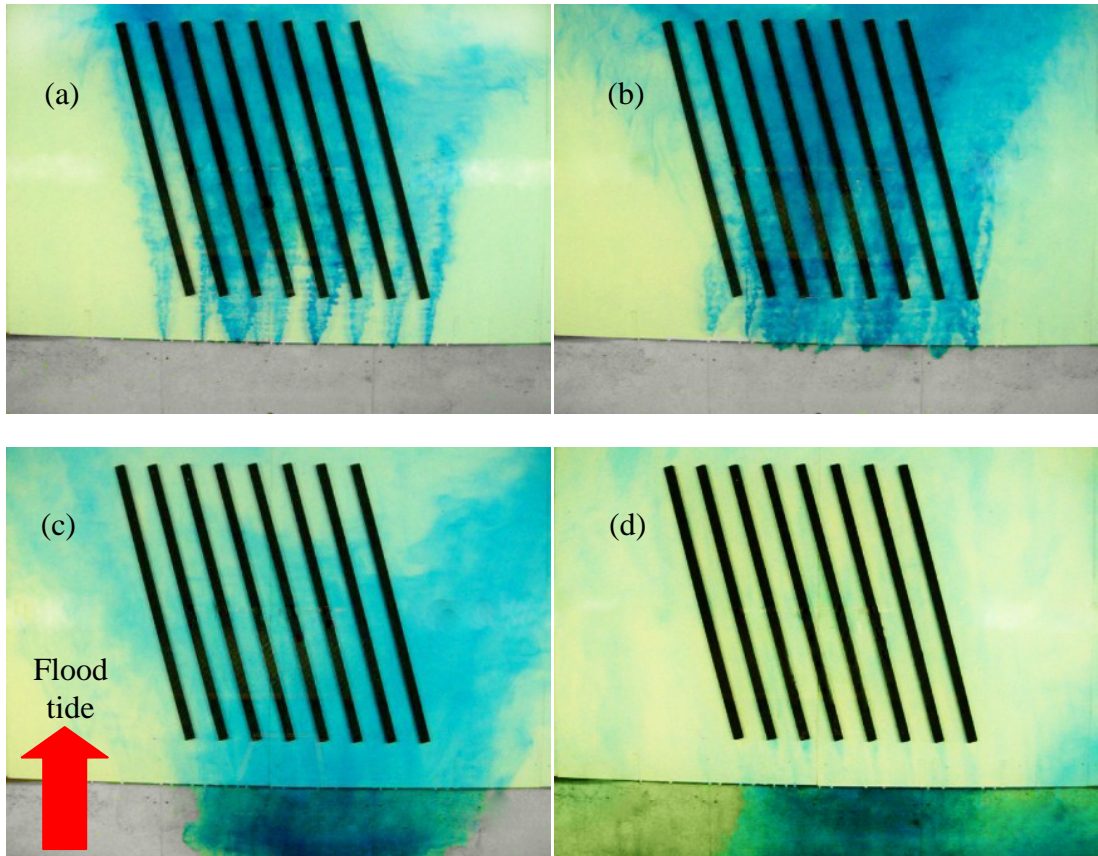


**Figure A-14: Dye transport recorded in the tidal basin with trestles orientated at 15° to the direction of flow at four different stages of the tidal cycle; (a) flood tide, (b) high water mark, (c) ebb tide and (d) low water mark**

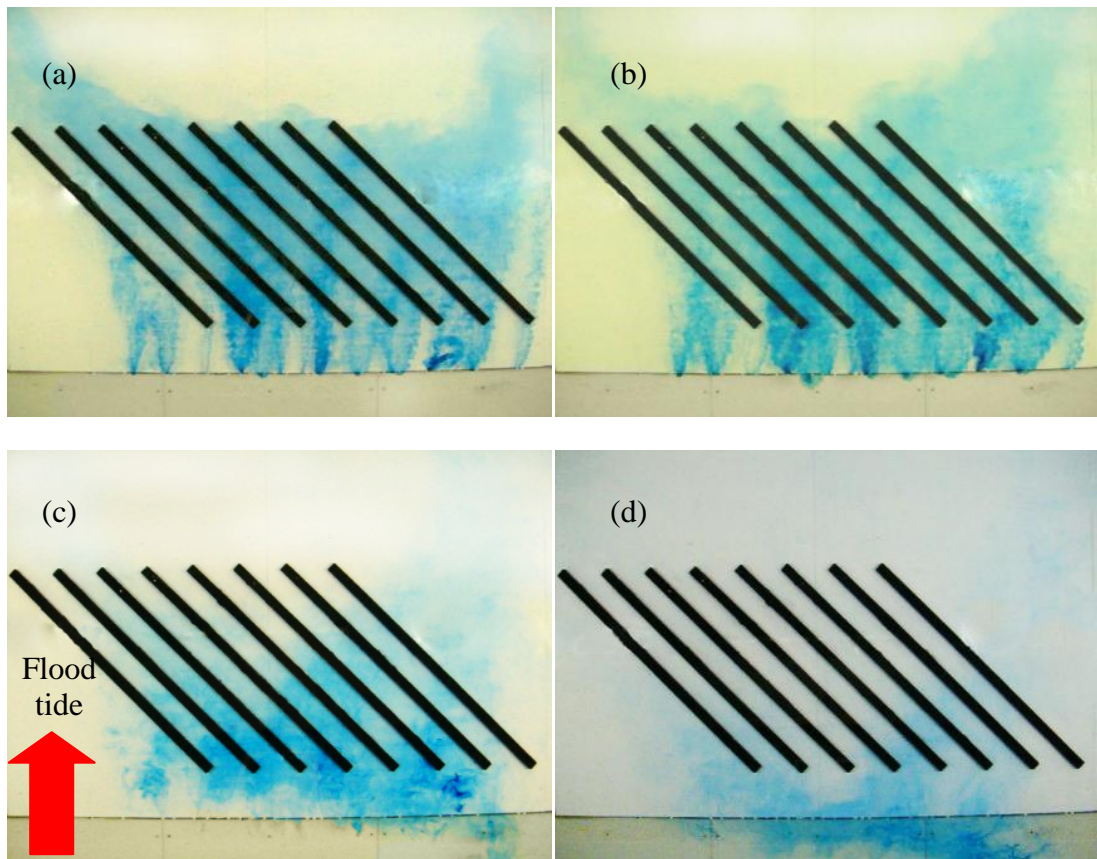


**Figure A-15: Dye transport recorded in the tidal basin with trestles orientated at 45° to the direction of flow at four different stages of the tidal cycle; (a) flood tide, (b) high water mark, (c) ebb tide and (d) low water mark**

Varying the orientation of the trestles has two primary physical implications for an oyster farm installation:

1. Aligning the farm at an angle to the direction of flow reduces the streamwise length of the farm and hence can help remedy the problem of nutrient depletion at the downstream extents of the farm due to intensive particulate feeding by the feeders;.
2. Aligning the farm at an angle to the direction of flow increases the lateral dimensions of the farm; which may have implications for the spatial optimization of farm layouts within a bay.

Previous studies have suggested that the additional bottom roughness that the bottom-feeding bivalves essentially constitute, may increase the nutrient supply to the feeders via enhanced vertical diffusion (Frechette et al., 1989). Hence, the depletion of nutrients by the organisms is partially counteracted by the transport of nutrients

from the upper layers due to the enhanced mixing. In order to assess the effect of the structures on vertical diffusion in the laboratory, underwater tracer transport experiments investigated the vertical profile of solute transport. The experimental procedure was identical to the previous solute transport studies with the sole exception being the placement of the camcorder. The recorder was enclosed in a watertight unit and placed upstream of the scaled system at a level with the system. Material transport was recorded over a full tidal cycle. This enabled an investigation of the transport of tracer over the entire water column, for a full tidal cycle.

Figure A-16 presents a vertical profile of the transport of tracer through the system on the flood tide. The camcorder is aligned perpendicular to the direction of the trestles, and flow is at a 45° angle to the trestles. The two primary features of interest in this study are: (1) the transport of tracer over the structures, and (2) the secondary flow processes that induce recirculation between the structures. This recirculation of flow is evident in Figure A-16. Initially, the trestles divert flows over the system as displayed in Figure A-16(a). The ambient direction of transport is then altered by internal circulation within the flow. Figure A-16(b) presents a snapshot of material transport 20 seconds later. A significant concentration of material is observed between the individual trestles, and tracer is dispersed over the entire water column. This induced turbulent transport will be assessed and discussed in later sections by numerical modelling studies.



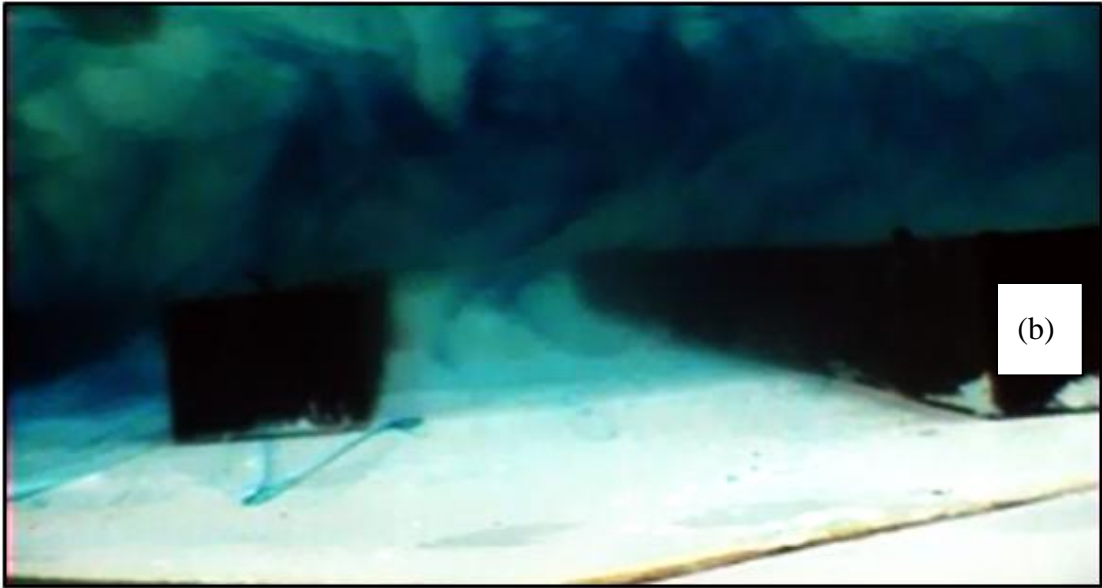


**Figure A-16: Vertical profile of tracer transport through a scale model of bottom-feeding bivalves (a) transport of tracer over trestles and (b) transport of tracer between trestles**

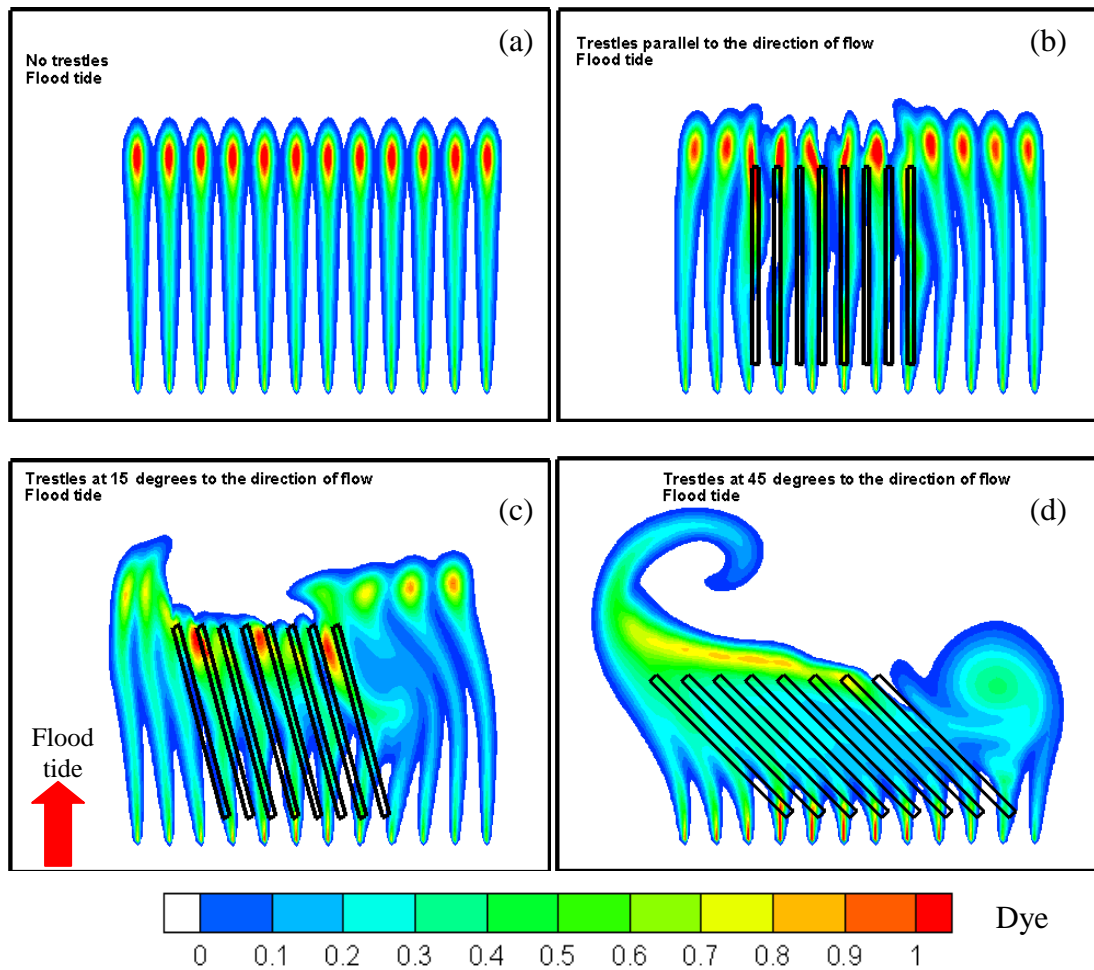
#### **A.2.2 Numerical model solute transport studies**

Numerical tracer transport experiments were conducted in conjunction with the laboratory experiments. The solute transport module in DIVAST was used to assess material transport within the prototype model. A conservative tracer was introduced at 8m intervals at a distance of 6m upstream of the oyster farm. The material transport fate was evaluated over a full tidal cycle with synoptic snapshots of concentration output every 200 seconds.

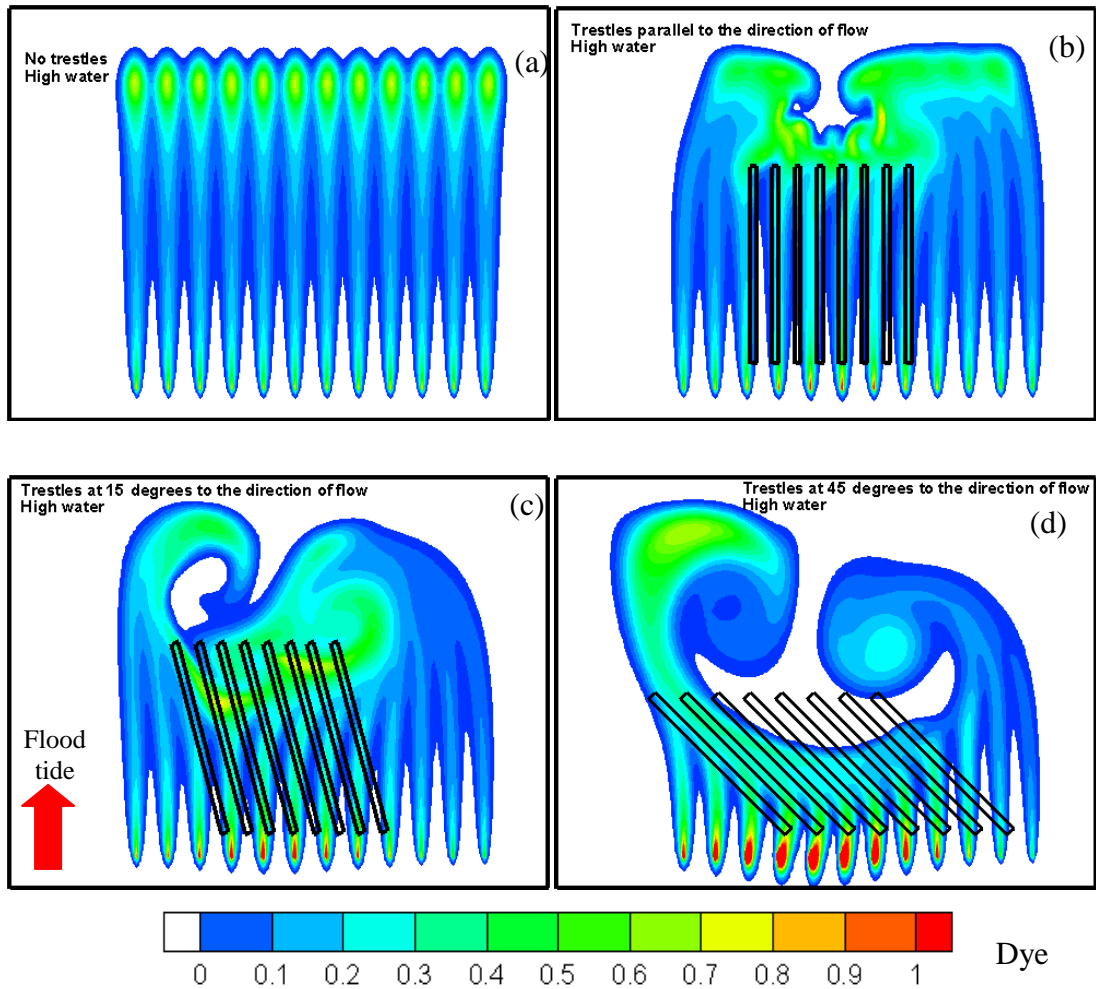
Material transport simulations were conducted for three different orientations of the trestles; to replicate physical modelling dye transport simulations. Data collected in the laboratory was used to assess the performance of the numerical model and provide qualitative information to fine-tune dispersion and diffusion coefficients. Of particular interest were the longitudinal transport of the material on the flood tide and the flushing of dye on the ebb.

Figure A-17 presents predicted transport on the flood tide for four different configurations, namely: no trestles included in the model; trestles parallel to the direction of flow; trestles at a 15° angle to the direction of flow; and trestles at a 45° angle to the direction of flow. Subsequent figures present flows through equivalent mariculture configurations at different stages of the tidal cycle. Figure A-18 presents tracer transport at the high water mark; Figure A-19 presents tracer transport at mid-

ebb and finally, Figure A-20 presents the remaining concentration of material at the low water mark.



**Figure A-17: Tracer transport predicted by DIVAST at mid-flood with four different mariculture scenarios: (a) no oyster trestle installations, (b) trestles parallel to the direction of flow (c) trestles at a 15° to the direction of flow and (d) trestles at a 45° angle to the direction of flow. Dye released upstream of the system at the low water mark.**



**Figure A-18: Tracer transport predicted by DIVAST at high water with four different mariculture scenarios: (a) no oyster trestle installations, (b) trestles parallel to the direction of flow (c) trestles at a 15° to the direction of flow and (d) trestles at a 45° angle to the direction of flow. Dye released upstream of the system at the low water mark.**

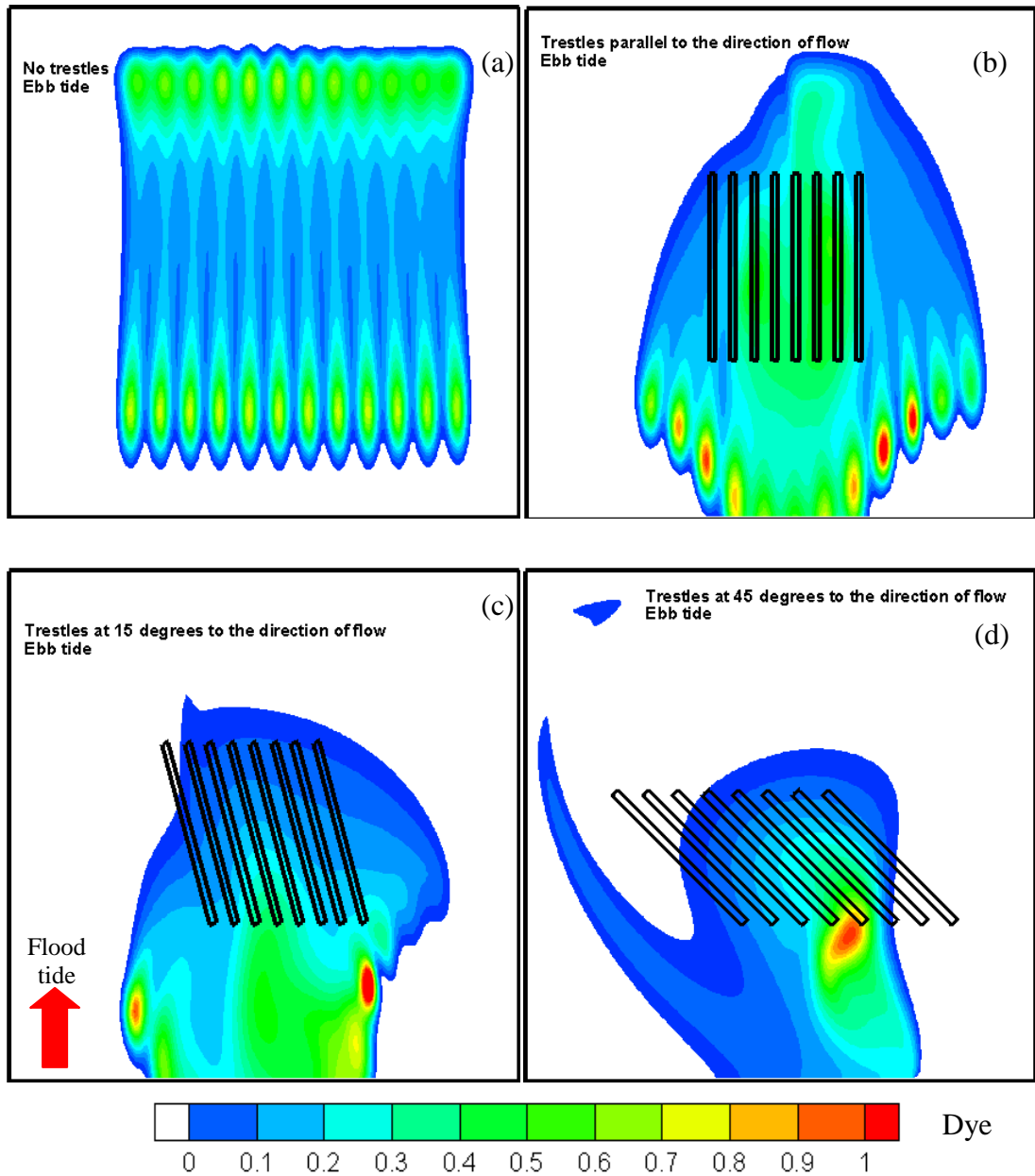


**Figure A-19: Tracer transport predicted by DIVAST at mid-ebb with four different mariculture scenarios: (a) no oyster trestle installations, (b) trestles parallel to the direction of flow (c) trestles at a 15° to the direction of flow and (d) trestles at a 45° angle to the direction of flow. Dye released upstream of the system at the low water mark.**

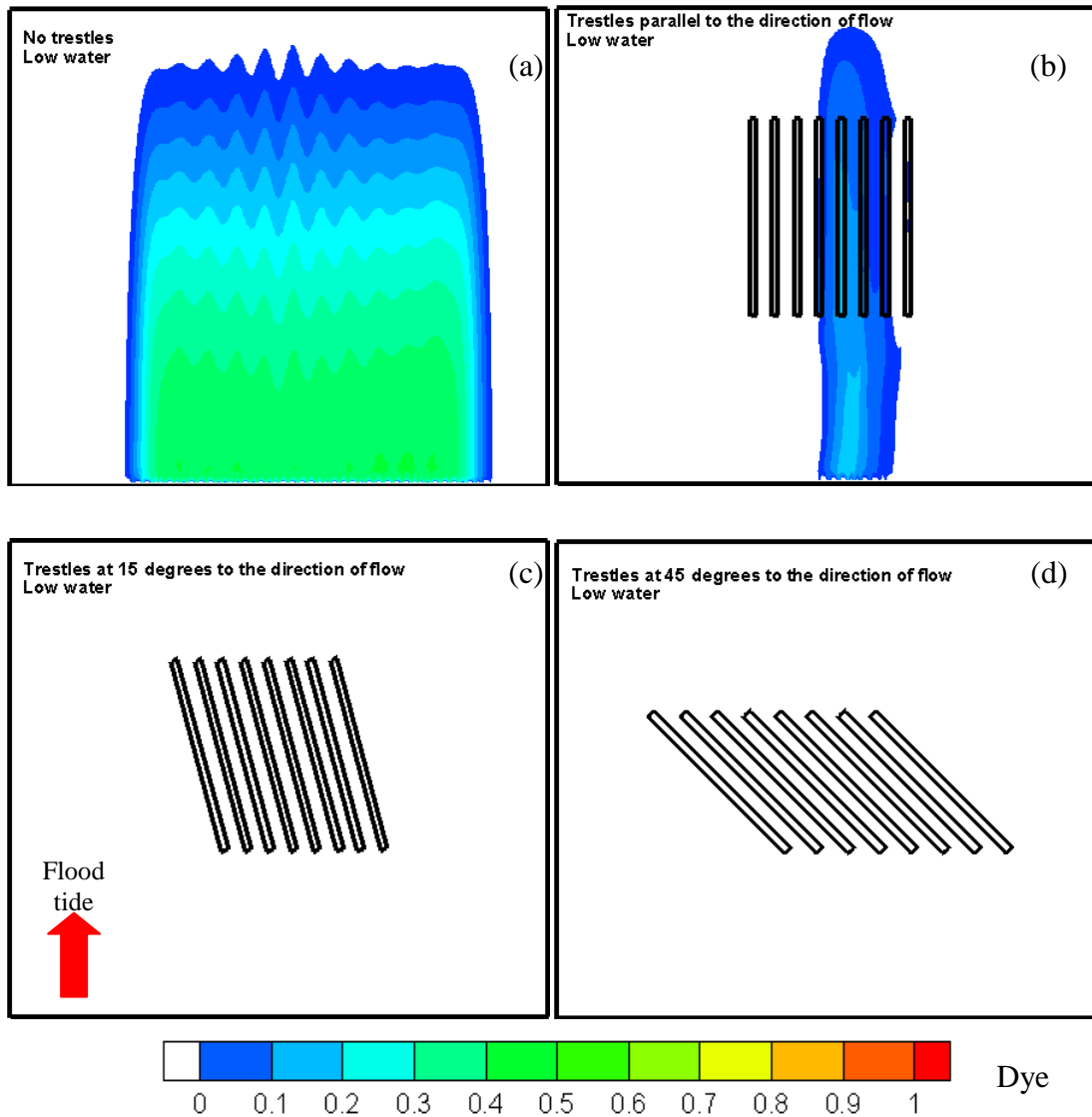


**Figure A-20: Tracer transport predicted by DIVAST at low water with four different mariculture scenarios: (a) no oyster trestle installations, (b) trestles parallel to the direction of flow (c) trestles at a 15° to the direction of flow and (d) trestles at a 45° angle to the direction of flow. Dye released upstream of the system at the low water mark.**

### A.3 Discussion and conclusions

The combined physical and numerical tracer transport experiments conducted as part of this research allow a number of conclusions to be drawn on flow through an oyster trestle system:

- The installation of an oyster trestle farm in a bay retards ambient flows and consequently material transport. The longitudinal transport of material through the central axis is retarded by circa 20% by the inclusion of the trestles,

regardless of orientation. This has major repercussions for the supply of nutrients to oysters within the system

- The orientation of the trestles relative to ambient flow direction also affects material transport. This is particularly evident when the trestles are orientated at a large angle to the direction of flow. In this case, the transport of material through the central region of the bay is significantly reduced. A hypothesis accounting for this increased retardation was previously discussed: the orientation of the trestles at an angle (particularly a large angle) increases the number of trestles that obstruct the flow in the centre of the system, and hence present a greater impediment to flows. In addition, a channelling of flows in the direction of the trestle alignment is observed with a resultant accumulation of material at a downstream location. When the trestles are aligned with the direction of flow, material is channelled along the longitudinal axis. However, when the trestles are placed at an angle to the direction of flow the channelling of flows directs material away from the central axis. This may contribute to the reduced transport observed through the central region of the system.
- The removal of material from the system is also affected by the presence of the trestles. Figure A-20 displays the concentration of material at the low water mark, and provides a synoptic view of material remaining within different mariculture configurations after a complete tidal cycle. Despite the longitudinal transport distance of the dye across the domain being approximately equal for all configurations, a complete flushing of the system only occurs when the trestles are orientated at an angle to the direction of flow. When no trestles are included a significant concentration of the flood tide material remains, as does when trestles are aligned parallel to the direction of flow.
- The inclusion of the trestles, particularly when aligned at an angle to flow, also affects circulation patterns within the domain. Figure A-18(c) and (d) illustrates this occurrence. The ambient advective transport of the material is clearly affected by the structures with evidence to suggest the formation of a rotating vortex present in Figure A-18(d). This suggests that the inclusion of a bottom-feeding mariculture installation affects mixing within the system. Figure A-16 demonstrates a vertical profile of solute transport within the physical model.

The inclusion of the structures affects vertical mixing patterns significantly within the system. These secondary circulation patterns and induced turbulent flows have been hypothesized to increase the supply of nutrients to the feeders. Frechette et al., (1989), investigated the concentration and supply of nutrients to an inter-tidal bottom feeding mussel culture via field measurements and a two-dimensional model. The depletion of nutrients within the bottom culture due to intense feeding by the bivalves was found to be partially replenished by diffusion from the upper layers of the water column. This vertical diffusion was found to increase as bed roughness was increased (representing the increased frictional resistance of the structures). The research suggested that the installation of a bottom-feeding mariculture farm enhanced turbulent mixing and increased the flux of material to the feeders. Peterson and Beal, (1989), observed an increase in growth rates of 15-21% when enclosure walls surrounded the benthic feeders. The authors suggested that the increase in growth rates may be a result of the hydrodynamic roughness of the projecting walls increasing mixing into the otherwise depleted bottom waters.

These results demonstrate the significant effects that a mariculture installation may have on flow processes within a bay. The inclusion of the structures alters material transport quite drastically. In addition, the orientation of the structures plays a major role. Orientating the structures at even a slight angle (here 15°) affects: the lateral distribution of material, the longitudinal transport distances, and the flushing of the system on the ebb tide.

A feature of interest from a numerical modelling perspective is the pronounced asymmetry evident in the material transport study. While, this can be partially explained by the asymmetry of the system (e.g. when trestles are orientated at an angle), the numerical discretization may also be a factor. The system being simulated is a relatively complex system involving sharp bathymetric changes and a significant portion of the domain drying out during the inter-tidal period. Simulating the dynamics of the system requires the consideration of a large number of processes that occur at a number of different scales, from the large-scale advective transport to fine-scale eddy formations. The turbulence closure model plays a central role in incorporating these different flow processes. As mentioned, DIVAST incorporates the

one-equation mixing length turbulence closure model. This relatively simple turbulence model may not accurately compute turbulent viscosity values in complex flow situations and may be another factor explaining the asymmetry observed in this system. Simulations incorporating a more sophisticated turbulence model have been shown to provide greater accuracy (Olbert, 2006), and may better represent the dynamics of the system. The performance of different turbulence models in simulating material transport are discussed in greater detail in Chapter 5.

Another feature worthy of further research is the apparent channelling of material that is observed through the system. A similar phenomenon was observed in the scale modelling studies (Figure A-15). This suggests that rather than material being transported downstream in the direction of ambient flow, the actual orientation of the trestles themselves significantly affects the direction of transport. This would have major repercussions for downstream processes within a waterbody. This is particularly true for trestle farms located sequentially where the supply of nutrients may be computed based on ambient flows.

The combined physical and numerical model studies of flow through bottom trestles conducted as part of this research demonstrate a number of interesting features, namely: flows on both the flood and ebb tide are significantly impeded; the orientation of the trestles plays an important role in the supply of nutrients; turbulent and mixing processes within the waterbody are increased; the orientation of the trestles may have far-field effects on flow directions; and the flushing rates of the system are also affected. It is clear that a disregard for these factors will have significant implications for both aquaculture developments and the environmental health of the containing waterbody.

## **Appendix B**

### **Meteorological data**

---

## B.2 Met Eireann

Table B-1: Belmullet weather station data, April-May 2007

Date	Time	Rainfall (mm)	Wind Speed (m/s)	Wind Direction (Degrees from North)	Relative Humidity (%)	Temperature (Degrees Celsius)	Pressure (hPa)
23/04/2007	00:00	0.2	5	290	91	5.4	990.8
	01:00	0.7	7	320	79	5.9	991.4
	02:00	0	7	330	79	6.5	991.5
	03:00	0	7	340	77	6	991.6
	04:00	0	7	330	79	6.3	992
	05:00	0.1	6	320	85	6.5	993
	06:00	0	6	340	80	6.3	993.8
	07:00	0	6	330	83	6	994.3
	08:00	0	6	340	86	5.9	995.1
	09:00	0	5	340	82	6	996
	10:00	0	4	330	84	7.5	996.8
	11:00	0	6	320	73	8.4	997.8
	12:00	0.2	3	350	79	8	998.4
	13:00	0	5	330	74	9.3	998.5
	14:00	0	6	320	72	9.4	998.8
	15:00	0	4	340	72	9.4	999.1
	16:00	0	2	310	69	9.4	999.3
	17:00	0	2	260	77	8.3	999.7
	18:00	0	3	260	77	7.3	1000.3
	19:00	0	3	240	87	6.5	1000.8
	20:00	0	3	230	89	5.8	1000.7
	21:00	0	3	230	92	4.9	1001
	22:00	0	2	220	94	4.8	1001.2
	23:00	0	2	160	95	5.1	1001.3
24/04/2007	00:00	0	4	180	95	4.3	1000.7
	01:00	0	3	160	95	3.8	1000.4
	02:00	0	5	170	90	5	999.7
	03:00	0	4	170	90	4.9	998.7
	04:00	0	6	170	91	5.9	997.8
	05:00	0	8	170	94	6.4	997
	06:00	0.1	8	180	94	7.4	996.6
	07:00	0	8	190	94	7.5	996.1
	08:00	0.1	7	190	93	8	995.9
	09:00	0.1	6	210	93	8.5	995.6
	10:00	0	5	220	94	8	995.3
	11:00	0	7	230	80	10.5	995.1
	12:00	0	7	230	75	10.9	995
	13:00	0	7	230	72	10.5	994.3

Table B-1 continued

	14:00	0	6	230	74	11.1	993.7
	15:00	0.1	6	230	80	10.3	993.4
	16:00	0	6	230	82	9.5	993.1
	17:00	0.8	5	220	90	7.9	993.3
	18:00	0.5	5	220	94	8	993.3
	19:00	0	4	220	79	6.8	993.5
25/04/2007	20:00	0	4	220	97	7	993.7
	21:00	0	4	250	90	7.4	993.9
	22:00	0.9	6	260	87	7	994.3
	23:00	1.4	4	270	80	7.6	994.7
	00:00	0	7	270	74	8.1	995.2
	01:00	0.1	8	270	78	7	995.6
	02:00	0	6	260	85	7	995.7
	03:00	0.6	6	280	81	7.4	996.2
	04:00	0.4	6	280	87	6.8	996.5
	05:00	0	7	280	79	7.6	997.3
	06:00	0	6	270	76	7.8	997.9
	07:00	0	7	270	81	7.4	998.9
	08:00	0	8	260	84	7	999.5
	09:00	0.2	6	250	85	7.1	1000.4
	10:00	0	7	270	76	8.8	1001.3
	11:00	0.3	7	270	71	9	1002.4
	12:00	0	8	270	76	9.4	1003
	13:00	0	7	270	70	10.3	1003.6
	14:00	0.3	8	260	74	9.8	1004.2
	15:00	0	8	260	75	9.3	1004.7
	16:00	0	7	260	67	10	1005.1
	17:00	0	6	260	76	8.9	1005.7
	18:00	0	4	280	81	8.2	1006
	19:00	0	4	230	80	7.3	1006.5
	20:00	0	4	230	88	6	1006.6
	21:00	0	3	220	94	5.8	1006.8
	22:00	0	3	160	94	5.1	1006.7
	23:00	0	4	160	94	5.4	1006.5
26/04/2007	00:00	0	4	160	88	5.9	1005.4
	01:00	0	5	150	85	5.9	1003.9
	02:00	0	5	130	88	5.7	1001.9
	03:00	0	6	130	88	5.7	999.7
	04:00	0	7	130	86	5.9	997
	05:00	0	8	130	85	6.2	994.8
	06:00	0	12	140	85	7	991
	07:00	0	13	130	82	8	986.5
	08:00	0	14	130	87	8.1	984
	09:00	1.7	13	140	93	8.4	981.2
	10:00	2	13	160	95	8.8	979.7

Table B-1 continued

	11:00	1.8	13	180	87	9.8	979
	12:00	0	15	190	74	11	977.1
	13:00	0	20	190	72	10.3	975.8
	14:00	0.6	20	200	86	8.1	975.2
	15:00	0.1	22	210	76	8.6	975.4
	16:00	0	22	210	69	8.4	976
	17:00	0.7	20	210	79	7.6	977.1
	18:00	0	20	220	70	8.2	977.7
	19:00	0.3	21	220	85	5.8	977.8
	20:00	0.1	21	230	76	7.3	978.1
	21:00	0.4	18	220	83	7.1	979.2
	22:00	0.1	17	230	85	6.8	980.2
	23:00	0.9	15	240	91	6.1	981.2
27/04/2007	00:00	0.6	14	250	85	6.7	983
	01:00	0.1	14	260	79	7.4	985
	02:00	0	14	260	72	7.4	986.4
	03:00	0	13	250	59	7.2	987.3
	04:00	0.1	12	260	68	6.5	988.8
	05:00	0	12	250	74	5.9	989.8
	06:00	0	11	250	71	5.9	990.4
	07:00	0	10	240	75	6.7	991
	08:00	0	10	240	71	7.2	991.2
	09:00	0	10	220	72	7.6	990.9
	10:00	0.1	11	210	87	7.3	989.7
	11:00	0.6	12	200	94	7.2	987.9
	12:00	1.4	14	190	94	7.3	984.8
	13:00	2.6	16	190	94	7.8	981.1
	14:00	2.2	16	210	96	9.3	978.4
	15:00	3.3	17	210	97	9.5	975.3
	16:00	2.2	19	210	99	9.8	973.3
	17:00	1.9	18	210	99	9.7	971.7
	18:00	0.8	17	210	99	10	970.4
	19:00	1.4	15	220	99	10.1	970.1
	20:00	0	12	220	93	9.8	970.7
	21:00	0.2	12	230	93	9.2	972
	22:00	0	9	300	90	8	974.6
	23:00	0.1	8	300	83	7.7	977
28/04/2007	00:00	0	8	300	87	7.4	979.1
	01:00	0	8	290	65	7.8	980.3
	02:00	0	9	280	69	7.2	981.6
	03:00	0	11	280	82	5.7	982.5
	04:00	0	10	260	67	7.1	982.7
	05:00	0	10	260	66	7.4	983.6
	06:00	0.7	11	260	75	7	983.6
	07:00	0.1	11	250	79	6.4	983.8

Table B-1 continued

	08:00	0	11	250	77	7.3	983.9
	09:00	0.2	12	250	70	8.1	984.2
	10:00	0	13	240	73	8.8	985
	11:00	0	13	240	70	9.7	985.1
	12:00	0	14	250	68	10.1	985.9
	13:00	0	12	250	74	9.8	986.2
	14:00	0	13	250	75	10.8	986.3
	15:00	0.8	11	260	87	8	986.9
	16:00	0.5	8	280	92	8	987.5
	17:00	1.3	8	270	81	9	988.1
	18:00	0.2	8	260	84	8.5	988.9
	19:00	0.1	9	270	83	8.2	989.5
	20:00	0	8	270	78	8.7	990.1
	21:00	0.5	8	270	85	8.1	990.5
	22:00	0	8	260	79	8.5	990.9
	23:00	0	8	270	79	8.5	991.2
29/04/2007	00:00	0	7	270	79	7.6	991.7
	01:00	0	5	260	83	7.6	992
	02:00	0	6	270	82	7.8	992.5
	03:00	0	4	280	84	7.2	992.7
	04:00	0	4	260	86	7.4	993.2
	05:00	0	3	260	92	6.2	993.9
	06:00	0	4	270	85	6.9	994.7
	07:00	0	2	260	92	6.4	995.7
	08:00	0	3	230	90	7.8	996.8
	09:00	0	3	230	92	8.4	997.7
	10:00	0	2	210	90	8.8	998.4
	11:00	0	2	210	89	9	999
	12:00	0.9	1	170	88	8.5	999.9
	13:00	2.5	5	270	94	6.5	1001.4
	14:00	3.1	5	330	94	6.4	1002.8
	15:00	2.4	6	360	95	6.1	1004.4
	16:00	0.1	4	10	93	7.2	1006.2
	17:00	0	3	340	87	7.9	1007.5
	18:00	0	5	320	85	8	1008.9
	19:00	0	5	320	79	7.8	1010.3
	20:00	0	5	310	80	7.5	1011.5
	21:00	0	5	320	84	7.6	1013.2
	22:00	0	5	290	85	7	1014.1
	23:00	0	4	290	82	7.9	1014.6
30/04/2007	00:00	0	5	290	81	8.2	1015.8
	01:00	0	5	280	83	8	1016.2
	02:00	0	4	280	84	7.9	1015.9
	03:00	0	5	270	81	7.1	1016.5
	04:00	0	4	260	78	6.8	1016.6

Table B-1 continued

	05:00	0	4	240	81	7.1	1016.3
	06:00	0	5	220	85	6.9	1016.1
	07:00	0	6	220	86	8.1	1015.7
	08:00	0	9	200	88	8.7	1014.9
	09:00	0	11	210	87	9.2	1013.9
	10:00	0	13	200	87	9.7	1012.6
	11:00	0	14	200	86	10	1011.2
	12:00	0	16	200	86	9.9	1010.2
	13:00	2	16	200	97	9	1008.9
	14:00	0.5	16	200	97	9.2	1007.9
	15:00	0.8	14	210	95	11	1007.7
	16:00	0	12	250	91	11.4	1008.7
	17:00	0	11	260	79	10.8	1010
	18:00	0.1	11	270	76	9.4	1011.9
	19:00	0	10	270	68	9.2	1013
	20:00	1.4	10	280	68	7.8	1014.5
	21:00	0	10	280	63	7.9	1015.6
	22:00	0	9	280	62	8	1016.2
	23:00	0	8	260	71	7.7	1016.7
01/05/2007	00:00	0	10	260	76	7.8	1017.1
	01:00	0	9	250	78	7.1	1017.5
	02:00	0	9	260	73	7.3	1017.5
	03:00	0	8	250	74	7.2	1017.8
	04:00	0	9	280	79	6.7	1018.4
	05:00	0	9	270	78	7.8	1018.9
	06:00	0.1	10	270	75	7.7	1019.4
	07:00	0	10	260	74	8.2	1020.4
	08:00	0.3	10	280	85	6.8	1021.6
	09:00	0	9	270	82	6.7	1023
	10:00	0.1	9	280	66	8.3	1023.9
	11:00	0	9	290	68	9.6	1024.8
	12:00	0	9	290	64	10.3	1026
	13:00	0	10	270	71	9.9	1027
	14:00	0	9	270	71	10.6	1027.3
	15:00	0	9	270	71	10.1	1028
	16:00	0	8	260	72	10.4	1028.2
	17:00	0	8	250	74	9.9	1028.7
	18:00	0	8	250	77	9.8	1028.9
	19:00	0	8	250	83	9.3	1028.6
	20:00	0	9	230	80	9.2	1028.3
	21:00	0	9	220	85	8.9	1028
	22:00	0	9	230	89	9.1	1028
	23:00	0	10	250	87	9.9	1028
02/05/2007	00:00	0	10	240	88	9.7	1027.5
	01:00	0	10	240	88	9.8	1027.8

Table B-1 continued

	02:00	0	10	240	90	10.1	1027.9
	03:00	0	10	230	90	10.1	1027
	04:00	0	10	230	91	10.1	1026.6
	05:00	0	11	230	93	10.1	1026.4
	06:00	0	11	220	93	9.9	1026.1
	07:00	0.7	11	220	97	9.7	1025.9
	08:00	0	11	220	97	10	1026
	09:00	0	12	220	94	10.7	1026.1
	10:00	0	13	220	94	11	1025.5
	11:00	0	14	220	88	11.8	1025.3
	12:00	0	15	230	91	11.5	1025.3
	13:00	0	15	230	89	11.8	1024.9
	14:00	0	14	220	90	11.6	1024.4
	15:00	0	12	220	91	11.3	1023.6
	16:00	0	13	210	92	11	1023
	17:00	0	13	220	95	10.9	1022.3
	18:00	0	13	220	95	10.9	1021.7
	19:00	0	14	220	96	10.5	1021.1
	20:00	0	15	220	97	10.3	1020.6
	21:00	0.1	15	210	99	10.2	1019.7
	22:00	0	15	210	99	10.2	1019.1
	23:00	0	15	210	99	10.1	1018.5
03/05/2007	00:00	0.3	14	210	99	10	1017.4
	01:00	0.1	15	210	99	9.8	1016.8
	02:00	0.1	14	210	99	10	1015.9
	03:00	0.2	15	210	99	10	1014.8
	04:00	1	14	210	97	9.8	1015.3
	05:00	1.3	6	270	97	8.4	1015.8
	06:00	0.7	6	250	97	8	1016.3
	07:00	0.7	5	260	99	8.2	1016.6
	08:00	1.2	5	230	99	8.1	1016.9
	09:00	0.9	6	260	97	8.3	1017.6
	10:00	0.2	7	260	83	8	1017.8
	11:00	0	7	240	81	8.2	1017.8
	12:00	0	6	220	84	8.8	1017.5
	13:00	0	5	240	72	9	1017.1
	14:00	0	5	250	73	8.9	1017.4
	15:00	0	4	240	81	8.7	1016.2
	16:00	0	4	220	86	8.8	1015.4
	17:00	0	6	210	83	7.9	1015.7
	18:00	0	8	210	87	7.4	1015.7
	19:00	0	6	200	90	7.3	1014.4
	20:00	0	6	190	90	7.1	1015
	21:00	0	7	210	88	7	1014.3
	22:00	0	7	210	90	7.1	1014.1

Table B-1 continued

	23:00	<b>0.3</b>	<b>8</b>	<b>210</b>	<b>94</b>	<b>6.2</b>	<b>1013.9</b>
04/05/2007	00:00	<b>0.2</b>	<b>8</b>	<b>210</b>	<b>94</b>	<b>6.5</b>	<b>1013.7</b>
	01:00	<b>0.1</b>	<b>8</b>	<b>200</b>	<b>95</b>	<b>6.4</b>	<b>1013.5</b>
	02:00	<b>0.1</b>	<b>9</b>	<b>210</b>	<b>96</b>	<b>6.8</b>	<b>1013</b>
	03:00	<b>0</b>	<b>8</b>	<b>210</b>	<b>81</b>	<b>7</b>	<b>1012.7</b>
	04:00	<b>0</b>	<b>7</b>	<b>220</b>	<b>81</b>	<b>7.5</b>	<b>1012.4</b>
	05:00	<b>0.2</b>	<b>10</b>	<b>230</b>	<b>88</b>	<b>6.9</b>	<b>1012.9</b>
	06:00	<b>0.1</b>	<b>8</b>	<b>230</b>	<b>85</b>	<b>7</b>	<b>1013.2</b>
	07:00	<b>0</b>	<b>8</b>	<b>270</b>	<b>84</b>	<b>7</b>	<b>1014.2</b>
	08:00	<b>0</b>	<b>8</b>	<b>260</b>	<b>87</b>	<b>6.6</b>	<b>1015</b>
	09:00	<b>0.1</b>	<b>7</b>	<b>270</b>	<b>88</b>	<b>7</b>	<b>1016.4</b>
	10:00	<b>0</b>	<b>8</b>	<b>260</b>	<b>75</b>	<b>9.1</b>	<b>1017.4</b>
	11:00	<b>0.1</b>	<b>8</b>	<b>250</b>	<b>78</b>	<b>8.9</b>	<b>1018.3</b>
	12:00	<b>0</b>	<b>8</b>	<b>260</b>	<b>71</b>	<b>10.1</b>	<b>1018.9</b>
	13:00	<b>0</b>	<b>9</b>	<b>250</b>	<b>70</b>	<b>10.4</b>	<b>1019.4</b>
	14:00	<b>0</b>	<b>9</b>	<b>250</b>	<b>70</b>	<b>10.3</b>	<b>1019.6</b>
	15:00	<b>0</b>	<b>9</b>	<b>250</b>	<b>68</b>	<b>10.6</b>	<b>1019.7</b>
	16:00	<b>0</b>	<b>9</b>	<b>250</b>	<b>67</b>	<b>9.9</b>	<b>1019.9</b>
	17:00	<b>0</b>	<b>9</b>	<b>250</b>	<b>72</b>	<b>9</b>	<b>1020.4</b>
	18:00	<b>0</b>	<b>8</b>	<b>250</b>	<b>71</b>	<b>8.2</b>	<b>1020.9</b>
	19:00	<b>0</b>	<b>8</b>	<b>240</b>	<b>76</b>	<b>8.1</b>	<b>1021.3</b>
	20:00	<b>0</b>	<b>8</b>	<b>250</b>	<b>71</b>	<b>7.9</b>	<b>1021.9</b>
	21:00	<b>0</b>	<b>8</b>	<b>240</b>	<b>75</b>	<b>7.9</b>	<b>1021.9</b>
	22:00	<b>0</b>	<b>8</b>	<b>250</b>	<b>82</b>	<b>7.7</b>	<b>1022.2</b>
	23:00	<b>0</b>	<b>8</b>	<b>250</b>	<b>82</b>	<b>8.2</b>	<b>1022.8</b>
05/05/2007	00:00	<b>0</b>	<b>8</b>	<b>250</b>	<b>81</b>	<b>8.7</b>	<b>1022.3</b>
	01:00	<b>0</b>	<b>9</b>	<b>240</b>	<b>82</b>	<b>9</b>	<b>1022.1</b>
	02:00	<b>0.2</b>	<b>10</b>	<b>240</b>	<b>88</b>	<b>8.7</b>	<b>1022.1</b>
	03:00	<b>1</b>	<b>9</b>	<b>250</b>	<b>90</b>	<b>7.6</b>	<b>1022.5</b>
	04:00	<b>0</b>	<b>7</b>	<b>260</b>	<b>90</b>	<b>8.7</b>	<b>1022.7</b>
	05:00	<b>0</b>	<b>6</b>	<b>270</b>	<b>84</b>	<b>8.8</b>	<b>1023.4</b>
	06:00	<b>0</b>	<b>6</b>	<b>280</b>	<b>87</b>	<b>9.3</b>	<b>1023.9</b>
	07:00	<b>0</b>	<b>6</b>	<b>270</b>	<b>83</b>	<b>9.2</b>	<b>1024.7</b>
	08:00	<b>0.6</b>	<b>6</b>	<b>280</b>	<b>89</b>	<b>8.8</b>	<b>1025.8</b>
	09:00	<b>0</b>	<b>5</b>	<b>280</b>	<b>89</b>	<b>9.6</b>	<b>1026.8</b>
	10:00	<b>0</b>	<b>5</b>	<b>280</b>	<b>83</b>	<b>10.1</b>	<b>1027.6</b>
	11:00	<b>0</b>	<b>4</b>	<b>280</b>	<b>83</b>	<b>11</b>	<b>1028.1</b>
	12:00	<b>0</b>	<b>4</b>	<b>280</b>	<b>79</b>	<b>11.8</b>	<b>1028.8</b>
	13:00	<b>0</b>	<b>5</b>	<b>280</b>	<b>76</b>	<b>12.1</b>	<b>1029.5</b>
	14:00	<b>0</b>	<b>5</b>	<b>270</b>	<b>82</b>	<b>11.3</b>	<b>1029.7</b>
	15:00	<b>0</b>	<b>6</b>	<b>270</b>	<b>80</b>	<b>11.2</b>	<b>1030.1</b>
	16:00	<b>0</b>	<b>6</b>	<b>270</b>	<b>85</b>	<b>10.9</b>	<b>1030.2</b>
	17:00	<b>0</b>	<b>5</b>	<b>260</b>	<b>81</b>	<b>10.5</b>	<b>1030.5</b>
	18:00	<b>0</b>	<b>4</b>	<b>250</b>	<b>87</b>	<b>10</b>	<b>1030.9</b>
	19:00	<b>0</b>	<b>5</b>	<b>250</b>	<b>92</b>	<b>9.4</b>	<b>1031.1</b>

Table B-1 continued

	20:00	0	4	250	89	9.8	1031.5
	21:00	0	5	250	92	9	1031.6
	22:00	0	5	240	92	9	1031.8
	23:00	0	5	220	95	9	1031.8
06/05/2007	00:00	0	6	220	95	9.1	1031.7
	01:00	0	7	230	92	9	1031.5
	02:00	0	8	230	93	9.2	1031.5
	03:00	0	9	230	92	9.6	1031.1
	04:00	0	9	230	93	9.6	1030.8
	05:00	0	9	230	93	9.7	1030.4
	06:00	0	8	230	93	9.7	1030.3
	07:00	0	8	220	91	9.8	1030.2
	08:00	0	9	220	92	10	1030.4
	09:00	0	10	220	91	10.5	1030.6
	10:00	0	11	230	86	11.1	1030.6
	11:00	0	11	230	88	11.2	1030.4
	12:00	0	11	230	84	11.4	1030.3
	13:00	0	12	230	90	10.4	1029.7
	14:00	0	12	230	90	10.9	1029.6
	15:00	0	12	220	86	11.2	1028.9
	16:00	0	12	230	89	11.1	1028.5
	17:00	0	12	220	86	10.9	1028.1
	18:00	0	12	220	89	10.8	1027.8
	19:00	0	12	220	85	10.7	1027.3
	20:00	0	11	220	94	10.5	1026.9
	21:00	0	10	220	90	10.2	1026.1
	22:00	0	11	220	84	10.8	1025.7
	23:00	0	14	220	87	10.8	1025
07/05/2007	00:00	0	14	220	86	10.8	1024.2
	01:00	0	13	220	87	10.8	1023
	02:00	0.1	13	220	96	10	1022.3
	03:00	1.5	13	220	97	9.6	1021.3
	04:00	1.9	13	220	99	9.6	1020.6
	05:00	3.1	12	230	99	9.7	1020.4
	06:00	1.7	11	240	99	9.9	1020.4
	07:00	1.6	6	280	97	8.6	1021.9
	08:00	0.1	6	290	93	8.8	1022.7
	09:00	0	8	320	89	8.5	1023.6
	10:00	0	7	320	78	8.7	1024.7
	11:00	0	7	330	69	10	1025.7
	12:00	0	7	330	64	10	1026.5
	13:00	0	7	330	68	10.2	1027.2
	14:00	0	7	330	64	10.2	1027.9
	15:00	0	6	320	58	10	1028.1
	16:00	0	5	310	61	10.1	1028.4

Table B-1 continued

	17:00	0	5	300	61	9.6	1028.4
	18:00	0	4	290	62	8.4	1028.6
	19:00	0	4	300	74	7.1	1028.8
	20:00	0	4	280	74	7.2	1029.1
	21:00	0	5	260	88	6.8	1029.2
	22:00	0	6	270	69	7.8	1029.1
	23:00	0	7	270	69	7.8	1029.1
08/05/2007	00:00	0	7	270	76	7.6	1028.8
	01:00	0	8	260	76	8	1028.3
	02:00	0	8	260	81	7.4	1027.6
	03:00	0	8	260	80	7.6	1026.6
	04:00	0	9	270	74	8.5	1026.1
	05:00	0	10	260	81	8.7	1025.9
	06:00	0	10	260	78	8.9	1025.3
	07:00	0	10	260	83	9.3	1024.9
	08:00	0.3	11	270	89	8.7	1025
	09:00	0	11	270	89	8.9	1024.7
	10:00	0.3	10	260	95	9	1024.6
	11:00	0	10	270	93	9.5	1024.3
	12:00	0.2	10	270	93	9.6	1024.2
	13:00	0	10	270	93	10	1024.1
	14:00	0.4	8	270	93	10	1023.9
	15:00	0	9	270	93	10	1023.3
	16:00	0.1	8	270	95	10	1023.3
	17:00	0.3	8	270	95	10	1023.3
	18:00	0.2	8	280	96	10.1	1023.6
	19:00	0.1	7	280	96	10.1	1024
	20:00	0.1	7	280	96	10.1	1024.1
	21:00	0	7	280	95	10.2	1024.2
	22:00	0	7	280	91	10.6	1024.4
	23:00	0	8	280	90	10.7	1024.7
09/05/2007	00:00	0	8	280	89	10.7	1024.9
	01:00	0	8	270	91	10.4	1024.6
	02:00	0	8	280	93	10.1	1024.4
	03:00	0	8	270	87	10	1023.7
	04:00	0	9	280	81	9.4	1023.5
	05:00	0	9	280	78	9.3	1023.5
	06:00	0	9	280	83	9.3	1022.9
	07:00	0	10	270	84	9.4	1022.3
	08:00	0	9	260	87	9.4	1021.8
	09:00	0.1	9	260	92	9.4	1021.1
	10:00	0.9	9	250	97	9.2	1020.5
	11:00	0.5	10	250	97	9.7	1019
	12:00	0.2	10	250	97	10.3	1018.2
	13:00	0.6	10	250	97	10.8	1017.1

Table B-1 continued

	14:00	0.2	11	250	97	11	1015.1
	15:00	0	12	250	95	11	1013.8
	16:00	0	13	250	96	11	1012.4
	17:00	0.8	12	260	96	10.8	1010.6
	18:00	0.1	12	260	94	11.2	1009.7
	19:00	0	12	270	92	10.8	1008.9
	20:00	0	11	280	81	10.3	1008.9
	21:00	0	11	280	68	10	1009
	22:00	0.5	11	290	90	7.3	1009
	23:00	0.2	11	300	68	6.8	1009.3
10/05/2007	00:00	0.1	13	300	79	6.5	1010
	01:00	0.2	12	310	61	6.7	1009.6
	02:00	0.3	12	300	59	5.6	1009.9
	03:00	0.2	14	310	66	5.2	1009.5
	04:00	0.2	13	310	76	4.8	1009.1
	05:00	0.6	14	320	83	3.8	1009.2
	06:00	0.5	13	330	81	3.2	1008.8
	07:00	0.3	14	320	76	4.6	1008.4
	08:00	0.6	15	320	79	4.1	1008.7
	09:00	0.6	12	320	79	4.7	1008.2
	10:00	0.1	15	320	87	4.1	1007.7
	11:00	0.2	14	320	73	4.8	1007.3
	12:00	0.2	15	320	70	5.8	1006.6
	13:00	0.1	14	320	84	4.5	1006
	14:00	0.3	15	330	85	4.5	1005.4
	15:00	0.6	14	330	70	5	1004.6
	16:00	0.6	13	330	93	3.2	1004.4
	17:00	0.7	13	330	80	3.8	1003.5
	18:00	0.2	16	330	61	4.8	1003.3
	19:00	0.1	13	340	64	4	1002.7
	20:00	0.2	13	330	79	4.2	1002.3
	21:00	1.7	15	330	88	4	1002.9
	22:00	0	15	330	81	4.5	1003.4
	23:00	0	14	350	69	5.5	1004.1
11/05/2007	00:00	0.5	14	360	82	4	1005
	01:00	0.9	12	360	65	5	1006
	02:00	0.3	14	350	63	5.1	1006.7
	03:00	0.2	15	360	64	4	1007.3
	04:00	0.4	12	360	84	3.2	1007.9
	05:00	0.8	12	10	70	4.1	1008.5
	06:00	0	13	360	74	4.7	1009.7
	07:00	0.1	13	360	84	4.5	1011
	08:00	0	13	10	70	4.9	1011.9
	09:00	0.1	13	360	77	4.6	1013.4
	10:00	0	13	360	77	5.9	1014.7

Table B-1 continued

	11:00	0	12	360	79	6.3	1015.6
	12:00	0.3	12	360	81	5.2	1016.9
	13:00	0	13	10	76	6	1017.6
	14:00	0	12	360	69	7.8	1018.1
	15:00	0	13	10	58	7.6	1018.6
	16:00	0	13	10	63	7.2	1019.7
	17:00	0	12	10	69	6.4	1020.7
	18:00	0	11	360	67	6.9	1021.3
	19:00	0	12	10	78	5.5	1022.5
	20:00	0	11	20	79	4.8	1023.1
	21:00	0	11	10	71	5.8	1023.5
	22:00	0	10	10	68	5.8	1024.2
	23:00	0	10	10	70	5.2	1024.9
12/05/2007	00:00	0	10	20	78	5.2	1025.2
	01:00	0	10	20	77	4.6	1025.5
	02:00	0.4	7	10	87	4.2	1025.7
	03:00	0	9	20	76	4.7	1026
	04:00	0	8	40	81	4.5	1026.6
	05:00	1	8	10	75	3.9	1026.5
	06:00	0	7	20	74	4.4	1027
	07:00	0.1	9	30	74	4.4	1027.3
	08:00	0	8	10	84	4.2	1027.7
	09:00	0	7	50	83	5.7	1027.9
	10:00	0.4	6	20	86	5	1028.4
	11:00	0	6	50	76	6.2	1028.3
	12:00	0	6	40	73	7.2	1028.4
	13:00	0	6	40	66	7.6	1028.4
	14:00	0	5	30	72	7.7	1028.2
	15:00	0	4	40	66	7.5	1027.5
	16:00	0	5	50	67	7.4	1027.6
	17:00	0	5	40	78	7	1027.9
	18:00	0	4	40	81	6.4	1028
	19:00	0	2	10	82	5.9	1028
	20:00	0	1	90	88	4	1028.1
	21:00	0	1	160	88	2.9	1027.9
	22:00	0	1	240	97	3.2	1026.9
	23:00	0	1	220	96	2.6	1027
13/05/2007	00:00	0	2	140	91	3	1026.7
	01:00	0	3	170	91	2.9	1026.1
	02:00	0	4	170	88	3.3	1025.6
	03:00	0	4	170	90	4.2	1024.3
	04:00	0	5	180	94	5.2	1023.4
	05:00	0	4	200	83	6.2	1023.1
	06:00	0	5	210	88	6.5	1022.1
	07:00	0	6	210	90	6.7	1021.1

Table B-1 continued

	08:00	0	7	210	93	7	1020.9
	09:00	0	6	210	93	7.5	1020.2
	10:00	0	8	200	94	8	1019.5
	11:00	0.3	7	200	96	8.4	1019
	12:00	1.4	7	220	97	9.4	1018.6
	13:00	0.3	5	240	97	10.5	1018.2
	14:00	0	5	270	96	10.5	1017.9
	15:00	0	5	270	95	10.5	1017.6
	16:00	0	5	260	95	10.7	1017.2
	17:00	0	5	260	96	10.4	1017.2
	18:00	0	5	270	95	10.4	1016.9
	19:00	0	5	270	95	10.2	1017.2
	20:00	0	5	270	96	10	1017.1
	21:00	0	5	260	96	9.9	1017.4
	22:00	0	5	260	95	10	1017.3
	23:00	0	5	260	97	10	1017.2
14/05/2007	00:00	0	5	270	97	10	1017.5
	01:00	0	4	280	96	9.8	1017.7
	02:00	0	3	330	96	9.1	1018.3
	03:00	0	5	20	95	9	1019
	04:00	0	5	20	92	8.8	1019.7
	05:00	0	3	30	93	8.5	1020.4
	06:00	0	3	20	92	8.3	1021
	07:00	0	3	30	93	8.1	1021.6
	08:00	0	3	30	92	8.8	1022.4
	09:00	0	3	40	89	9.5	1023
	10:00	0	3	50	79	10.8	1023.4
	11:00	0	3	70	76	11.3	1023.6
	12:00	0	3	50	71	12.3	1023.6
	13:00	0	3	70	66	13	1023.8
	14:00	0	3	60	67	13	1023.7
	15:00	0	3	50	65	13.2	1023.5
	16:00	0	4	40	67	12.8	1023.4
	17:00	0	4	60	68	11	1023.2
	18:00	0	3	60	74	9.4	1023.2
	19:00	0	3	70	83	7.4	1023.4
	20:00	0	2	80	85	6.1	1023.4
	21:00	0	1	60	91	5.6	1023.5
	22:00	0	1	160	91	5.6	1023.5
	23:00	0	1	170	89	5.6	1023.5
	00:00	0	1	160	95	4.6	1023.1
	01:00	0	1	180	94	5	1022.9
	02:00	0	3	170	94	5	1022.6
	03:00	0	3	180	95	5.2	1022.2
	04:00	0	3	170	95	4.7	1022

Table B-1 continued

	05:00	0	2	160	94	5	1021.6
	06:00	0	3	160	94	5.8	1021.5
	07:00	0	5	170	93	7	1021.4
	08:00	0	4	170	93	7.5	1021.5
	09:00	0	4	190	90	8.9	1021.2
	10:00	0	4	200	88	10	1021.1
	11:00	0	4	200	84	10.9	1021.1
	12:00	0	5	200	80	11	1021
	13:00	0	7	210	80	12.5	1020.4
	14:00	0	7	210	80	12.7	1020.2
	15:00	0	6	210	80	12.8	1019.6
	16:00	0	5	220	81	11.7	1019.7
	17:00	0	4	220	79	12.1	1019.6
	18:00	0	4	240	86	11	1019.7
	19:00	0	3	250	86	10	1019.9
	20:00	0	3	250	92	9.5	1020
	21:00	0	2	240	89	9.5	1020.1
	22:00	0	2	180	95	9.4	1020.2
	23:00	0	3	170	96	9	1020.3
15/05/2007	00:00	0	2	160	93	9.1	1020.4
	01:00	0	4	170	92	8.1	1020.5
	02:00	0	3	170	92	8	1020.9
	03:00	0	4	160	87	7.8	1020.9
	04:00	0	3	160	87	7.5	1020.7
	05:00	0	3	150	87	7.5	1021
	06:00	0	3	170	87	7.5	1021.2
	07:00	0	2	150	88	7.3	1021.8
	08:00	0	2	160	86	8.1	1022
	09:00	0	3	160	84	9	1022.4
	10:00	0	3	180	78	9.8	1022.6
	11:00	0	3	180	85	11	1022.8
	12:00	0	4	180	82	11.5	1023
	13:00	0	4	190	77	12	1023.2
	14:00	0	5	210	76	12	1023.3
	15:00	0	5	200	80	11.9	1023.2
	16:00	0	6	210	77	11.7	1023.5
	17:00	0	5	210	80	11	1023.7
	18:00	0	4	230	82	10.7	1024
	19:00	0	3	240	84	10	1024.3
	20:00	0	2	240	92	9.4	1024.4
	21:00	0	1	180	92	9.4	1024.7
	22:00	0	1	190	95	9.2	1024.9
	23:00	0	1	140	91	9.1	1024.9
16/05/2007	00:00	0	1	180	92	9	1025
	01:00	0	0	0	95	8.8	1025.1

Table B-1 continued

	02:00	0	1	90	92	8.8	1025.2
	03:00	0	1	110	92	8.8	1024.9
	04:00	0	1	110	95	6.4	1024.7
	05:00	0	1	110	95	6	1024.7
	06:00	0	0	0	97	5	1024.8
	07:00	0	0	0	97	4.5	1024.9
	08:00	0	1	90	94	6	1024.9
	09:00	0	1	90	83	9.7	1025
	10:00	0	1	90	72	12.2	1024.8
	11:00	0	2	80	69	13.7	1024.9
	12:00	0	4	70	67	13.5	1024.6
	13:00	0	4	70	62	14.2	1024.2
	14:00	0	5	60	62	13.7	1023.8
	15:00	0	5	60	68	12.7	1023.3
	16:00	0	5	60	68	12.7	1022.9
	17:00	0	4	110	72	11.3	1022.5
	18:00	0	4	120	73	10	1022.6
	19:00	0	3	80	86	7.5	1023
	20:00	0	3	80	86	6	1023.2
	21:00	0	2	90	89	5.9	1023.1
	22:00	0	3	90	86	6	1022.8
	23:00	0	1	100	89	5	1022.7
17/05/2007	00:00	0	1	90	92	4.4	1022.4
	01:00	0	2	110	95	5	1022.1
	02:00	0	2	120	92	4.6	1022
	03:00	0	1	130	92	4.8	1021.5
	04:00	0	1	140	93	4.5	1021
	05:00	0	1	110	97	3.8	1021.1
	06:00	0	1	130	95	4.4	1021.2
	07:00	0	1	110	97	3.8	1021.5
	08:00	0	1	160	97	5	1021.7
	09:00	0	1	200	93	7.6	1021.5
	10:00	0	1	180	86	9.9	1021.3
	11:00	0	2	180	78	12	1021
	12:00	0	3	190	75	13.4	1020.6
	13:00	0	4	200	71	13.7	1020.5
	14:00	0	4	200	67	14.1	1020.1
	15:00	0	4	220	68	13.1	1019.9
	16:00	0	4	210	67	12.7	1019.6
	17:00	0	4	210	71	12.1	1019.2
	18:00	0	4	220	70	10.9	1019.2
	19:00	0	2	230	76	10	1019.4
	20:00	0	1	230	82	9.7	1019.4
	21:00	0	1	110	85	9.5	1019
	22:00	0	1	120	83	9.5	1018.8

Table B-1 continued

	23:00	0	1	150	85	9.4	1018.7
18/05/2007	00:00	0	1	160	92	8	1018.4
	01:00	0	3	190	89	8.2	1018.2
	02:00	0	4	160	89	8.6	1018
	03:00	0	4	180	92	8.4	1017.6
	04:00	0	4	180	90	7.9	1017.3
	05:00	0	2	160	88	7.2	1017
	06:00	0	2	160	91	6.4	1016.9
	07:00	0	1	170	89	6	1017.1
	08:00	0	1	150	88	6	1017.1
	09:00	0	1	120	85	8.9	1016.9
	10:00	0	1	170	80	10.8	1017.2
	11:00	0	1	190	67	12.7	1017.1
	12:00	0	1	190	64	14	1016.9
	13:00	0	1	220	58	14.8	1017.1
	14:00	0	2	220	57	14	1017
	15:00	0	3	270	60	12.5	1016.8
	16:00	0	3	250	65	12.2	1016.7
	17:00	0	4	260	78	11	1017.2
	18:00	0	4	260	88	9.9	1017.5
	19:00	0	3	260	92	9	1018.1
	20:00	0	6	340	92	8.2	1019
	21:00	0	6	340	89	8	1019.5
	22:00	0	5	350	91	7.7	1019.6
	23:00	0	6	360	96	7.1	1019.8
19/05/2007	00:00	0.6	6	360	91	7	1019.9
	01:00	0.1	5	350	90	6.8	1020
	02:00	0	5	360	81	6.5	1020.1
	03:00	0	4	360	82	6.2	1019.9
	04:00	0	4	360	79	6.4	1020.1
	05:00	0	4	350	82	6.2	1020.4
	06:00	0	4	360	86	5.1	1020.7
	07:00	0	3	10	87	4.7	1021
	08:00	0	3	350	73	7.8	1021.4
	09:00	0	4	340	66	8.5	1021.5
	10:00	0	5	340	65	9.5	1021.5
	11:00	0	5	350	66	9.9	1021.9
	12:00	0	4	340	60	10	1021.7
	13:00	0	5	330	54	10	1021.6
	14:00	0	5	300	58	9.9	1021.4
	15:00	0	4	300	58	10.2	1021.2
	16:00	0	4	310	64	9	1020.9
	17:00	0	4	280	68	7.5	1020.6
	18:00	0	2	280	67	8	1020.4
	19:00	0	4	280	82	6	1020.2

Table B-1 continued

	20:00	2.2	4	330	92	4.7	1020.5
	21:00	1.6	3	360	95	4.6	1020.5
	22:00	0.3	1	310	95	3.5	1020.3
	23:00	0.5	4	350	92	3.8	1020.2
20/05/2007	00:00	0.1	3	350	92	3.7	1020
	01:00	0	3	10	90	3.8	1020.1
	02:00	0.1	3	360	93	3.2	1019.8
	03:00	0	2	340	90	3.1	1019.5
	04:00	0	4	350	85	4.2	1019.3
	05:00	0	3	20	89	4.6	1019.4
	06:00	0.1	4	20	78	4.8	1019.6
	07:00	0	5	340	84	4.8	1019.7
	08:00	0.4	5	40	84	4.8	1020
	09:00	0	5	30	81	6.5	1020
	10:00	0.2	4	350	81	7	1020.2
	11:00	0	7	360	68	9.1	1020.2
	12:00	0	6	360	70	9.6	1020.1
	13:00	0	6	10	66	10.4	1020
	14:00	0	7	20	70	10.1	1019.8
	15:00	0.1	7	30	63	10	1019.6
	16:00	0	8	30	62	10.3	1019.5
	17:00	0	8	30	75	9.1	1019.4
	18:00	0	8	20	76	8.8	1019.3
	19:00	0	6	40	80	7.5	1019.5
	20:00	0	6	40	84	7.7	1019.5
	21:00	0	7	50	86	8.3	1019.7
	22:00	0	7	40	85	8.1	1019.6
	23:00	0	6	40	87	8.2	1019.8
21/05/2007	00:00	0	6	50	86	8.2	1019.8
	01:00	0	6	40	87	8.2	1019.9
	02:00	0	5	40	88	8.4	1019.8
	03:00	0	5	50	88	8.4	1019.7
	04:00	0	5	40	89	8.4	1019.6
	05:00	0	4	50	93	8.3	1019.8
	06:00	0	5	50	92	8.4	1020.1
	07:00	0	5	50	92	8.5	1020.1
	08:00	0	6	50	89	9	1020.6
	09:00	0	6	50	87	9.5	1021.1
	10:00	0	5	50	88	9.5	1021.5
	11:00	0	6	50	78	11.4	1021.7
	12:00	0	8	50	76	11	1022
	13:00	0	8	50	77	11.8	1021.9
	14:00	0	7	50	77	11.5	1022.1
	15:00	0	8	50	77	11.5	1022.2
	16:00	0	7	50	77	11.1	1023.1

Table B-1 continued

	17:00	0	7	50	79	10.7	1023.2
	18:00	0	7	50	79	10	1023.9
	19:00	0	6	50	88	8.9	1024.7
	20:00	0	5	50	92	8.3	1025.5
	21:00	0	3	60	93	7	1026.3
	22:00	0	4	50	94	8	1026.8
	23:00	0	3	60	94	7.6	1027.5
22/05/2007	00:00	0	4	80	93	7.5	1027.8
	01:00	0	2	70	92	6	1028.2
	02:00	0	4	80	93	6.9	1028.4
	03:00	0	4	70	93	7	1028.7
	04:00	0	6	70	91	7.1	1029.2
	05:00	0	3	80	91	6.9	1030
	06:00	0	2	90	88	6.8	1030.4
	07:00	0	1	110	88	6.8	1031
	08:00	0	1	60	89	7.7	1031.7
	09:00	0	1	130	82	10.3	1032.2
	10:00	0	3	60	76	11.4	1032.5
	11:00	0	4	70	68	12.8	1032.7
	12:00	0	5	70	68	13.9	1032.9
	13:00	0	5	70	68	14.5	1033.2
	14:00	0	4	60	67	14	1033.3
	15:00	0	4	60	67	14	1033.3
	16:00	0	5	50	71	12.9	1033.3
	17:00	0	6	50	78	11.7	1033.7
	18:00	0	5	50	81	10.8	1034.2
	19:00	0	4	50	88	9.1	1034.6
	20:00	0	4	50	90	8.2	1034.9
	21:00	0	3	50	93	7.7	1035.2
	22:00	0	4	50	90	7.5	1035.5
	23:00	0	4	70	88	7.2	1035.9
23/05/2007	00:00	0	2	70	88	6.8	1036
	01:00	0	3	70	88	6.8	1036
	02:00	0	3	60	91	6.8	1035.7
	03:00	0	4	70	94	6.4	1035.7
	04:00	0	2	70	95	5.5	1035.6
	05:00	0	4	70	95	5.8	1035.5
	06:00	0	4	60	95	6.3	1035.7
	07:00	0	4	70	95	6.1	1036.2
	08:00	0	4	70	93	7.8	1036.2
	09:00	0	4	80	87	9.7	1036.6
	10:00	0	3	80	84	10.7	1036.6
	11:00	0	4	70	75	12	1036.8
	12:00	0	4	60	75	12.1	1036.8
	13:00	0	5	50	75	11.1	1036.8

Table B-1 continued

	14:00	0	5	60	74	12.2	1036.4
	15:00	0	6	60	76	11.9	1036.1
	16:00	0	7	60	80	11.4	1035.5
	17:00	0	5	60	80	11.2	1035.4
	18:00	0	5	60	86	10	1035.7
	19:00	0	5	60	90	8.5	1036
	20:00	0	4	70	96	7.2	1036.2
	21:00	0	3	80	94	6.9	1036.4
	22:00	0	3	40	96	6.9	1036.6
	23:00	0	3	40	94	7	1036.6
24/05/2007	00:00	0	4	70	96	6.9	1036.6
	01:00	0	2	60	94	5.7	1036.7
	02:00	0	3	70	95	5.3	1036
	03:00	0	4	90	92	5.6	1035.7
	04:00	0	3	90	95	4.9	1035.3
	05:00	0	3	70	94	5.6	1035.5
	06:00	0	5	60	95	6.6	1035.6
	07:00	0	4	80	91	7.5	1036.1
	08:00	0	5	80	93	8.1	1036.5
	09:00	0	5	70	89	9.4	1036.8
	10:00	0	6	60	92	11	1036.5
	11:00	0	6	70	72	12.5	1036.3
	12:00	0	6	70	76	13	1036.2
	13:00	0	7	60	77	12.5	1036.1
	14:00	0	6	50	78	12.4	1035.9
	15:00	0	6	60	72	12.5	1035.5
	16:00	0	7	60	69	12.4	1034.7
	17:00	0	7	60	76	10.8	1034.6
	18:00	0	7	60	80	9.8	1034.4
	19:00	0	6	60	88	8.9	1034.6
	20:00	0	6	60	93	8.3	1034.8
	21:00	0	4	60	88	8.8	1035.1
	22:00	0	4	70	85	8.8	1034.4
	23:00	0	6	60	88	9	1033.7